Response of Grooved Composite Laminates to Out-of-Plane Contact Loading via Numerical Models

by

Jaffar S. Iqbal

B.S. Aerospace Engineering
Massachusetts Institute of Technology, 2008

Submitted to the Department of Aeronautics and Astronautics
in partial fulfillment of the requirements for the degree of

Master of Science in Aeronautics and Astronautics

at the

MASSACHUSETTS INSTITUTE OF TECHNOLOGY

September 2011

Author .....
Department of Aeronautics and Astronautics
August 18, 2011

Certified by .....
Professor Paul A. Lagacé
Professor of Aeronautics and Astronautics and Engineering Systems
Thesis Supervisor

Accepted by .....
Professor Eytan H. Modiano
Professor of Aeronautics and Astronautics
Chair, Graduate Program Committee

Response of Grooved Composite Laminates to Out-of-Plane Contact Loading via Numerical Models

by

Jaffar S. Iqbal

Submitted to the Department of Aeronautics and Astronautics on August 18, 2011,
in partial fulfillment of the requirements for the degree of
Master of Science in Aeronautics and Astronautics

Abstract

The response of grooved composite laminates to out-of-plane contact loading is examined using numerical modeling through the consideration of contact pressure and stresses within the laminate, with particular focus on the area local to the groove. Finite element analysis is employed via ABAQUS, a commercial finite element modeling software. The indentor is modeled as a rigid body, and the validity of this approximation is assessed through comparison with a deformable, linear elastic indentor. The influence of ply angle is investigated through consideration of a family of $[\pm\theta/0]_{13S}$ laminates for values of θ of 15°, 30°, 45°, and 60°, along with a quasi-isotropic $[\pm 45/0/90]_{10S}$ and a crossply $[0/90]_{20S}$ configuration, all using T700/2510 graphite/epoxy. The linearity of the response is investigated, and two loading configurations are studied and compared: a two-dimensional, cylinder-loaded configuration, and a three-dimensional, sphere-loaded configuration. Results show that the Hertzian contact model for isotropic bodies cannot be used to determine contact pressure due to an inability of that model to analytically determine the appropriate contact length. The basic form of the contact pressure curve is similar to the Hertzian model, but with significant local variations superposed due to stiffness variation, particularly in the longitudinal direction, due to ply orientation angle. Thus, if the contact length is supplied, the Hertzian model can be a valid overall approximation. Total vertical load magnitude is determined to be a primary factor in the response, as it determines contact length, and thus the distribution of contact pressure and the form of the stress field. The response is found to vary with significant nonlinearity with respect to applied load due to the relationship with contact length. The rigid body approximation of the steel indentor is deemed sufficiently accurate to capture the overall behavior, due to the high difference in stiffness between the steel indentor and the through-thickness stiffness of the composite. There is significant variation between the two-dimensional models and the three-dimensional models, particularly in determining the magnitude of the response. However, the two-dimensional model is sufficient to observe trends, and could be of use in preliminary design and analysis, although the full three-dimensional model is required to accurately determine the response in the final analysis, largely due to important issues of variation along the groove. In general, stress behavior is dependent on the laminate and the particular stress, with stress fields between laminates showing some similar trends, but also high variability depending on the composition of the laminate.

Thesis Supervisor: Professor Paul A. Lagacé
Title: Professor of Aeronautics and Astronautics and Engineering Systems

Acknowledgments

First and foremost, all my thanks to my advisor, Professor Paul Lagacé. Without his help, guidance, and patience, I might never have been able to complete this work. Through the last weeks of completing this work especially, he has gone above and beyond in helping me finish on time. This thesis, and my research, are immeasurably better because of his help. He will always have my most sincere gratitude.

My thanks also to my labmates in TELAMS that helped me complete this work. A special thank you to Brandon Reynante, for allowing me to use his mighty computer to complete my simulations, without which, those three-dimensional models would have taken weeks to run. Despite having his own research to do, Brandon was always accommodating to my intrusions, and all his help is much appreciated. Thanks are also due to Holly Jeffrey, who helped me so much when I was starting out, and is always a great support and help in discussing both her research and mine. I owe a great deal to the preceding work of Chris Bastien, who I have never even met, but whose work provided a solid foundation for my own. My thanks also go out to all of the other members of TELAMS who patiently listened to my research talks, and were incredibly helpful in bouncing ideas around with, despite my infrequent appearances in the office.

Finally, a sincere thanks to all of my family. I could never be where I am today if it wasn't for the support of my parents. Their guidance has always been appreciated, and I can't even say how much their support means to me.

Foreword

This work was performed in the Technology Laboratory for Advanced Materials and Structures (TELAMS) of the Department of Aeronautics and Astronautics at the Massachusetts Institute of Technology. This work was sponsored by The Boeing Company under the General Terms Agreement between MIT and Boeing as Boeing Award Number MIT-BA-GTA-1.

Table of Contents

List of Figures

List of Tables

Nomenclature

a_C	semi-major axis of elliptical contact area in the ϕ-x_2 plane
a_H	semi-major axis of projected elliptical contact area in the x_1-x_2 plane for Hertzian contact model
b_C	semi-minor axis of elliptical contact area in the ϕ-x_2 plane
E_{avg}	average Young's modulus for Hertzian contact model
E_i	Young's modulus in the i-direction ($i = 1, 2, 3$)
G_{ij}	shear modulus in the i-j plane ($i, j = 1, 2, 3$)
L	plate dimension in 1-direction corresponding to length
L_C	contact length along the arc of the groove
P	applied load
p_C	contact pressure
p_C^*	normalized contact pressure
$p_{C_{max}}^*$	maximum normalized contact pressure
r	radial component of the (r, ϕ, x_2) cylindrical coordinate system originating at the groove center of curvature
r_C	radial position of maximum compressive stress
r_g	groove radius
r_S	radial position of maximum shear stress
r_T	radial position of maximum tensile stress
t	plate dimension in 3-direction corresponding to thickness
t_{ply}	laminate ply thickness
w	plate dimension in 2-direction corresponding to width

x_1	coordinate axis parallel to the 1-direction in the (x_1, x_2, x_3) rectangular coordinate system originating at the center of the laminate
x_2	coordinate axis parallel to the 2-direction in the (x_1, x_2, x_3) rectangular coordinate system originating at the center of the laminate
x_{2_C}	x_2-coordinate of the location of maximum compressive stress
x_{2_P}	x_2-coordinate of the location of maximum contact pressure
x_{2_S}	x_2-coordinate of the location of maximum shear stress
x_{2_T}	x_2-coordinate of the location of maximum tensile stress
x_3	coordinate axis parallel to the 3-direction in the (x_1, x_2, x_3) rectangular coordinate system originating at the center of the laminate
θ	ply orientation angle, measured from x_1
ν_{avg}	averaged Poisson's ratio for Hertzian contact model
ν_{ij}	Poisson's ratio relating strain in the i-direction to strain in the j-direction ($i, j = 1, 2, 3$)
σ_C^*	maximum normalized compressive stress
σ_{ij}	stress tensor component ($i, j = 1, 2, 3$)
σ_{ij}^*	normalized stress tensor component ($i, j = 1, 2, 3$)
σ_{max}	maximum pressure parameter for Hertzian contact model
σ_S^*	maximum normalized shear stress
σ_T^*	maximum normalized tensile stress
ϕ	angular component of the (r, ϕ, x_2) cylindrical coordinate system originating at the groove center of curvature
ϕ_C	angular position of maximum compressive stress
$\phi_{contact}$	maximum angle of contact
ϕ_P	angular position of maximum contact pressure
ϕ_S	angular position of maximum shear stress
ϕ_T	angular position of maximum tensile stress

Chapter 1

INTRODUCTION

Carbon-fiber/epoxy composites, a material in which aligned carbon fibers are embedded in an epoxy matrix, are seeing increased use in aircraft and space systems. This is primarily due to the high strength-to-weight and stiffness-to-weight ratios of the material, and the ability to highly tailor structures to the expected loading. In aerospace applications, where the weight on a system is at a premium, the weight savings of a light but strong and/or stiff material can greatly increase performance. For example, recently aerospace companies have been leveraging these composites to construct the next generation of lightweight aircraft, such as the Boeing 787 and the Airbus A350-XWB. In these applications, where composite materials make up as much as 80% of the airframe structure by volume, but only 50% by weight, the weight savings lead to greatly increased fuel efficency [1, 2, 3]. This efficiency is an enticing prospect for airlines looking to buy new aircraft in an era of greatly increased fuel prices.

However, widespread adoption of these materials has been relatively slow. Despite being around for nearly half a century, these materials are only recently finding large scale adoption on major jet airliners. This is mostly due to the complexity of designing an advanced composite structure. The response of these materials is often much more difficult to predict, compared to the standard aluminum structure, due to some unique properties and a gap in the understanding of some of the fundamental behavior. First, the composite formed from aligned carbon fibers and epoxy is orthotropic, thereby

having a different response depending on the direction in which the material is loaded. This is in contrast to an isotropic material, like most metals, that are uniform in response irrespective of the direction in which they are loaded. Second, carbon-fiber/epoxy composites are primarily used in a laminate form, allowing a given layer of aligned fibers to stiffen a structure in a specific direction. These layers can then be stacked at varying angles to form a structure that is uniquely designed to withstand a very specific loading. This is ideal for aircraft designers as it utilizes a material effectively to create as light a structure as possible for a given performance. However the individual layers of a laminated composite, which can be aligned at any particular angle, can have complex interactions. These interactions, at the most basic level, are due to the orthotropic nature of the individual composite plies. The plies, which are potentially aligned in many different directions, can all respond in very different ways when subjected to a single loading. This generates a complex interaction between the layers of a full-scale structure. In order to understand these interactions, and the overall response of the structure to a given load, a detailed structural analysis must be performed. For most complex aerospace structures, this analysis is beyond what is possible with a closed-form, analytical solution.

As with all materials, there are some compromises when using a composite material. While these composites are good at carrying a load in the plane of the plies, they are less effective at carrying other loads. Carbon-fiber/epoxy composites are primarily used in a laminated form, allowing the layers of aligned fibers to stiffen a structure in a specific direction. This design makes laminated composites very effective at transmitting loads in the plane of the laminate, along the direction of the aligned fibers. However there are some applications that also place a structure in a transverse, out-of-plane, loading, applying a load to the laminate perpendicular to the composite plies and orthogonal to all the fibers. In this scenario, the material is much worse at transmitting load compared to a metal structure. The metal structure is equally strong in all directions, whereas the aligned nature of the composite structure makes it stronger in some directions at the expense of strength in other directions. An aligned carbon-fiber epoxy composite that is equally effective in all

three dimensions, and cost effective, has yet to be designed.

Out-of-plane loading of composites has been studied at length. These types of loads put a structure at the greatest risk due to the low strength of the material in that transverse direction. As such, the response of a structure to this loading needs to be understood. Most of the work in this area is focused on short time-frame loadings such as impact or quasi-static loading. These represent studies of real world events such as debris impact, arms fire, and bird strikes on composite plates, such as an aircraft skin. There has been relatively little work done on analyzing composite structures that are intended to take a sustained static transverse contact load. This is mostly because few such composite structures exist.

There are a few composite structures designed to take a transverse load that would benefit from further analysis and understanding, for example the telescoping spar designed by Sahr et al [4]. This spar is designed for use in the spanwise morphing wing of a roadable aircraft, what is essentially a flying car, in which the wings are stored in the roof of the vehicle in a telescoping fashion. The spar for this wing is composed of two composite tubes, used for their weight savings in a structure that primarily sees a bending load. These tubes are encircled by grooves and are connected to each other by steel ball-bearings that allow the tubes to extend or retract in a rolling manner within one another, along with the rest of the wing. The steel balls would then be responsible for transmitting the lifting load from one section of wing to the other, acting perpendicular to the composite tube. Such a wing design is not only useful for a flying car concept, but also has other potential applications such as compact wings on unmanned aerial vehicles (UAV) and spanwise morphing wings on fixed-wing aircraft. This design and its loading represent a complex structural interaction. The steel balls will load the grooved composite tubes transversely in a mechanism that has not been studied and is little understood. It represents a combination of two difficult analyses, a composite structure under transverse loading, and an introduction of load through the contact of two bodies. Individually, these mechanisms have been studied in detail, but combined represent a new avenue for research.

The technology to model and investigate such structures exists, and has recently advanced to a level capable of producing meaningful results. Since the 1980's, engineers have used the finite element method to model structures via computer. As computing power has increased, so has the ability to model composite structures in even greater detail. It is now possible to computationally model individual plies within a composite structure to observe the stress and strain at increasingly small lengthscales, where it is impossible or impractical to do so in the lab with a real structure. In addition, a set of tools exist that enable the computational modeling of contact between two bodies, developed in part to enable analysis of the transverse impact events, as described above.

Through this work, the basic understanding of the basic response of a grooved composite structure to a contact loading from a steel ball bearing is sought. This represents a case that can be applied to an application such as that described above, of the telescoping composite spar concept as described. Previous initial work [5, 6] has been done on understanding the underlying principles in the response of a grooved structure to out-of-plane loading, and this work makes use of the conclusions reached in that research. The purpose of this investigation is to determine the major factors and trends that describe the contact pressure between the loaded steel ball and the composite groove, and the resulting stress distribution within the composite laminate.

Chapter 2

PREVIOUS WORK

Carbon-fiber composites, while generally strong and tailored to loading in the plane of the laminate, are not usually designed to carry sustained transverse loads, normal to the fiber direction. Thus, little prior work specific to that structural situation has been done. Fortunately, work in other areas, specifically low-velocity impact and quasi-static indentation, can be applied to the current investigation. Modeling of the contact pressure between two bodies was initially developed for use in optics, but can be applied to use in composites and indentation, and by extension, transversely loaded grooved composites. Quasi-static indentation was developed as a means to study low-velocity impact and the resulting damage, but its static nature lends itself to application in sustained static loading and the response of composites. Finally, two previous investigations from the current line of research lay the foundation for the investigation of the transverse loading of grooved composites.

2.1 Contact Modeling

Initial work in the contact of two curved bodies was done by Heinrich Hertz in 1881 [7]. Hertz developed an analytical approximation for contact pressures and areas for contact between two linear elastic isotropic bodies with constant radii of curvature. Hertz assumed an elliptical contact area, the parameters of which are dependent on the materials involved and the shapes of the interacting bodies. The matching con-

tact stress is now referred to as a Hertzian Pressure Distribution, the parameters of which depend on the shape of the interacting bodies and the magnitude of the applied load. Willis extended the theory of Hertz to apply to anisotropic bodies [8], requiring the implementation of a Fourier Transform and the numerical evaluation of the final contour integrals. This was not a complete analytical solution, but remains applicable to numerous contact situations. This includes particular transverse isotropic materials, such as carbon-fiber/epoxy composites. Willis' work not only provides a contact pressure distribution between two bodies, but also the consequent force-deflection equation or "Contact Law". For a transverse isotropic half-space this equation was found to follow a 3/2 power law form.

Yang and Sun verified Willis' contact law with static load testing, investigating the loading behavior of glass/epoxy and graphite/epoxy composite laminates [9]. Good correlation with Willis' 3/2 power law was found for loading of the composites, though unloading was found to follow a 5/2 power law due to damage developed during the loading cycle. Tan and Sun applied Willis' power law for static contact loading to a numerical low-velocity impact model of graphite/epoxy composites, and found good correlation with experimental low-velocity impact testing [10].

Work by Keer and Miller [11], and Sankar and Sun [12] investigated the pressure distribution for indentation of a finite orthotropic layer in bending, as opposed to the solution for a semi-infinite anisotropic half-space developed by Willis. They found that, for small ratios of contact length to plate thickness, the Hertzian distribution is an accurate approximation of the pressure between the two bodies. However at larger ratios, the pressure distribution took on a saddle shape as the plate began to conform to the semi-spherical indentor, lowering the contact pressure near the center of contact. Wu and Yen extended this investigation to look specifically at laminated composite plates in bending [13]. For lower loadings, the pressure distribution again took on the familiar semi-elliptical shape of the Hertzian distribution. At higher loadings, a similar saddle shape was found, primarily in the more compliant transverse direction. This finding converged with the theory that the saddle shape is created when the surfaces in contact have a similar radius of curvature in the deformed state,

due either to high load or low stiffness. For example, a low-stiffness simply-supported beam loaded by a contacting body in the center of the span will assume the radius of curvature of the indentor due to a curving of the beam around the indentor from deformation due to the load. The lower the stiffness or higher the load, the greater the deformation and thus the greater the region of the beam where the radius of curvature matches the radius of curvature of the indentor.

2.2 Quasi-Static Composite Indentation

Work in static contact loading of composites is rare, but the response of composites to impact is a heavily studied area, as composites are particularly susceptible to impact damage. Response to low-velocity impact, a specific subcase of impact events, and static loading were long considered to be intuitively similar. In the late 1980's and early 1990's, various researchers conducted numerous studies to determine the extent of these similarities using laminated composites [14, 15, 16, 17]. They found that impact behavior, as measured by damage size, energy absorption, and load-deflection curves, was similar to the static response. It was concluded that static indentation tests can be used to represent low-velocity impact events when considering equivalent maximum transverse forces. Further testing was conducted on a broad range of specimens by Nettles and Douglas at NASA's Marshall Space Flight Center with similar findings and conclusions, further verifying the procedure [18]. The work on this topic led to the establishment of an ASTM testing standard to use quasi-static indentation testing to measure the impact resistance of a laminated composite [19]. Static testing meant to simulate low-velocity impact is considered quasi-static and is performed as a method to analyze the damage from a low-velocity impact while being able to precisely control the load and displacement achieved but neglecting the dynamic effects essential to higher velocity impacts. This controlled set-up allows tests to be stopped or paused before failure to examine damage at various stages of loading. Much of the work done in quasi-statics is performed using a laminated plate and a spherical steel indentor.

Analytical studies were initially used to predict the laminate response to quasi-static loading. Popular methods primarily investigated the elastic response regime, and used simplifying assumptions such as symmetry, or smeared material properties to simplify the analysis to a manageable but mathematical level. This technique was useful for determining locations of maximum stress, and thus the locations with the highest probability of failure. Cairns and Lagace provided an analytical approach to solve for deflections and strains in the elastic range for a homogeneous orthotropic plate subjected to a lateral loading through a Hertzian distribution, and found good correlation with experimental data [20]. Using this method, it was found that the classical plate solution was recovered at a normalized plate radius of 0.4 from the point of contact. Sankar investigated a similar case and considered a circular plate with transversely isotropic layers [21]. Interlaminar shear stresses were calculated via the finite difference method. In this investigation, the maximum interlaminar stress was found at a radial distance normalized by the indentor radius of 0.90 to 0.95.

Numerical simulation of contact loading allows for the solution of problems outside of immediate purview of Hertzian mechanics, specifically complex geometries and complex material substrates, such as laminated composites. With the increased availability of computational resources, the response of a material to rigid contact indentation loading could be studied numerically using finite element analysis as early as 1985 by iteratively using imposed displacements on surface nodes conforming to the shape of the indentor [22]. This technique was later applied to quasi-static impact of composites using the assumption of a quasi-isotropic uniform medium [23], and later to laminated composites [24]. As contact computation developed further, it became possible to model not just rigid indentors, but also elastic indentors. Faulkner et al [25] conducted the first real comparison of models with rigid indentors to models with deformable indentors. A ceramic-steel substrate was the material being indented. It was found that the differences in response of the medium due to the indentor type, rigid or deformable, could be of significance.

Recently, contact modeling has been used extensively to simulate the response of composites to both static and dynamic loadings using commercial FEA software that

specializes in such analysis, such as Abaqus [26, 27, 28]. Tita at al [26] developed a custom material definition for use with the finite element solver ABAQUS that allowed a more accurate simulation of the failure mechanisms of composite laminates in low-velocity impact test. Johnson et al [27] worked to develop a material degradation model to include the effects of damage from impact in their finite element model in ABAQUS, specifically attempting to more accurately model delamination. This investigation employed a discretized indentor and modeled contact using a small sliding approximation used when the movement between two contacting bodies is negligible. Creating a finite element model with the desired mesh size and a reasonable run time was found to be a particular obstacle for this dynamic analysis due to the high mesh density needed near the point of contact. Rizov [28] investigated the response of a laminated sandwich structure to static indenting. A two-dimensional model with a vertical plane of symmetry at the contact point and an increased mesh density near the contact point was used to model the laminate, with the indentor modeled as a rigid body. Good agreement was found with comparable test data.

2.3 Grooved Composites

The behavior of grooved composites has seen relatively little study. The little research that has been conducted with grooved composites focuses primarily on specific designs for particular applications. For example, Hoppel et al. [29] studied buttress grooves, a structure typically used to transmit shear loads, using composites. The work focused on investigating the strength of a single groove, and determining an optimized laminate configuration that would maximize the ability of the structure to carry shear loads. Montay et al. [30] investigated creating grooves in composites as a method to determine the residual stresses from the manufacturing process. The flat-bottomed groove in this work is drilled incrementally, allowing the composite to deform between increments to reach a new equilibrium due to the removal of the groove material. Using the compliance method, the deformation that occurs provides information about the residual stresses previously carried by the removed material.

Stress gradients could be studied due to the incremental approach to material removal. Neither the groove nor the laminate were loaded in this scenario.

However, more relevant studies regarding grooved composites under load have also been done. Bastien [5, 31] performed the initial analytical investigation of grooved composites with a transverse loading, looking first at grooved composites with a uniform loading along the length of the groove, dubbed a cylindrical loading. Studies were performed using finite element analysis on primarily two-dimensional isotropic bodies, and these results were then compared to a baseline, quasi-isotropic composite laminate, and to a three-dimensional model. The three-dimensional model retained the two-dimensional loading distribution, as if the grooved composite were loaded by a a cylindrical indentor running the length of the groove. He performed a parametric investigation on the effect of groove depth, plate thickness, and loading angle, as well as an investigation of the effect of various boundary conditions. It was concluded that the response consisted of three primary parts: 1) a global response due to the structural configuration and loading, 2) a local response due to the removal of material for the groove, and 3) a response due to the specifics of load introduction. In comparing the laminate and isotropic configurations, Bastien found the response to be similar in the body of the material, but with high strain gradients around the face of the groove. This is due to the varying stiffness of each ply around the groove and the uniform applied stress distribution, leading to an unrealistic, non-uniform displacement around the groove. In comparing two- to three-dimensional results, it was found that two-dimensional models were a good match to the response in the three-dimensional model except for edge effects in the region a half-plate-thickness from the edges in the width direction.

Experimental work observing the behavior of grooved composites to out-of-plane contact loading was performed by Kobayashi [6]. In establishing a testing methodology, he noted the need to use a rigid backface support to isolate the particular effects of transverse loading of the groove. In these experiments, loads were applied through a cylindrical indentor running the length of the groove in an attempt to get a consistent stress distribution through the width. Kobayashi noted two distinct failure

modes. Mode A was described as a delamination failure originating near the groove bottom. In mode B, which was only observed in quasi-isotropic layups, a vertical crack runs from near the bottom of the groove to a delamination failure near the midplane of the composite. In analyzing the load-displacement data, a knee, or bend, was observed as the point at which the curve deviated from its initial linear shape [6].

The analytical work conducted on the contact mechanics of curved bodies is of limited use to investigations of grooved laminates, as these methods cannot account for the piecewise-varying stiffness encountered around the groove of a grooved laminate. Work in grooved composites are rare, and much research is focused on specific configurations and applications, or grooves that are not loaded. The majority of previous work conducted in out-of-plane contact loading of composites is primarily focused on low-velocity impact events, and the damage from such events. While little of this research focuses on composite structures designed to carry out-of-plane loading, these investigations have produced a number of procedures and computational tools of use in modeling such structures. The work that has been conducted in load-bearing grooved composites has laid a solid foundation of information about the system through analytical investigations of isotropic systems and preliminary analysis of laminate systems. However, these previous investigations relied on a two-dimensional applied pressure loading scenario which may or may not accurately capture the response in the true three-dimensional case. The experimental laboratory testing of grooved composites has similarly yielded a great deal of information about this configuration, but such tests cannot resolve the response of the laminate at the ply level, only at the laminate level.

It is in response to these issues that the current investigation is focused. The previous investigations justify further research to determine the details of the local loading introduced by the steel ball-bearing indentor to the grooved laminate. In the current work, the local details of the contact loading of grooved composites are studied numerically using tools developed primarily for indentation and low-velocity impact

studies. The response is investigated through finite element analysis, a process that can resolve stresses and pressure at the ply level. Procedures used in the analytical method by Bastien [5] are adopted in this work, and improved upon with regard to the modeling of contact.

Chapter 3

OBJECTIVES & METHODOLOGY

This work seeks to further the understanding of the response of grooved composite laminates to transverse loading by a spherical indentor by building on previous work and findings in the field. Particular attention is paid to the loading interaction between the indentor and the grooved laminate, and the local response of the laminate near the groove. The goals and objectives for this work are outlined herein. An overview of the methodology followed in the achievement of these objectives is presented along with a description of the geometry, laminates, loads, and boundary conditions to be used in this work.

3.1 Overall Objectives

The primary objective of the present work is to study the response of grooved laminated composites to contact loading through a round indentor, with particular focus on the area local to the groove. In this work "conformal contact loading" is used and is defined as a loading situation in which the groove is forced to conform to the geometry of the indentor through deformation, or the groove and the indentor jointly deform to conform to a new common geometry. This kind of loading is in contrast to an applied force, traction, or pressure loading in which the body of interest is

arbitrarily deformed at the point of loading according only to the applied load. The focus is on the response local to the groove, as this is the primary region of interest. The local loading situation of a grooved composite is the primary aspect that makes this structural configuration unique, and is the least studied and understood aspect of the configuration.

There are three sub-objectives to the primary objective. First, the linearity of the response across designated load levels is to be assessed. This is investigated by studying the response at varying load levels. Linearity in the response would allow testing at a single load and allow a scaling of stresses and strains, simplifying analysis. However the contact conditions, and the increase of contact surface area as load increases, can cause nonlinearity. Second, the effect of ply angle and orthotropy on the response is to be assessed. This is studied by examining a family of laminates with a variable ply angle, a cross-ply laminate, and a quasi-isotropic laminate. Laminated composites offer a unique ability to tailor the material properties to the loading condition. Examining multiple layups should give an indication as to the manner in which various laminates respond to the loading, and could potentially aid in selection of an efficient layup in future applications. Third, the stress response across the laminates is assessed, in particular the locations of maximum stress. This should allow for some measurable comparison in the response due to the various changes studied, and also provide locations of probable areas for failure initiation in physical implementations.

In order to aid in the accomplishment of the primary objective and the sub-objectives, there are three additional supporting objectives. First is the assessment of whether a Hertzian load distribution represents a good approximation to the more accurate conformal contact loading that is the focus of the current work. The Hertzian distribution has been used as the load application method in previous work by Bastien and was imposed as a precalculated pressure distribution on the groove surface [5]. An applied pressure distribution such as the Hertzian distribution would run more quickly in a finite element model, and if accurate, would provide a much quicker solution. However, several assumptions are made in calculating the Hertzian distribution

to fit the grooved laminate configuration that do not hold for laminated composites in general, primarily the assumption of isotropy in both contacting bodies. A second supporting objective is to assess the effectiveness of modeling the indentor as a rigid body, as compared to modeling it as a linear elastic solid, in conformal contact loading. The transverse stiffness of the laminate is significantly less than that of a steel indentor, with the implication that the rigid body assumption should be reasonably accurate. In addition, if the assumption holds, the modeling of a rigid indentor should conserve computational resources, as compared to modeling the indentor as a linear elastic solid. However, previous work indicates that the elasticity of the indentor could be of significance [25]. Finally, this work examines the loading of the groove by a cylindrical indentor, essentially a two-dimensional problem, and the loading of the groove by a spherical indentor, a fully three-dimensional problem, and a comparison of the response in each case is made with an assessment of the ability of the cylindrical case to represent a two-dimensional slice of the spherical case. Previous work by Bastien [5] initially made this assumption, but the plane strain condition used to work in the two-dimensional space is a questionable assumption, as the stresses in the three-dimensional case have not been shown to be constant through the width of the laminate. However, if the two-dimensional analysis does yield an accurate slice of the three-dimensional case, this would also conserve computational resources and allow for a more detailed finite element mesh and faster solutions.

3.2 General Approach

This investigation is focused on resolving stress gradients and contact pressure variations in grooved composite laminates. These variations are likely to occur across small lengthscales, on the order of a ply thickness, due to the laminated nature of the body. For example, where the indentor contacts the grooved surface, the stiffness changes around the circumference of the groove are anticipated to cause corresponding changes in contact pressure. These stiffness changes are due to the laminated nature of the material, with the groove spanning several plies of varying orientations, and

hence varying stiffness in the contact direction. In addition, stiffness changes from ply to ply due to varying ply angles are likely to affect stresses and strains on the ply scale. With these scale considerations in mind, experimental testing using strain gauges would be of only limited use in such an investigation as current technology for strain gauges and optical strain mapping could not report stresses or contact pressures at the necessary lengthscales. An analytical solution would be ideal, as it would yield the continuous stress and strain distribution for the entire space of the laminate. However, as discussed in Section 2.1, a closed-form, analytical solution for the contact pressure across the cut face of an orthotropic laminate has yet to be found and is beyond the scope of the current work. The numerical solution of a finite element model is the next best approach.

The finite element model requires a sufficiently high density of nodes and elements in order to report stress and strain changes at the lengthscales necessary, while still having a manageable computational run time. For this work, the commercial finite element software ABAQUS is used to set up and analyze the model. ABAQUS provides a well-developed body contact algorithm and iterative solver that is necessary for this investigation. This is key, as the current work investigates the use of an indentor in applying load to the groove, in contrast to previous work in which load was introduced via a pressure distribution with a Hertzian shape [5].

3.3 Laminates and Geometry

One of the benefits of laminated composite materials is the ability to adapt a structure to different loadings and geometries through the use of different laminate configurations. The key to this adaptability is the ply structure of the material and the ability to vary ply angles to change the stiffness and strength of the material as desired to best suit a given situation. This leads to many different combinations of ply angles, or layups, even for composites that utilize the same base materials. This presents a challenge for composites, as each individual combination of layup and configuration must be analyzed independently, with results from one not being

directly applicable to another. While it would be impossible to model and compare every possible layup, this work investigates a number of different laminates that, through their variability, give a broad view of the trends involved in contact loading of grooved composites.

Regarding materials, two different carbon fiber/epoxy combinations are studied. The first, an AS1/3501-6 graphite/epoxy composite is used for a direct comparison to previous work [5]. The second, a Toray Composites T700/2510 graphite/epoxy composite composes the majority of the models and is used to relate this investigation with a parallel experimental effort using the same materials [32]. Properties for these two materials are provided in Table 3.1.

Seven total layups are studied, with a summary of the laminates provided in Table 3.2. The initial layups studied explore the quasi-isotropic case, as one of the most common and multi-purpose layups in use. Comparison to previous work [5] necessitates a $[0/\pm45/90]_{15S}$ layup of AS1/3501-6. A second, thinner, quasi-isotropic case of a $[\pm45/0/90]_{10S}$ layup of T700/2510 is studied to examine the quasi-isotropic response in comparison to other laminates of the same material and similar laminate thickness. The quasi-isotropic case also represents a combination of individual characteristics seen in the other laminates with angled, lateral, and transverse plies all present in a common working layup. A laminate family is also studied to independently observe the effects of changing ply angle using a $[\pm\theta/0]_{13S}$ layup of T700/2510. Values of θ of 15°, 30°, 45°, and 60° are considered. Finally, to observe the maximum effects of ply mismatch, a cross-ply $[90/0]_{20S}$ layup of T700/2510 is studied. These T700/2510 laminates were chosen in conjunction with a parallel experimental effort for convenient comparison [32].

The configuration under study consists of a rectangular brick of composite material two inches in length by one inch in width, as shown in Figure 3.1. These dimensions are based on those developed in previous work by Kobayashi in determining test methods and specimens for grooved composites in the laboratory setting [6]. Analysis by Bastien determined that these lengths were sufficient such that edge effects did not adversely affect stress results [5]. The thickness range of the laminates was determined

Table 3.1 Unidirectional ply properties for AS1/3501-6 and T700/2510 graphite/epoxy composite materials

Property	**AS1/3501-6**	**T700/2510**
E_1 $[Msi]$	19.0	18.2
E_2 $[Msi]$	1.54	1.22
E_3 $[Msi]$	1.54	1.22
G_{12} $[Msi]$	0.870	0.613
G_{13} $[Msi]$	0.870	0.613
G_{23} $[Msi]$	0.566	0.399
ν_{12}	0.280	0.309
ν_{13}	0.280	0.309
ν_{23}	0.540	0.596

Table 3.2 Summary of laminates considered

Material	**Layup**	**Thickness** $[in]$
AS1/3501-6	$[0/\pm 45/90]_{15S}$	0.625
T700/2510	$[\pm 15/0]_{13S}$	0.450
T700/2510	$[\pm 30/0]_{13S}$	0.450
T700/2510	$[\pm 45/0]_{13S}$	0.450
T700/2510	$[\pm 60/0]_{13S}$	0.450
T700/2510	$[90/0]_{20S}$	0.462
T700/2510	$[\pm 45/0/90]_{10S}$	0.462

based on previous work [5, 6], and in coordination with an parallel experimental effort [32]. The exact thickness of a laminate is dependent on the number of plies involved in the layup multiplied by the ideal ply thickness, as cited in the material specification sheet of the manufacturer. For the laminates studied, the various thicknesses are 0.45-inches for the 78-ply layups, 0.46-inches for the 80-ply layups, and 0.63-inches for the 120-ply layup. Based on the findings of previous work, these thicknesses should be sufficient to isolate the local effects of loading on the groove without significant influence from boundary condition effects. A semi-circular groove of radius 0.125-inches runs though the width of the block with the center of the groove coincident with the mid-length line of the top surface.

For the purpose of this study, two coordinate systems are used in referencing points of interest, as illustrated in Figure 3.2. The primary rectangular coordinate system has its origin at the geometric center of the composite block, midway through the length, midway through the width, and at the midplane through the thickness. The 1-direction, or x_1-axis runs parallel to the length, the 2-direction, or x_2-axis, runs parallel to the width, and the 3-direction, or x_3-axis, is perpendicular to the plane of the plies, running through the thickness. It also becomes convenient to discuss locations on or near the groove. For this purpose, a secondary coordinate system is used, with rotational coordinate, ϕ, and a radial coordinate, r, with an origin at the center of curvature of the groove. The 0° point is the center of the groove bottom, while the 90° point is the upper edge of the groove along the top surface of the composite. In the three-dimensional case, this coordinate system is combined with the x_2 coordinate to form a cylindrical coordinate system sufficient to describe locations in three dimensions.

3.4 Loading and Boundary Conditions

A key differentiating feature of the current work is the use of contact modeling. Previous efforts have used an applied pressure distribution on the groove face to introduce load. This approach can encounter problems when the pressure is applied

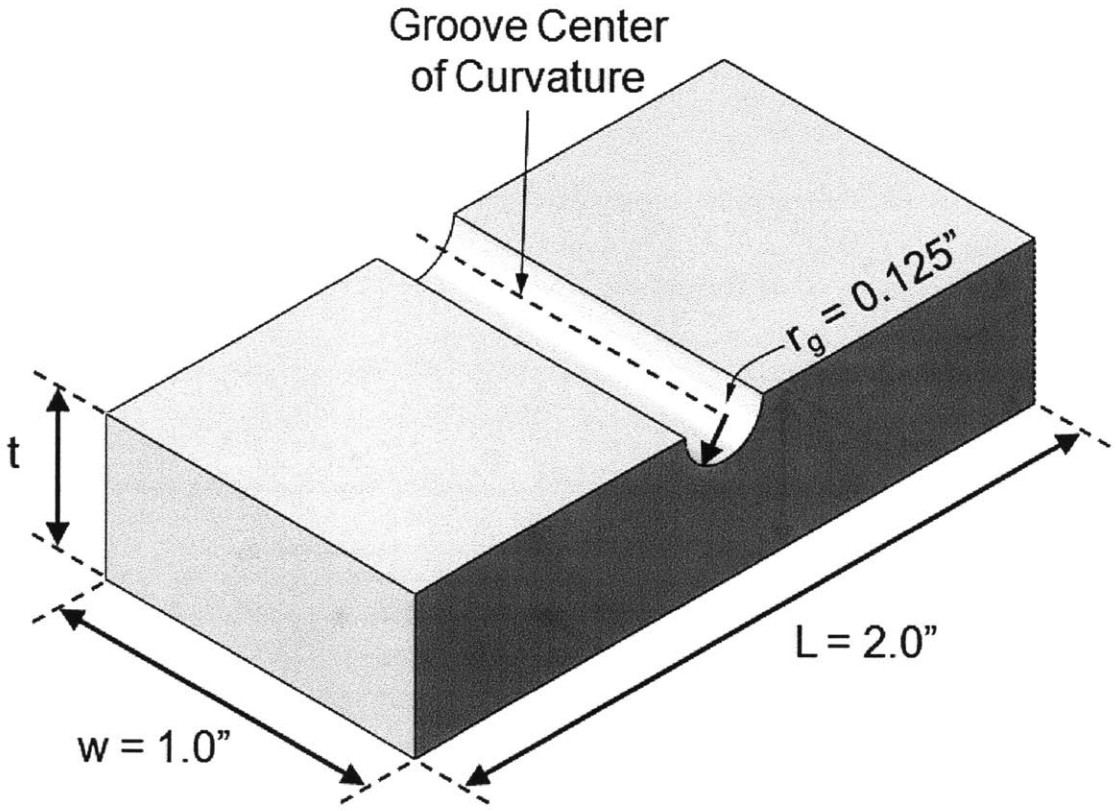

Figure 3.1 Dimensions of grooved laminated configuration studied.

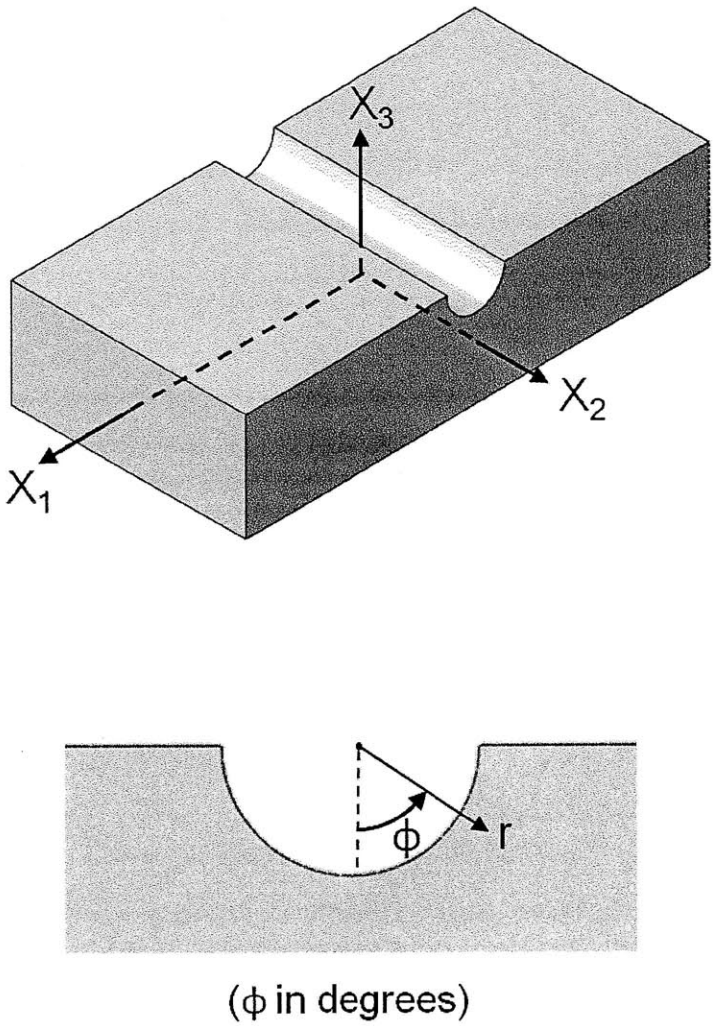

Figure 3.2 Diagram of (*top*) primary coordinate system, and (*bottom*) cylindrical coordinate system at the groove.

to a surface with variable stiffness, such as the groove face of the current work [5]. Whereas a continuous pressure distribution in such a case will cause a discontinuous strain distribution around the groove face, a modeled indentor will force a conformal deformation in the groove, leading to a continuous strain distribution. This is much closer to the reality of the grooved composite/ball bearing configuration.

The size of the indentor is based on previous work. Radial ball bearing systems, such as the one under investigation, typically have a groove radius to ball diameter ratio between 0.51 and 0.53 [33]. As the ball and groove here represent a load transfer mechanism, the ideal match would see a smaller groove radius to ball diameter ratio in order to maximize contact area and minimize high point stresses. As such, this work employs a ratio of 0.51. With a given groove radius of 0.125 inches, this yields an indentor diameter of .245 inches, thus an indentor radius of 0.1225 inches. The indentor is modeled as AISI M7 steel, a high modulus, high strength steel with the material properties given in Table 3.3. This is as similar as possible to the steel used in parallel experimental efforts, when previous work found that softer steel would permanently deform under grooved contact loading [6, 32].

Two different loadings are investigated. The first is the case of a cylindrical indentor acted on by a distributed line load, as shown in Figure 3.3. The second is the loading case of a spherical indentor acted on by a point load, as seen in Figure 3.4. The cylinder-loaded model has been used in previous work to represent a two-dimensional slice of the spherical indentor case, specifically a slice going through the point of maximum contact [5]. It has been found that the configuration of cylinder loading can be modeled in two dimensions as plane strain and will give accurate representation of this case, neglecting edge effects found when modeled in three dimensions. The three-dimensional sphere-loaded model is more plainly representative of the grooved composite and ball bearing interaction. Since three-dimensional analysis of this problem has not been performed previously, it remains to be seen whether the two-dimensional case is truly representative of the three-dimensional case, and determining the applicability of the two-dimensional case is a sub-objective of the current work. It is also important to determine whether the steel indentor can be

Table 3.3 Material properties for AISI M7 Steel

Property	**Value**
Young's Modulus $[Msi]$	30.5
Shear Modulus $[Msi]$	12.0
Poisson's Ratio	0.270

modeled as a rigid body, or must be modeled as a linear elastic solid. This comparison is primarily performed in the two-dimensional modeling as this places fewer demands on computational resources. The results of the comparison are carried over into the three-dimensional modeling.

For the case of cylindrical loading, selecting the load to be applied has its own set of issues. Using preliminary data from a parallel experimental effort, an attempt was made to select loads well within the linear region of the load-displacement data of the experiments [32]. It was also desired that the loading produce a contact area similar to that studied in previous work by Bastien [5], and a similar contact area to the case of spherical loading. With this as criteria, and based on preliminary numerical studies, with a preference toward round numbers, a maximum load of 5000 lb/in was selected. Making use of the incremental nature of the finite element solution for the contact problem, incremental loads up to the determined maximum loads are analyzed to determine whether the response of the composite to loading is linear or nonlinear. For the case of spherical loading, previous analysis by Sarh [4] estimates the maximum contact force observed between a single ball bearing and the grooved composite spar in the telescoping wing design to be 300 pounds. This load meets the requirements imposed on the case of cylindrical loading, namely to be within the linear response region of the load-displacement data in a parallel experimental effort [32], and likely to produce a similar contact area to previous finite element analysis in work by Bastien [5]. As such, the load of 300 lb was selected as the primary load for the three-dimensional case. As in the case of the cylindrical loading, smaller, incremental loads are also studied to determine whether the response is linear or nonlinear.

Previous work [5, 6] found that the boundary conditions of the configuration of a transversely loaded grooved composite have a significant effect on the response. As discussed in Chapter 2, the structural response of a grooved plate is composed of three key items: the global response due to the overall structural configuration and loading, the local response due to the removal of groove material, and the local response due to the specifics of the load introduction. For simply-supported, fixed-free, and fixed-

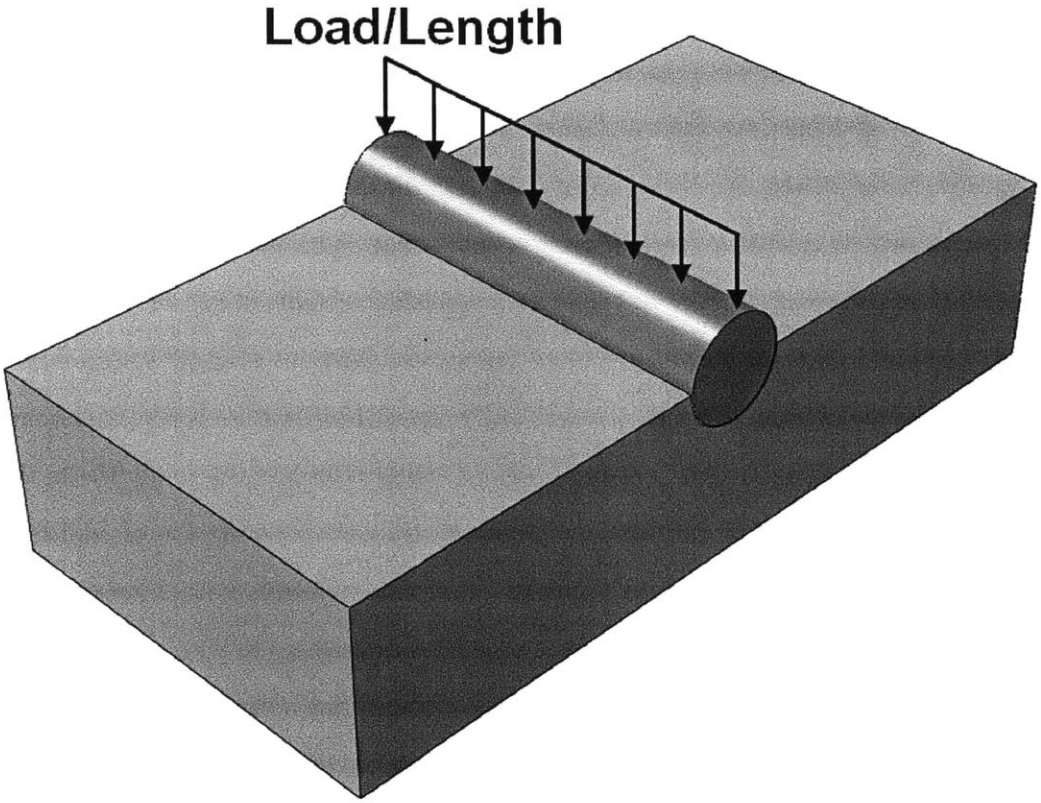

Figure 3.3 Illustration of cylindrical loading.

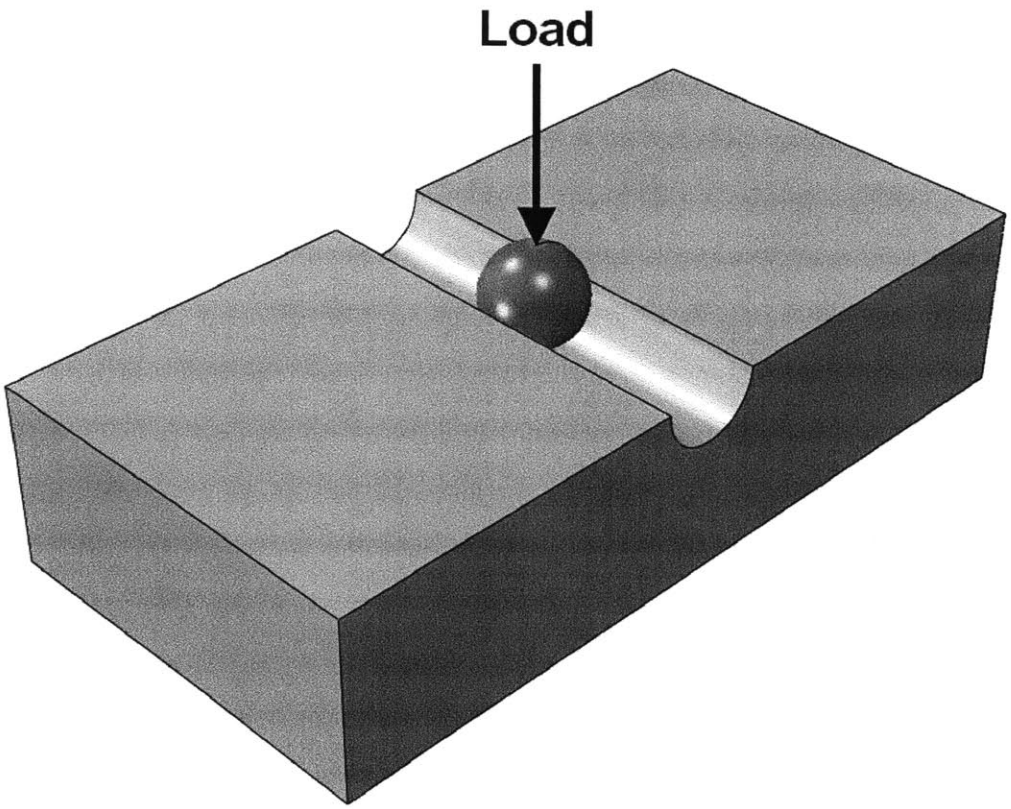

Figure 3.4 Illustration of spherical loading.

fixed boundary conditions, the response is dominated by the effect of the overall loading configuration. In order to isolate and study the response of the composite to the local details of transverse loading of the groove, the best boundary condition supports the bottom surface of the laminate across its entire surface, allowing no vertical motion or rotation about that plane, designated the rigid backface condition. These boundary conditions eliminate the aspect of the response due to the global loading configuration in order to more easily study the response of interest due the local loading of the groove by the indentor. Previous work by Kobayashi [6] found that the rigid backface was the best boundary condition for laboratory testing of grooved composites under contact loading, and parallel experimental work by Jeffrey [32] follows these same conclusions and uses the rigid backface condition in testing. In addition, previous analysis of grooved composites by Bastien [5] used the rigid backface condition, though other boundary conditions were investigated with isotropic bodies. The consistency of boundary conditions across these studies thus allows for a more direct comparison between those works and this current work. All models in this work progress with the rigid backface boundary condition.

Chapter 4

MODEL

The focus of the current work is to investigate the response of a grooved laminated composite to transverse contact loading. As discussed in the previous chapter, the approach taken makes extensive use of finite element modeling to simulate the structural response to this loading situation. A computational method is needed to resolve contact pressure that defines the load on the grooved composite and the stress gradients within the structure on lengthscales on the order of a ply thickness. The laminated nature of the body and the variable material properties of the plies due to ply orientations make this kind of behavior likely. The finite element method is a well-known, widespread approach to structural simulation and analysis, and provides a platform for studying this configuration. The finite element program ABAQUS, versions 6.8 and 6.9, is used for pre-processing, analysis, and post-processing, in conjunction with MATLAB for some additional post-processing visualization. Technical information in this chapter is drawn from the extensive ABAQUS documentation library [34, 35, 36]. The set-up and formulation of the finite element models used in this investigation are described in the following sections. An in-depth description of the finite element method and contact mechanics is not given, as these have been well studied and documented in previous work. The focus is on the rationalization for the methods selected, and a sufficient description of all models and settings that would allow creation of a similar or identical model in future work.

4.1 Contact Model

The transfer of load to the laminated composite through an indentor is a major focus of this work. Thus, the contact model employed in ABAQUS bears some detailing. In order to isolate the effects of load pressure from the indentor, a frictionless formulation was used between the groove surface and the indentor surface. This allows for the analysis of the contact problem in isolation, and is a good way to first study the basic principles of grooved composite contact loading. In addition, modeling the friction involved would add another layer of complexity to the system, and would require further experimental investigation of the properties of frictional contact between an indentor and the open face of a cut laminated composite.

The first step in generating a contact model in ABAQUS is to determine the two surfaces that are interacting, and define one of them to be the "master" surface and the other to be the "slave" surface. This definition is not arbitrary. The master surface should be on the body that undergoes the most motion and is the stiffer of the two bodies. The slave surface should be on the more deformable of the two bodies, and should have a finer mesh than the master surface. For this investigation, the indentor is always defined as the master surface, and the groove in the composite laminate is always defined as the slave surface. This is based on the laminate being the more stationary body of the two, and being the more compliant of the two as well, particularly in the through-thickness direction in which the loading is primarily acting.

A tracking method must be selected that determines the manner by which ABAQUS tracks nodes and elements on the master and slave surfaces in order to determine whether contact has occurred, and, if so, help determine the appropriate contact pressure. ABAQUS has two options for the tracking method. The first is "Small Sliding", considered for cases where the movement between the two surfaces is small relative to the element size (less than one element length). The other is "Finite Sliding". This is the more general formulation, and is used for cases where relative motion between the two surfaces is larger, but finite. The models used in this investigation

employ the "Finite Sliding" formulation. Although sliding is likely to be small, the elements involved are also quite small, so the motion relative to the element size could be significant. Selecting the "Finite Sliding" formulation results in the automatic generation of contact elements on the slave surface. These elements have zero stiffness, are invisible to the user, and connect the master surface to the slave surface. The primary purpose of these elements is to construct a measure of the distance between the two surfaces at all points where contact may occur. Once surfaces are in contact, these elements are used to determine "overclosure", and the relative shear sliding. "Overclosure" is a measure of the distance between the master and slave surfaces and is defined as the distance a point on the slave surface penetrates through the master surface. Overclosure is used to determine the pressure between the two contacting bodies.

A contact discretization scheme is selected, in which the kinematic data from the selected tracking method determines the displacements and pressures involved in the contact situation. ABAQUS features two contact discretization methods and each of these uses a different method of contact constraint enforcement to determine the displacements and contact pressures associated with the contact condition. The first is a traditional "Node-to-Surface" discretization. This method treats the slave surface as a set of nodes and the master surface as a fully defined surface. Contact only occurs if the nodes on the slave surface come in contact with the master surface. Specifically, each node on the slave surface interacts with a small corresponding region on the master surface, so that each contact condition involves a single slave node and multiple corresponding master nodes. The contact is measured along the normal to the master surface. "Node-to-Surface" discretization employs a "Direct Method" of contact constraint enforcement. In such a case, when contact occurs, slave nodes are constrained to lie exactly on the master surface. Computationally, Lagrange multipliers are used to enforce the contact condition on the slave nodes using a hard pressure-overclosure relationship, as shown in Figure 4.1. The hard pressure-overclosure relation is defined as having zero pressure until the two surfaces are in contact, at which point the pressure can take on any positive value, but over-

closure cannot be positive. This means there can be no pressure between the two surfaces until they are touching, and once touching, they cannot overlap. This relation minimizes penetration of slave nodes through the master surface, since negative overclosure (surface overlap) is not possible at any given slave node, and does not transfer tensile stresses between the two contacting surfaces, since contact pressure cannot be negative. The "Node-to-Surface" discretization has two potential problems. Because the slave surface is defined only as disconnected nodes, the master surface could penetrate the slave surface in the region between nodes, depending on the curvature of the bodies, as illustrated in Figure 4.2. This is only a problem when the master surface has a significantly finer mesh than the slave surface and the radii of curvature of the two surfaces are highly dissimilar. This point-based contact method can also generate highly concentrated contact pressures when two discretized surfaces are used in contact.

The second surface discretization scheme is "Surface-to-Surface" discretization. This method enforces contact in a more average sense over the slave surface, as compared to the discrete point contact used in the "Node-to-Surface" scheme. This is done in an attempt to address the weaknesses of the other method. In this method, contact is considered between a local group of slave nodes and the corresponding local points on the master surface. The contact direction is based on the average normal in the local region of the slave surface. The contact constraint in this scheme is enforced by the linear penalty method, and Lagrange multipliers are not used. In the linear penalty method, the pressure-overclosure relationship is not the "hard" relation, but a linear approximation of the hard relation, as shown in Figure 4.3, that accounts for the local averaging method used on the slave surface. Like the hard relation, this approximation cannot take on negative pressure values. However, some overlap is possible, and the pressure between the two surfaces is determined by this overlap. The relationship between contact pressure and overlap is linear with a slope ten times the linear material stiffness in order to penalize and discourage, but not rule out, overlap. The result is a discretization scheme in which no large penetration of the slave surface by the master surface can occur (though small local overlaps are possible), and in

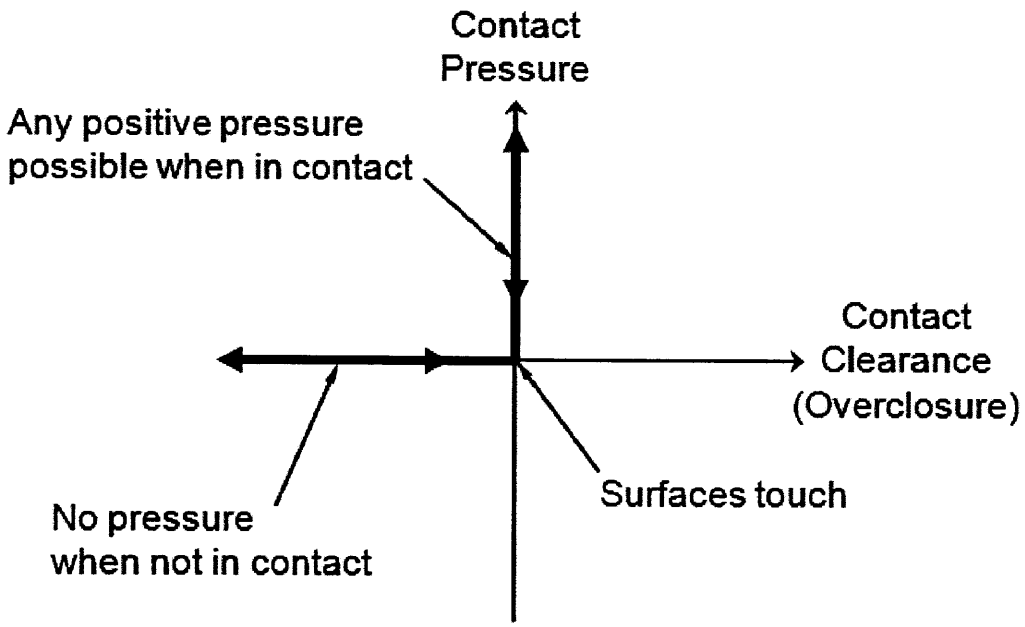

Figure 4.1 Plot of the hard pressure-overclosure relation used in the "Node-to-Surface" contact discretization.

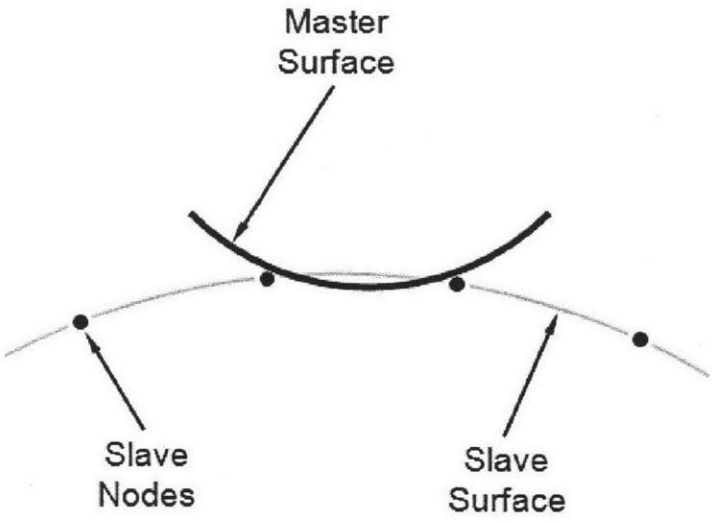

Figure 4.2 Illustration of a potential pitfall of the "Node-to-Surface" method in failing to capture contact between nodes when using a coarse mesh and opposite curvature directions.

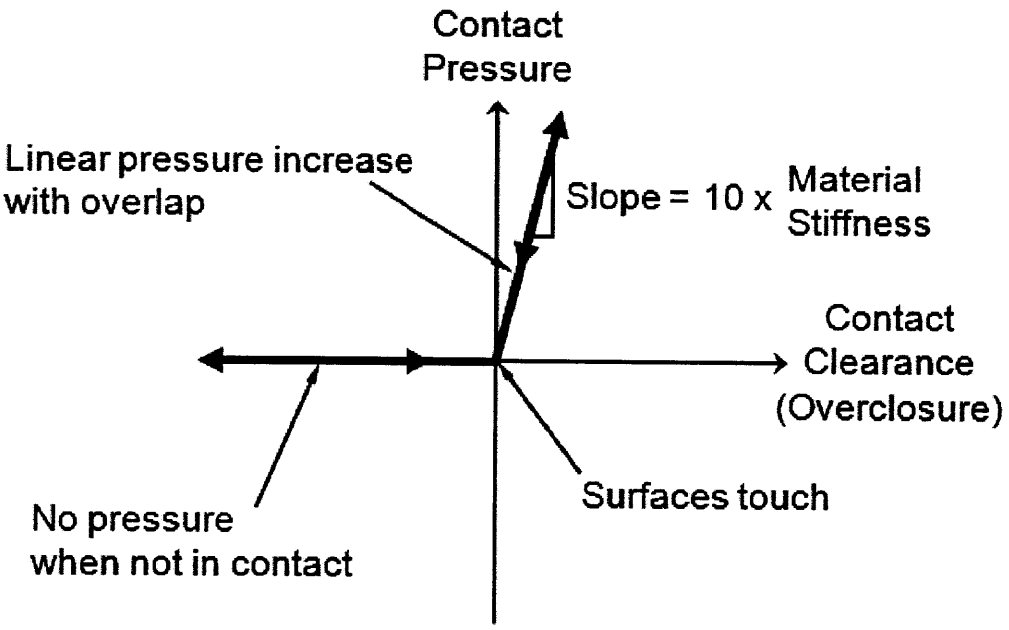

Figure 4.3 Plot of the linear penalty approximation of the hard pressure-overclosure relation used in the "Surface-to-Surface" contact discretization.

which contact stresses are more evenly distributed when used with two discretized surfaces. Large peaks or valleys that might appear when using "Node-to-Surface" discretization are smoothed out by the averaging contact method of the "Surface-to-Surface" discretization. This leads to a more accurate determination of contact pressure that is not as dependent on the particular finite element discretization and mesh employed to model the surfaces. However, this method also requires significantly more computational power to include the multiple averaging constraint equations for each local node group. The usefulness of this method is also limited when one of the surfaces is already smooth and not discretized, as in an analytical body, as the contact stresses are already relatively smooth.

In this investigation, "Node-to-Surface" discretization is used when an analytical rigid body is employed to model the indentor. The smooth surface of the rigid body prevents pressure spikes common using this discretization with two discretized surfaces. This method is likely the more accurate method to use in this case as the groove surface, which is discretized as a series of points connected by linear lines, is a curved surface in reality. Modeling this surface as a set of points that lie on the actual curves, and having those points interact with the indentor body, with a radius of curvature closer to that of the groove, should present a more accurate result. Finally, this method is the less computationally intensive of the two, while generating similar results for this case. When the indentor is modeled as a discretized linear elastic body, the "Surface-to-Surface" contact discretization is used. While this is a more computationally intensive method, it was found to give smoother contact pressures for the two discretized surfaces in this particular case.

4.2 Finite Element Models

The finite element models used in the current work are constructed in ABAQUS/CAE, a graphical front-end interface for constructing ABAQUS models. To create a finite element model in ABAQUS/CAE, the geometry is first defined, then settings for the finite element mesh are defined. Using these settings, ABAQUS will then auto-

matically generate a finite element mesh to match the geometry and mesh settings. The following subsections detail the type of finite elements used, the geometry of the laminate and indentor models, the mesh seeds that determine node placement on edges, and the mesh controls that define the form of mesh generation within a body. For many of these parameters, there are considerable differences between the two-dimensional and three-dimensional models, so these cases are frequently discussed individually.

4.2.1 Elements Used

The ABAQUS finite element library contains a number of unique finite element formulations, each suited to a different task, and each named in accordance with its characteristics. Elements types are first classified based on what is being modeled, solids versus fluids, for example. Next, the dimensionality of the element is considered, whether the model is intended to be two-dimensional or three-dimensional, or is to use the plane strain or plane stress assumptions, for example. The number of nodes required per element comes next, with a higher number of nodes generally representing higher order elements. For example, quadrilateral elements can come in 4-node first-order, linear form, or an 8-node second-order, quadratic form. Last come any special considerations for the model at hand. Generally, the models in this work utilize continuum, displacement-based elements, used for modeling solids. Only first-order elements are used in both the three-dimensional and two-dimensional models due to concerns over computational cost and accuracy of the contact model. All elements are isoparametric, meaning elements can be reshaped or distorted within reason to fit the required geometry without affecting the results.

The two-dimensional models, representing the cylinder-loaded system as described in Section 3.4, utilize the CPE4R element in ABAQUS. This is a continuum, plane strain, 4-node, linear, quadrilateral, isoparametric, reduced integration element. Since the two-dimensional models represent a plane strain slice through a cylinder-loaded composite plate, an element type that supports plane strain modeling was needed. Linear elements were selected over quadratic elements since quadratic elements can

occasionally cause inaccurate contact behavior related to the loading of the mid-edge nodes.

The three-dimensional models, representing the sphere-loaded system as described in Section 3.4, utilize the C3D8R element in ABAQUS. This is a continuum, three-dimensional, 8-node, linear, hexahedral, isoparametric, reduced integration element. An element type was needed that supported three-dimensional stress analysis. This particular element type was selected because hexahedral elements are preferable to tetrahedral elements, which can artificially stiffen a system in some cases, and because second-order quadratic elements can cause inaccurate contact behavior related to the loading of the mid-edge and mid-face nodes.

4.2.2 Meshing Settings

All finite element models were meshed, that is mapped with nodes and finite elements, using automatic meshing routines in ABAQUS/CAE, the front-end software for model creation and visualization in the ABAQUS software suite. There are a number of settings that largely define the form of the mesh generated by the automatic meshing routine. The model must first be broken into appropriate geometric sections that define boundaries of sections of finite element mesh based on regions of different material properties and mesh density in a model. "Mesh seeds" are then applied to the edges of each geometric section, and mesh controls are assigned to the body of each section. A "mesh seed" on an edge tells the meshing program to put a node on every point in the seed, and thus defines the concentration of elements along the edge. Mesh controls determine how elements are formed on surfaces and in volumes that lie between edges, since mesh seeds cannot be defined in this open space.

Mesh seeds can be defined in ABAQUS in one of three ways, by element size, by number of elements on an edge, or using a biased concentration method. The element size method will seed node points along an edge at a given repeating distance, yielding elements with edges of the desired size. This method allows for good explicit control over the size of elements. The element number method divides the length of the edge being seeded by the number of desired elements and seeds the nodes such that the

length of the edge is constructed of the desired number of elements. This method is useful in generating meshes with a specific number of elements, but where element size is indirectly determined by the length of the edge being seeded and the number of elements used. The biased concentration method is a variation on the element number method and requires three parameters as input to seed an edge: a bias parameter, a bias direction, and the number of desired elements. This creates a seed with the desired number of elements, but with those elements preferentially clustered in the desired direction and at the specified bias ratio, where the bias ratio is defined as the size of the largest element in the seed divided by the size of the smallest element. This method allows the concentration of elements toward one end of an edge or region with smaller elements near a point of interest, and larger elements farther away.

Mesh control methods are defined for each section or volume, and are used to determine how the automatic mesh generator fills in the space between the edges where the mesh seeds are defined. There are three types of mesh control methods in ABAQUS: "Free Meshing", "Structured", and "Swept". In the "Free Meshing" method, a mesh is generated in an unstructured fashion to fill complex topologies with well-formed elements that are sized based on the mesh seeds on the boundaries of the section. The "Structured" mesh control applies predefined mesh topologies to well-defined geometric regions, creating regularly structured, grid-like meshes. This method is only applicable for certain basic section shapes. The "Swept" mesh control method is only applicable for three-dimensional models, and uses a two-dimensional mesh pattern from one face of a three-dimensional volume and repeats this pattern through the thickness of the volume. The two-dimensional mesh pattern is generated on the front face of the volume using the "Free Meshing" method, and this pattern is then extruded perpendicular to the original surface and broken up at intervals by a mesh seed parallel to the direction of the extrusion to generate a three-dimensional mesh until the opposite surface of the volume is reached. This technique requires a volume that is a three-dimensional prismatic extrusion of a two-dimensional shape.

Three factors determined the mesh seeds and mesh controls used in the models for this work. The first factor is that previous experience with such models by Bastien

was considered [5]. In that work, a minimum element edge size of 0.02 inches was determined to be sufficient to accurately capture stresses that occurred in the work using a convergence criterion for the stresses and strains in the model. Bastien also performed preliminary work in determining that finer mesh densities, with elements on the order of 0.01 inches, were required in the region near the groove, but a coarser mesh, with elements on the order of 0.04 to 0.17 inches, could be allowed farther from the groove, approximately two groove radii away or greater. This variety in mesh density was accomplished through the appropriate sectioning of separate meshing regions. This allows a higher concentration of elements in regions of interest without needlessly increasing the computational costs by having lots of elements in regions with low stresses and stress gradients.

The second factor is that primary items of interest in this work are the contact pressure on the groove surface and the stresses local to the groove. Previous work gave an indication that the contact pressure in this work should vary from ply-to-ply, due to the ply-to-ply variation in strains due to an applied stress state in those models [5]. To account for this possibility, it is necessary to have elements on the scale of a ply thickness or smaller to capture these potential stress features. For the laminates used here, the ideal ply thickness is approximately 0.006 inches. However, elements should not be so small so as to be on the order of a fiber diameter. This is because this work uses a smeared material property model for the ply properties, ignoring the separate properties of the fibers and matrix of the composite, and instead treating a ply as a uniform medium. Having elements on the order of a fiber diameter would invalidate this mode and would require additional micromodeling considerations to model the fibers and matrix individually. The average diameter of a carbon fiber is approximately 0.0002 inches. This puts the ideal element edge length somewhere between 0.0002 and 0.0060 inches.

The third factor is that the computational cost plays a significant role when a large number of models needs to be analyzed. Computational cost per finite element grows nonlinearly, so creating a model that can be run in a reasonable amount of time requires a balance with the lengthscale fidelity desired.

Taking into consideration these three factors, mesh seeds and mesh controls were applied to the models in the work based largely on trial and error in an attempt to balance the lengthscale fidelity desired with a reasonable computational cost. The specific settings that were found to achieve that balance in each model are described in the subsequent subsections for each of the different models considered.

4.2.3 Two-Dimensional Models

The two-dimensional models have three different sets of dimensions due to the selected layups resulting in three different numbers of plies for the laminates. The $[\pm\theta/0]_{13S}$ laminates have 78 plies. The models for these cases are 2 inches in length and 0.45 inches in thickness, with a semi-circular groove with a radius of 0.125 inches cut out centered halfway along the upper surface. The models for the $[\pm 45/0/90]_{10S}$ and $[90/0]_{20S}$ laminates are also 2 inches in length, but are slightly thicker at 0.462 inches due to the two additional plies. A semi-circular groove with a 0.125-inch radius is again cut out centered halfway along the upper surface. As the two-dimensional models are plane strain in nature, the width dimension along the x_2-axis is not given and should be considered infinite. These configurations share a common mesh seed and mesh control method.

For creation of the finite element mesh, the two-dimensional models are divided into sections that define individual plies in order to account for the laminated nature of the configuration. This ensures that when the finite element mesh is generated, the ply boundaries are clear, flat, and straight in the mesh, and that appropriate material properties can be applied to each individual ply based on the layup angle of that ply. In the region near the groove, these ply boundaries end at the physical face of the groove. To control element density, the models are divided into three meshing regions that encompass multiple plies, as illustrated in Figure 4.4. Region 1 is the region local to the groove, from the top surface of the laminate, to the laminate midplane, with edges 0.25 inches from the center of the groove on either side. Since previous work has shown this to be the region with some of the highest stress gradients, and since the primary goal of this work is to study the effect of contact groove loading

local to the groove, this region features the highest element density. Region 2 is immediately under Region 1 and runs from the laminate midplane to the bottom surface of the laminate, and has edges 0.25 inches on either side of the center of the groove, just as Region 1 does. Stress gradients in this region are expected to be smaller than in Region 1, but larger than in Region 3. Thus, due to computational cost considerations, this region has a lower mesh density than Region 1, but a higher mesh density than Region 3. Region 3 consists of two disconnected blocks that make up the remainder of the model. Previous work [5] has shown that stress and strain gradients in this region are quite low, with stresses dropping off quickly as one moves away from the groove in the 1-direction. As such, the element density in this region can be low to reduce computational cost without compromising the integrity of the model.

Region 1 is the primary area of interest. For mesh seeding purposes, it features four types of edges: the edge at the top of the laminate, the groove face, the ply boundaries, and the vertical (parallel to x_3-axis) edges of the region. An illustration of the mesh seeding applied to Region 1 is presented in Figure 4.5. As previously discussed, the groove face is the region where the largest stress gradients are expected, with features likely to be on the order of a ply thickness or potentially smaller. In addition, a major objective of this work involves capturing and describing the contact pressure distribution between the laminate and the indentor. In order to capture these features, an element size mesh seed was placed on the groove face, with a desired element size of 0.001 inches ($0.17t_{ply}$). This size is sufficient to place at least 6 elements through the thickness of each ply on the groove face, and one element approximately every 0.5° around the groove. This should be sufficient to give an idea of how the pressure changes from ply to ply, and even within a ply, without generating elements on the microscale order of a fiber diameter. The horizontal edges in this region, including the top edge of the laminate and the ply boundaries, determine the internal discretization of the laminate. In order to capture potential variation within a ply, it is desirable to have at least three elements through the thickness of each ply. An element size mesh seed was used on these edges with a desired element

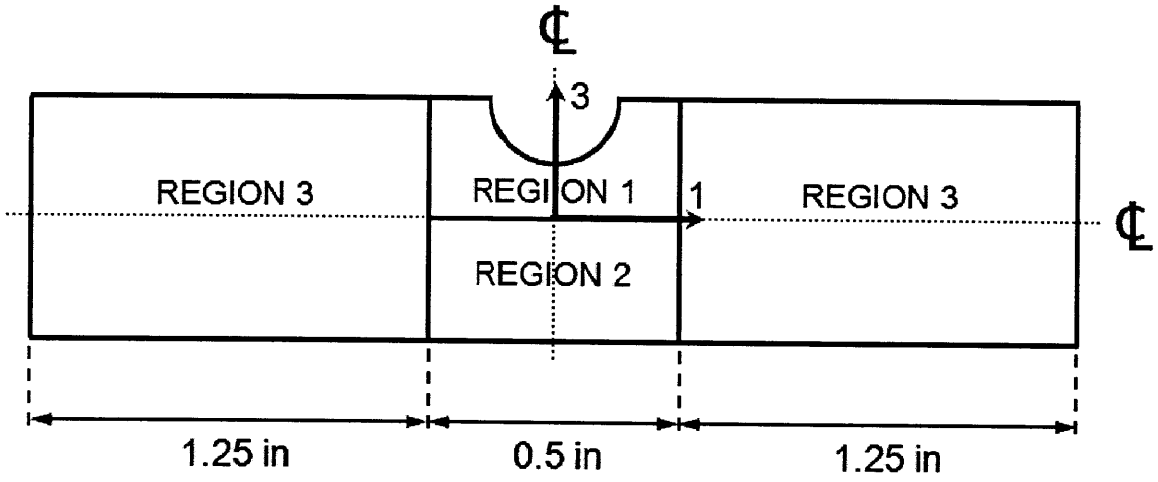

Figure 4.4 Illustration of meshing regions for two-dimensional finite element models.

size of 0.002 inches ($0.35t_{ply}$), yielding three elements through the plies on average. Smaller seeds were found to generate too many elements with a high computational cost, while larger seed sizes were found to generate too few elements through the thickness of each ply. The vertical edges in this region connect Region 1 to Region 3. As such, these edges represent a transition from the high mesh density of Region 1 to the low mesh density of Region 3. As is subsequently discussed, the goal for Region 3 is to have a minimum of two elements through the thickness of a ply. As such, these vertical edges are defined with the required element size mesh seed of 0.003 inches ($0.52t_{ply}$). The "Free Mesh" meshing control is used in Region 1 due to the unique geometry presented by the rounded edges of the groove. This meshing method yields an average element edge length of 0.002 inches ($0.35t_{ply}$) and places three elements through the thickness of each ply, on average. The resulting mesh in this region is shown in Figure 4.6.

Region 2 is a region with a medium mesh density, reflecting the expectation of low, but non-negligible, stress gradients in this region. Region 2 features three types of edges: the ply boundaries, the bottom edge of the laminate, and the vertical edges of the region. An illustration of the mesh seeding applied to Region 2 is presented in Figure 4.7. All edges in this region have the same mesh seed applied. This is an element size seed of 0.003 inches ($0.52t_{ply}$). This mesh seed was selected due to the desire to have two elements through the thickness of each ply. Some stress variation is expected in this region, especially from one ply to the next. Stress variation within a ply is considered less likely due to the lower stress gradients expected, so the configuration of three elements per ply as used in Region 1 is not required. The vertical edges retain the same mesh seed as seen in Region 1 and Region 3, which is the same 0.003 inch ($0.52t_{ply}$) element size seed. A "Free Mesh" meshing control is used in Region 2. This yields an average element edge length of 0.003 inches ($0.52t_{ply}$) and places two elements through the thickness of each ply. The resulting mesh for Region 2 is shown in Figure 4.8.

Region 3 is the farthest from the groove and the loading, and the mesh in this region is thus coarser. This region has five types of edges: the top edge of the laminate,

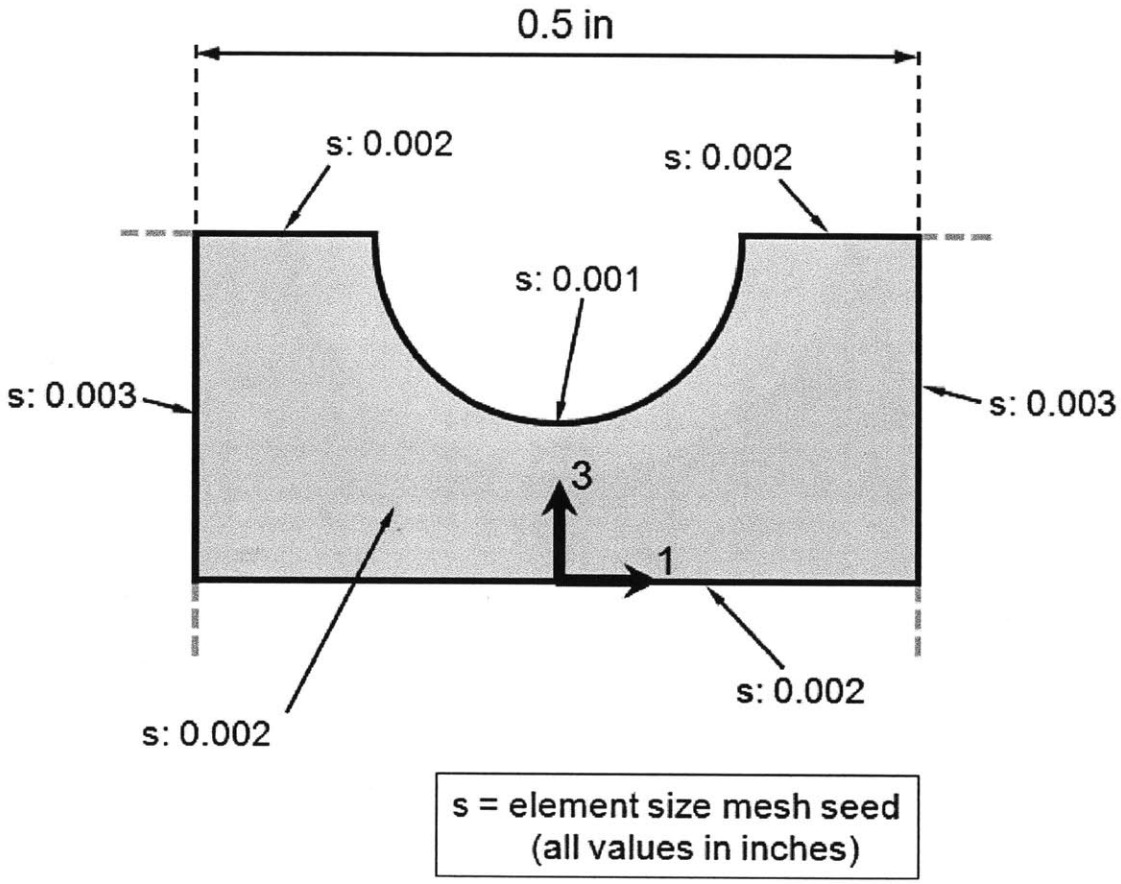

Figure 4.5 Illustration of mesh seeds in Region 1 for two-dimensional finite element models.

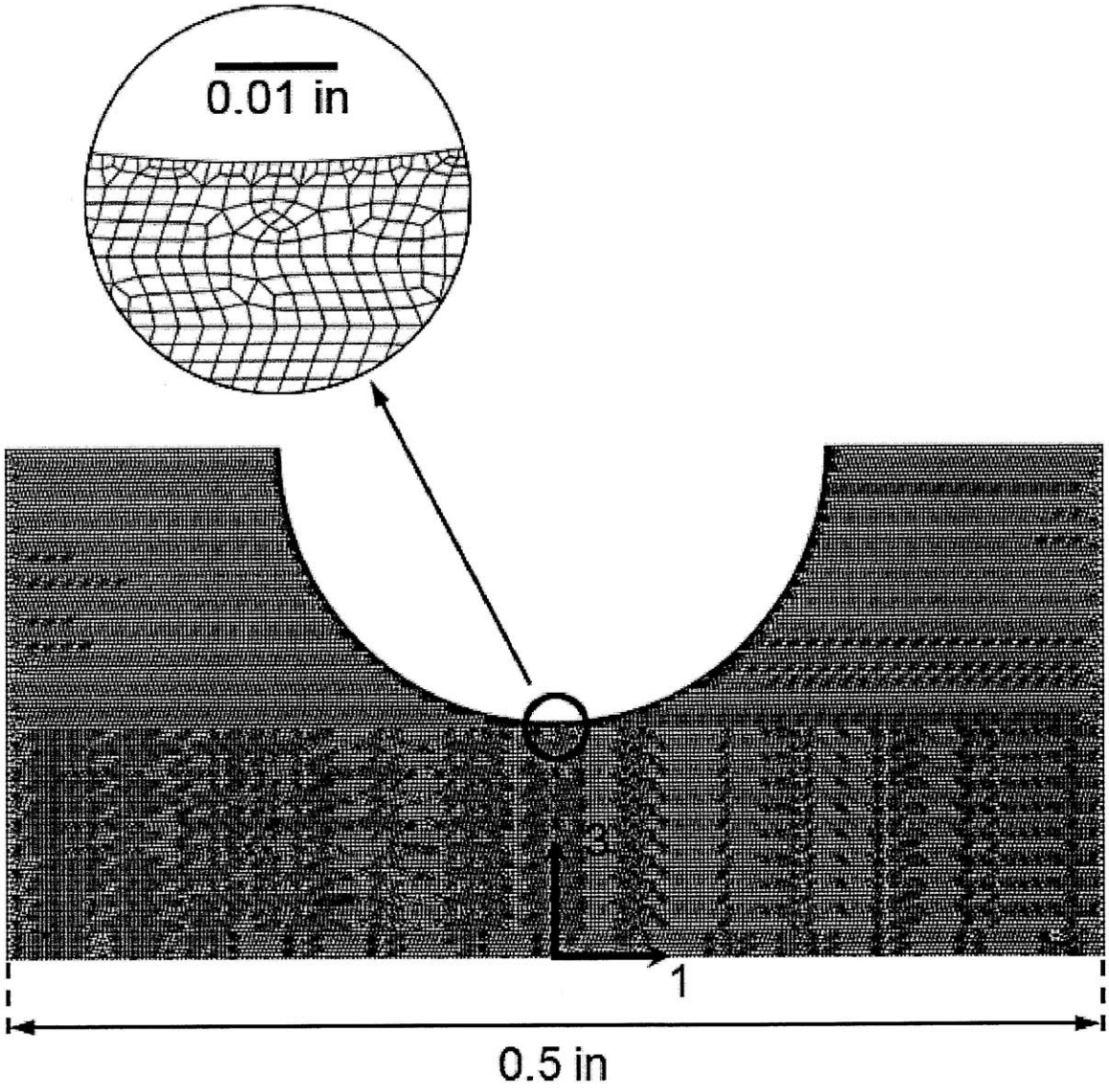

Figure 4.6 Typical finite element mesh in Region 1 for two-dimensional finite element models.

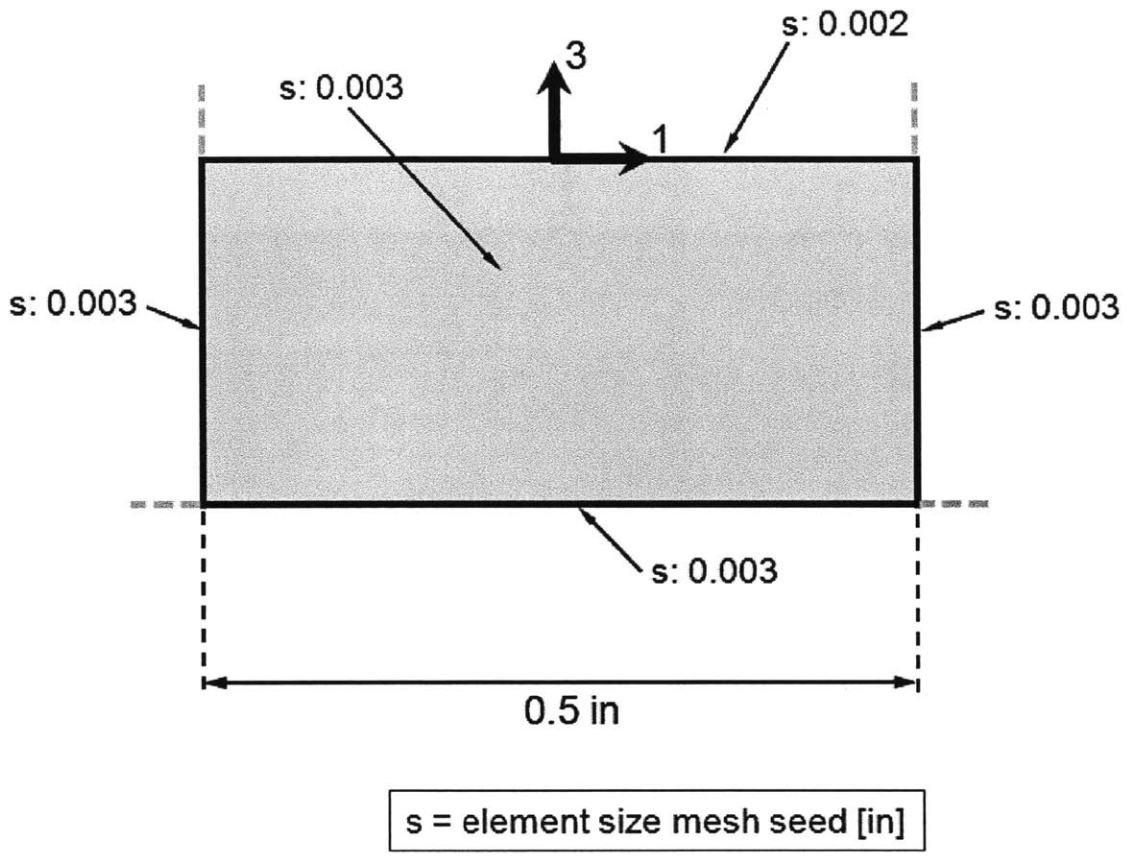

Figure 4.7 Illustration of mesh seeds in Region 2 for two-dimensional finite element models.

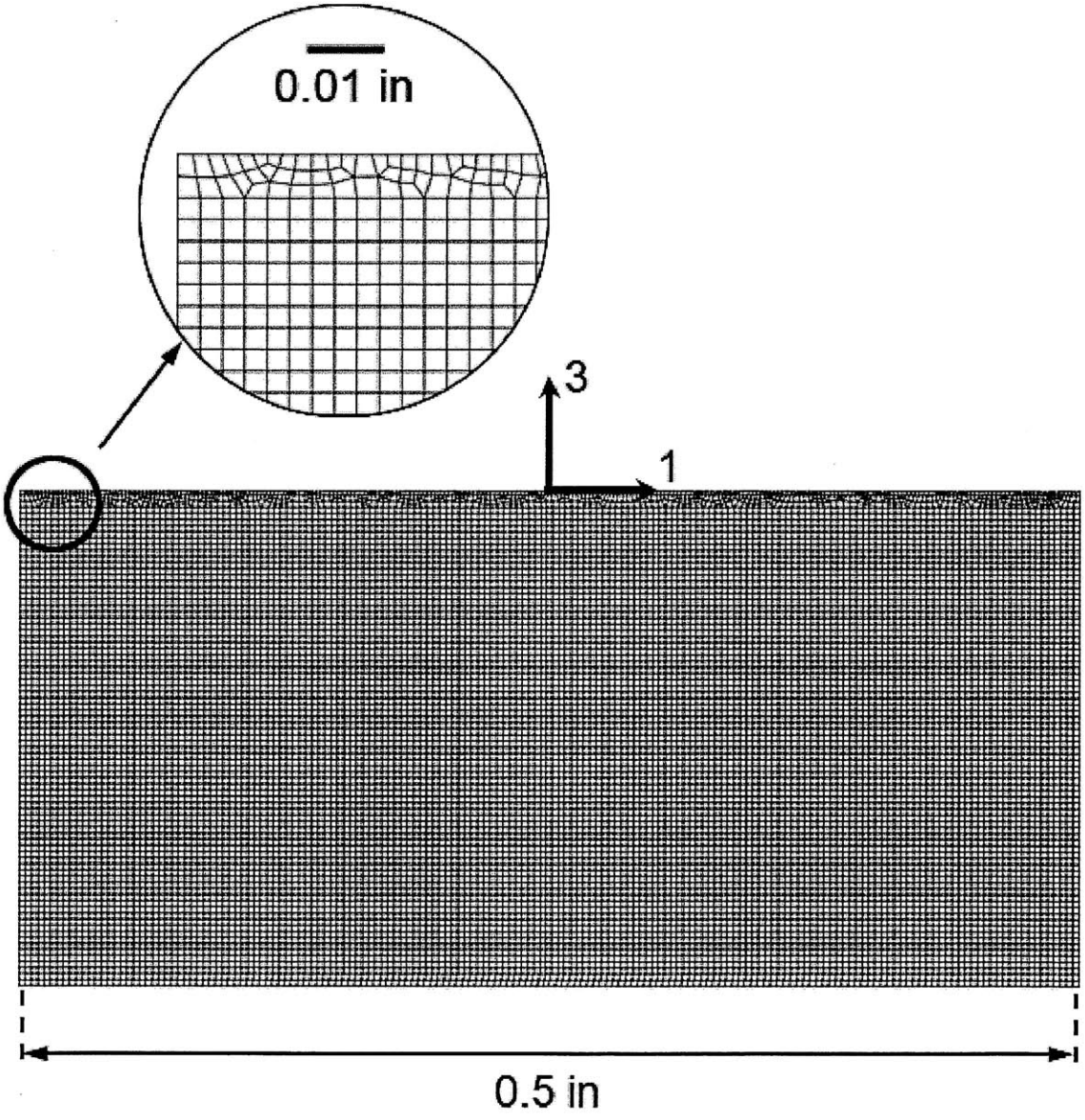

Figure 4.8 Typical finite element mesh in Region 2 for two-dimensional finite element models.

the bottom edge of the laminate, the ply boundaries, the vertical boundary between Regions 1 and 2 (parallel to the x_3-axis), and the vertical free edges. An illustration of the mesh seeding applied to Region 3 is presented in Figure 4.9. The top edge of the laminate, the bottom edge of the laminate, and the ply boundaries share a mesh seed, all using the biased method with a bias ratio of 4.0, and 16 elements per edge. This creates elements of the minimum required size of 0.02 inches ($3.5t_{ply}$) near the groove, while allowing the elements to become larger near the free edges. These settings were largely adopted from previous work by Bastien [5] on isotropic grooved structures, which used an identical bias ratio, but with 8 elements per edge. However, the elements used in that work were 8-node, second-order elements, each with a mid-edge node, meaning the number of nodes along the section edges are consistent with the current work, which uses 4-node first-order elements. These mesh seed settings also meet the minimum size requirement near the groove while not generating too many elements in consideration of computational cost. The vertical boundaries between the Regions and the free vertical edges also share a common mesh seed setting, with both using an element size mesh seed of 0.003 inches ($0.52t_{ply}$). This setting comes from a desire to have at least two elements through the thickness of each ply in order to capture any stress variation within the ply, though little is expected this far from the groove. The "Structured Mesh" meshing control is used for this region in order to lay out a well-structured mesh with a grid format to match the well-defined rectangular shape of the region. This yields gradually longer elements as distance from the groove increases, and a constant number of two elements through the thickness of each ply. The resulting mesh for Region 3 is shown in Figure 4.10 and the full mesh for the laminate is shown in Figure 4.11.

The model for the $[0/\pm45/90]_{15S}$ laminate is slightly different than all other laminates investigated, as it is designed to more closely match that used in the previous work by Bastien [5]. That model is 6.25 inches in length and 0.625 inches in thickness, with a semi-circular groove with a 0.125 inch radius centered halfway along the upper surface. The major distinctions of this model are the increased length, and increased thickness of the laminate. As compared to the 78- and 80-ply models of

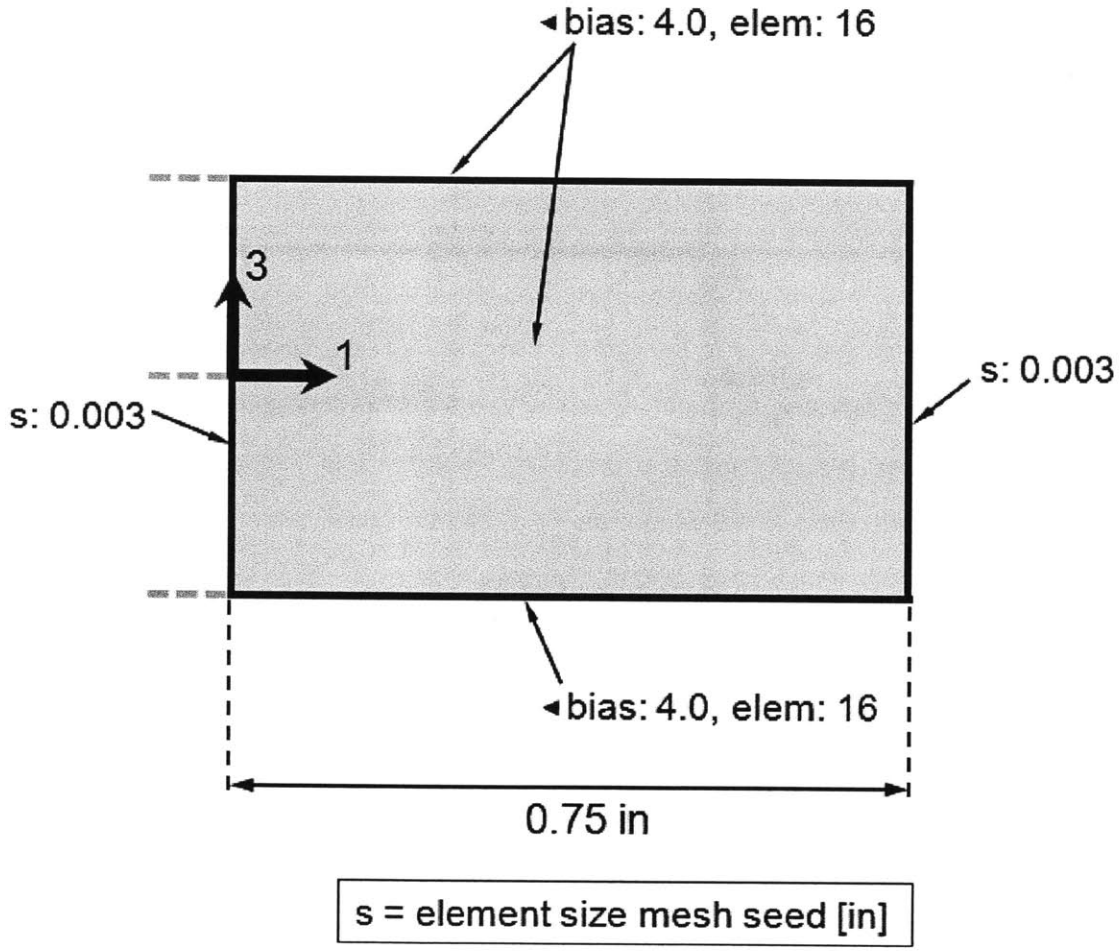

Figure 4.9 Illustration of mesh seeds in Region 3 for two-dimensional finite element models.

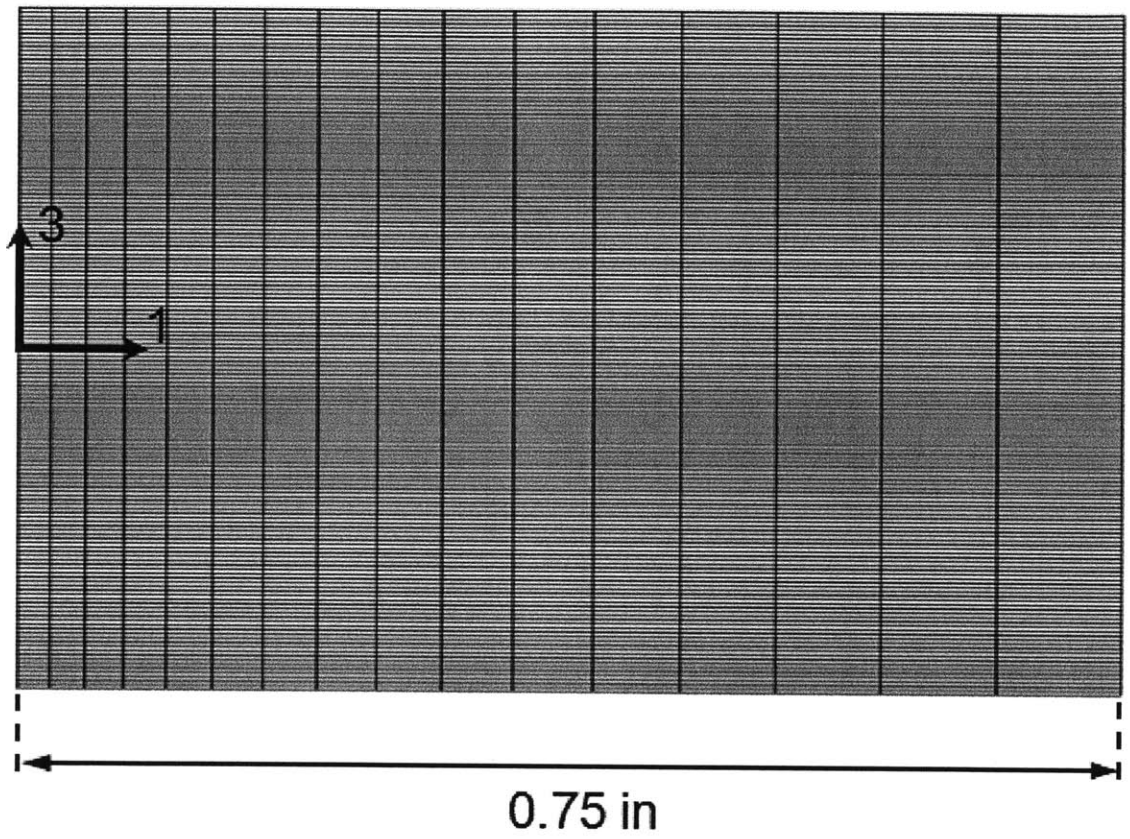

Figure 4.10 Typical finite element mesh in Region 3 for two-dimensional finite element models.

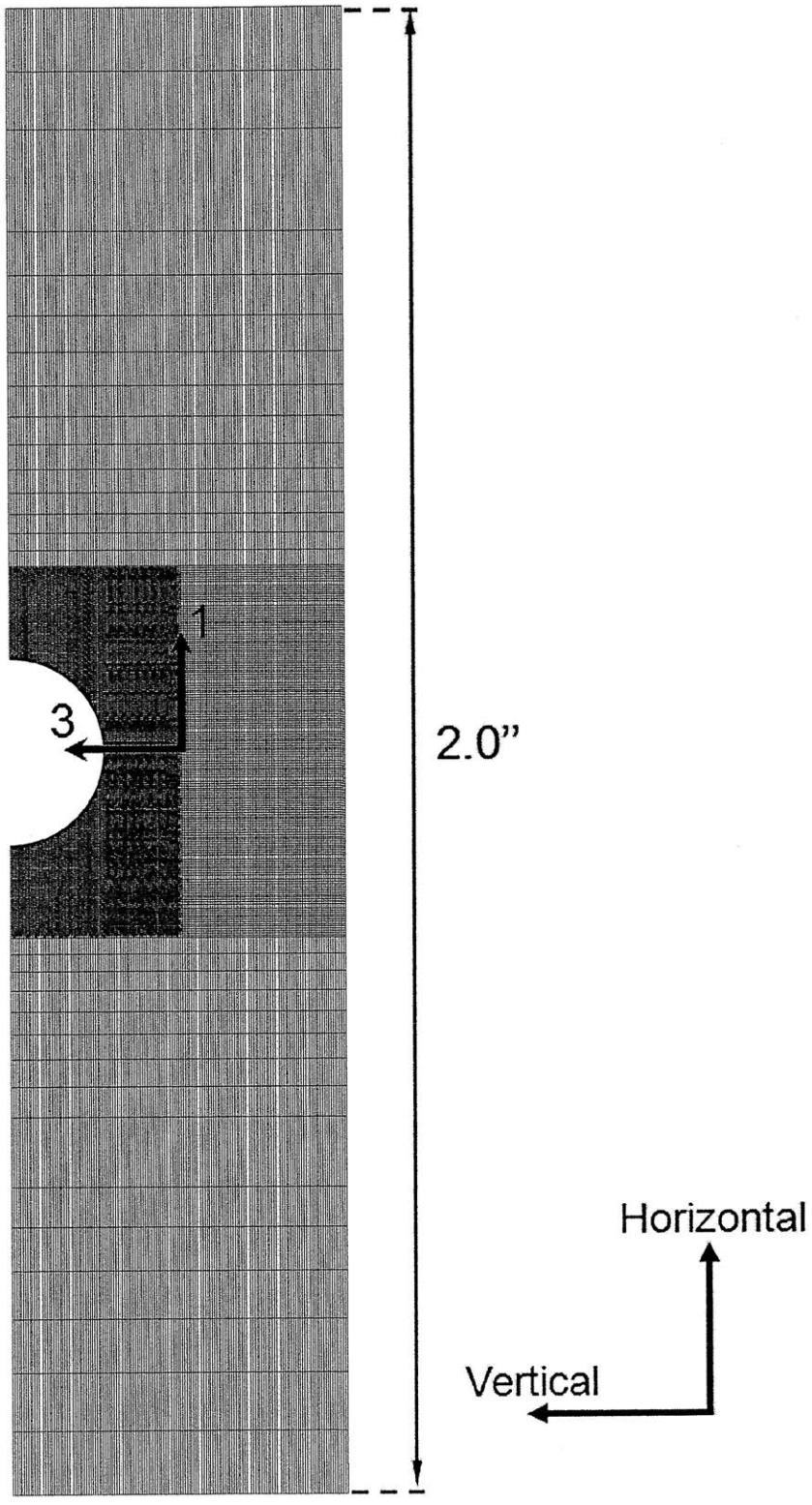

Figure 4.11 Typical complete two-dimensional finite element model of the grooved composite laminate.

the $[\pm\theta/0]_{13S}$, $[\pm 45/0/90]_{10S}$ and $[90/0]_{20S}$ laminates, these differences only require a change in the mesh seeds of Region 3, since Region 3 is comparatively longer in $[0/\pm 45/90]_{15S}$ model. Since the mesh seeds along the horizontal edges in Region 3 are defined by the bias method, the size of the elements is dependent on the number of elements defined to be on the edge. With longer edges in Region 3, using an identical mesh seed for this model as the other models would generate long, distorted elements in Region 3. Consequently, the mesh seed along the horizontal edges in Region 3 are modified for the $[0/\pm 45/90]_{15S}$ laminate model to have a biased seed with a bias ratio of 8.0, and 24 elements per edge. The mesh seeds on the free vertical edges in Region 3 remain the same as in the other models, and have an element size mesh seed of 0.003 inches ($0.52t_{ply}$). As in the other models, this results in the creation of a mesh with the desired two elements through the thickness of a ply. The "Structured" meshing control is again used for this region. The results are similar to other models, with gradually lengthening elements as distance from the groove increases and a constant 2 elements through the thickness of each ply. In the $[0/\pm 45/90]_{15S}$ model, meshing methods for Regions 1 and 2 remain the same as the mesh seeds in these regions are defined by element size and are not adversely affected by the change in dimensions of the laminate in this model.

Two different indentor models are used to apply load in the present work: a rigid body indentor, and a linear elastic indentor. The rigid indentor is defined as an analytical rigid body with motion defined by a single point, known as the "Reference Node", to which all loads and displacements are applied. The surface of the indentor is defined in reference to this "Reference Node". Analytical rigid bodies in ABAQUS are defined as a series of lines or curves defining the surface of the body. They are beneficial to contact modeling because their surfaces are smooth, in comparison to discretized surfaces, thus providing a smoother application of contact pressure. Rigid bodies are also less computationally costly. In the two-dimensional models using a rigid indentor, the rigid body is defined as a circle with a radius of 0.1225 inches. The motion of the indentor is constrained to translate only in the 3-direction to ensure centered load application to the laminate. These boundary conditions, as well as the

loading, are applied through the "Reference Node".

For the two dimensional models using a steel indentor, the model of the indentor is defined as a circle with a radius of 0.1225 inches. The indentor is defined by two surfaces, the top half surface, and the bottom half surface. The top surface of the indentor is less of a concern for this model, though this is where the initial load is applied, but the stress distribution in the indentor is not of interest, nor will it participate in any contact behavior of interest. Thus, a coarser mesh can be used for the top surface than for the lower surface. The lower surface of the indentor is in contact with the grooved surface of the laminate. Thus, a finer mesh is desired to model the curved surface of the indentor as accurately as possible, and to transmit the contact force as realistically as possible. For reasons related to contact modeling and discussed in the following section, the mesh of the indentor should be slightly coarser than the mesh of the groove face of the laminate. Thus, the bottom face of the indentor is covered by an element size mesh seed of 0.0015 inches. For the top of the indentor, an element size mesh seed is used as well. It is desirable to have a larger seed on the top of the indentor to yield a coarser mesh to save computational resources. After some preliminary trial and error, it was determined that too large of a mesh seed on the top surface distorted the internal mesh of the indentor. An element size mesh seed of 0.01 inches was found to produce a good balance between a coarse mesh and well-formed elements.

The indentor was split into two equal sections through the vertical centerline. This creates a vertical boundary through the center of the indentor, ensuring that the interior of the mesh has nodes lying along this vertical line for use in defining the boundary conditions necessary to keep the motion of the indentor purely vertical. The line splits the indentor symmetrically, but the automatic mesher in ABAQUS does not create a symmetric mesh across this line, so it would not accurately be described as a line of symmetry. A "Free Meshing" mesh control is used for the whole of the indentor. The mesh seeding applied to the indentor is presented in Figure 4.12 and the resulting mesh is shown in Figure 4.13. The nodes on the centerline of the indentor is constrained to only move in the 3-direction, and the full load is applied

to the top-most center node of the indentor.

4.2.4 Three-Dimensional Models

The cost of computation for the three-dimensional models is considerably higher than the two-dimensional models due to the increased number of elements required to model the third dimension, and the increase in degrees of freedom from three to six (three translation and three rotation). In order to moderate the cost of computation, a plane of symmetry in the 2-3 plane that runs parallel to the groove across the width of the laminate is employed for the three-dimensional models, as shown in Figure 4.14. This formulation is not ideal because it produces stress concentrations near the plane of symmetry in angled plies. This is due to the mathematical formulation of the symmetry condition that ensures that there is no movement in the 1-direction, and that there are no rotations along the 2- and 3- directions, forcing the plane of symmetry to remain planar and immobile. This is an accurate formulation for 0° and 90° plies, and for isotropic materials. However, due to the resultant stress in angled plies, this condition creates stress concentrations when applied to angled plies. This is a result of the directionality of the orthotropic nature of the material properties for these plies and having coefficients of mutual influence.

A simple investigation was conducted to estimate the effect of the plane of symmetry, consisting of a quasi-isotropic $[0/\pm45/90]_{4S}$ laminated plate, with no groove, in simple tension applied in the 1-direction. Two finite element models were created, one modeling the full plate, and one modeling half the plate with a 2-3 plane of symmetry. In the half-plate model with a plane of symmetry, the longitudinal stresses, σ_{11}, at the plane of symmetry in the ±45° plies decreased by an average of 31.9% from the full plate value. Stresses in the 0° and 90° plies consequently rose by 5.1% and 17.2%, respectively, to balance the load across the cross-section of the laminate. Stresses within 5% of the full plate value are recovered within 3.5 ply thicknesses of the plane of symmetry, and stresses within 1% are recovered within 6 ply thicknesses. No such variation in stresses was observed for a $[0/90]_{8S}$ laminate with identical loading, with no noticable change in stress at the plane of symmetry. The loading of this

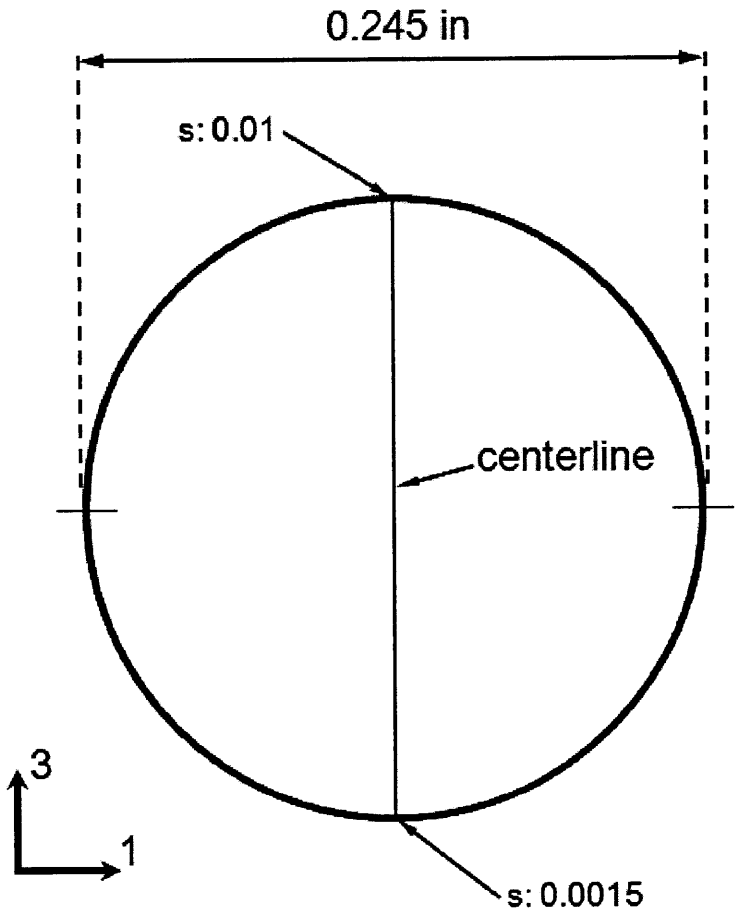

Figure 4.12 Illustration of mesh seeds on the linear elastic indentor in the two-dimensional finite element models.

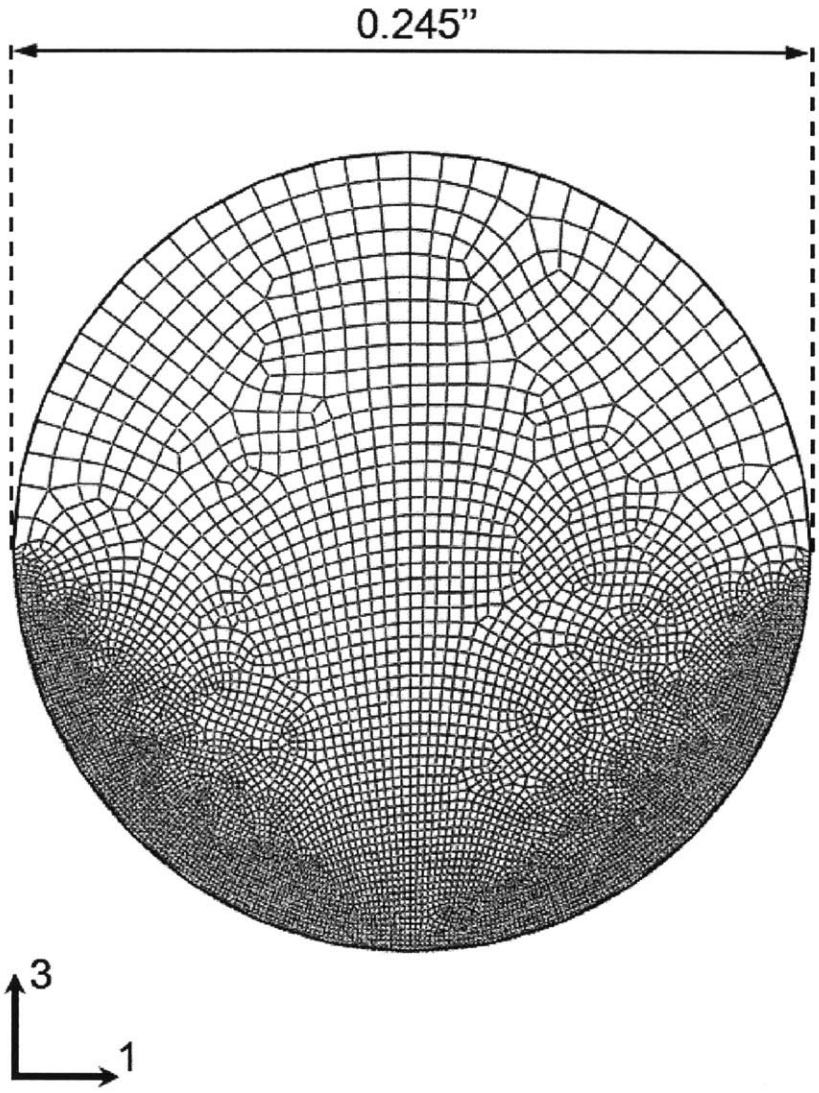

Figure 4.13 Finite element mesh of the linear elastic indentor for two-dimensional finite element models.

simple longitudinal tension case is clearly different than the unique loading presented in the grooved composite model, but similar principles still apply. Thus, this gives a sense of the potential higher end error for the stresses local to the plane of symmetry. While these stress concentrations are not ideal, this plane of symmetry remains the best solution for analysis accuracy without doubling the number of elements in the model, which would make the computational cost prohibitive.

The three-dimensional models have two slightly different sets of dimensions resulting from the difference in the number of plies for the different laminates. The models are both 1 inch in length and 1 inch in width with a semi-circular groove with a radius of 0.125 inches centered halfway along the upper surface. The $[\pm\theta/0]_{13S}$ laminates have 78 plies, giving a thickness of 0.450 inches. The $[\pm 45/0/90]_{10S}$ and $[90/0]_{20S}$ laminates have 80 plies, and thus are slightly thicker at 0.462 inches due to the two additional plies. These configurations share a common mesh seed and mesh control method.

For creation of the finite element mesh, the three-dimensional models are divided into sections that define individual plies in order to account for the laminated nature of the configuration, as for the two-dimensional models. This ensures that when the finite element mesh is generated, the ply boundaries are clear, flat, and straight in the mesh, and that appropriate material properties can be applied to each individual ply based on the layup angle of that ply. In the region near the groove, these ply boundaries end at the physical face of the groove. To control element density, the models are divided into three meshing regions that encompass multiple plies, as shown in Figure 4.14. The goal in dividing the laminate in this manner is to concentrate elements in the region of interest near the point where the indentor contacts the laminate, and where stress gradients are expected to be highest. This is similar to the two-dimensional case, with additional considerations for the variation in the 2-direction.

Region 1 is the area most local to contact, running from the center of the groove, at x_1 equal to 0, to two groove radii away at x_1 equal to 0.25 inches, similar to the two-dimensional case. In the 2-direction, Region 1 extends a groove radius away from

the origin along the x_2-axis in either direction. This makes the region 0.25 inches wide from x_2 equals $-0.125''$ to $+0.125''$. Region 1 runs the full thickness of the laminate in the 3-direction. Region 2 is the area local to the groove, but away from the point of contact, and comprises two disconnected volumes, both going from the groove center at x_1 equal to 0 to two groove radii away at a value of x_1 equal to 0.25 inches. Both sections of Region 2 run the full thickness of the laminate. While one runs from an x_2 value of $+0.125$ inches to the laminate edge at x_2 equal to $+0.5$ inches, the other is the mirror image from x_2 equal to -0.125 inches to x_2 equal to -0.5 inches. Region 3 is the main body of the laminate away from the groove, and runs away from the groove from two groove radii from the center of the laminate at an x_1 value of $+0.125$ inches to the free edge of the laminate at x_1 equal to $+1.0$ inches. This region runs the full width of the laminate, and the full thickness of the laminate.

The location of the boundary between Regions 1 and 3 is carried over from the two-dimensional case. The boundary between Regions 1 and 2 was determined such that all contact would occur within Region 1, requiring the region to span the indentor diameter in the 2-direction in the worst case scenario. Additionally, Region 1 is intended to capture the majority of the stress gradients in the response. The width of Region 1 was expanded slightly to a groove diameter, or a groove radius on either side of the origin along the x_2-axis, to make the boundaries consistent with the geometry and terminology of the laminate, independent of the indentor size. Regions 2 and 3 are intended to capture any additional stress behavior beyond the area of contact, and stress gradients in these regions are expected to be low, based on previous two-dimensional work [5].

Due to concerns about the computational cost of the three-dimensional model, the finite element mesh is particularly tailored in order to be able to show appropriate resolution of stress and contact pressure gradients, while minimizing the number of elements. The goal is to achieve a balance between a good concentration of elements near regions of high stress and large stress gradients, while minimizing the computational cost. These models stress the available computational resources far more severely than the two-dimensional models. The primary area of interest, as

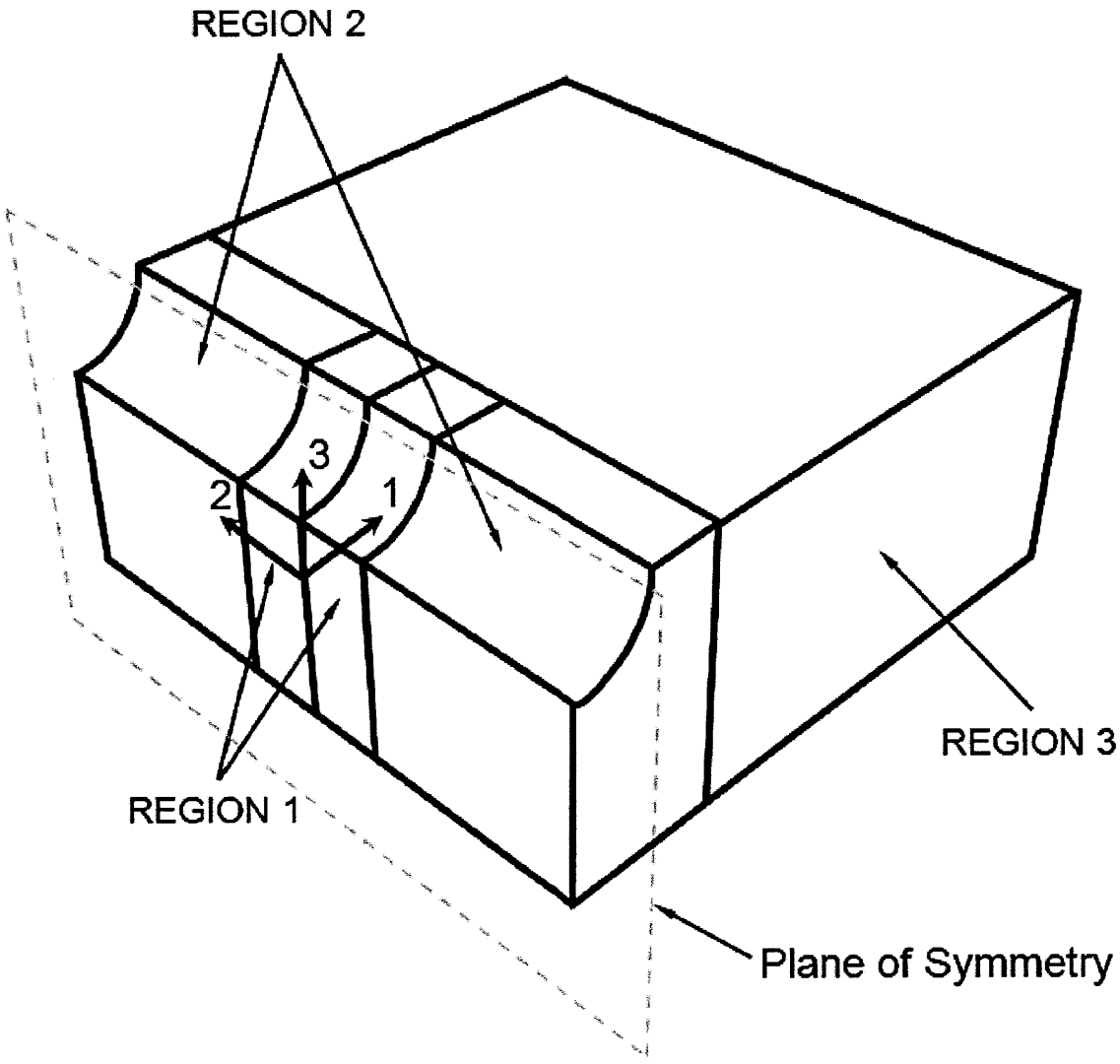

Figure 4.14 Illustration of meshing regions for three-dimensional finite element models.

in the two-dimensional models, is the groove face, and the area near the point of contact. It is again desirable to have multiple elements through the thickness of each ply in this location in order to capture any potential contact pressure variation from ply to ply, and even within each ply. Near areas of interest, at least two elements should be present through the thickness of the laminate. The three or four elements through the thickness used in the two-dimensional models are not feasible in the three-dimensional models due to computational costs. Similarly, away from areas of interest, a coarser mesh should suffice. One element through the thickness of each ply can suffice in these locations, as the two elements through the thickness seen in the two-dimensional model are again not feasible due to computational costs. An extensive trial and error method was used to arrive at the mesh seeds and exact values used. These numbers are based partially on the guidelines discussed, partially on limiting the number of elements to a manageable size, and partially on generating a regular, well-formed mesh.

Regions 1 and 2 share a common mesh cross-section in the 1-3 plane, perpendicular to the groove. This two-dimensional mesh plane is swept through the width of the laminate in the 2-direction to form a three-dimensional mesh. The mesh seeding used for this common cross-section is presented in Figure 4.15. The edges composing the groove face have element size mesh seeds. The element size along the groove through the top nine plies, where contact is not expected, is 0.003 inches ($0.52t_{ply}$). The element edge length through the rest of the groove face is 0.0011 inches ($0.19t_{ply}$). This is a variation from the two-dimensional model necessary to reduce the number of elements while not substantially reducing the resolution of the contact pressure distribution. Starting from the top surface of the laminate and running nine plies deep, the horizontal edges and ply boundaries have a biased mesh seed with a bias ratio of 3.0, and 20 elements, placing a greater concentration of elements near the groove, with elements ranging in size from 0.0034 inches ($0.59t_{ply}$) to 0.01 inches ($1.73t_{ply}$). Continuing through the laminate to the bottom of the groove, the ply boundaries then have an element size mesh seed of 0.0037 inches ($0.64t_{ply}$). This value was arrived at through trial and error in an attempt to avoid a malformed mesh

in this region. From the bottom of the groove to the laminate midplane, the ply boundaries again have a biased mesh seed with a bias ratio of 3.0, and 50 elements, placing a greater concentration of elements near the plane of symmetry, with elements ranging in size from 0.0027 inches ($0.47t_{ply}$) to 0.0082 inches ($1.4t_{ply}$). From the laminate midplane to the bottom face of the laminate, ply boundaries have a seed that generates a slightly coarser mesh, with a biased mesh seed with a bias ratio of 2.0, and 28 elements, resulting in elements ranging in size from 0.0062 inches ($1.1t_{ply}$) to 0.012 inches ($2.1t_{ply}$). The vertical edges of Regions 1 and 2 have an element size mesh seed, and more explicitly define the number of elements through the thickness of each ply. From the top of the laminate to nine plies deep, the edge length is 0.01 inches ($1.73t_{ply}$), yielding one element per ply in sections where stresses and stress gradients are expected to be low. From ten plies deep to the laminate midplane, the edge length is 0.003 inches ($0.52t_{ply}$), yielding two elements per ply. And from the laminate mid-plane down to the bottom face of the laminate, the element edge length is 0.01 inches ($1.73t_{ply}$), again yielding one element per ply. The resulting mesh cross-section is shown in Figure 4.16.

The cross-section described is swept along the 2-direction through Region 2 with the "Swept Mesh" mesh control. The sweep through the region is controlled by placing mesh seeds on the edges running in the 2-direction defining the region boundary and the ply boundaries. The seed is a biased mesh seed with a bias ratio of 6.0, and 7 elements, with a higher element concentration toward the point of contact at x_2 equal to 0, resulting in elements ranging in size from 0.018 inches ($3.1t_{ply}$) to 0.11 inches ($19t_{ply}$). This seed was arrived at mostly through trial and error optimization and is constrained by requirements to match the element size at the boundary with Region 1, and to minimize the number of elements used in this region. The same cross-section is swept along the 2-direction through Region 1 at a higher element density. A biased mesh seed with a bias ratio of 17.0, and 24 elements is used, with the higher concentration of elements toward the point of contact at x_2 equals 0, resulting in elements ranging in size from 0.0009 inches ($0.16t_{ply}$) to 0.015 inches ($2.6t_{ply}$). This seed generates a very large number of elements, and thus was also subject to trial

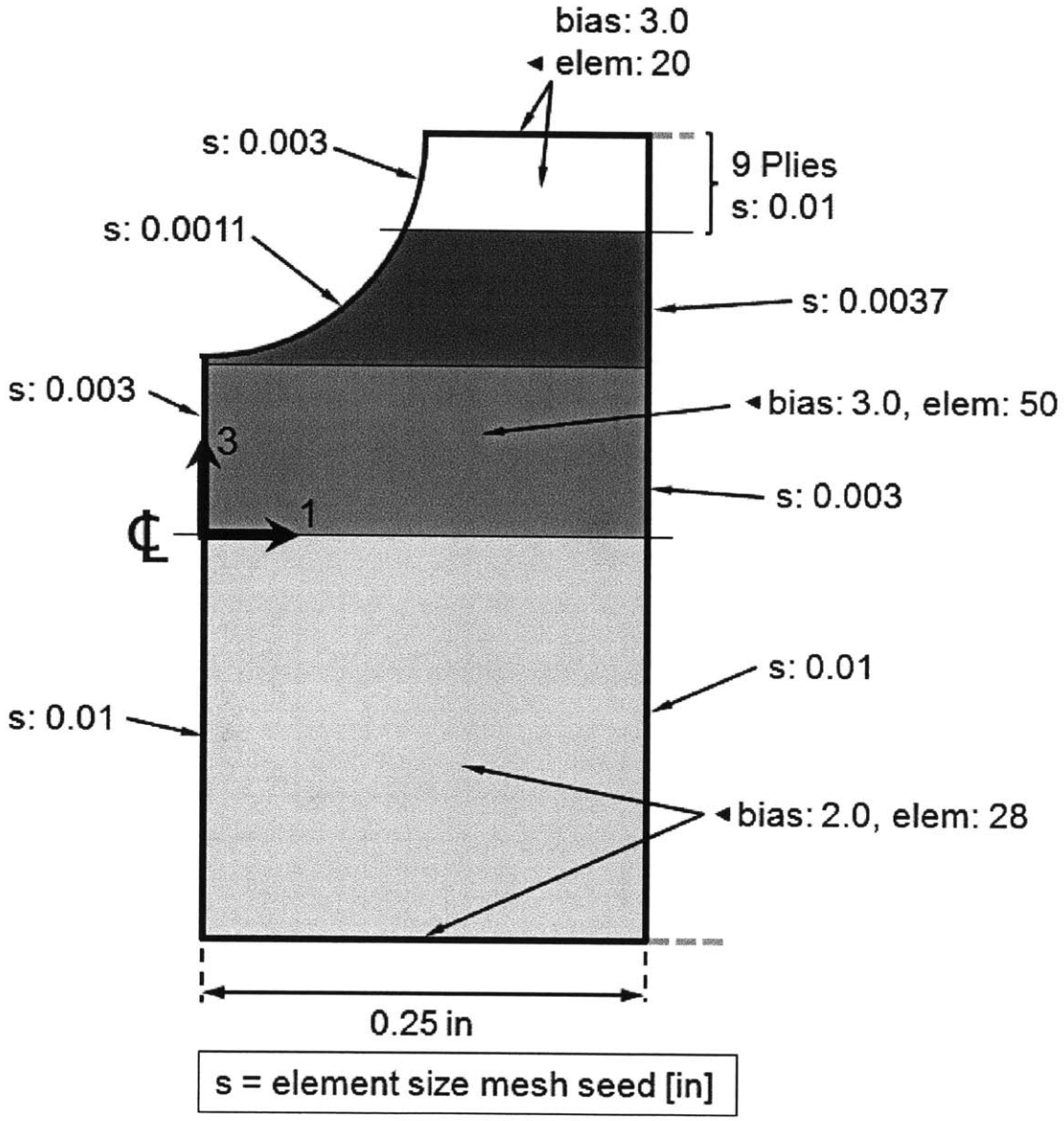

Figure 4.15 Illustration of mesh seed cross-section in the 1-3 plane for Regions 1 and 2 for three-dimensional finite element models.

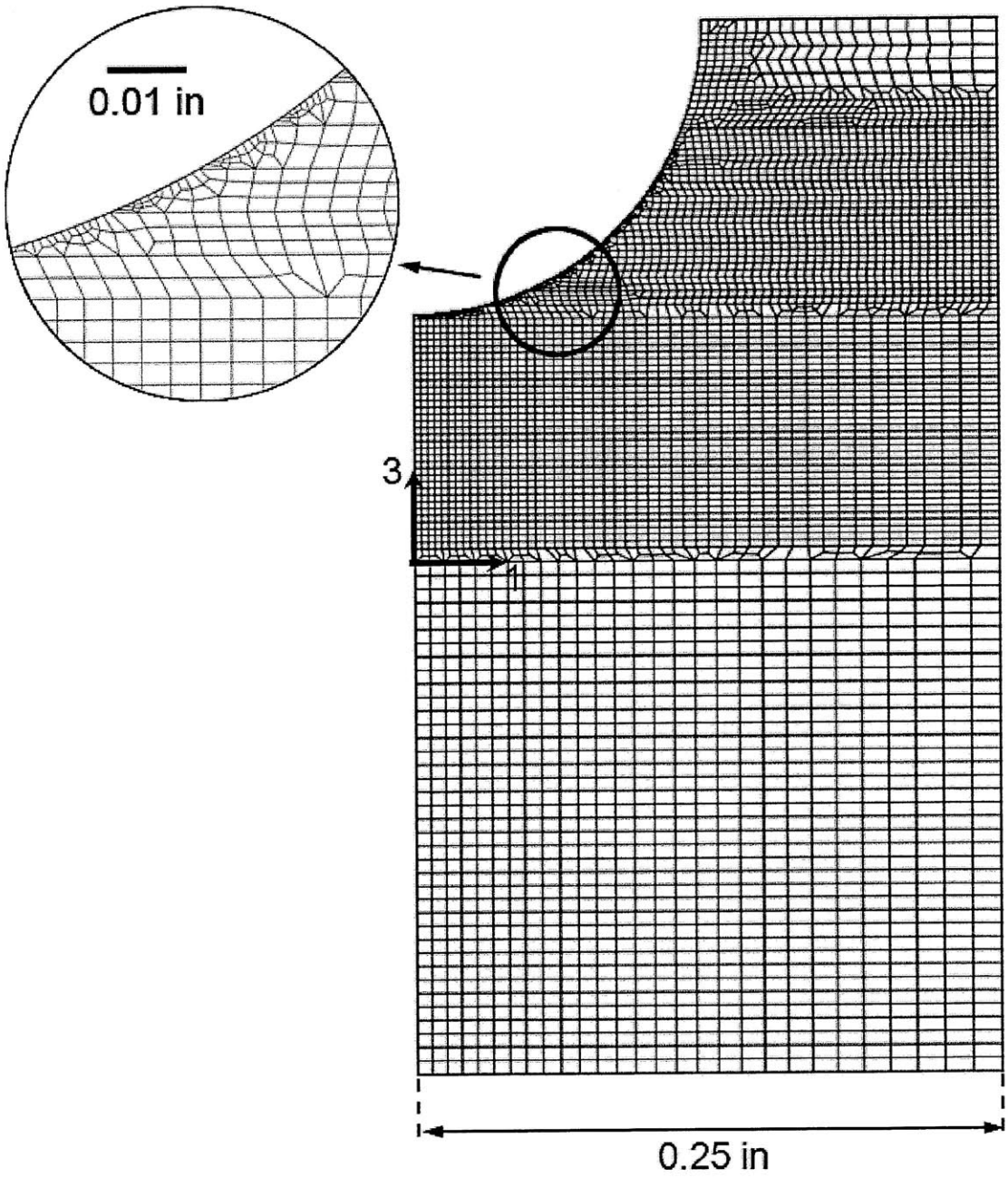

Figure 4.16 Typical finite element cross-section for the 1-3 plane, swept in the 2-direction through Regions 1 and 2 of the three-dimensional finite element models.

and error optimization. The size of the elements near the point of contact needed to be on the order of 0.001 inches in order to match the element size seed on the groove face in the 1-3 plane, and to maintain a similar element size for the largest anticipated contact width of 0.01 inches on either side of the center of contact at the x_1-axis. The number of elements needed to be minimized within these constraints.

Region 3, which is farthest from the groove and center of contact, features a single coarse mesh cross-section that is defined in the 1-2 plane and swept through the thickness of the laminate. The settings for this region are largely adapted from prior work done by Bastien [5]. Edges running in the 1-direction are seeded with a biased mesh seed with a bias ratio of 8.0, and 8 elements, clustering elements closer to the groove, and coarsening the mesh toward the free edge. This biased seed results in elements ranging in size from 0.027 inches ($4.7t_{ply}$) to 0.21 inches ($36t_{ply}$). The edge of the laminate farthest from the groove has an element size mesh seed of 0.16 inches ($27t_{ply}$). Mesh seeds on the edges defining the boundary between Regions 1 and 3 and Regions 2 and 3 retain the mesh seed described for those regions. This region has a "Swept Mesh" mesh control with the direction of sweep being through the thickness of the laminate along the 3-direction. An illustration of the mesh seeding used for sweeping the mesh in Regions 1 and 2, and the mesh seeding used for Region 3, is presented in Figure 4.17. The resulting mesh, as viewed from the top, is shown in Figure 4.18, and a full isometric view of the mesh for the three-dimensional model is shown in Figure 4.19.

In the three-dimensional model, the indentor is a rigid sphere. Three-dimensional analytical rigid bodies in ABAQUS are defined as a series of lines or curves that can either be extruded or revolved to define the surface of a body. They are beneficial to contact modeling because their surfaces are smooth, in comparison to discretized surfaces, thus providing a smoother application of contact pressure. Rigid bodies are also less computationally costly, since they are not deformable and hence contribute no degrees of freedom to the analysis system. The indentor used in the three-dimensional modeling is a sphere with a radius of 0.1225 inches. This sphere is defined as an analytical rigid body with a corresponding "Reference Node", used to define the

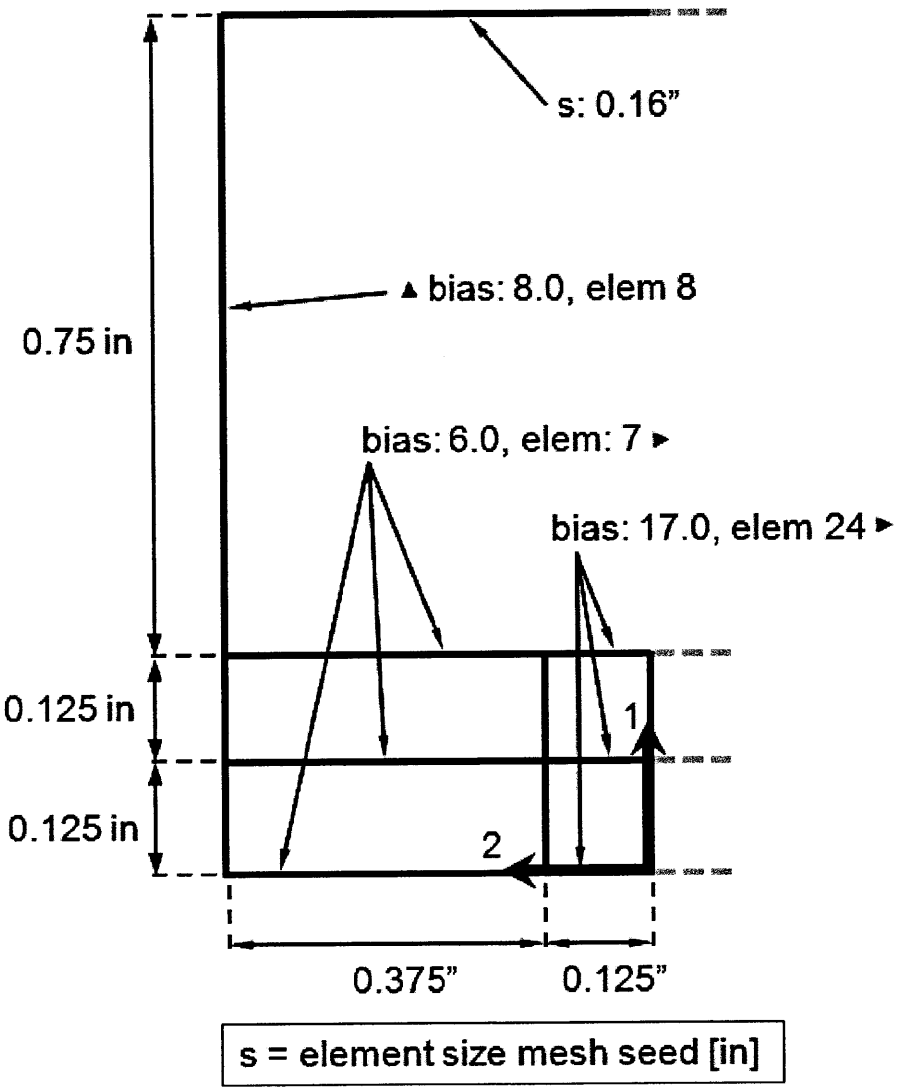

Figure 4.17 Illustration of mesh seed cross-section in the 1-2 plane for Regions 1, 2 and 3 for three-dimensional finite element models.

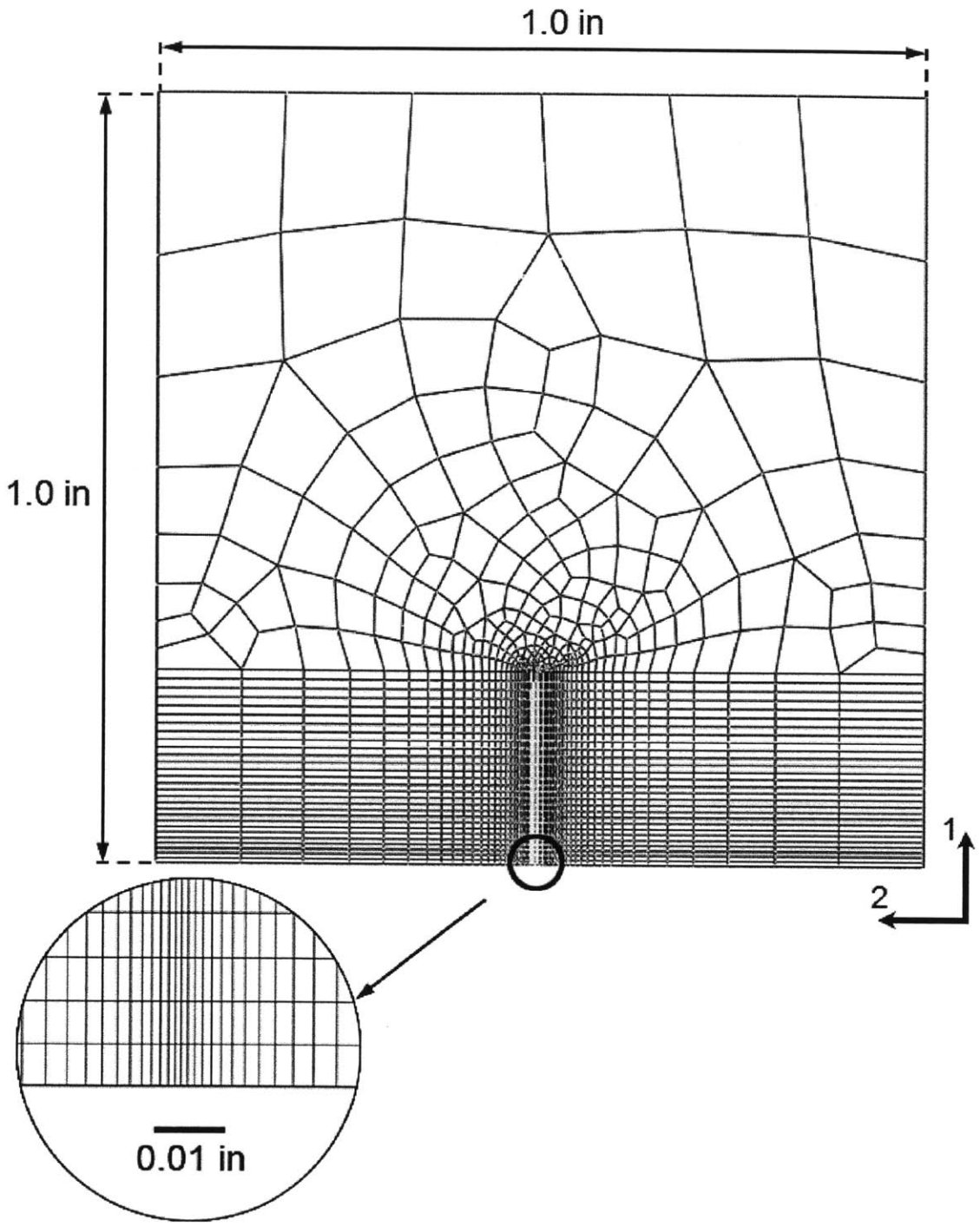

Figure 4.18 Typical three-dimensional finite element model of the top surface, showing the mesh in Region 3 swept in the 3-direction, and the seedings for the 2-direction sweep through Regions 1 and 2.

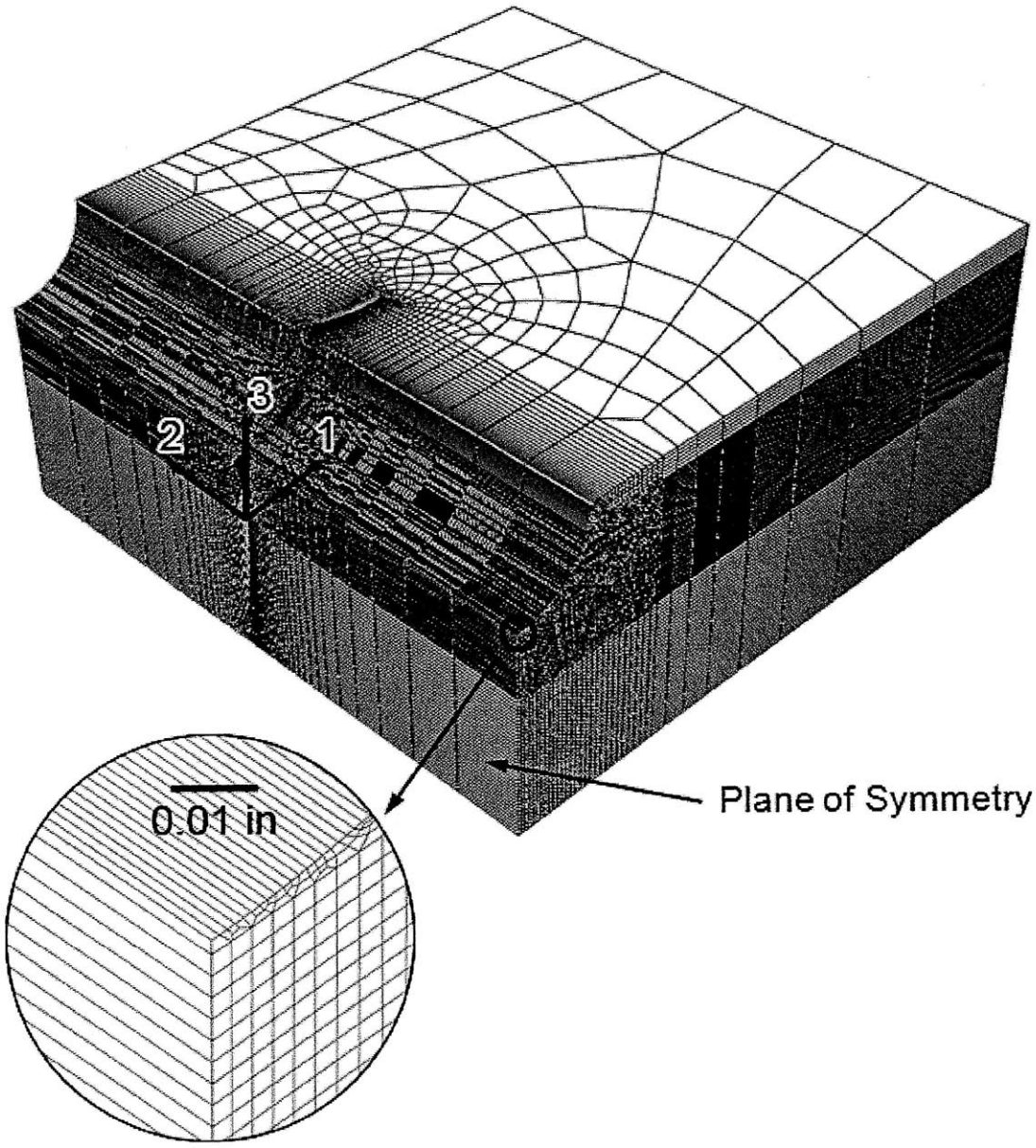

Figure 4.19 Typical full three-dimensional finite element model of the grooved composite laminate.

motion of the body and its surface. Constraints are placed on the motion of the body ensuring only motion in the 3-direction. These boundary conditions, as well as the loading, are applied through the "Reference Node".

A list of all finite element models created for this work, both two-dimensional and three-dimensional, are provided in Table 4.1. This list details the dimensionality of the model (two-dimensional or three-dimensional), the material and laminate used, and the indentor type (rigid body or deformable linear elastic).

4.3 Finite Element Analysis

Since the focus of this work is the response of a grooved composite to a static contact load, the described models were run using a nonlinear, static stress analysis. The formulation is required to be nonlinear due to nonlinearities in the contact area and with regard to the contact pressure distribution. For example, the contact area is known to increase nonlinearly with load in isotropic contact [7]. A similar nonlinearity is expected here, although the specifics will likely differ due to the orthotropic and laminated nature of the material. The use of contact in this model requires an incremental increase of the load applied to the indentor. The increment levels for the two-dimensional case were the default levels for ABAQUS. The increment levels in the three-dimensional case were assigned to minimize the computational time, as the complete model is solved for every iteration. Thus, controlling the number of iterations can decrease the solution time. The iteration load levels for both the two-dimensional and three-dimensional cases are shown in Table 4.2. Loads are given as ratio of applied load to maximum load.

At each of these stepwise increments, a series of equilibrium iterations are performed by ABAQUS in order to determine the pressure distribution over the whole set of nodes in contact using force and moment equilibrium. These iterations within each increment are solved using Newton's Method to obtain final equilibrium within each increment. Severe Discontinuity Iterations are also performed by ABAQUS in

Table 4.1 Summary of all finite element models created for the current work

Model	Dimensionality	Material	Laminate	Indentor
1	Two-dimensional	T700/2510	$[\pm 15/0]_{13S}$	Rigid
2	Two-dimensional	T700/2510	$[\pm 30/0]_{13S}$	Rigid
3	Two-dimensional	T700/2510	$[\pm 45/0]_{13S}$	Rigid
4	Two-dimensional	T700/2510	$[\pm 60/0]_{13S}$	Rigid
5	Two-dimensional	T700/2510	$[90/0]_{20S}$	Rigid
6	Two-dimensional	T700/2510	$[\pm 45/0/90]_{10S}$	Rigid
7	Two-dimensional	AS1/3501-6	$[0/\pm 45/90]_{15S}$	Rigid
8	Two-dimensional	T700/2510	$[\pm 15/0]_{13S}$	Elastic
9	Two-dimensional	T700/2510	$[\pm 30/0]_{13S}$	Elastic
10	Two-dimensional	T700/2510	$[\pm 45/0]_{13S}$	Elastic
11	Two-dimensional	T700/2510	$[\pm 60/0]_{13S}$	Elastic
12	Two-dimensional	T700/2510	$[90/0]_{20S}$	Elastic
13	Two-dimensional	T700/2510	$[\pm 45/0/90]_{10S}$	Elastic
14	Two-dimensional	AS1/3501-6	$[0/\pm 45/90]_{15S}$	Elastic
15	Three-dimensional	T700/2510	$[\pm 15/0]_{13S}$	Rigid
16	Three-dimensional	T700/2510	$[\pm 30/0]_{13S}$	Rigid
17	Three-dimensional	T700/2510	$[\pm 45/0]_{13S}$	Rigid
18	Three-dimensional	T700/2510	$[\pm 60/0]_{13S}$	Rigid
19	Three-dimensional	T700/2510	$[90/0]_{20S}$	Rigid
20	Three-dimensional	T700/2510	$[\pm 45/0/90]_{10S}$	Rigid

Table 4.2 Load increment levels for two-dimensional and three-dimensional cases, given as ratio of applied load to maximum load

Increment	Load Increment Ratio	
	2-D Case	3-D Case
1	0.1	0.2
2	0.2	0.4
3	0.35	0.6
4	0.575	0.8
5	0.9125	1.0
6	1.0	-
Maximum Load	5000 lb/in	300 lb

contact situations. These iterations are a form of equilibrium iteration that track abrupt changes in the stiffness matrix of the system, such as new nodes coming into contact, and thus being applied with a contact constraint. These iterations continue until there are no further severe discontinuities, at which point normal equilibrium iterations resume. Once equilibrium is achieved, the next load increment is started.

Chapter 5

RESULTS

The response of a structure is determined primarily by the material, the loading, and the boundary conditions. In this investigation, the material and boundary conditions are predetermined, but the specifics of the loading are determined by the contact condition with the indentor. This makes the contact pressure distribution of particular interest, as this pressure is not predetermined, and cannot be determined analytically. The various distributions of contact pressure, as determined through finite element analysis, are examined through a series of contact pressure plots that show how contact pressure changes around the groove, and from one ply to the next. The structural response of the laminate to this loading is examined through the stress distributions. The primary stresses of interest are σ_{11}, σ_{33}, and σ_{13}, which are the primary stresses available in two-dimensional modeling in the 1-3 plane. When presented, these stresses are normalized by the applied loading. The stress distributions, as determined by the finite element analysis of this work, are shown through the use of isostress plots. These are contour plots that connect points of equivalent stress through the laminate. Isostress lines are plotted at intervals of regular value of stress and are labeled to indicate the magnitude and sign (compression or tension) of stress. Tightly packed isostress lines indicate a high stress gradient.

5.1 Cylinder Loading – Rigid Indentor

The first set of results presented are from the models of a grooved composite laminate transversely loaded by a rigid cylindrical indentor. In this case, the models are two-dimensional plane strain, representing a slice of a laminate and indentor that are infinitely long in the 2-direction. A rigid body represents the indentor due to the high stiffness of the steel indentor relative to the transverse stiffness of the laminate. A load of 5000 lb/in is applied to the rigid indentor in the 3-direction. The load is transfered to the grooved composite. The composite is constrained with a rigid backface boundary condition, as described in Chapter 4. Seven laminates were studied in this configuration. A single laminate of AS1/3501-6 in a $[0/\pm 45/90]_{15S}$ layup is used to compare results from loading with a rigid indentor to loading with a Hertzian pressure distribution done in previous work [5]. Four laminates of T700/2510 in $[\pm\theta/0]_{13S}$ layups are used to study the effects of varying ply angle in the laminate. A laminate of T700/2510 in a $[90/0]_{20S}$ layup is used to study the effects of ply mismatch, and a T700/2510 layup of $[\pm 45/0/90]_{10S}$ is used to examine the essential quasi-isotropic case.

5.1.1 Contact Pressure

The term "contact pressure" refers to the pressure that results on the surface of the groove from the loaded rigid body. It is this pressure distribution, along with the global boundary conditions of the laminate, that determines the response of the laminate. This contact pressure cannot be analytically determined for a laminated, orthotropic grooved surface using methods currently available. The use of a numerical method allows the pressure distribution to be determined with relative accuracy. However, there is a limitation for this method since the contact pressure is only computed at the nodes of the finite element model, and is defined as piecewise linear between these points. It is possible that the actual pressure distribution could reach peaks or troughs between nodes, and thus this model could miss that type of extreme behavior. Thus, as discussed in Section 4.2, it was important in constructing the

model to have a high node density on the groove surface to minimize the potential of missing small features characterized by high gradients in the pressure distribution and maximize resolution of the curve.

The following plots of contact pressure show the contact pressure along the vertical axis, with the angle around the groove, ϕ, on the horizontal axis. The angle around the groove, ϕ, can be easily mapped to x_1 and x_3 coordinates using the geometry of the groove with the equations:

$$x_1 = r_g * \sin\phi \tag{5.1}$$

$$x_3 = \frac{t}{2} - r_g * \cos\phi \tag{5.2}$$

where r_g is the groove radius, and t is the laminate thickness. The displayed contact pressure has been normalized by the applied load. This load is noted for each figure in the figure caption. The primary load under investigation for the two-dimensional case is 5000 lb/in, with lesser loads being used to study the linearity or nonlinearity of the response. This gives stress and pressure results with units of [psi/(lb/in)]. Ply boundaries are indicated in the plots by light gray dashed lines, and ply angles are given along the top of the figure.

For the family of T700/2510 laminates used for examination of ply angle, $[\pm\theta/0]_{13S}$, the contact pressure distributions are presented in Figures 5.1, 5.2, 5.3, and 5.4 for ply angles, θ, of 15°, 30°, 45°, and 60°, respectively. The contact pressure distribution for the cross-ply T700/25010 laminate, $[90/0]_{20S}$, is shown in Figure 5.5. The contact pressure distribution for the quasi-isotropic T700/2510 laminate, $[\pm45/0/90]_{10S}$, is shown in Figure 5.6. The contact pressure distribution for the quasi-isotropic AS1/3501-6 laminate, $[0/\pm45/90]_{15S}$, is shown in Figure 5.7. The maximum normalized contact pressure, $p^*_{C_{max}}$, and its location, ϕ_P, along with the maximum contact angle, $\phi_{contact}$, are listed in Table 5.1 for all the laminates above.

The contact pressure data exhibit some features common to all the laminates examined. The maximum pressure occurs near the bottom of the groove, always within the lowest ply in the groove, and generally at a groove angle, ϕ, of 2.1° or lower, with the one exception being the $[\pm60/0]_{13S}$ laminate. In all cases, contact

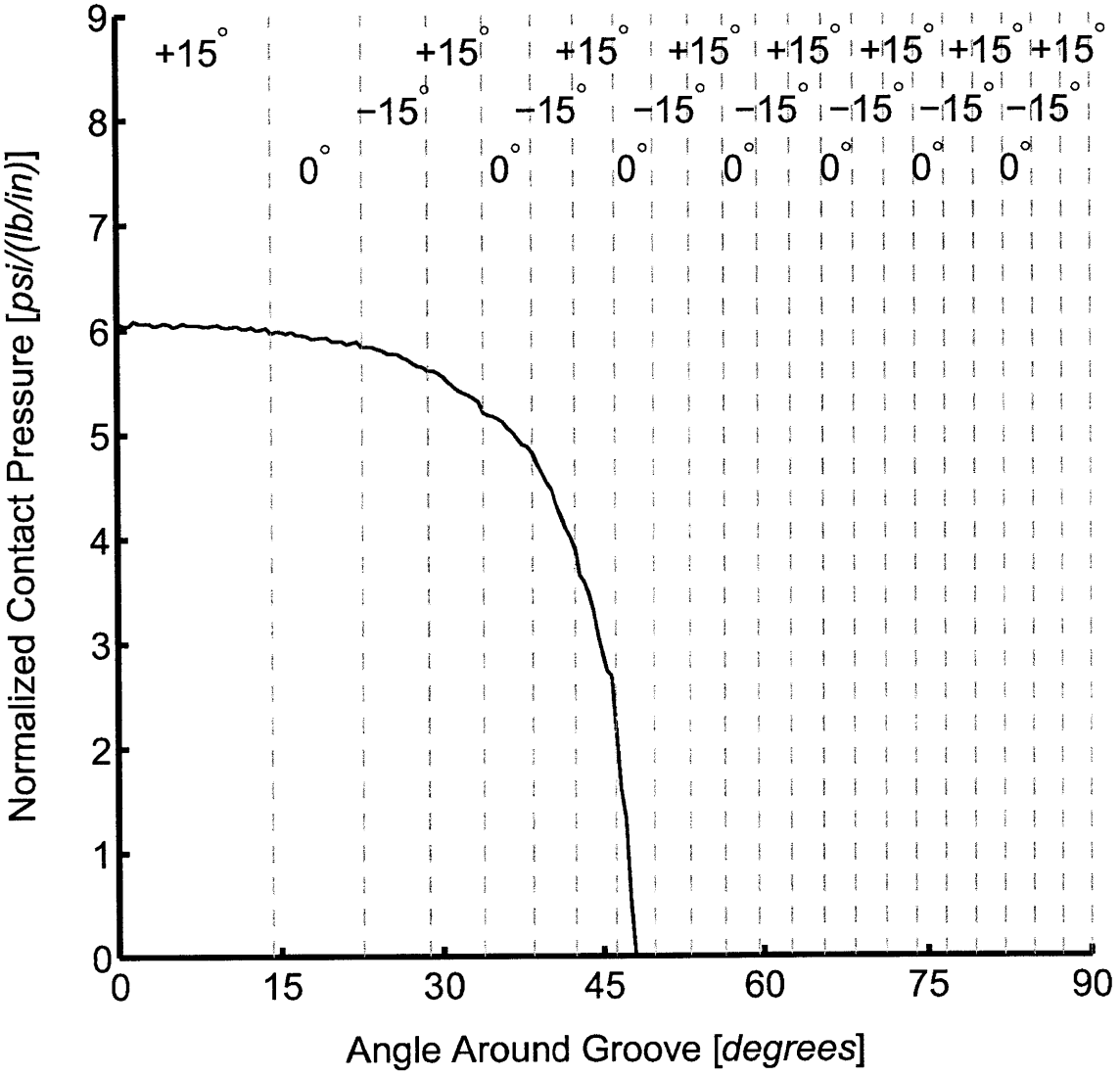

* Note: All pressures normalized by applied load, and given in units of [psi/(lb/in)].

Figure 5.1 Normalized contact pressure for two-dimensional T700/2510 $[\pm 15/0]_{13S}$ laminate model loaded at 5000 lb/in.

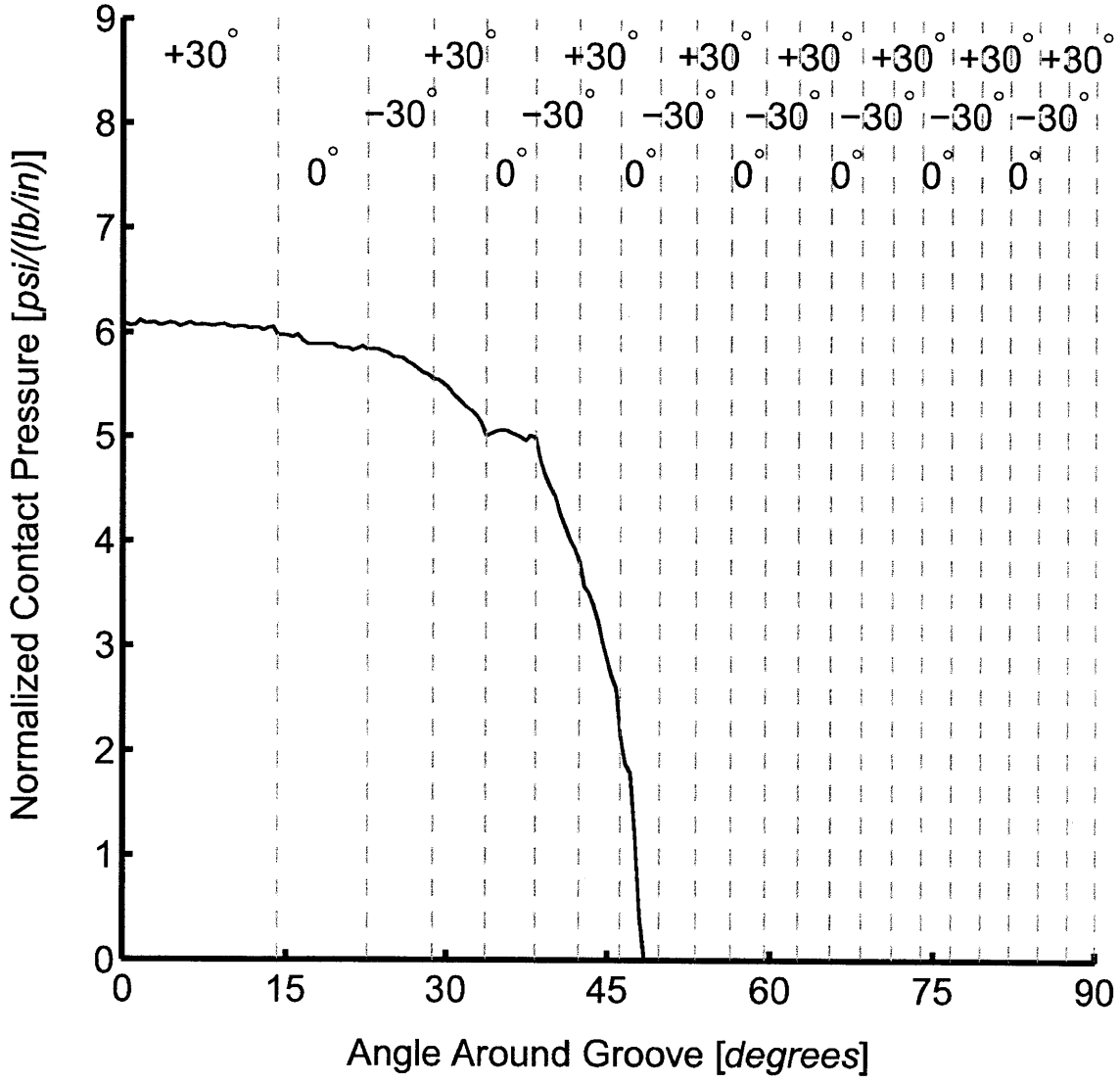

* Note: All pressures normalized by applied load, and given in units of [psi/(lb/in)].

Figure 5.2 Normalized contact pressure for two-dimensional T700/2510 $[\pm 30/0]_{13S}$ laminate model loaded at 5000 lb/in.

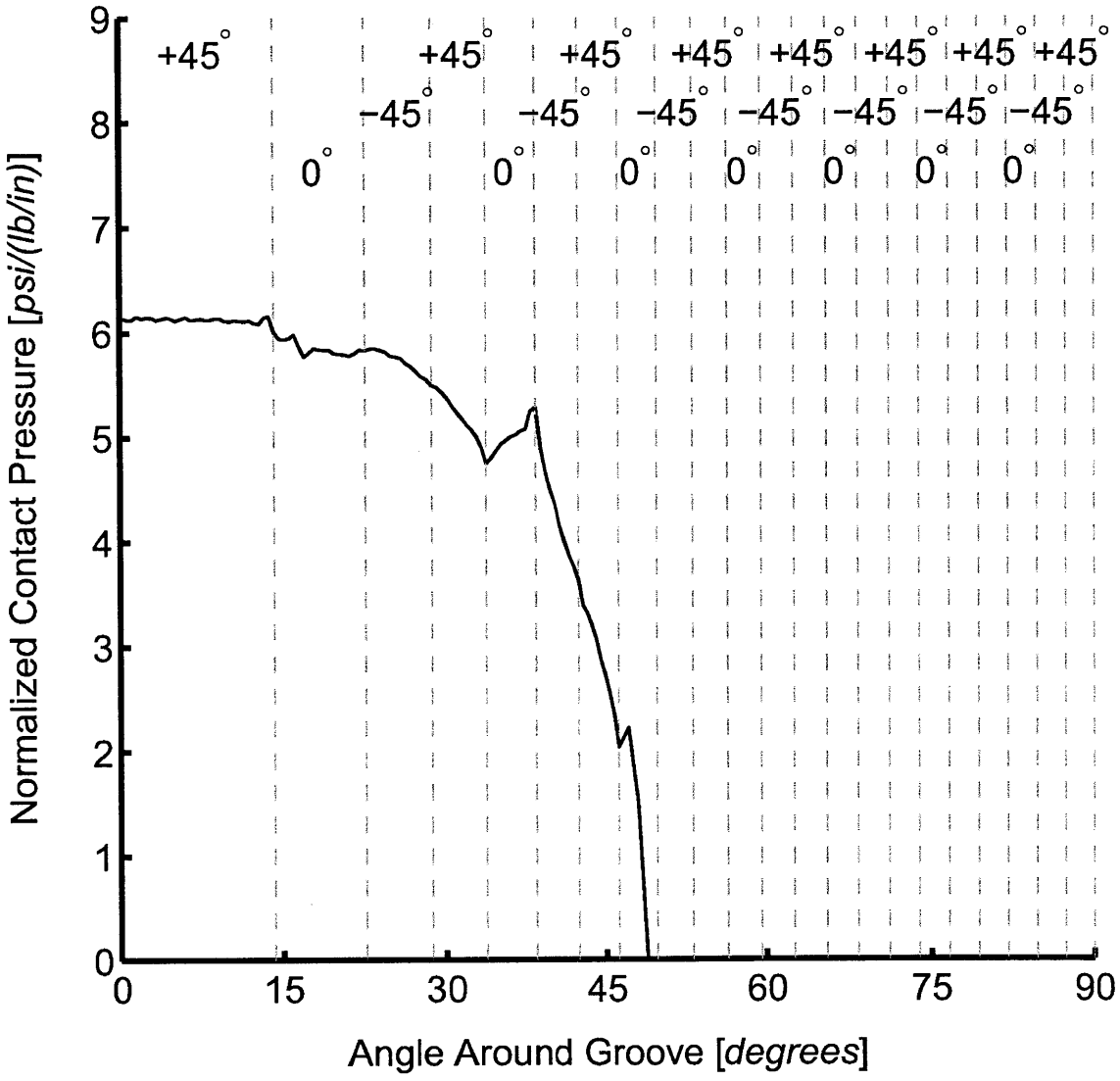

* Note: All pressures normalized by applied load, and given in units of [psi/(lb/in)].

Figure 5.3 Normalized contact pressure for two-dimensional T700/2510 $[\pm 45/0]_{13S}$ laminate model loaded at 5000 lb/in.

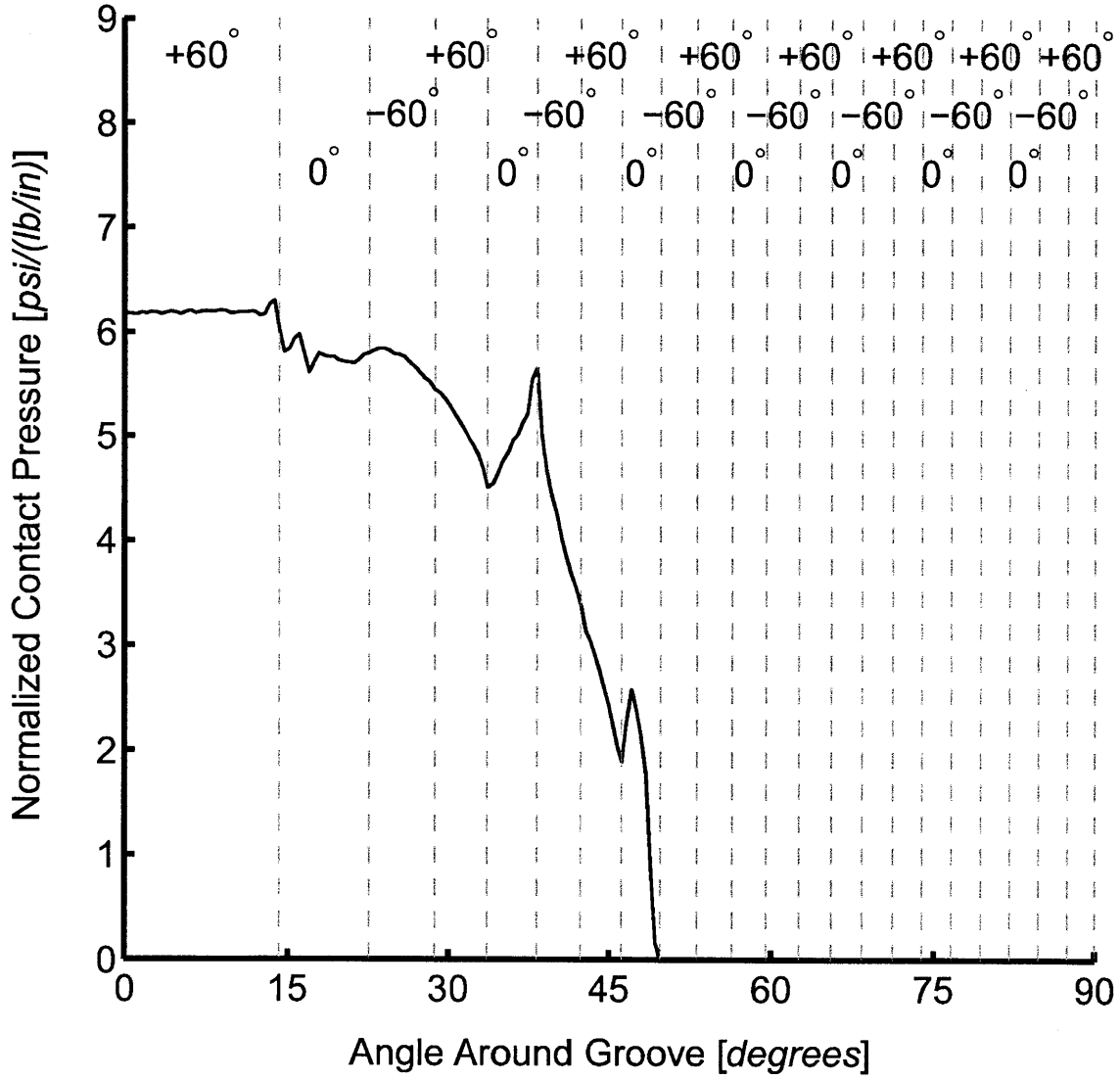

* Note: All pressures normalized by applied load, and given in units of [psi/(lb/in)].

Figure 5.4 Normalized contact pressure for two-dimensional T700/2510 $[\pm 60/0]_{13S}$ laminate model loaded at 5000 lb/in.

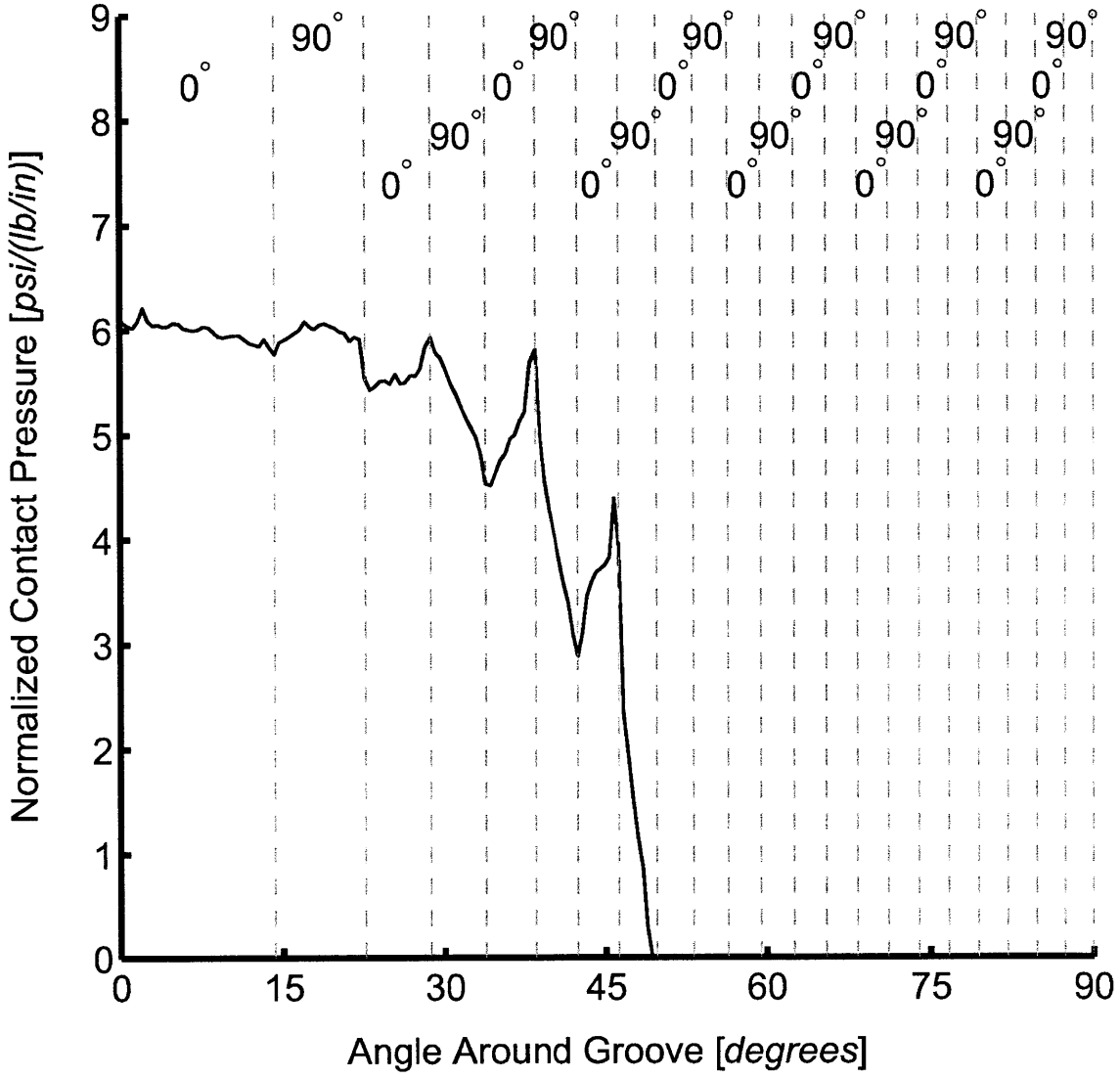

* Note: All pressures normalized by applied load, and given in units of [psi/(lb/in)].

Figure 5.5 Normalized contact pressure for two-dimensional T700/2510 $[90/0]_{20S}$ laminate model loaded at 5000 lb/in.

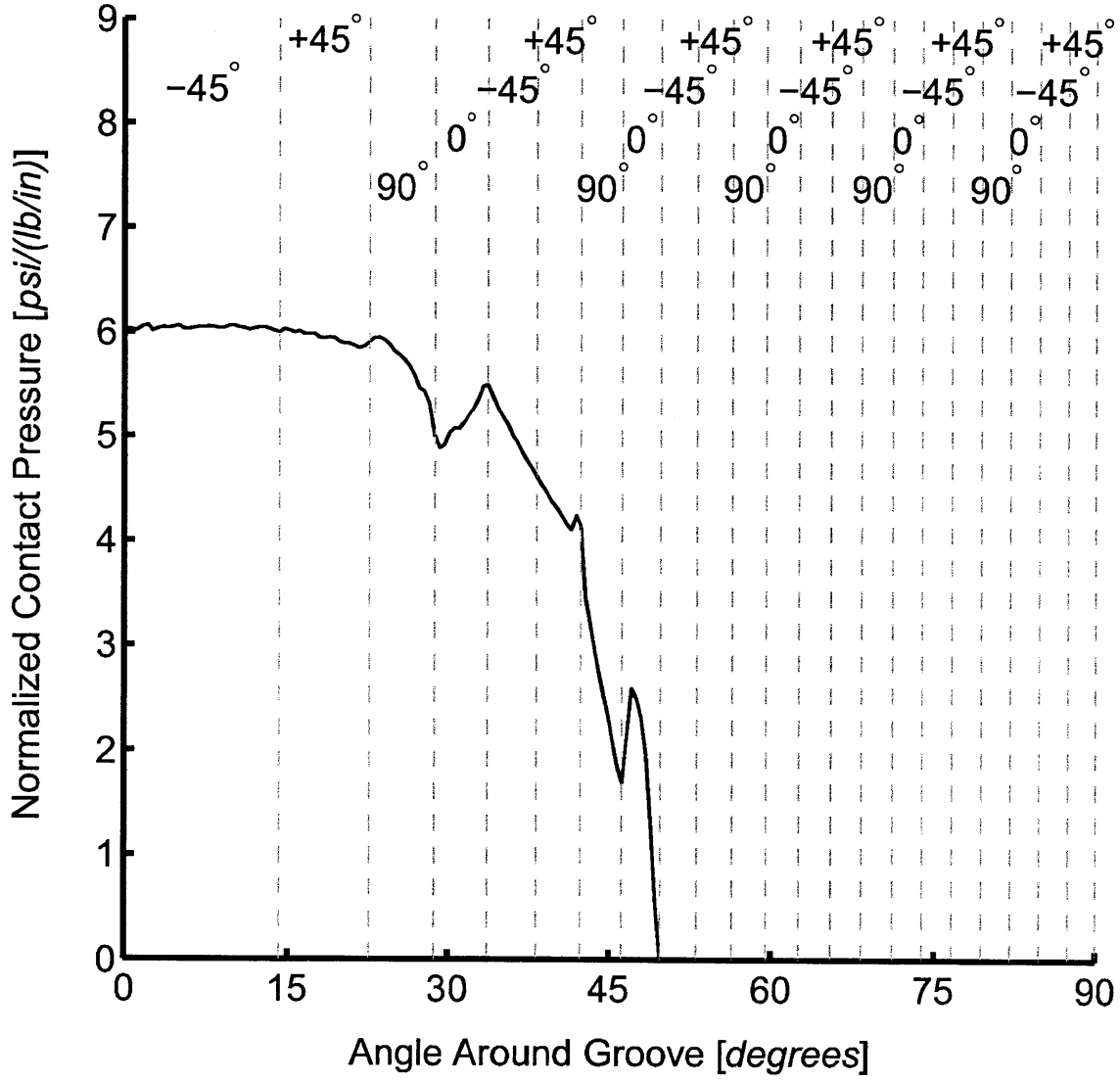

* Note: All pressures normalized by applied load, and given in units of [psi/(lb/in)].

Figure 5.6 Normalized contact pressure for two-dimensional T700/2510 $[\pm 45/0/90]_{10S}$ laminate model loaded at 5000 lb/in.

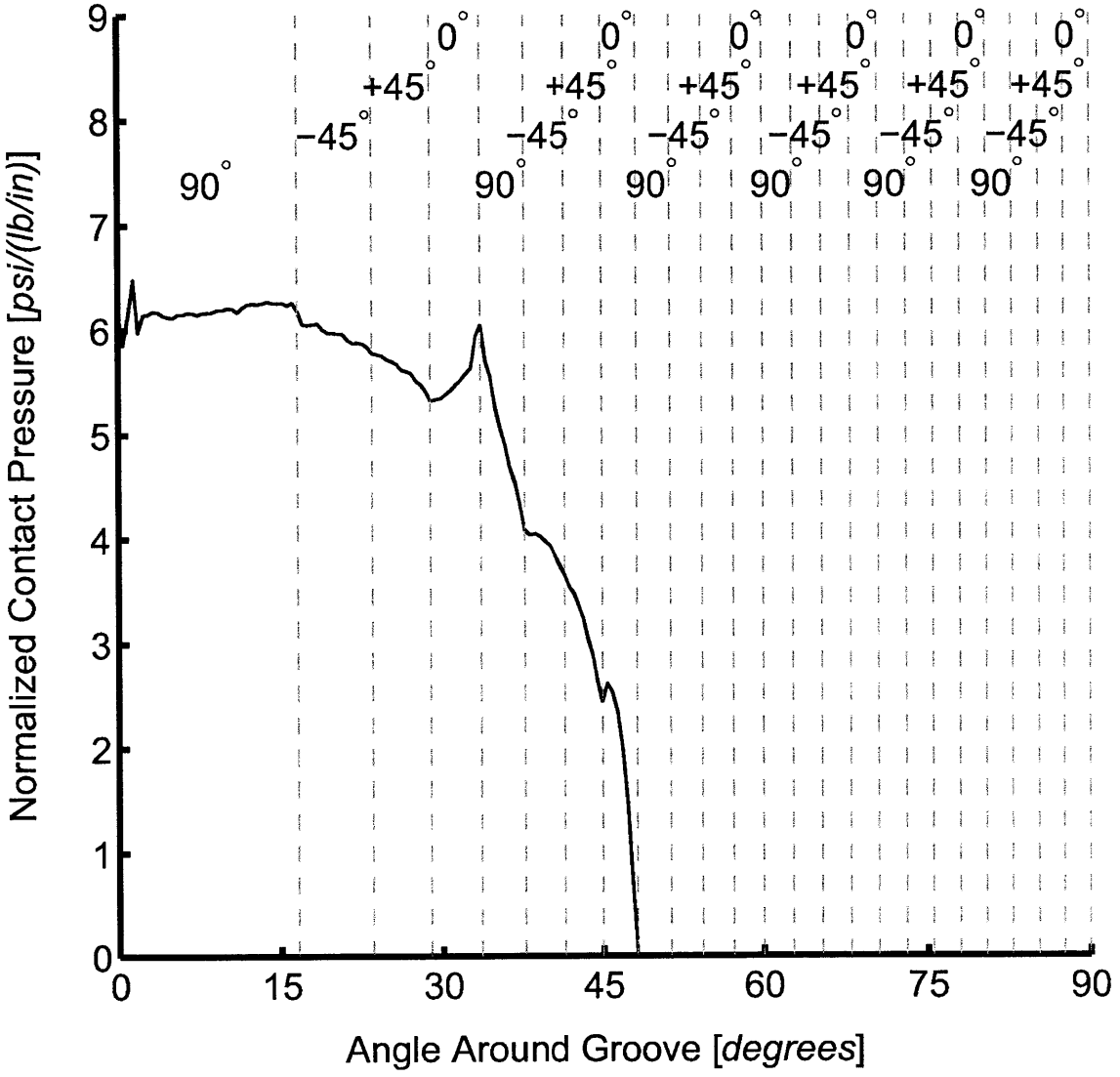

* Note: All pressures normalized by applied load, and given in units of [psi/(lb/in)].

Figure 5.7 Normalized contact pressure for two-dimensional AS1/3501-6 $[0/\pm 45/90]_{15S}$ laminate model loaded at 5000 lb/in.

Table 5.1 Maximum normalized contact pressure, $p^*_{C_{max}}$, and its location, ϕ_P, along with maximum contact angle, $\phi_{contact}$, for two-dimensional models with rigid indentor loaded at 5000 lb/in.

Laminate		**Pressure**		
Material	Layup	$p^*_{C_{max}}$ $[\frac{psi}{(lb/in)}]$	ϕ_P $[deg]$	$\phi_{contact}$ $[deg]$
T700/2510	$[\pm 15/0]_{13S}$	6.09	1.6	48.0
T700/2510	$[\pm 30/0]_{13S}$	6.12	1.6	48.4
T700/2510	$[\pm 45/0]_{13S}$	6.16	1.6	48.9
T700/2510	$[\pm 60/0]_{13S}$	6.30	13.8	49.7
T700/2510	$[90/0]_{20S}$	6.22	2.1	49.3
T700/2510	$[\pm 45/0/90]_{10S}$	6.07	2.1	49.7
AS1/3501-6	$[0/\pm 45/90]_{15S}$	6.48	1.4	48.2

ends at a groove angle, ϕ, between 48° and 50°. Contact is deemed to have ended when contact pressure, p_C drops to zero. In all laminates, pressure increases within 0° plies, and decreases within 90° plies. The behavior is only apparent for ϕ locations greater than 22.5°. For lower values of ϕ, the behavior is the opposite, with pressure decreasing in 0° plies and increasing within 90° plies. For all cases, the greater the difference in ply angle between adjacent plies, the greater the change in contact pressure between the plies. The angle around the groove, ϕ, at which the pressure is applied also has an effect on the relative change in pressure between adjacent plies of different angle. It is important to consider that the direction in which load is being applied to a composite ply is dependent on the angular location, ϕ, of the ply in the groove. Plies near the bottom of the groove will see a primarily vertical loading, while plies higher on the groove will see a combination of vertical and longitudinal loading. The laminates also exhibit bumpiness in the contact pressure near the bottom of the groove. This is a region where contact pressure does not vary greatly with ϕ on average, and ply angle stays consistent for larger areas of the groove face. As such, there is no physical reason for these bumps in the contact pressure. They are most likely artifacts of the finite element discretization and contact algorithm employed in the modeling. These bumps range in amplitude from 0.05 to 0.19 psi/(lb/in), or 0.8% to 3.1% of the maximum pressure.

Examining contact pressure data specifically from the $[\pm\theta/0]_{13S}$ laminates, a few trends are apparent. As the ply angle, θ, increases, the maximum contact pressure, $p^*_{C_{max}}$, increases. Similarly, as θ increases, the groove angle at which contact ends, $\phi_{contact}$, increases. The $[\pm\theta/0]_{13S}$ laminates also clearly show that the difference in pressure between 0° plies and other plies depends on the difference in orientation angle between the plies, as measured by θ, with the pressure difference increasing as θ increases.

For the $[\pm 15/0]_{13S}$ laminate, the pressure distribution is mostly smooth, with a few small bumps of negligible size. Pressure changes from ply to ply are not particularly apparent. For the $[\pm 30/0]_{13S}$ laminate, the pressure distribution remains largely smooth, with one smaller increase in pressure to a local maximum of 5.06 psi/(lb/in)

on the 0° ply at ϕ equal to 35.6°. For the $[\pm 45/0]_{13S}$ laminate, the pressure distribution takes on two peaks of increased pressure on the 0° plies near ϕ locations of 35° and 47°, and a slight trough of decreased pressure on the 0° ply near a value of ϕ of 18°. A local maximum of 5.28 psi/(lb/in) exists near the $0/-45°$ ply boundary at an angular location, ϕ, of 38.3°, and another of 2.22 psi/(lb/in) near the $+45/0°$ ply boundary at ϕ equal to 47.1°. For the $[\pm 60/0]_{13S}$ laminate, two prominent pressure spikes are evident in 0° plies. A large spike of pressure occurs near the $0/-60°$ ply boundary, reaching 5.65 psi/(lb/in) at ϕ equal to 38.3°. A smaller pressure spike of 2.58 psi/(lb/in) exists near the $+60/0°$ ply boundary at a value of ϕ of 47.1°. Smaller peaks and a small decrease in contact pressure are also evident in the 0° ply near the bottom of the groove from a value of ϕ of 14.2° to 22.6°.

The contact pressure distribution for the cross-ply T700/2510 laminate, $[90/0]_{20S}$, shows a more erratic behavior in contact pressure. Near the bottom of the groove, contact pressure slowly decreases in the 0° ply from an angular location, ϕ, of 0° to 14.2°, then has a small increase in the 90° ply from ϕ equal to 14.2° to 22.6°, reaching a local maximum of 6.08 psi/(lb/in) at a value of ϕ of 17.0°. As ϕ increases, contact pressure sharply rises in 0° plies and sharply drops in 90° plies. Local maxima tend to occur near the 0/90° ply boundaries, reaching 5.93 psi/(lb/in) at ϕ equal to 28.7°, 5.81 psi/(lb/in) at 37.9°, and 4.39 psi/(lb/in) at 45.8°. Local minima occur at the 90/0° ply boundaries, with pressure reaching 5.43 psi/(lb/in) at ϕ equal to 23.1°, 4.52 psi/(lb/in) at 34.3°, and 2.88 psi/(lb/in) at 42.4°.

For the quasi-isotropic T700/2510 laminate, $[\pm 45/0/90]_{10S}$, the contact pressure exhibits a generally continuous behavior through the $+/-45°$ plies, with a tendency to decrease sharply within 90° plies, and to increase sharply in 0° plies. Two local minima occur at the 90/0° ply boundaries, reaching 4.88 psi/(lb/in) at a value of ϕ of 29.2° and 1.69 psi/(lb/in) at ϕ equal to 46.2°. Two local maxima occur, one at the $0/-45°$ ply boundary up to 5.49 psi/(lb/in) at ϕ equal to 33.8° and the other in the 0° ply at ϕ equal to 47.1° at a value of 2.59 psi/(lb/in).

For the quasi-isotropic $[0/\pm 45/90]_{15S}$ layup of AS1/3501-6, the contact pressure distribution presents a few smaller pressure spikes near the bottom of the groove at

a value of ϕ of 0°, likely due to the discretization and contact computation method used. The pressure curve exhibits a local peak up to 6.04 psi/(lb/in) at the 0/90° ply boundary at a ϕ value of 33.6°, and three smaller local maxima of 6.26 psi/(lb/in) at ϕ equal to 16.1°, 4.05 psi/(lb/in) at 38.6°, and 2.61 psi/(lb/in) at 45.4°. Pressures through the other plies remains relatively smooth along the rest of the groove.

5.1.2 Stress Response

The isostress plots of results from the two-dimensional models are used to investigate the response of the grooved laminate to loading from a cylindrical indentor. The finite element models represent the full length of the laminate, as described in Section 4.2.3. While the full length of the laminate was modeled, results are presented only for the one half-length of the laminate with positive values of x_1 because stress results are expected to be symmetric for this case. Results are expected to be symmetrical about the x_3-axis because the factors that affect response (geometry, material properties, loading conditions, and boundary conditions) are symmetric about that axis. The only asymmetries that might arise can be attributed to the only asymmetry in the problem model: the finite element discretization. While the finite element mesh is similar on each side of the x_3-axis, elements are not exactly mirrored, so small asymmetries may arise in the response due to this difference. Due to the intended symmetry of the problem, results for the models are presented only for values of x_1 greater than or equal to 0.0 to maximize visibility of the isostress plots. Since only half of the model is presented, maximum stress values are always shown at positive x_1 or ϕ locations, even though in some cases a maximum stress value may have been found at a negative x_1 location or negative groove angle, ϕ, due to the discretization asymmetries discussed above. The stress value is simply shown at its corresponding positive x_1 location or ϕ angle.

The isostress plots of normalized longitudinal extensional stresses, σ^*_{11}, for the T700/2510 $[\pm\theta/0]_{13S}$ laminates are shown in Figures 5.9, 5.10, 5.11, and 5.12 for θ equal to 15°, 30°, 45°, and 60°, respectively. The isostress plot for the cross-ply T700/2510 $[90/0]_{20S}$ laminate is presented in Figure 5.13. The isostress plot for the

quasi-isotropic T700/2510 $[\pm 45/0/90]_{10S}$ is shown in Figure 5.14. Results for σ_{11}^* for the AS1/3501-6 $[0/\pm 45/90]_{15S}$ model are shown in Figure 5.15. The maximum tensile and compressive σ_{11}^* stresses, along with their locations in the cylindrical coordinate system of the groove, are shown in Table 5.2. These maximum values and locations are also shown on each isostress plot. As discussed previously, all stresses are normalized by dividing stress by the applied load, yielding a result in units of [psi/(lb/in)] for the two-dimensional case.

The σ_{11}^* isostress plots share some similar characteristics for all of the laminates. All laminates share a similar format to the overall stress field, and this is reminiscent of the comparable stress fields in previous work on grooved isotropic materials [5]. There are three primary zones of stress for σ_{11}^*, as illustrated in Figure 5.8, and the distinction between these regions is most easily seen in the isostress plot for the $[\pm 15/0]_{13S}$ laminate in Figure 5.9. Moving counterclockwise from the bottom of the groove, Zone 1 extends vertically from the bottom of the groove to the back face of the laminate and is primarily in tension, Zone 2 extends diagonally from the groove wall into the body of the laminate and is primarily in compression, and Zone 3 extends from the upper portion of the groove wall to the top face of the laminate and is primarily in tension. All laminates investigated also show higher σ_{11}^* stresses in the 0° plies, since these plies are stiffest in the 1-direction. The isostress plots for all laminates also show a great deal of segmentation along the ply boundaries due to the greatly varying stiffness in the 1-direction which is dependent on the ply angle. In general, the greater the ply angle, the lower the stiffness of the ply in the 1-direction as the fiber direction deviates farther from the 1-direction. Thus, for all laminates, the difference in stress between neighboring plies is dependent on the difference in orientation angle of those plies, with a greater difference in angle resulting in a greater difference in stress.

Examining the $[\pm\theta/0]_{13S}$ laminate series, a few trends are notable through the range of θ values modeled. First, as θ increases and the θ ply angles diverge from the 1-direction, the entire laminate becomes more compliant in the 1-direction. This has the effect of putting greater load on 0° plies, as they retain stiffness in the 1-direction.

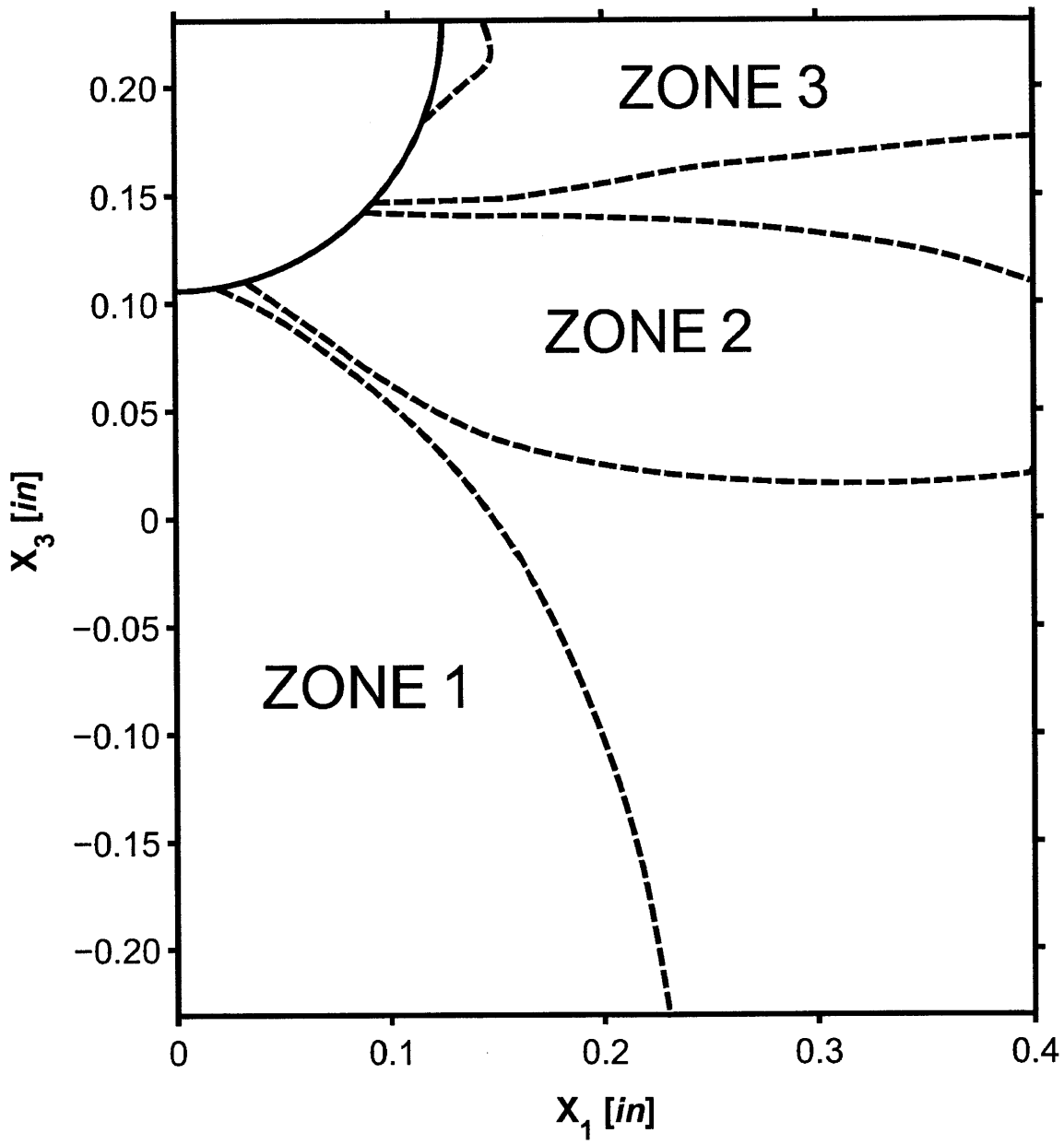

Figure 5.8 Illustration of stress zones and their locations for stress field of σ_{11}^{*}.

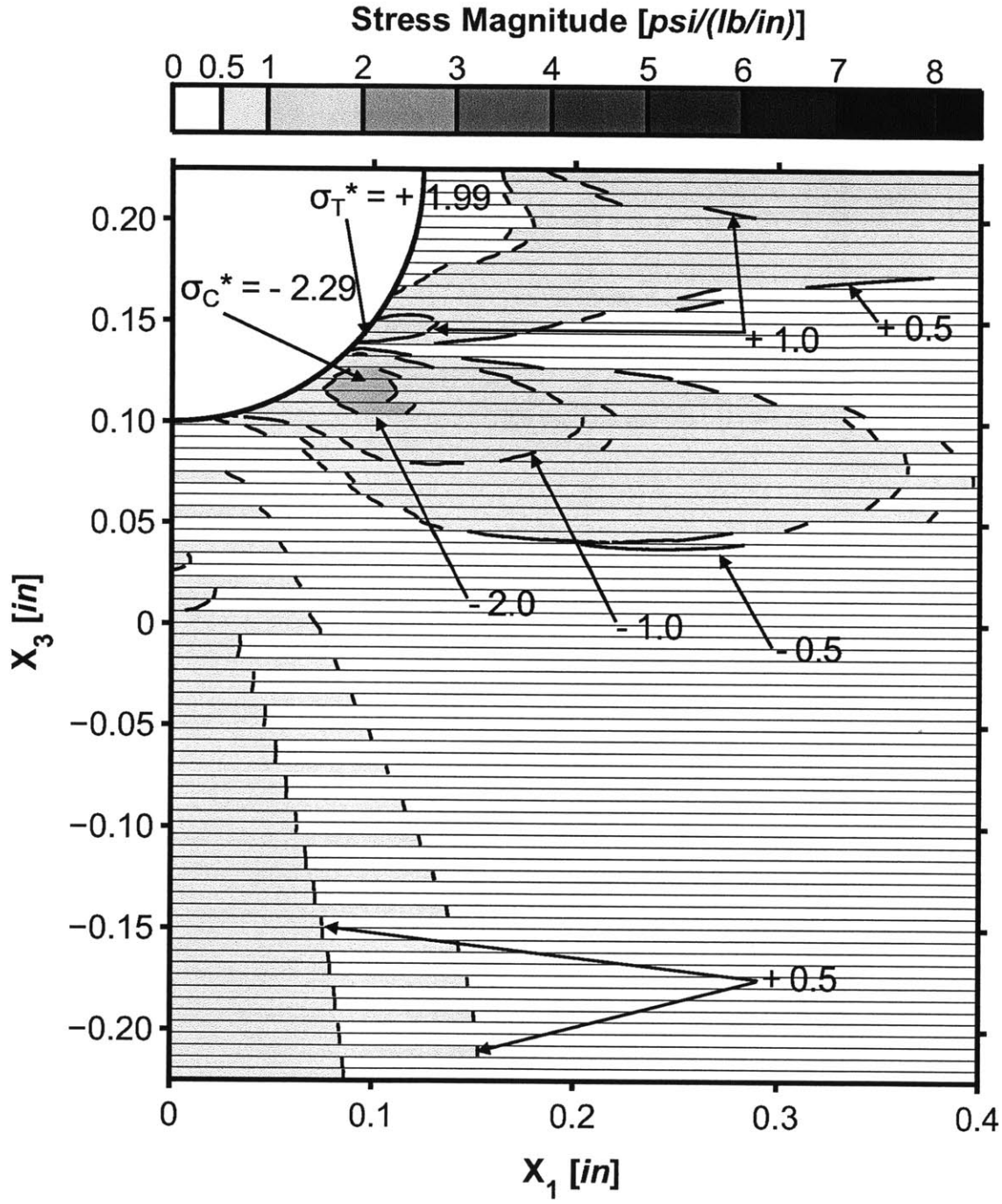

* Note: All stresses normalized by applied load, and given in units of [psi/(lb/in)].

Figure 5.9 Isostress plot of σ_{11}^{*} for a portion of the two-dimensional T700/2510 $[\pm 15/0]_{13S}$ laminate model with rigid indentor loaded at 5000 lb/in.

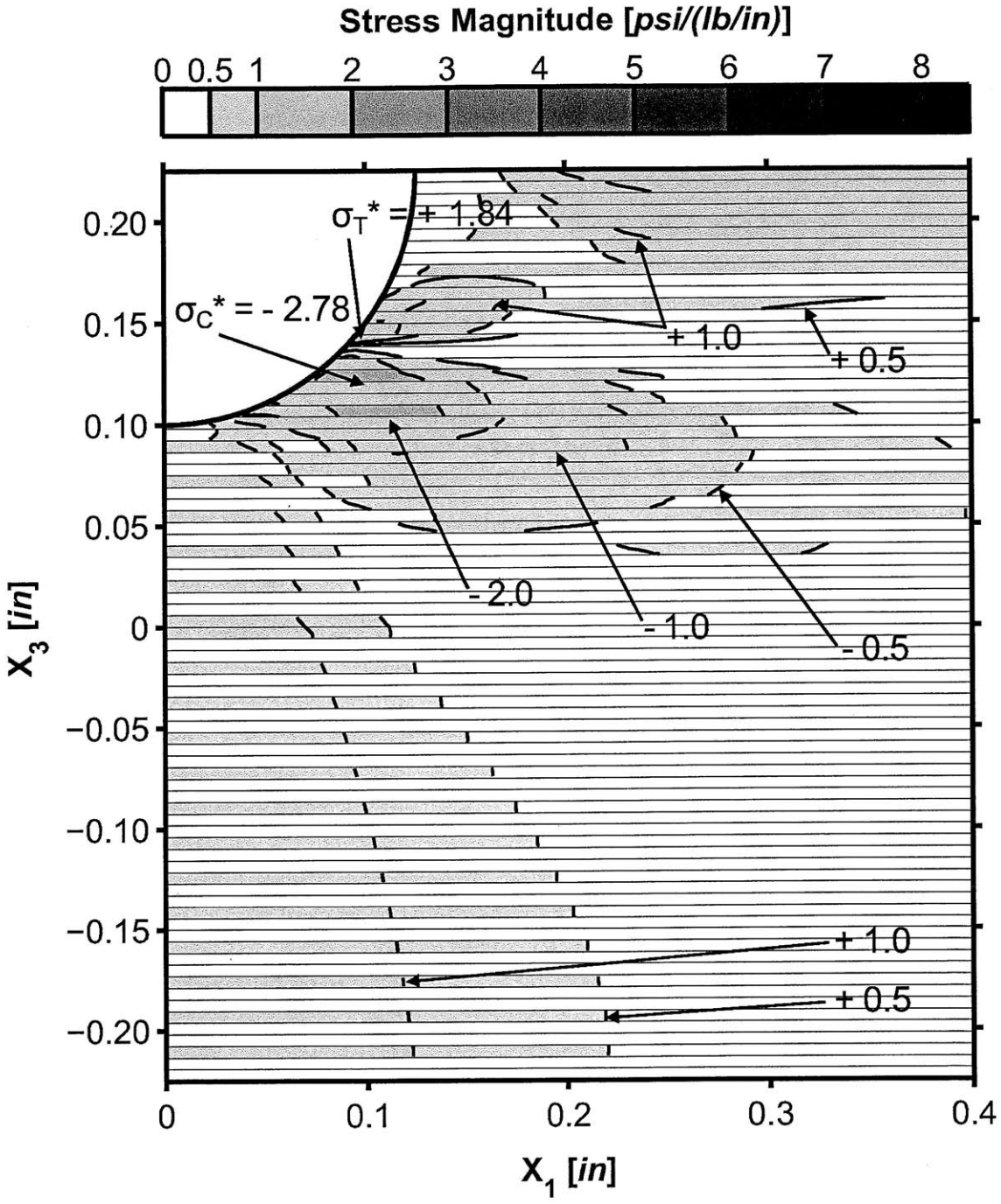

* Note: All stresses normalized by applied load, and given in units of [psi/(lb/in)].

Figure 5.10 Isostress plot of σ_{11}^{*} for a portion of the two-dimensional T700/2510 $[\pm 30/0]_{13S}$ laminate model with rigid indentor loaded at 5000 lb/in.

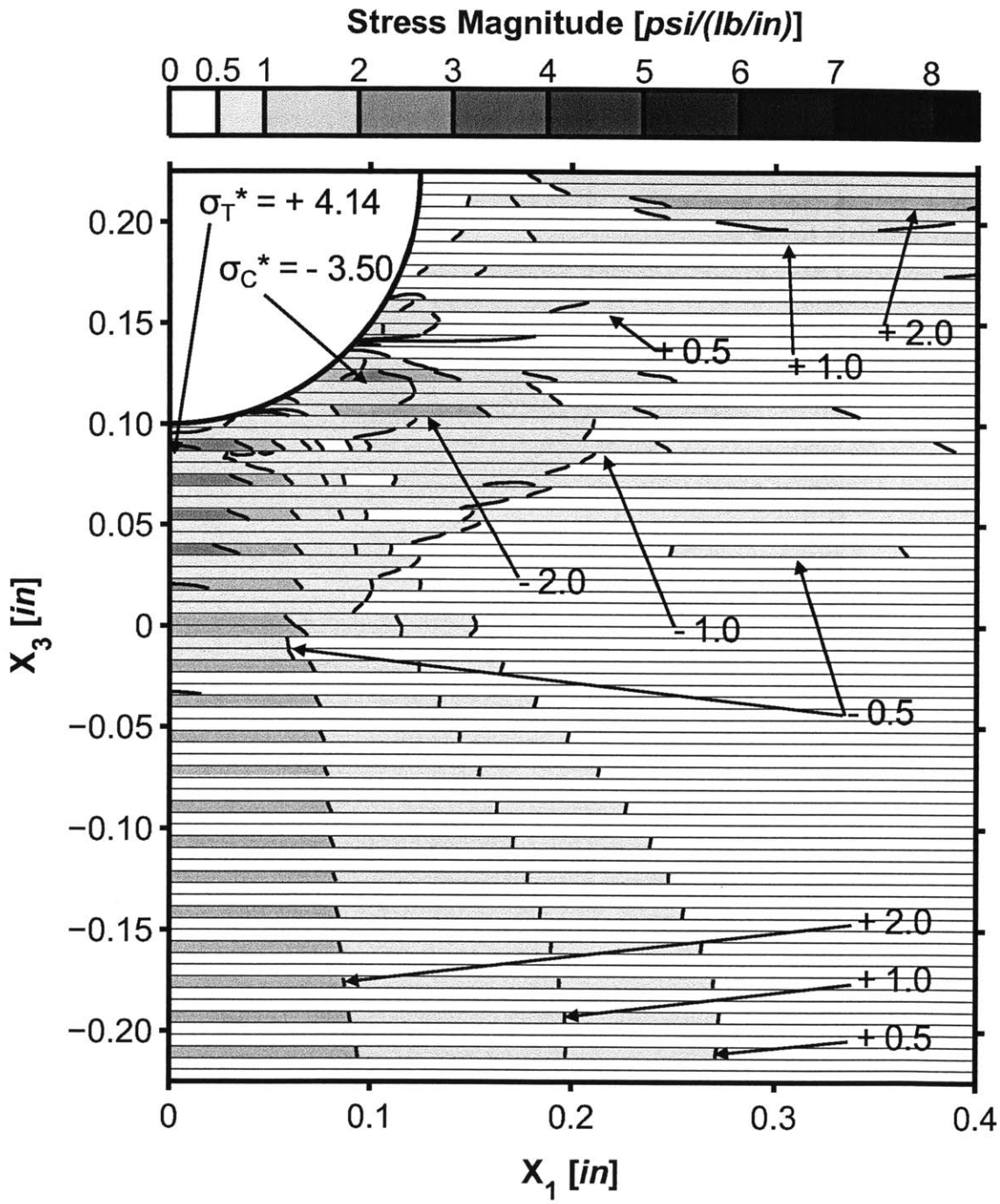

* Note: All stresses normalized by applied load, and given in units of [psi/(lb/in)].

Figure 5.11 Isostress plot of σ_{11}^{*} for a portion of the two-dimensional T700/2510 $[\pm 45/0]_{13S}$ laminate model with rigid indentor loaded at 5000 lb/in.

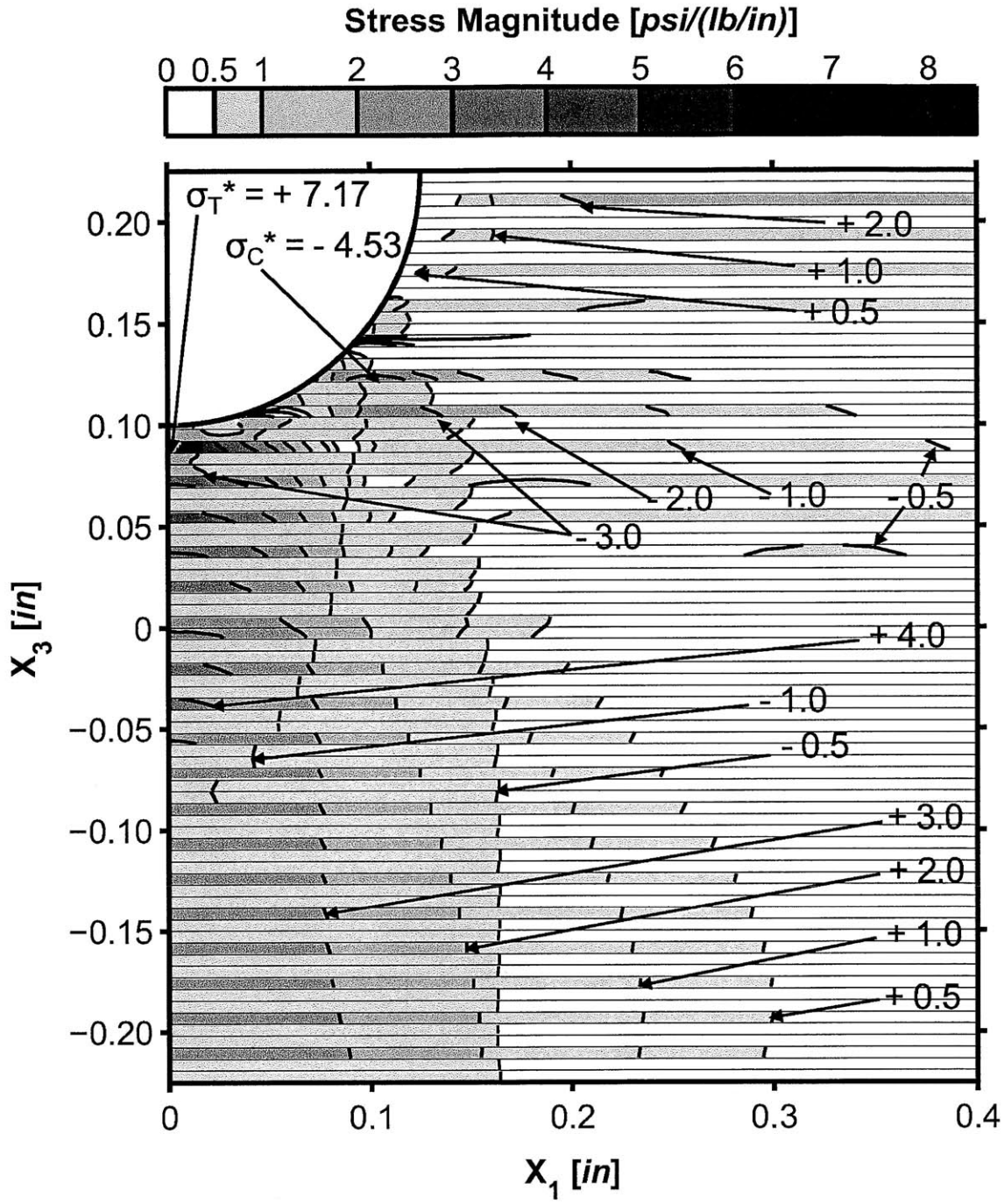

* Note: All stresses normalized by applied load, and given in units of [psi/(lb/in)].

Figure 5.12 Isostress plot of σ_{11}^{*} for a portion of the two-dimensional T700/2510 $[\pm 60/0]_{13S}$ laminate model with rigid indentor loaded at 5000 lb/in.

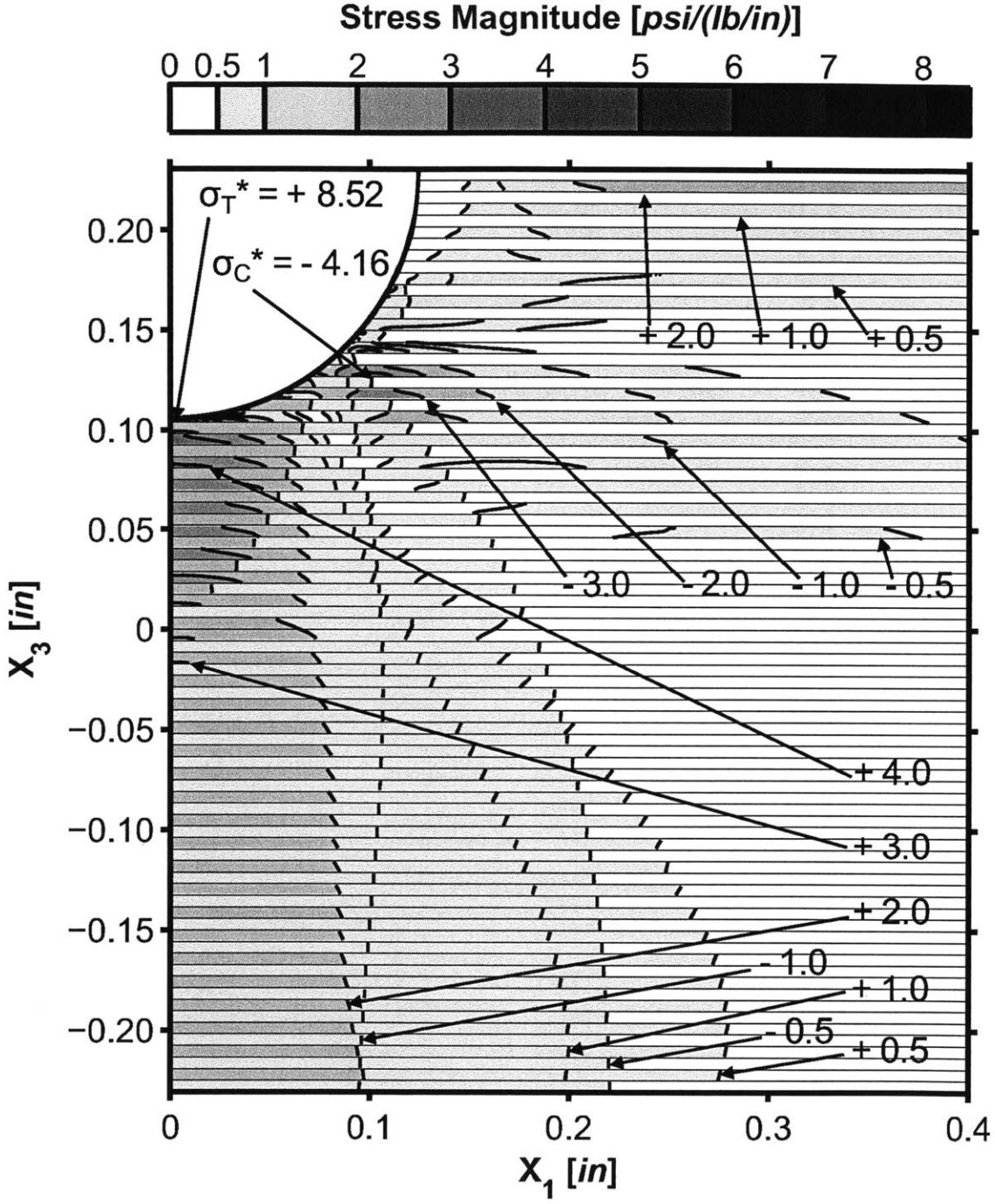

* Note: All stresses normalized by applied load, and given in units of [psi/(lb/in)].

Figure 5.13 Isostress plot of σ_{11}^{*} for a portion of the two-dimensional T700/2510 $[90/0]_{20S}$ laminate model with rigid indentor loaded at 5000 lb/in.

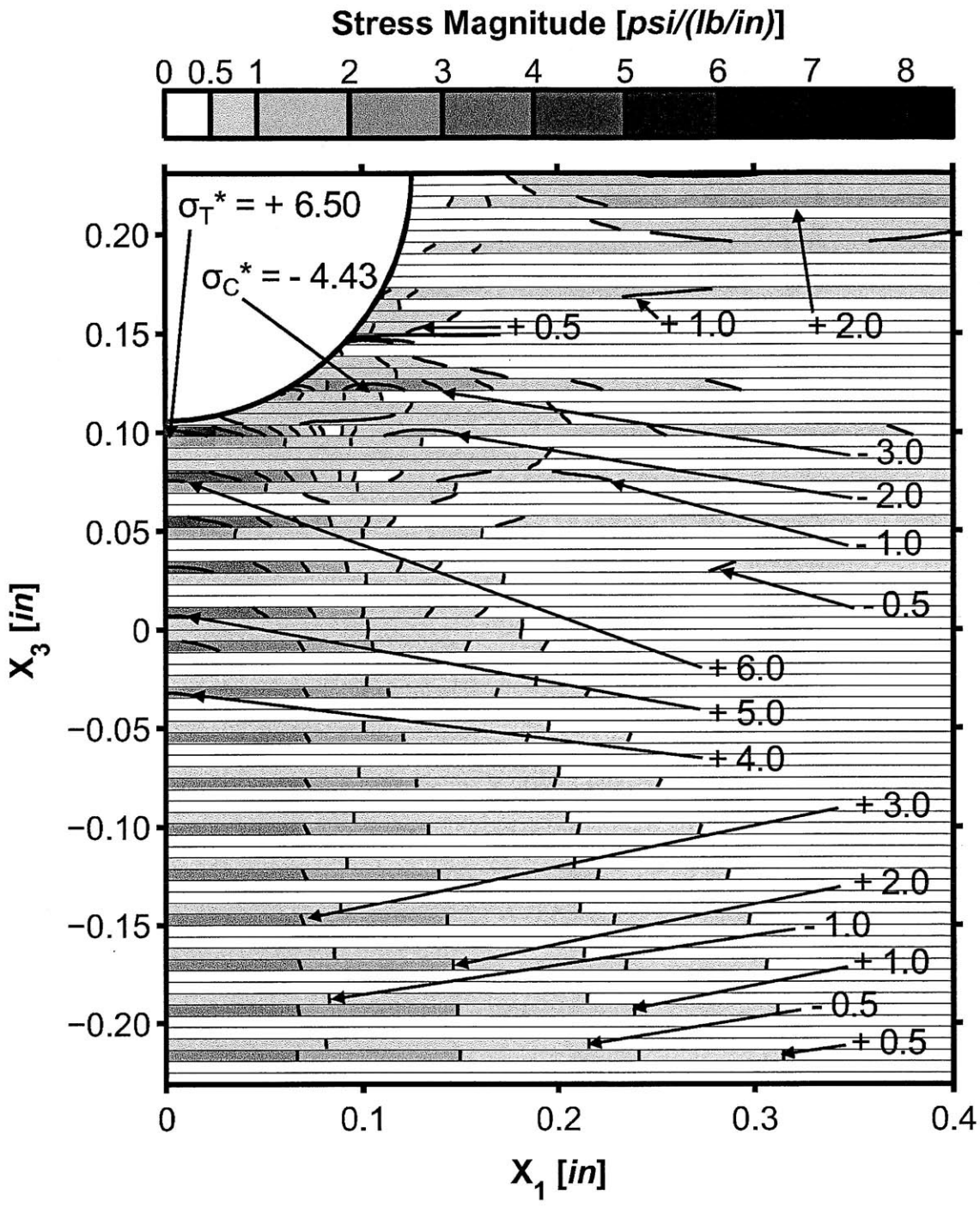

* Note: All stresses normalized by applied load, and given in units of [psi/(lb/in)].

Figure 5.14 Isostress plot of σ_{11}^{*} for a portion of the two-dimensional T700/2510 $[\pm 45/0/90]_{10S}$ laminate model with rigid indentor loaded at 5000 lb/in.

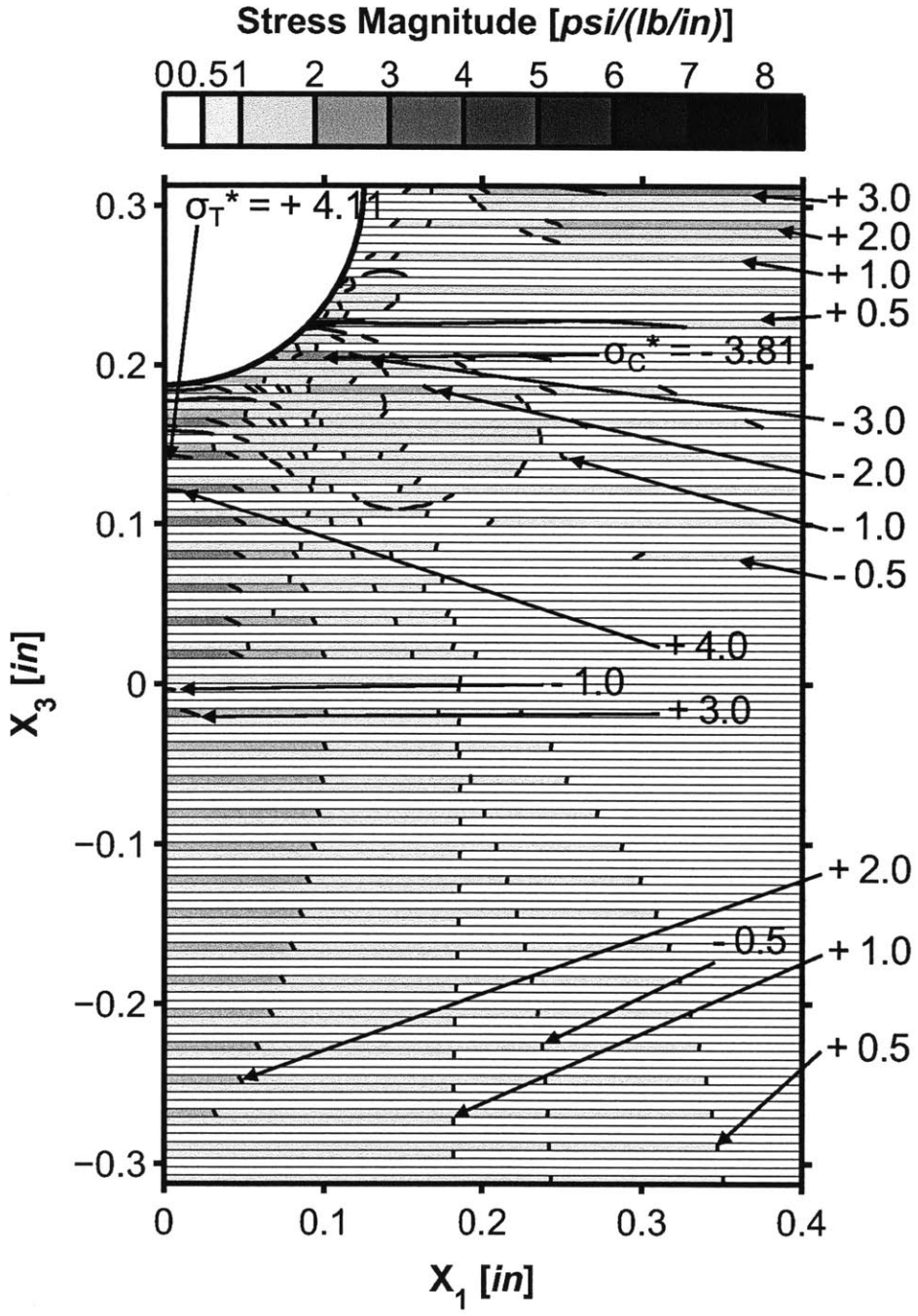

* Note: All stresses normalized by applied load, and given in units of [psi/(lb/in)].

Figure 5.15 Isostress plot of σ_{11}^* for a portion of the two-dimensional AS1/3501-6 $[0/\pm 45/90]_{15S}$ laminate model with rigid indentor loaded at 5000 lb/in.

Table 5.2 Maximum magnitudes of normalized stress values, σ_{11}^{*}, and locations in cylindrical coordinates for two-dimensional models with rigid indentor loaded at 5000 lb/in.

Laminate		Tensile			Compressive		
Material	Layup	σ_T^* $[\frac{psi}{(lb/in)}]$	ϕ_T $[deg]$	r_T $[in]$	σ_C^* $[\frac{psi}{(lb/in)}]$	ϕ_C $[deg]$	r_C $[in]$
T700/2510	$[\pm 15/0]_{13S}$	1.99	48.4	0.126	-2.29	43.7	0.142
T700/2510	$[\pm 30/0]_{13S}$	1.84	48.4	0.125	-2.78	43.7	0.142
T700/2510	$[\pm 45/0]_{13S}$	4.14	1.1	0.137	-3.50	43.7	0.142
T700/2510	$[\pm 60/0]_{13S}$	7.17	0.4	0.139	-4.53	44.3	0.143
T700/2510	$[90/0]_{20S}$	8.52	0.7	0.125	-4.16	44.3	0.143
T700/2510	$[\pm 45/0/90]_{10S}$	6.50	1.3	0.133	-4.43	43.4	0.149
AS1/3501-6	$[0/\pm 45/90]_{15S}$	4.11	0.3	0.170	-3.81	42.8	0.147

Thus, as θ increases, σ_{11}^* increases in the 0° plies, and decreases in the $\pm\theta$ plies. In Zone 1, stresses in $\pm\theta$ plies first decrease, then switch from tension to compression as θ increases. This results in alternating bands of tension and compression in Zone 1. In Zones 2 and 3, σ_{11}^* stresses decrease so as to be negligible as θ increases. As a result of this trend, the maximum tensile and compressive σ_{11}^* stresses increase in magnitude as θ increases. The maximum compressive stress, σ_C^*, remains relatively stable in Zone 2 across all values of θ. The maximum tensile stress, σ_T^*, shifts from a location in Zone 2 near the groove face for the $[\pm 15/0]_{13S}$ and $[\pm 30/0]_{13S}$ laminates, to a location in Zone 3 in a 0° ply beneath the groove for the $[\pm 45/0]_{13S}$ and $[\pm 60/0]_{13S}$ laminates.

The σ_{11}^* isostress field for the $[90/0]_{20S}$ laminate shows the same trends found for the other laminates as presented. The results align particularly well with the $[\pm\theta/0]_{13S}$ laminates with high θ values, and generally represent an extension of that trend. Stresses are higher in the 0° plies. Zone 1 exhibits a similar banded stress characteristic to the $[\pm 60/0]_{13S}$ laminate, with regions of tension in the 0° plies and regions of compression in the 90° plies, but with greater stress magnitudes in the compressive mode than are observed in the $[\pm 60/0]_{13S}$ case.

The two quasi-isotropic laminates combine the characteristics seen in the $[\pm\theta/0]_{13S}$ and $[90/0]_{20S}$ laminates. Higher stresses are apparent in the 0° plies. Zone 1 again shows a banded appearance with alternating tensile and compressive regions, with the 0° plies in tension and the 90° plies in compression. In Zones 2 and 3, the ±45° plies show reduced, but non-negligible, stresses, while the stresses in the 90° plies drop more significantly.

The normalized through-thickness extensional stress, σ_{33}^*, isostress plots for the $[\pm\theta/0]_{13S}$ laminates are shown in Figures 5.16, 5.17, 5.18, and 5.19 for θ equal to 15°, 30°, 45°, and 60°, respectively. The σ_{33}^* isostress plot for the $[90/0]_{20S}$ cross-ply laminate is shown in Figure 5.20. The σ_{33}^* isostress plot for the T700/2510 quasi-isotropic $[\pm 45/0/90]_{10S}$ is given in Figure 5.21. The σ_{33}^* isostress plot for the AS1/3501-6 $[0/\pm 45/90]_{15S}$ laminate is presented in Figure 5.22. Table 5.3 shows the values and locations of the maximum tensile and compressive σ_{33}^* stresses for all the above lam-

inates. These values and locations are also shown on each isostress plot.

The σ^*_{33} stress distributions are very similar for all laminates investigated, with only minor variations due to material and layup changes. All stress fields are composed of two regions: a large region of compressive stress originating along the bottom of the groove and continuing to the laminate back face, and a much smaller region of tensile stress of lesser magnitude on either side of the groove. The large compressive region begins beneath the groove where the indentor presses down on the laminate, and the stress decreases in magnitude and concentration as x_3 decreases. This represents a spreading out of the applied vertical force from the small area of contact with the indentor on the groove, to the larger area of the laminate backface. The maximum compressive stress, σ^*_C, is relatively consistent across all laminates, ranging from -6.04 to -6.50 psi/(lb/in), with a very consistent location on the bottom of the groove face. The small tensile region generally extends along a region on the groove face ranging from an angular location, ϕ, of 45° to 75°. These tensile stresses drop off rapidly as one moves into the laminate and away from the groove. The maximum tensile stress, σ^*_T, varies across the laminates, but ranges from 1.75 to 2.33 psi/(lb/in). The location is consistently between ϕ equal to 48.0° and 50.9°. Finally, for σ^*_{33}, ply-to-ply behavior between dissimilar plies is much more continuous than in the σ^*_{11} stress fields, since stiffness in the 3-direction does not vary significantly with ply angle.

Examining the $[\pm\theta/0]_{13S}$ laminates, a few trends are notable. In the main region of compressive stress, as θ increases, stresses generally increase nearer the vertical axis at x_1 equal to 0, and decrease farther from x_1 equal to 0, leading to an increased stress gradient near the vertical center line. These changes are very small, but most noticeable in the shrinking range of the -0.5 and -1.0 psi/(lb/in) isostress lines, and expansion of the -2.0 and -3.0 psi/(lb/in) isostress lines when comparing the $[\pm 15/0]_{13S}$ and $[\pm 60/0]_{13S}$ laminates. The small region of tensile stress decreases in size and intensity slightly as θ increases. For example, the +0.5 psi/(lb/in) isostress line has an angular range from a value of ϕ of 45.3° to 76.2° for the laminate with θ equal to 15°, while for the laminate with θ equal to 60°, it has a range from ϕ equal to 47.5° to 74.4°. As θ increases, the magnitude of the maximum compressive stress,

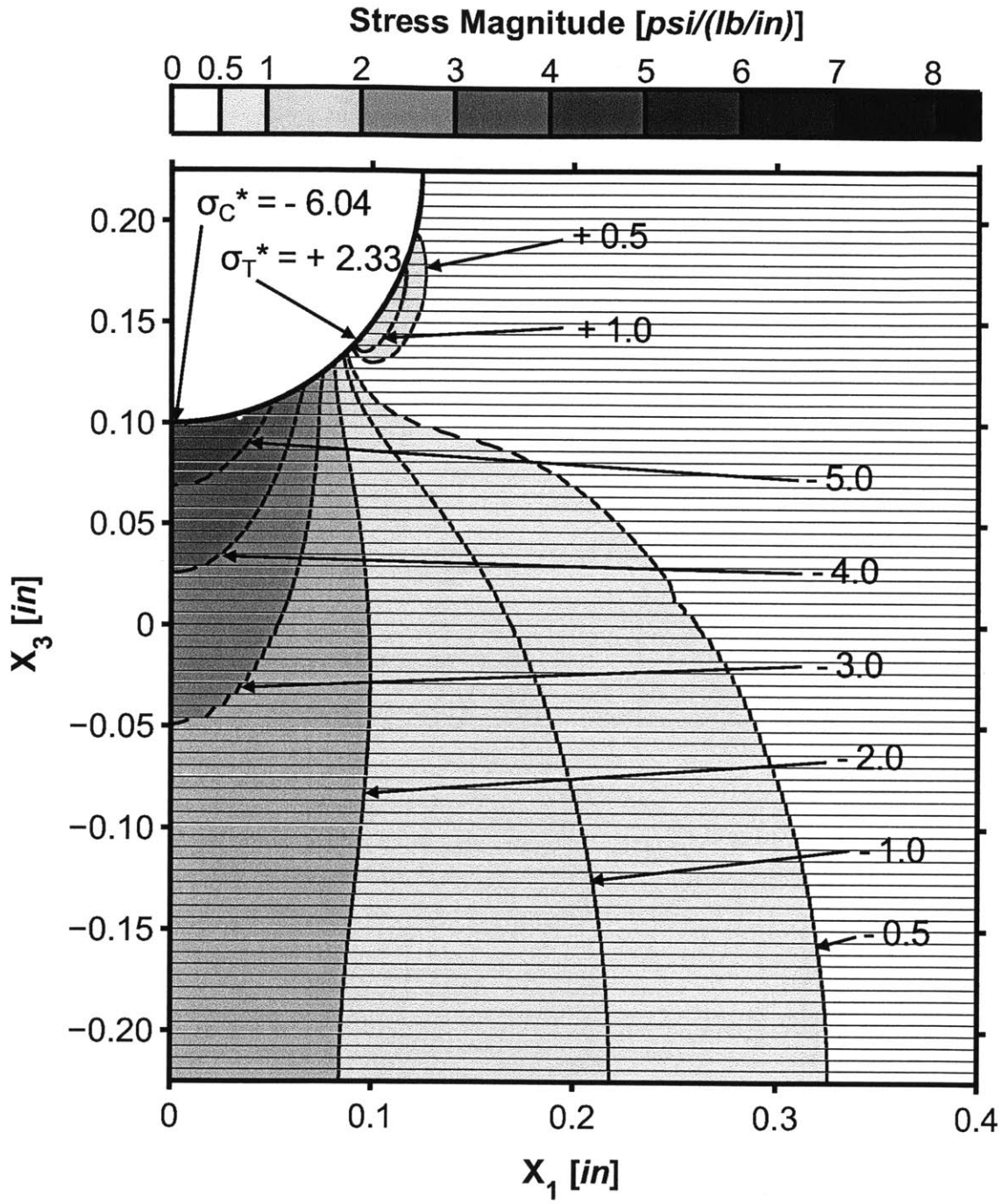

* Note: All stresses normalized by applied load, and given in units of [psi/(lb/in)].

Figure 5.16 Isostress plot of σ_{33}^{*} for a portion of the two-dimensional T700/2510 $[\pm 15/0]_{13S}$ laminate model with rigid indentor loaded at 5000 lb/in.

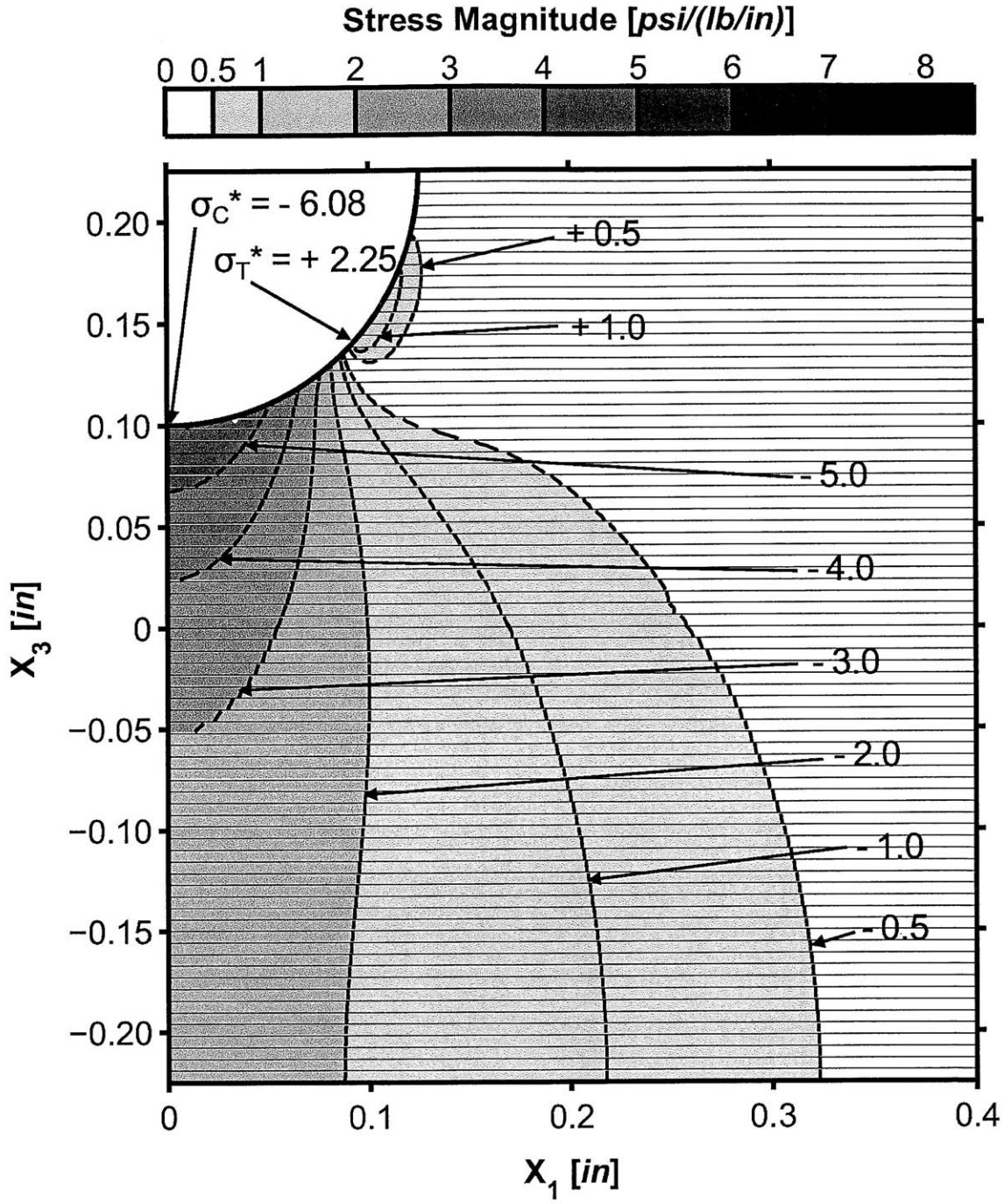

* Note: All stresses normalized by applied load, and given in units of [psi/(lb/in)].

Figure 5.17 Isostress plot of σ_{33}^{*} for a portion of the two-dimensional T700/2510 $[\pm 30/0]_{13S}$ laminate model with rigid indentor loaded at 5000 lb/in.

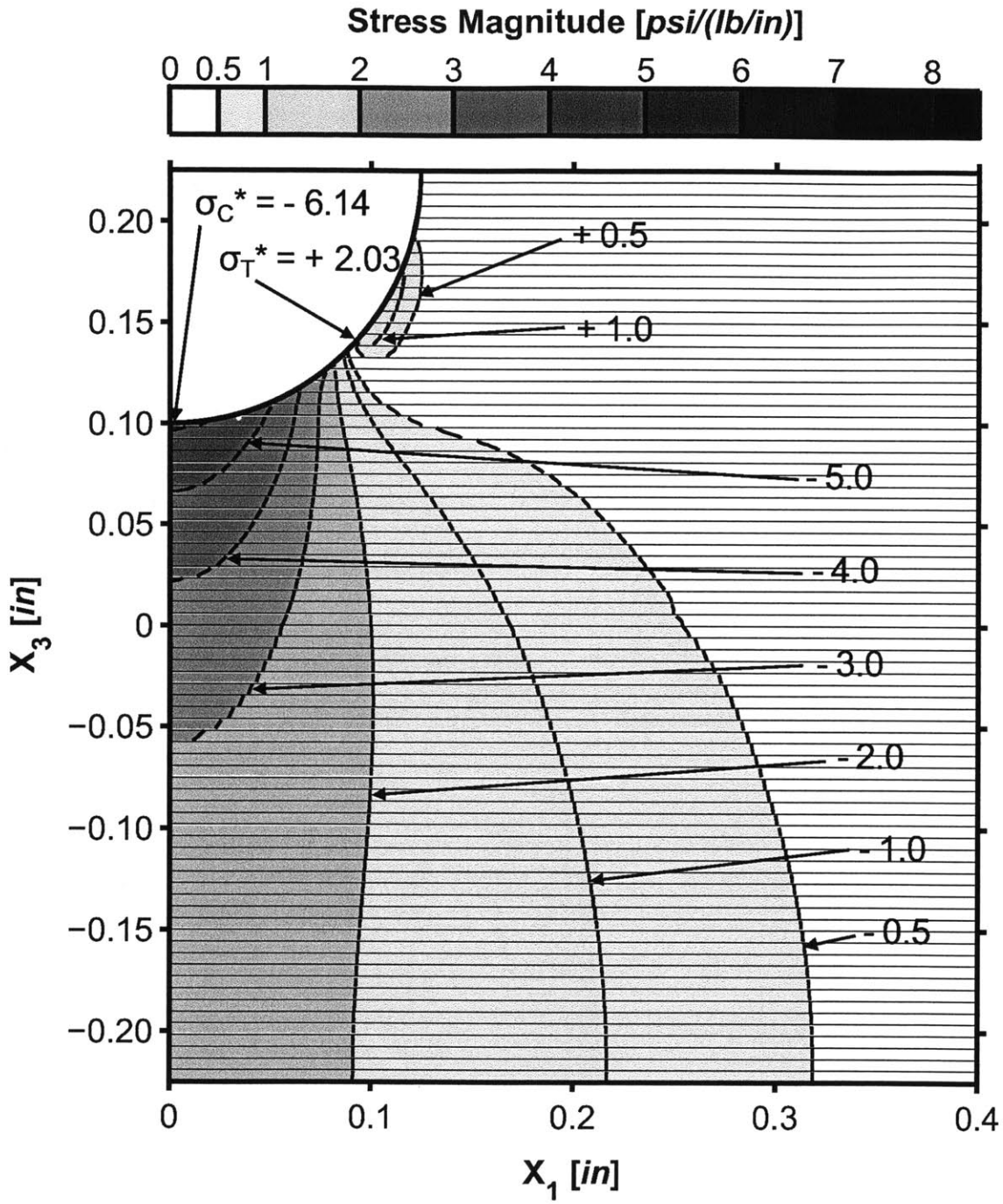

* Note: All stresses normalized by applied load, and given in units of [psi/(lb/in)].

Figure 5.18 Isostress plot of σ_{33}^{*} for a portion of the two-dimensional T700/2510 $[\pm 45/0]_{13S}$ laminate model with rigid indentor loaded at 5000 lb/in.

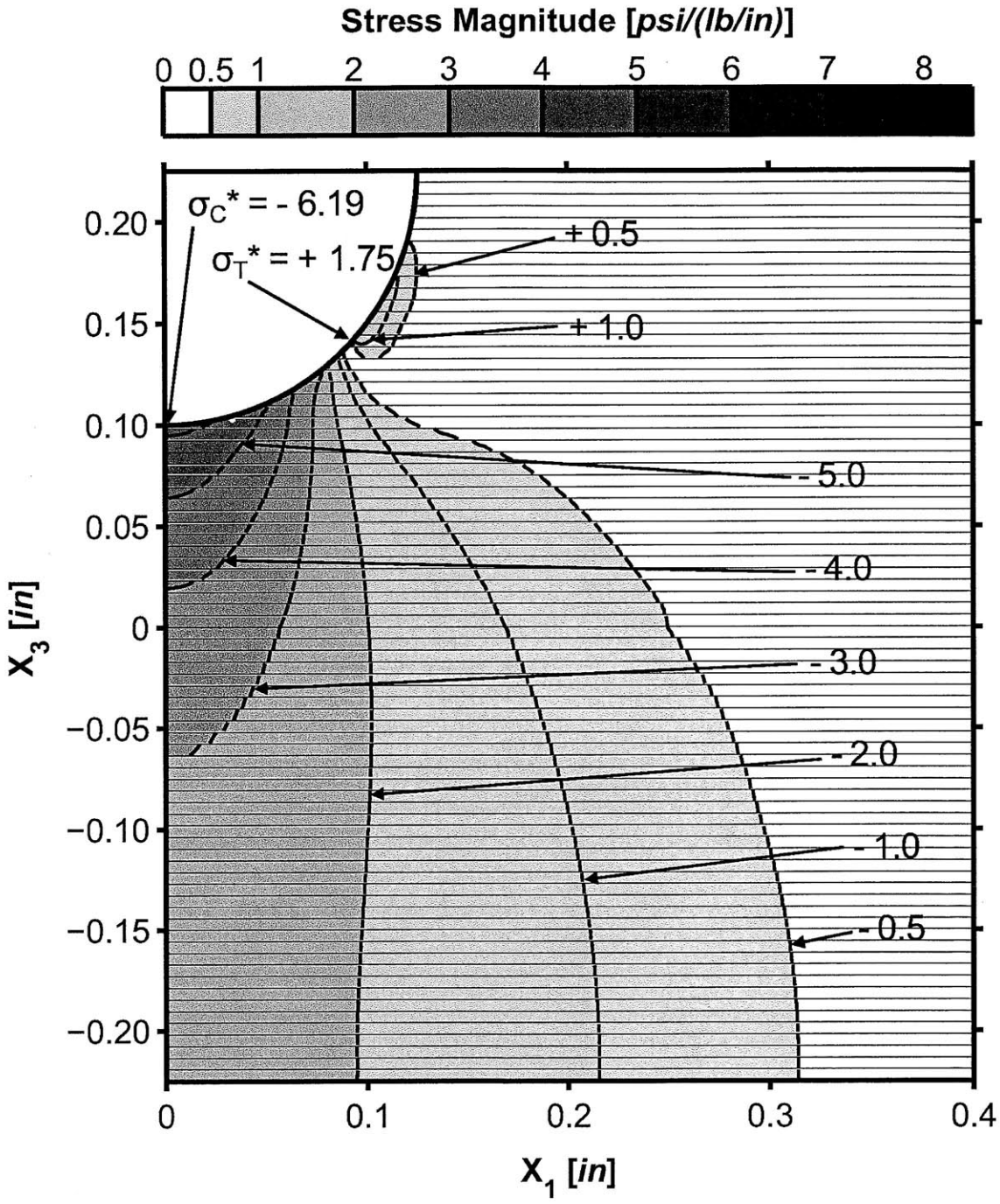

* Note: All stresses normalized by applied load, and given in units of [psi/(lb/in)].

Figure 5.19 Isostress plot of σ^*_{33} for a portion of the two-dimensional T700/2510 $[\pm 60/0]_{13S}$ laminate model with rigid indentor loaded at 5000 lb/in.

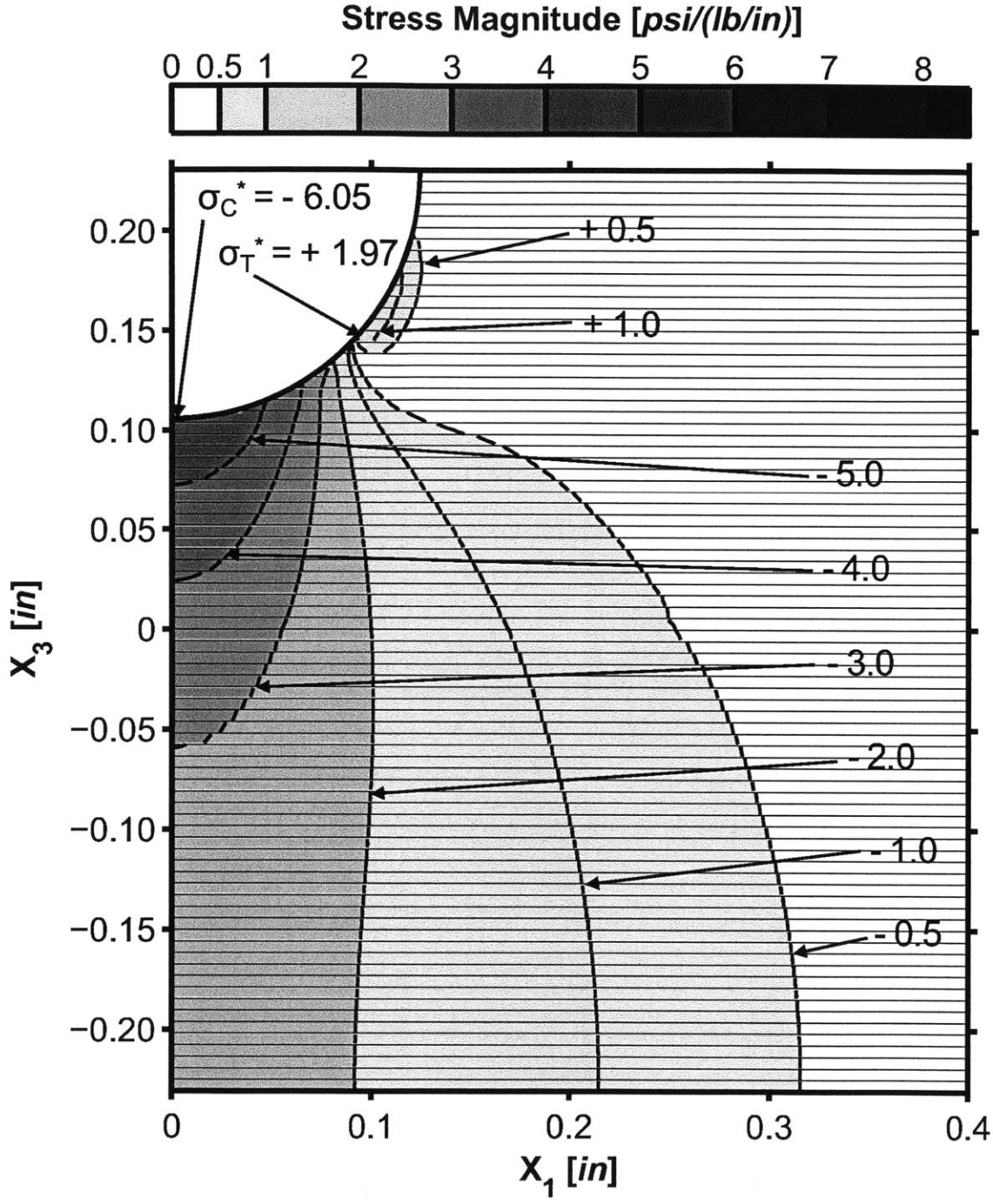

* Note: All stresses normalized by applied load, and given in units of [psi/(lb/in)].

Figure 5.20 Isostress plot of σ_{33}^{*} for a portion of the two-dimensional T700/2510 $[90/0]_{20S}$ laminate model with rigid indentor loaded at 5000 lb/in.

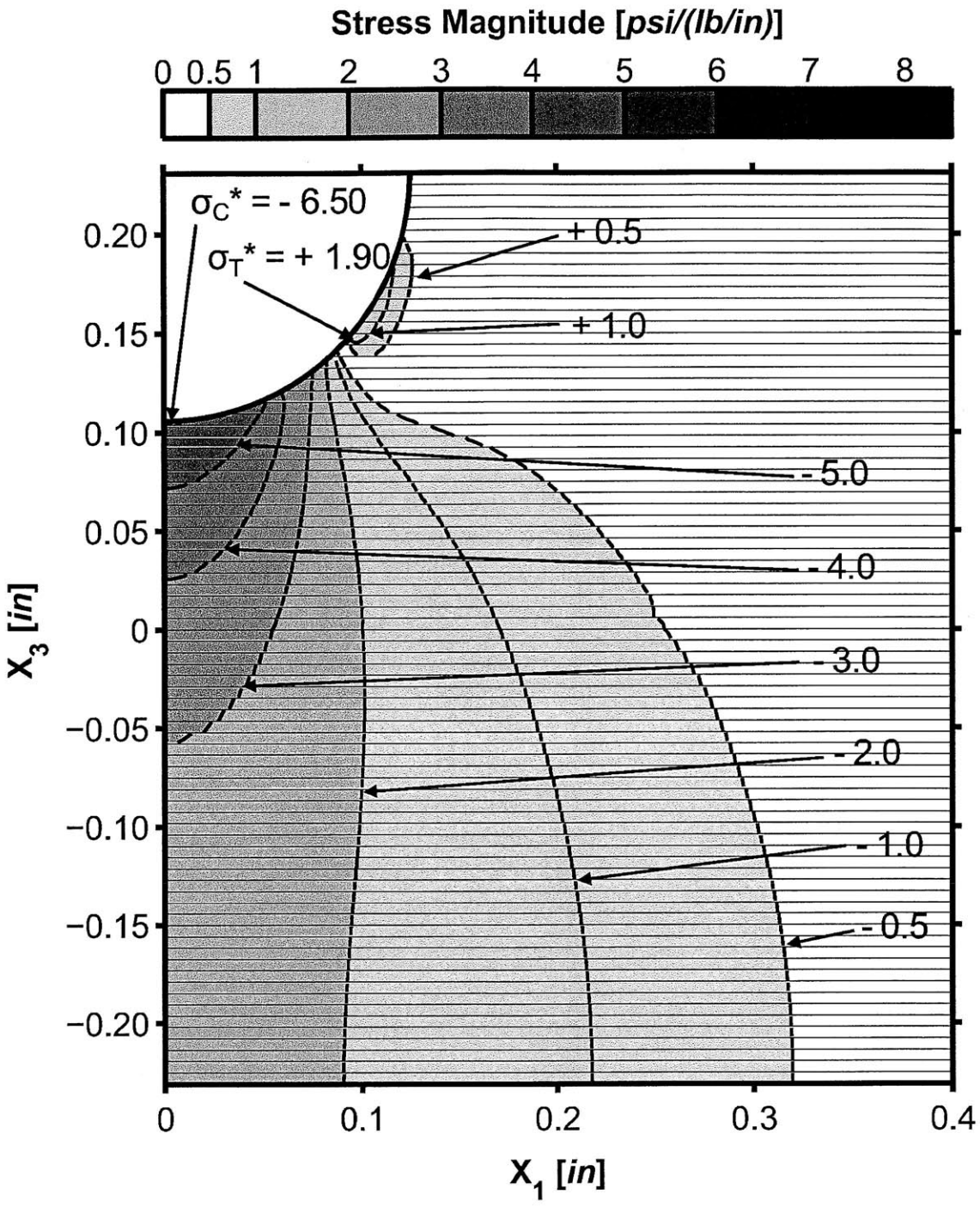

* Note: All stresses normalized by applied load, and given in units of [psi/(lb/in)].

Figure 5.21 Isostress plot of σ_{33}^{*} for a portion of the two-dimensional T700/2510 $[\pm 45/0/90]_{10S}$ laminate model with rigid indentor loaded at 5000 lb/in.

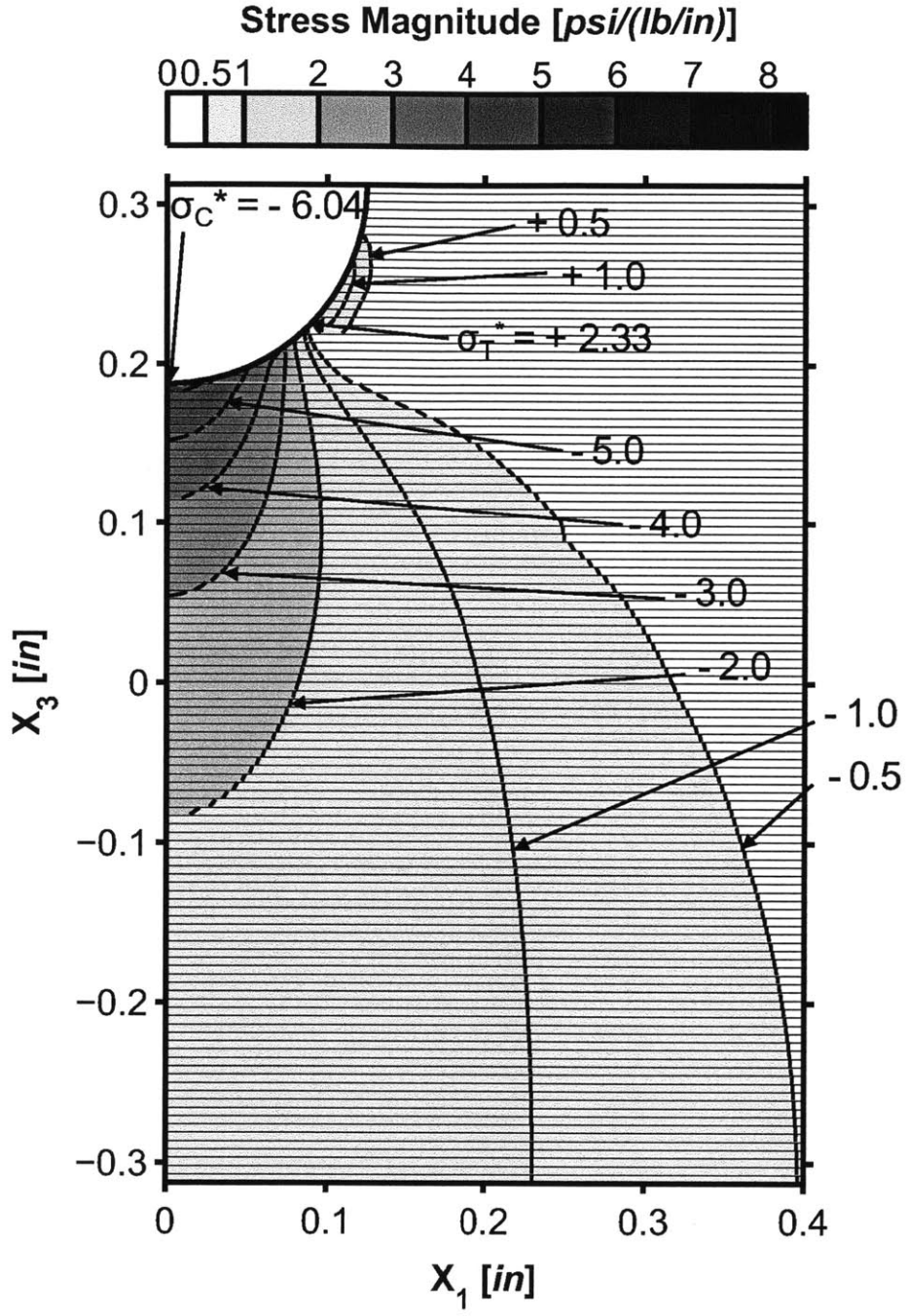

* Note: All stresses normalized by applied load, and given in units of [psi/(lb/in)].

Figure 5.22 Isostress plot of σ_{33}^{*} for a portion of the two-dimensional AS1/3501-6 $[0/\pm 45/90]_{15S}$ laminate model with rigid indentor loaded at 5000 lb/in.

Table 5.3 Maximum magnitudes of normalized stress values, σ^*_{33}, and locations in cylindrical coordinates for two-dimensional models with rigid indentor loaded at 5000 lb/in.

Laminate		Tensile			Compressive		
Material	Layup	σ^*_T $\left[\frac{psi}{(lb/in)}\right]$	ϕ_T $[deg]$	r_T $[in]$	σ^*_C $\left[\frac{psi}{(lb/in)}\right]$	ϕ_C $[deg]$	r_C $[in]$
T700/2510	$[\pm 15/0]_{13S}$	2.33	48.0	0.125	-6.04	1.1	0.125
T700/2510	$[\pm 30/0]_{13S}$	2.25	48.4	0.125	-6.08	1.1	0.125
T700/2510	$[\pm 45/0]_{13S}$	2.03	48.9	0.125	-6.14	1.1	0.125
T700/2510	$[\pm 60/0]_{13S}$	1.75	49.7	0.125	-6.19	1.1	0.125
T700/2510	$[90/0]_{20S}$	1.97	49.7	0.125	-6.05	1.2	0.125
T700/2510	$[\pm 45/0/90]_{10S}$	1.90	49.7	0.125	-6.04	1.2	0.125
AS1/3501-6	$[0/\pm 45/90]_{15S}$	1.97	50.9	0.125	-6.50	1.3	0.125

σ_C^*, increases slightly from 6.04 to 6.19 psi/(lb/in), a 2.5% increase. The location of σ_C^* is identical for all $[\pm\theta/0]_{13S}$ laminates. Conversely, as θ increases, the maximum tensile stress, σ_T^*, decreases from 2.33 to 1.75, a 24.9% decrease. The location of σ_T^* is fairly consistent on the face of the groove, but the angular position, ϕ_T, increases slightly as θ increases.

The stress distributions for the $[90/0]_{20S}$ and $[\pm45/0/90]_{10S}$ T700/2510 laminates are very similar to those for the $[\pm\theta/0]_{13S}$ laminates and have similar maximum tensile and compressive stresses. The isostress plot for the quasi-isotropic $[0/\pm45/90]_{15S}$ AS1/3501-6 laminate is very similar to the quasi-isotropic T700/2510 case. The AS1/3501-6 $[0/\pm45/90]_{15S}$ laminate is thicker than the T700/2510 $[\pm45/0/90]_{10S}$ laminate, thus the isostress plot appears slightly different near the bottom of the laminate, for example, the -2.0 psi/(lb/in) isostress line does not extend to the laminate backface in the AS1/3501-6 laminate. In addition, the maximum compressive stress for this laminate is higher than for any of the T700/2510 laminates, as this material is slightly stiffer in the 3-direction.

The normalized shear stress, σ_{13}^*, isostress plots for the $[\pm\theta/0]_{13S}$ laminates are shown in Figures 5.23, 5.24, 5.25, and 5.26 for θ equal to 15°, 30°, 45°, and 60°, respectively. The σ_{13}^* isostress plot for the $[90/0]_{20S}$ laminate is shown in Figure 5.27. The σ_{13}^* isostress plot for the quasi-isotropic T700/2510 laminate of $[\pm45/0/90]_{10S}$ is shown in Figure 5.28. For the AS1/3501-6 quasi-isotropic $[0/\pm/45/90]_{15S}$ laminate, the σ_{13}^* isostress plot is provided in Figure 5.29. Maximum values for σ_{13}^* in each of the laminates and the associated angular locations are provided in Table 5.4. These maximum values and locations are also shown on each isostress plot.

The distribution of normalized shear stress σ_{13}^* shares some core characteristics among the laminates under investigation. The isostress plots show two identical lobe-shaped regions of shear stress, one on either side of the x_3-axis, positive for x_1 values greater than 0, negative for x_1 values less than zero. While these regions of shear stress are mirror images in shape and magnitude, they are opposite in sign due to the conventions of shear stress signing. A shear stress is positive if the direction of the force is positive on a positive element face. Since the deformation on either side of

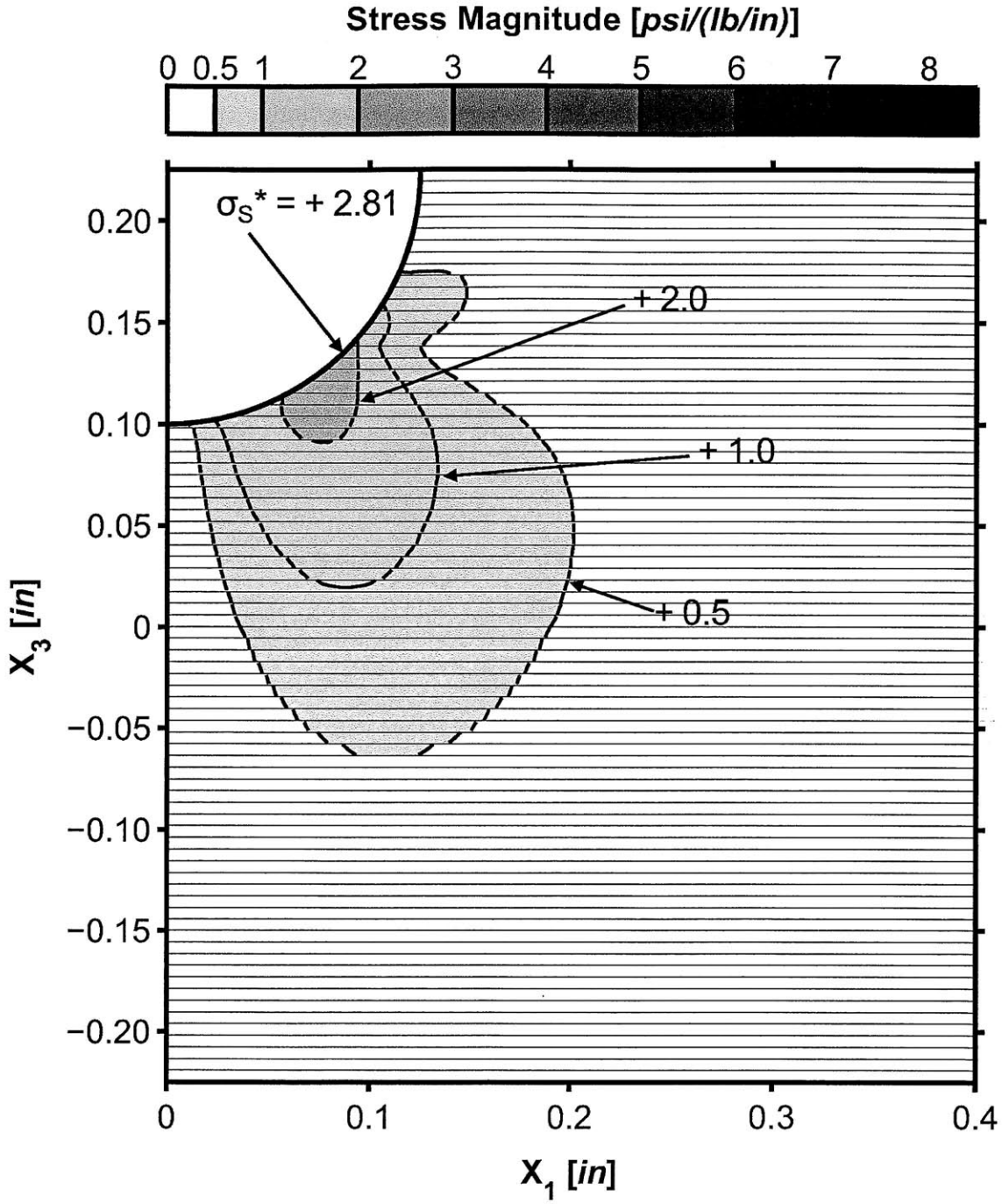

* Note: All stresses normalized by applied load, and given in units of [psi/(lb/in)].

Figure 5.23 Isostress plot of σ_{13}^{*} for a portion of the two-dimensional T700/2510 $[\pm 15/0]_{13S}$ laminate model with rigid indentor loaded at 5000 lb/in.

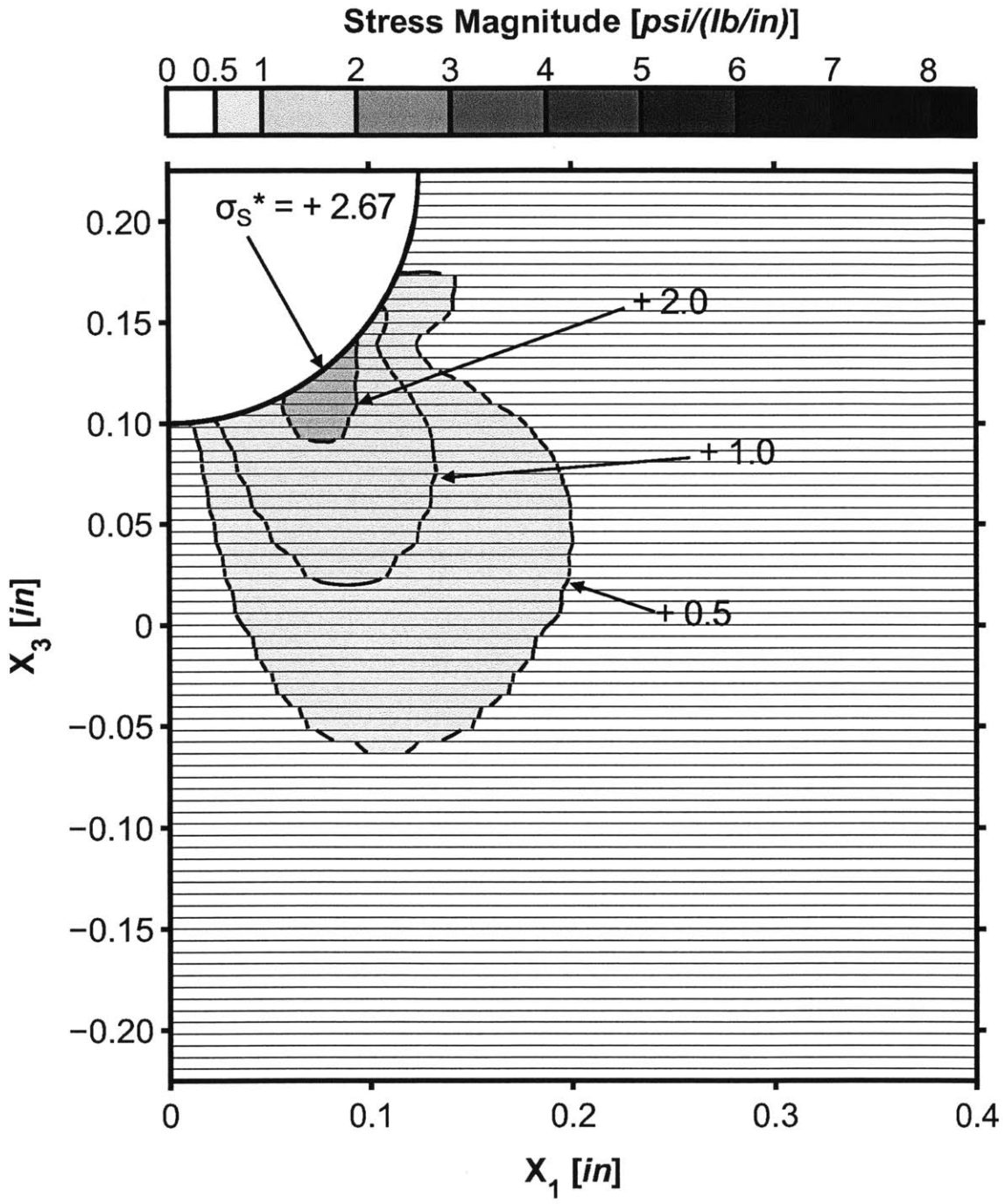

* Note: All stresses normalized by applied load, and given in units of [psi/(lb/in)].

Figure 5.24 Isostress plot of σ_{13}^{*} for a portion of the two-dimensional T700/2510 $[\pm 30/0]_{13S}$ laminate model with rigid indentor loaded at 5000 lb/in.

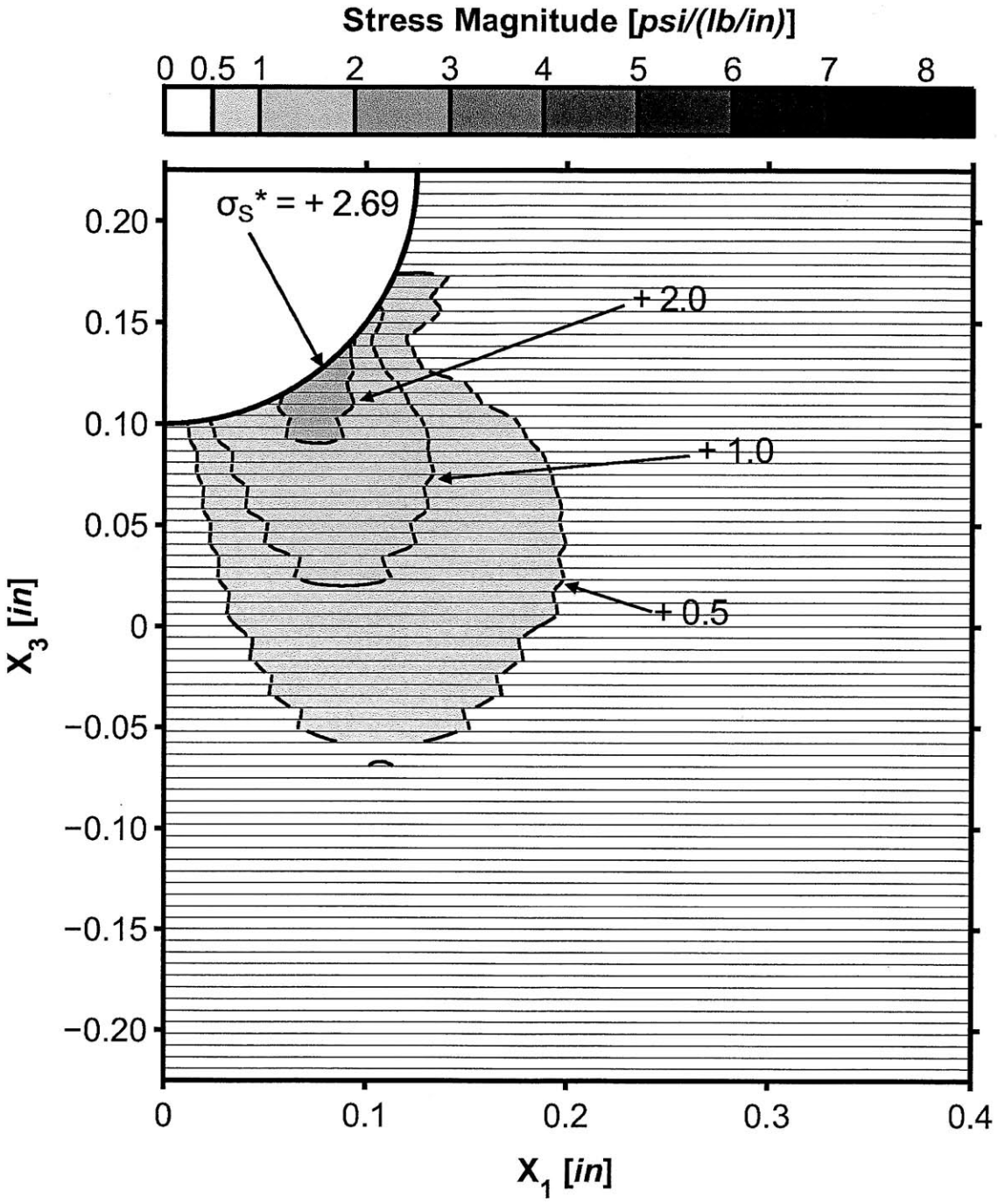

* Note: All stresses normalized by applied load, and given in units of [psi/(lb/in)].

Figure 5.25 Isostress plot of σ_{13}^{*} for a portion of the two-dimensional T700/2510 $[\pm 45/0]_{13S}$ laminate model with rigid indentor loaded at 5000 lb/in.

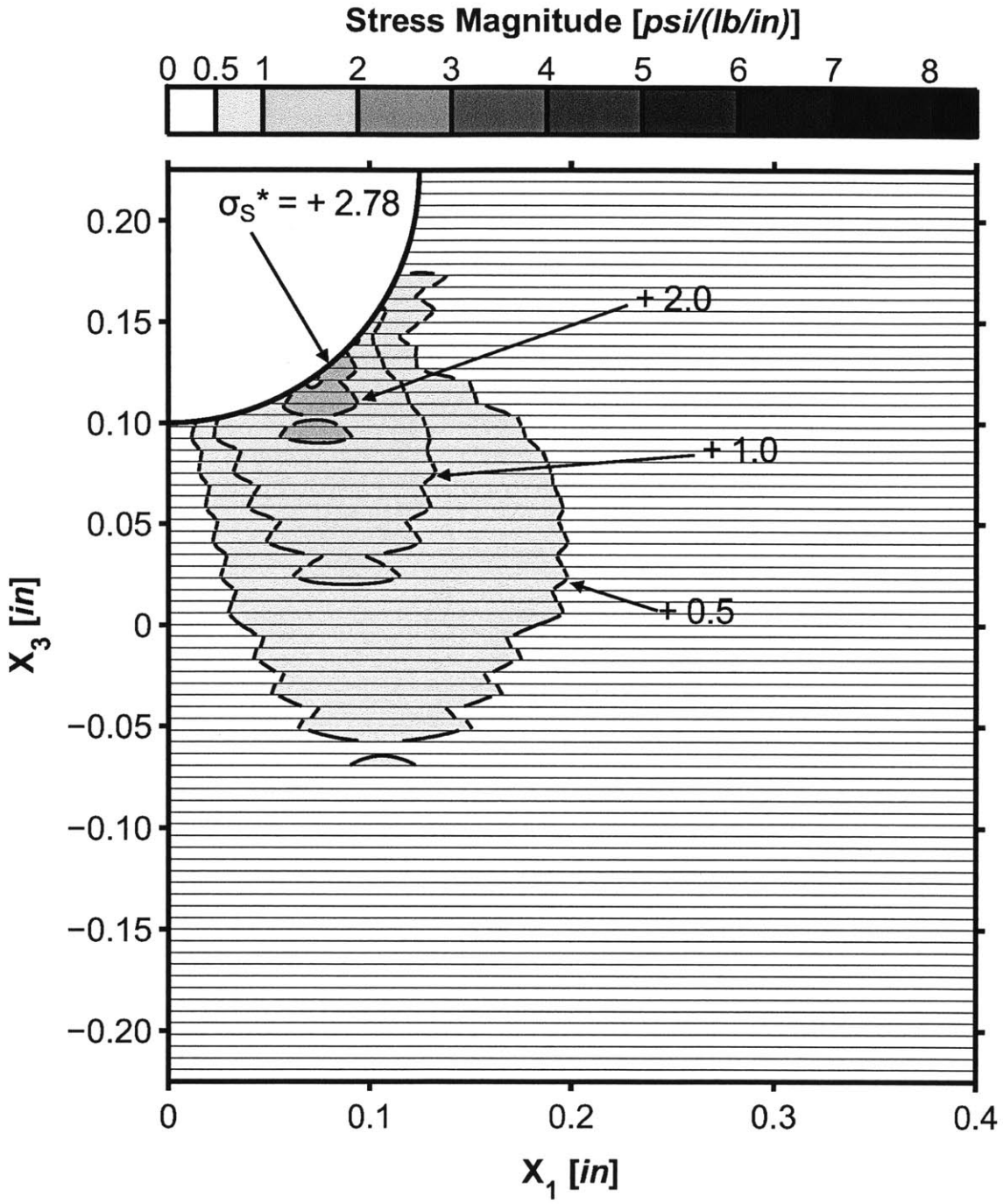

* Note: All stresses normalized by applied load, and given in units of [psi/(lb/in)].

Figure 5.26 Isostress plot of σ_{13}^{*} for a portion of the two-dimensional T700/2510 $[\pm 60/0]_{13S}$ laminate model with rigid indentor loaded at 5000 lb/in.

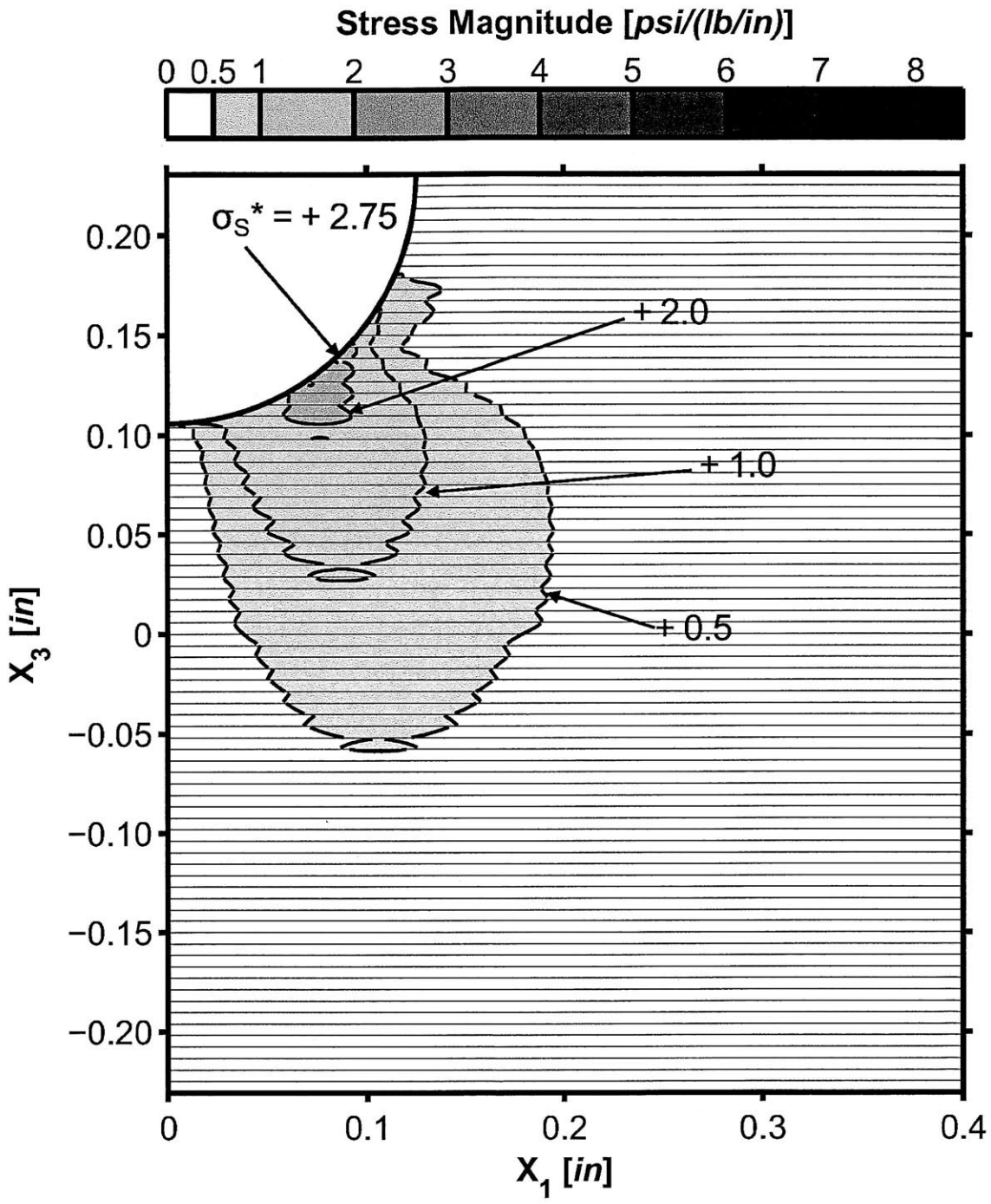

* Note: All stresses normalized by applied load, and given in units of [psi/(lb/in)].

Figure 5.27 Isostress plot of σ_{13}^{*} for a portion of the two-dimensional T700/2510 $[90/0]_{20S}$ laminate model with rigid indentor loaded at 5000 lb/in.

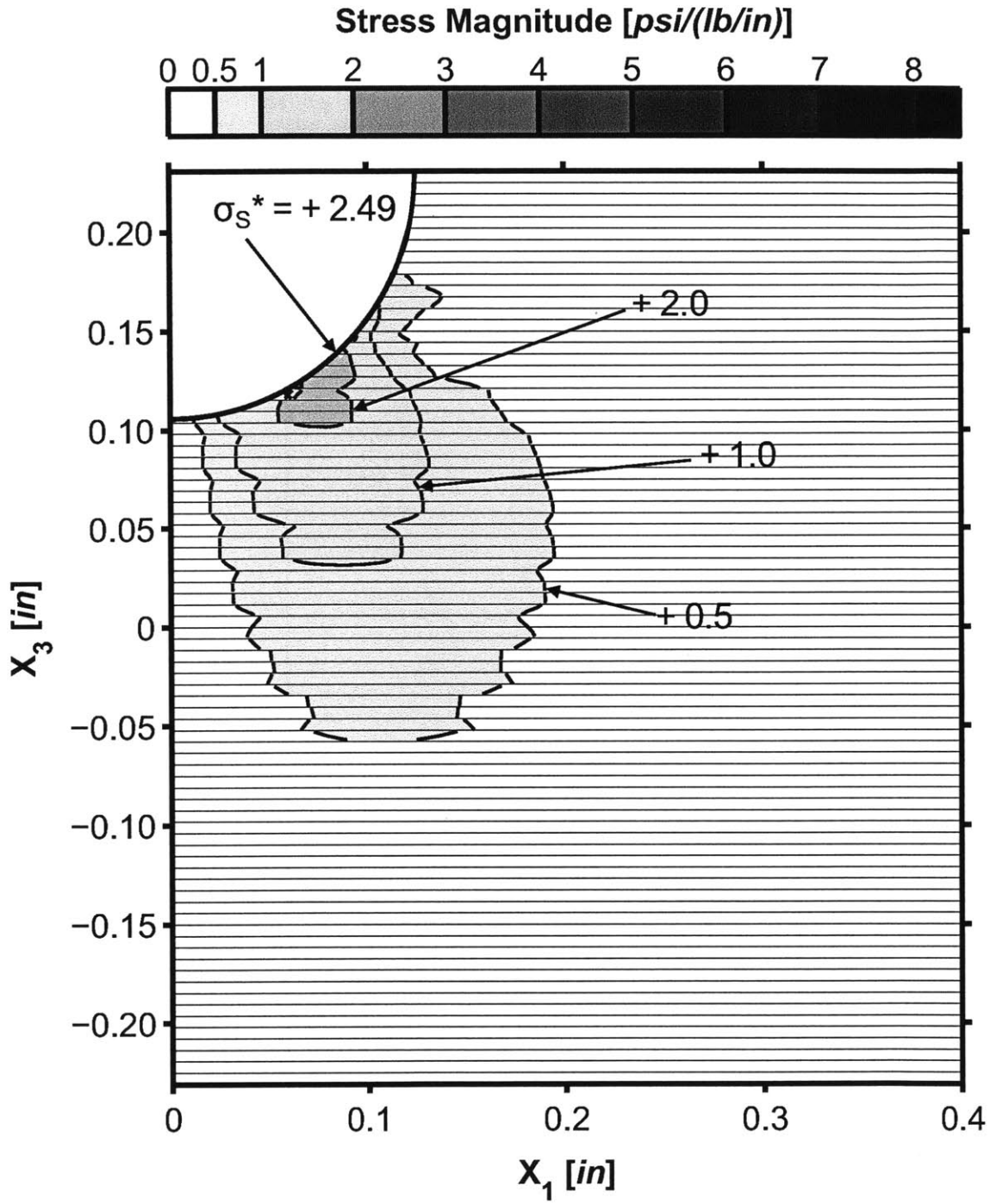

* Note: All stresses normalized by applied load, and given in units of [psi/(lb/in)].

Figure 5.28 Isostress plot of σ^*_{13} for a portion of the two-dimensional T700/2510 $[\pm 45/0/90]_{10S}$ laminate model with rigid indentor loaded at 5000 lb/in.

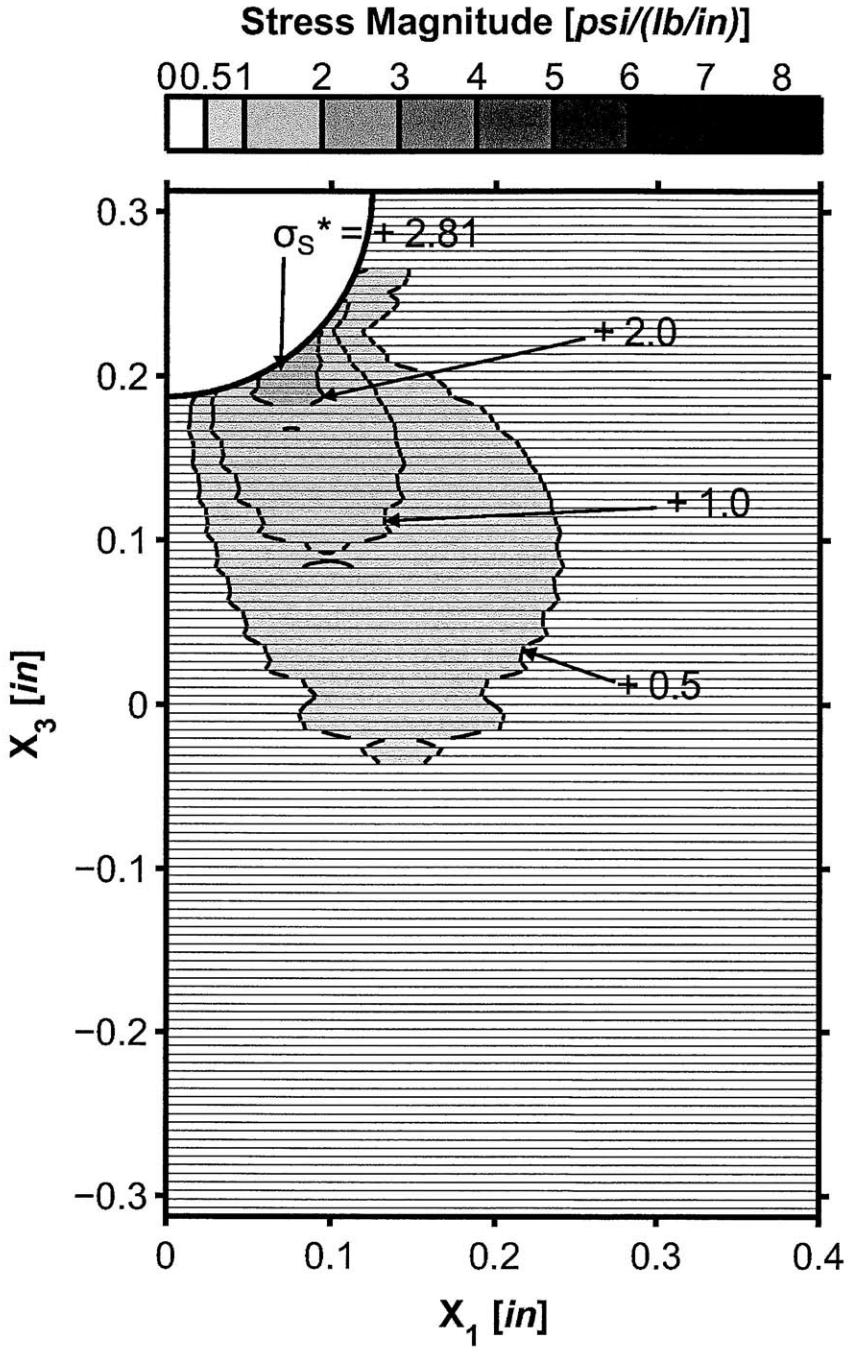

* Note: All stresses normalized by applied load, and given in units of [psi/(lb/in)].

Figure 5.29 Isostress plot of σ_{13}^{*} for a portion of the two-dimensional AS1/3501-6 $[0/\pm 45/90]_{15S}$ laminate model with rigid indentor loaded at 5000 lb/in.

Table 5.4 Maximum magnitudes of normalized stress values, σ^*_{13}, and locations in cylindrical coordinates for two-dimensional models with rigid indentor loaded at 5000 lb/in.

Laminate		**Shear**		
Material	Layup	σ^*_S $\left[\frac{psi}{(lb/in)}\right]$	ϕ_S $[deg]$	r_S $[in]$
T700/2510	$[\pm 15/0]_{13S}$	2.81	43.2	0.125
T700/2510	$[\pm 30/0]_{13S}$	2.67	38.8	0.125
T700/2510	$[\pm 45/0]_{13S}$	2.69	38.8	0.125
T700/2510	$[\pm 60/0]_{13S}$	2.78	38.8	0.125
T700/2510	$[90/0]_{20S}$	2.75	45.8	0.125
T700/2510	$[\pm 45/0/90]_{10S}$	2.49	42.2	0.126
AS1/3501-6	$[0/\pm 45/90]_{15S}$	2.74	35.1	0.127

the groove is a mirror of the other, the two sides will have opposite shear stress signs. These regions of shear stress originate along the sides and bottom of the groove and continue down and out diagonally into the laminate. Isostress lines do not touch the laminate top face or back face.

Examining the stress data for the $[\pm\theta/0]_{13S}$ laminates, some trends are apparent. The isostress plots show a more jagged distribution for the shear stresses as θ increases, with the narrower parts of the isostress curve corresponding to the 0° plies, meaning shear stress tends to decrease in 0° plies relative to the $\pm\theta$ plies as θ increases. The maximum normalized shear stress, σ_S^*, always occurs on the face of the groove, although the location varies slightly. For the $[\pm\theta/0]_{13S}$ laminate, the maximum shear stress occurs in a +15° ply. For all other laminates in this series, the maximum shear stress occurs at an identical location between a $-\theta$ and 0° ply. At the location of maximum shear stress for the other $[\pm\theta/0]_{13S}$ laminates, the $[\pm15/0]_{13S}$ laminate has a shear stress of 2.66 psi/(lb/in), a minimum for the laminate series. This implies that the natural location for the maximum shear stress is at a ϕ location of approximately 43.2°. A decrease in the shear stiffness of $\pm\theta$ plies decreases the stress in this location and shifts the maximum to a nearby 0° ply. Overall, maximum shear stress is at a maximum for the $[\pm15/0]_{13S}$ laminate, and at a minimum for the $[\pm30/0]_{13S}$ laminate, although the location of σ_S^* changes between these laminates, as mentioned. Shear stress then continuously increases as θ increases.

The σ_{13}^* isostress plot for the $[90/0]_{20S}$ laminate also exhibits isostress lines with a jagged appearance. Above the bottom of the groove, ripples of higher stress occur at the 0/90-degree ply boundary, and below the bottom of the groove the ripples of higher stress occur at the 90/0-degree ply boundary.

The σ_{13}^* distribution for the quasi-isotropic T700/2510 $[\pm45/0/90]_{10S}$ laminate is largely consistent with the characteristics found in the other laminates, and does exhibit some waviness in the isostress lines between plies. Below the bottom of the groove, isostress lines shrink in along the 0/90° ply boundary, above the bottom of the groove, isostress lines shrink in along the $-45/0°$ ply boundary, meaning shear stresses are generally lower in those regions. The AS1/3501-6 quasi-isotropic $[0/\pm/45/90]_{15S}$

laminate shows longer isostress lobes in the negative 3-direction than the other laminates. However, it should be noted that this laminate is thicker than the others, and this may have some effect on the extent of the shear stress distribution with consideration for the rigid backface boundary condition. Above the laminate mid-plane, stresses are higher in the 90° plies, and lower in the 0° plies. Below the laminate mid-plane, the stresses are higher in the ±45° plies.

5.1.3 Effect of Load Magnitude

In order to determine the linearity of the response of a grooved laminate to a contact load, the response is examined for the quasi-isotropic $[\pm 45/0/90]_{10S}$ T700/2510 laminate at a lower load level. While all laminates were modeled at the same various load levels, the quasi-isotropic laminate is chosen as it has characteristics of all laminates examined, having 0°, angled, and 90° plies. The maximum load examined in the two-dimensional cases is 5000 lb/in. To examine the effect of changing the load, the contact pressure and stress response is examined at 1000 lb/in, or twenty percent of the maximum load.

The contact pressure distribution for the quasi-isotropic laminate loaded at 1000 lb/in is shown in Figure 5.30. The contact press distribution for the same laminate at the higher load of 5000 lb/in is overlaid for comparison. Contact is maintained to an angular position, ϕ, of 30.1° for the loading of 1000 lb/in, as compared to 49.7° for the loading of 5000 lb/in. The maximum contact pressure of 11.18 psi/(lb/in) occurs at ϕ equal to 0.7° for the loading of 1000 lb/in, as compared to 6.07 psi/(lb/in) at ϕ equal to 2.1° for the loading of 5000 lb/in. Most notable is that the contact pressure relative to the applied load in the 1000 lb/in case is nearly twice as high as for the 5000 lb/in loading, while the contact area is significantly smaller. This indicates linear scaling of the response by the applied load would be highly inaccurate, and speaks to the nature of the nonlinearity of the response. The shape of the distribution is generally smooth, and exhibits no discernible trends based on the ply angle contacted. However, due to the smaller contact area, the number of plies available for comparison are low, as only three plies are contacted. There is also a lack of substantial contact on the 0° plies,

which see the largest increases in contact pressure at the higher loading. It cannot conclusively be stated to what degree the local ply angle has an effect on the local contact pressure.

The normalized longitudinal extensional stress σ_{11}^* is shown in Figure 5.31. The stress distribution shows the general characteristics common to σ_{11} in the other laminates and load levels, but with higher normalized stresses and stress gradients. Zone 1, the region immediately under the groove, is primarily in tension in the 0° plies, and in compression in the neighboring 90° plies. In Zone 2, a lobe of compressive stress is to the side of the groove, extending away from the bottom of the groove and down toward the bottom of the laminate, with the compressive stresses primarily concentrated in the 0° plies. In Zone 3, tensile stress extends out and up to the top face of the laminate, with stresses primarily concentrated in the 0° plies. Of the three zones of stress seen in the σ_{11}^* isostress plots, Zones 2 and 3 are larger at the 1000 lb/in loading than they are for the 5000 lb/in loading, while Zone 1 is slightly smaller. There is also more overlap between the zones for the 1000 lb/in loading. For the 1000 lb/in loading, the maximum tensile stress, σ_T^*, is 8.57 psi/(lb/in) and occurs beneath the groove in a 0° ply at an angular location, ϕ, of 1.11°, at a radius, r, of 0.156 inches, as compared to a σ_T^* of 6.50 psi/(lb/in) at a location of ϕ equal to 1.3°, and r equal to 0.133 inches, for the 5000 lb/in loading. For the 1000 lb/in loading, the maximum compressive stress, σ_C^*, is -7.09 psi/(lb/in) and occurs on the bottom of the groove in a $-45°$ ply at an angular location, ϕ, equal to 1.17° on the groove face, as compared to a σ_C^* value of -4.43 psi/(lb/in) at a location of ϕ equal to 43.4°, and r equal to 0.149 inches, for the 5000 lb/in loading.

The isostress plot for the normalized through-thickness extensional stress, σ_{33}^*, for the quasi-isotropic $[\pm 45/0/90]_{15S}$ T700/2510 laminate at the lower 1000 lb/in load is shown in Figure 5.32. The stress distribution shares a similar basic form with the σ_{33} distribution in other laminates at the higher load. The region beneath the groove is in compression, with a high stress gradient near the groove and near the x_2-axis. In this region, maximum normalized stresses and stress gradients are greater than they are at the higher loading. This implies that at a lower load, the laminate is carrying

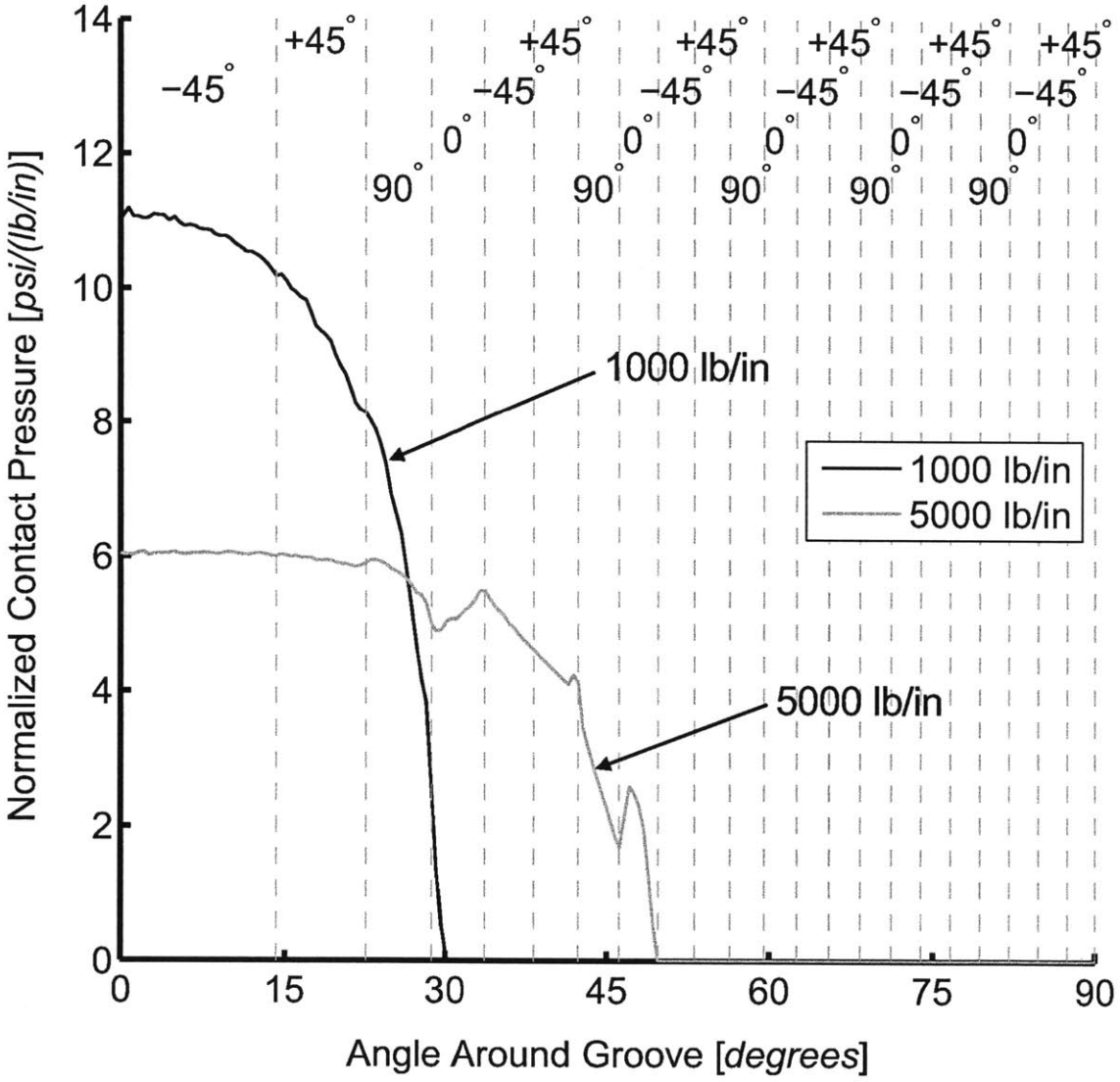

* Note: All pressures normalized by applied load, and given in units of [psi/(lb/in)].

Figure 5.30 Normalized contact pressure for two-dimensional T700/2510 $[\pm 45/0/90]_{10S}$ laminate model loaded at 1000 lb/in and 5000 lb/in.

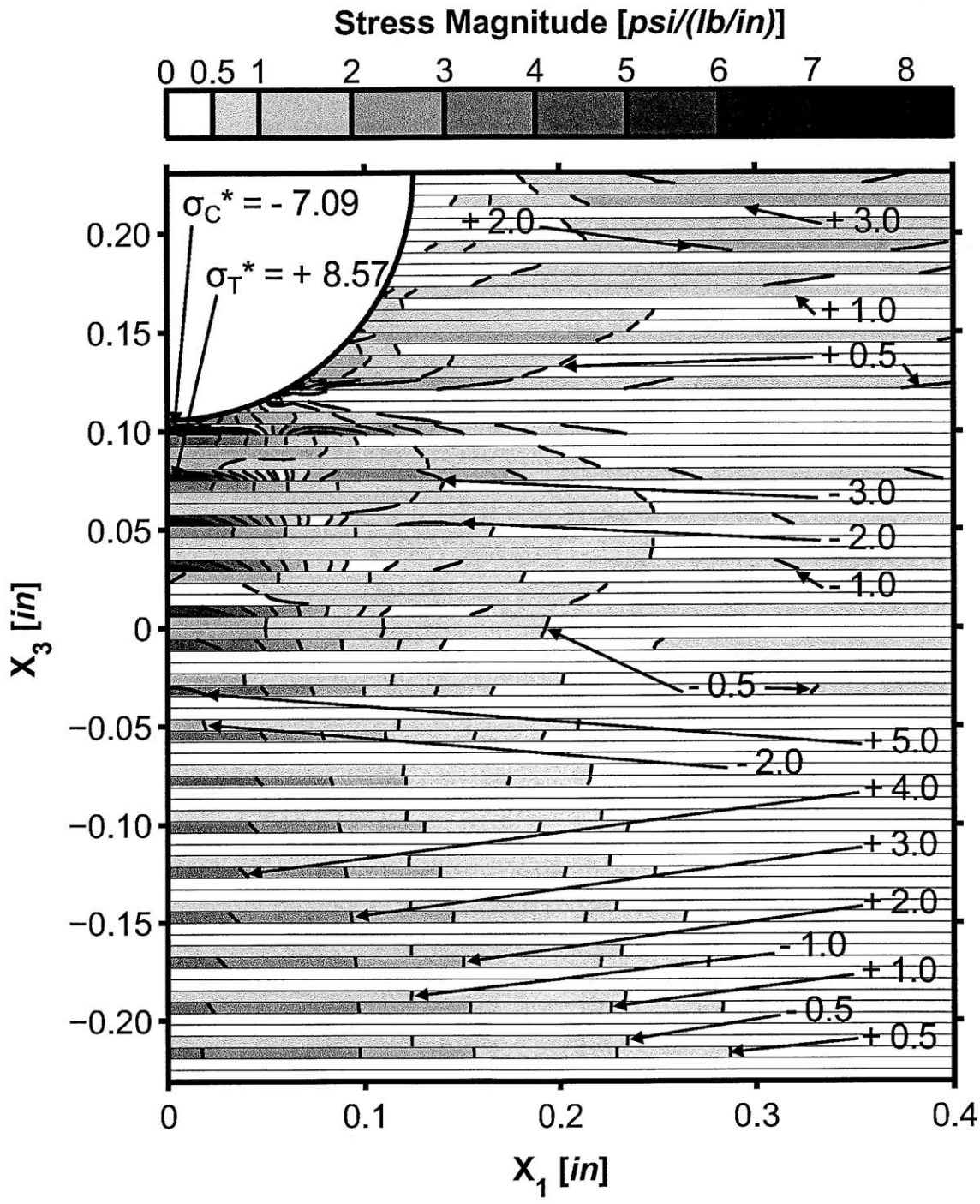

* Note: All stresses normalized by applied load, and given in units of [psi/(lb/in)].

Figure 5.31 Isostress plot of σ_{11}^{*} for a portion of the two-dimensional T700/2510 $[\pm 45/0/90]_{10S}$ laminate model with rigid indentor loaded at 1000 lb/in.

a higher proportion of the load in a narrower space, particularly along the x_1-axis. A small lobe of tensile stress is on either side of the groove, along the groove face approximately midway up. For the 1000 lb/in loading, the maximum tensile stress, σ_T^*, is 2.14 psi/(lb/in), and occurs along the groove face in a 0° ply at an angular location, ϕ, of 30.1°, as compared to the σ_T^* value of 1.90 psi/(lb/in) at the location on the groove surface of ϕ equal to 49.7° for the 5000 lb/in loading. For the 1000 lb/in loading, the maximum compressive stress, σ_C^*, is -11.1 psi/(lb/in), and occurs at the bottom of the groove on the groove face at a value of ϕ of 1.17°, as compared to the σ_C^* value of -6.04 psi/(lb/in) at the location on the groove surface of ϕ equal to 1.2° for the 5000 lb/in loading.

The isostress plot for the normalized shear stress, σ_{13}^*, for the quasi-isotropic $[\pm 45/0/90]_{15S}$ T700/2510 laminate at the lower 1000 lb/in load is shown in Figure 5.33. The shear stress occurs in symmetric lobes on either side of the groove, originating from the sides and bottom of the groove and extending down and out into the laminate, similar to the σ_{13}^* distribution at the higher load. The isostress lines exhibit some waviness showing higher shear stress in the ±45° plies. For the 1000 lb/in loading, the maximum shear stress, σ_S^*, is 4.52 psi/(lb/in) and occurs in a 0° ply on the groove face at ϕ equal to 29.2°, as compared to the σ_S^* value of 2.49 psi/(lb/in) at the location on the groove surface of ϕ equal to 42.2° for the 5000 lb/in loading. While the form of the stress distribution remains the same, normalized shear stresses are higher than they are at the higher load by as much as 82%.

5.2 Cylinder Loading – Elastic Indentor

The following results address the effect of changing the indentor from a rigid body to a linear elastic steel body in the two-dimensional, cylinder loaded case. Intuitively, this method would be a more realistic way to model the indentor, since the indentor under investigation is a stiff steel, but is still a deformable material. However, the use of a linear elastic model for the indentor requires the implementation of a finite element discretization for the indentor. Thus, the indentor surface is no longer per-

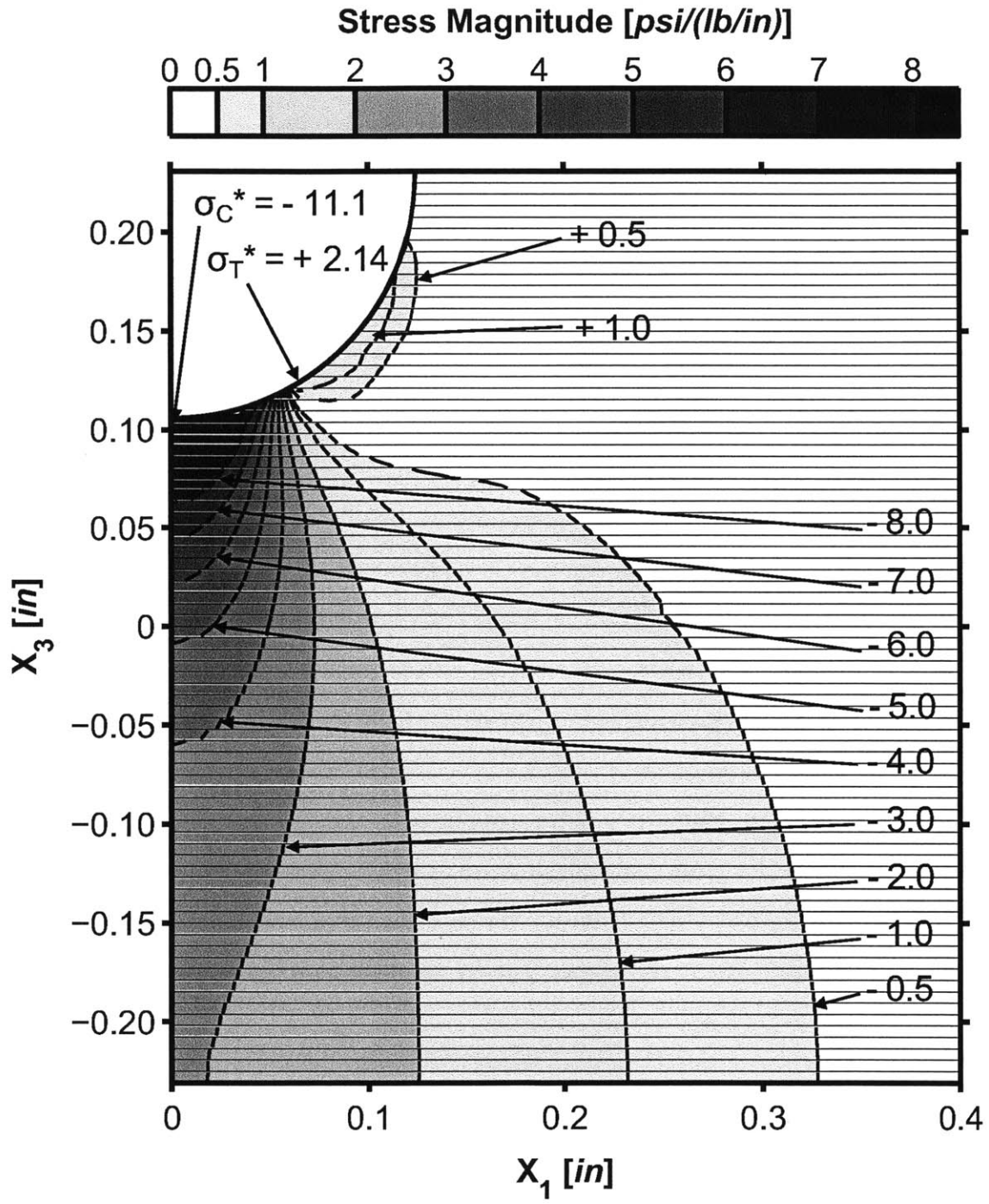

* Note: All stresses normalized by applied load, and given in units of [psi/(lb/in)].

Figure 5.32 Isostress plot of σ_{33}^{*} for a portion of the two-dimensional T700/2510 $[\pm 45/0/90]_{10S}$ laminate model with rigid indentor loaded at 1000 lb/in.

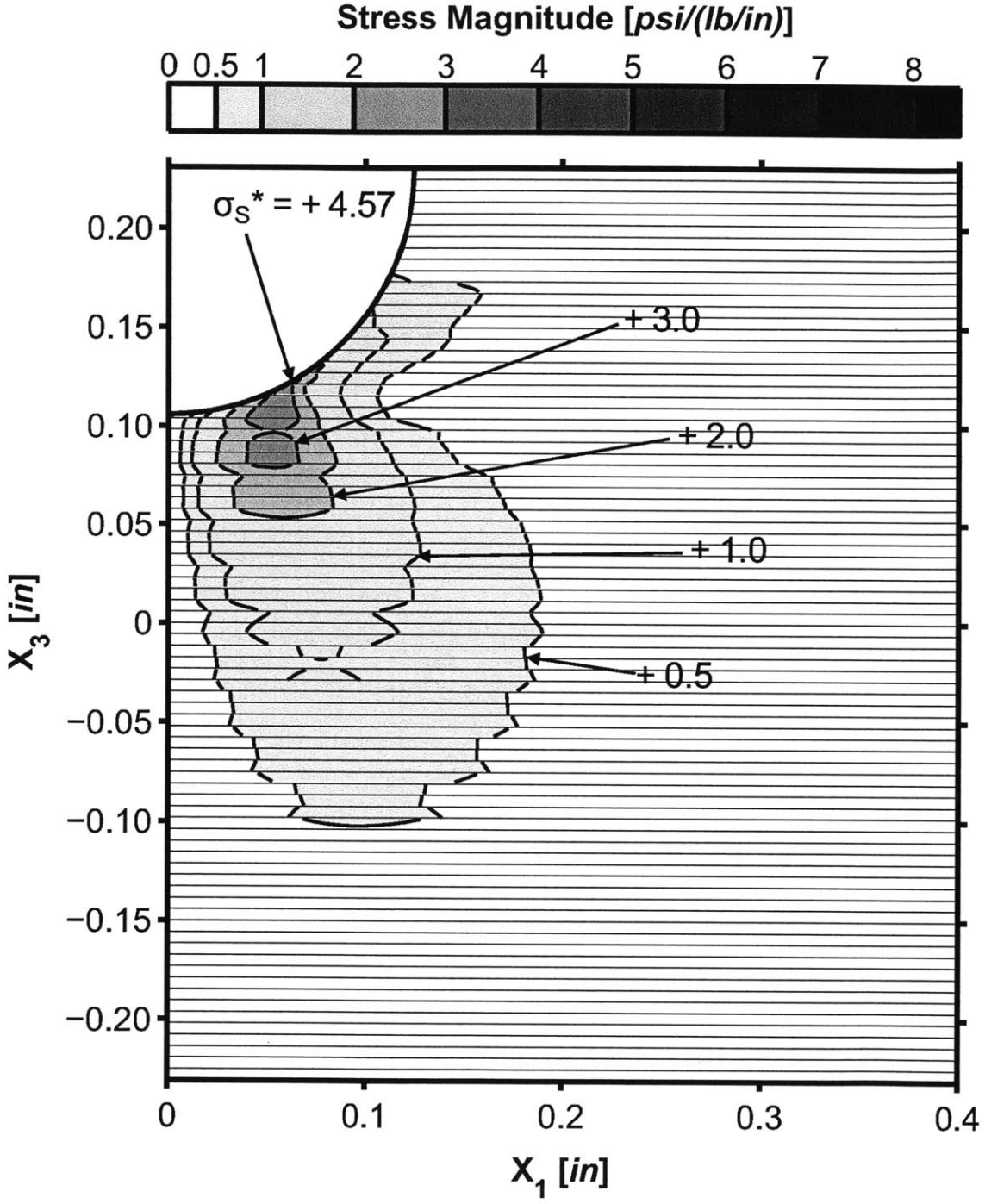

* Note: All stresses normalized by applied load, and given in units of [psi/(lb/in)].

Figure 5.33 Isostress plot of σ^*_{13} for a portion of the two-dimensional T700/2510 $[\pm 45/0/90]_{10S}$ laminate model with rigid indentor loaded at 1000 lb/in.

fectly smooth or round. The linear elastic implementation in this case also requires roughly twice the computational time compared to the same models with rigid body indentors. This is due partially to the increased number of elements in the solution from the discretization of the indentor, and partially due to the change in contact formulation that the discretized indentor requires, as discussed in Section 4.1. The following sections provide the results for the quasi-isotropic T700/2510 $[\pm 45/0/90]_{10S}$ laminate using a linear elastic indentor. While the effect of the indentor change was examined on all of the laminates, this quasi-isotropic laminate showcases most of the effects seen in the other models. A loading of 5000 lb/in is imposed on the linear elastic indentor.

5.2.1 Contact Pressure

The pressure distribution between the loaded indentor and the laminate groove for the representative case of the quasi-isotropic T700/2510 $[\pm 45/0/90]_{10S}$ is shown in Figure 5.34. The contact pressure from the rigid indentor model is presented for comparison. Pressures have been normalized by the total load on the indentor of 5000 lb/in for both cases.

Contact is maintained to an angular position, ϕ, of 51.2°. The maximum normalized pressure, $p^*_{C_{max}}$, is 6.11 psi/(lb/in), occurring near the bottom of the groove at ϕ equal to 0.7°. For comparison, the maximum normalized pressure, $p^*_{C_{max}}$, for the model with a rigid body indentor is 6.07 psi/(lb/in), a difference of 0.7%, and occurs at a similar location of ϕ equal to 2.1°, and has contact angle, $\phi_{contact}$, of 49.7°, a difference of 2.9%. The contact pressure distributions from the elastic indentor share the same trends as the pressure from the rigid body counterpart, with pressure rising in the 0° plies and falling in the 90° plies. The pressure distribution from the elastic indentor is characterized by a small jagged oscillation that is superposed on the overall trend of the pressure and is most apparent near the bottom of the groove and in areas where the pressure distribution should be otherwise smooth. This variation takes on a maximum peak-to-peak amplitude of approximately 0.2 psi/(lb/in), or about 3.3% of the local contact pressure. The wavelength of this jagged oscillation

appears to be related to the element size, as the wavelength is consistently three elements lengths, approximately 0.003 inches, implying the origin of this oscillation is related to discretization issues. The region of greatest variation from the rigid body case is at higher values of ϕ, particularly in the 0° ply at ϕ equal to 46.2°, where the difference in pressure from the linear elastic case to the rigid body case is closer to 12%. In this region, pressure is increasingly acting more in the 1-direction and less in the 3-direction. The indentor will encounter higher stiffness in the 1-direction, particularly in the 0° plies, due to the directional fibers of the composite, decreasing the ratio of the stiffness of the indentor to the stiffness of the ply, and decreasing the accuracy of the rigid body assumption. Thus the primary difference between the model with the rigid body indentor and model with the linear elastic indentor occurs near the end of contact, at angles of ϕ around 45° or greater. Even these differences are small.

5.2.2 Stress Response

The stress response for the T700/2510 $[\pm 45/0/90]_{10S}$ is presented as the characteristic case for the use of an elastic indentor, as compared to a rigid indentor. The stress magnitudes are normalized by the applied load of 5000 psi/(lb/in). Results for the elastic indentor model are presented and results for the rigid indentor are overlaid for comparison. For all stresses investigated, the stress distributions are nearly identical between the loadings from the rigid body and linear elastic indentors. In some cases, the rigid body results may not be visible as they are coincident with the linear elastic case. The normalized longitudinal extensional stress, σ_{11}^*, is shown in Figure 5.35. The maximum tensile stress, σ_T^*, is 6.67 psi/(lb/in) and occurs in a 0° ply beneath the groove at an angular location, ϕ, of 0.41° at a radial distance from the groove center of curvature, r of 0.133 inches. The maximum compressive stress, σ_C^*, is -4.54 psi/(lb/in) and occurs in a 0° ply at ϕ equal to 45.0°, r equal to 0.153 inches. Compared to the results from the rigid indentor, this is a 2.6% increase for σ_T^* and a 2.5% increase for σ_C^*. These stresses occur at similar locations in both models, as in the rigid body model, σ_T^* occurs at ϕ equal to 1.3°, and r equal to 0.133 inches,

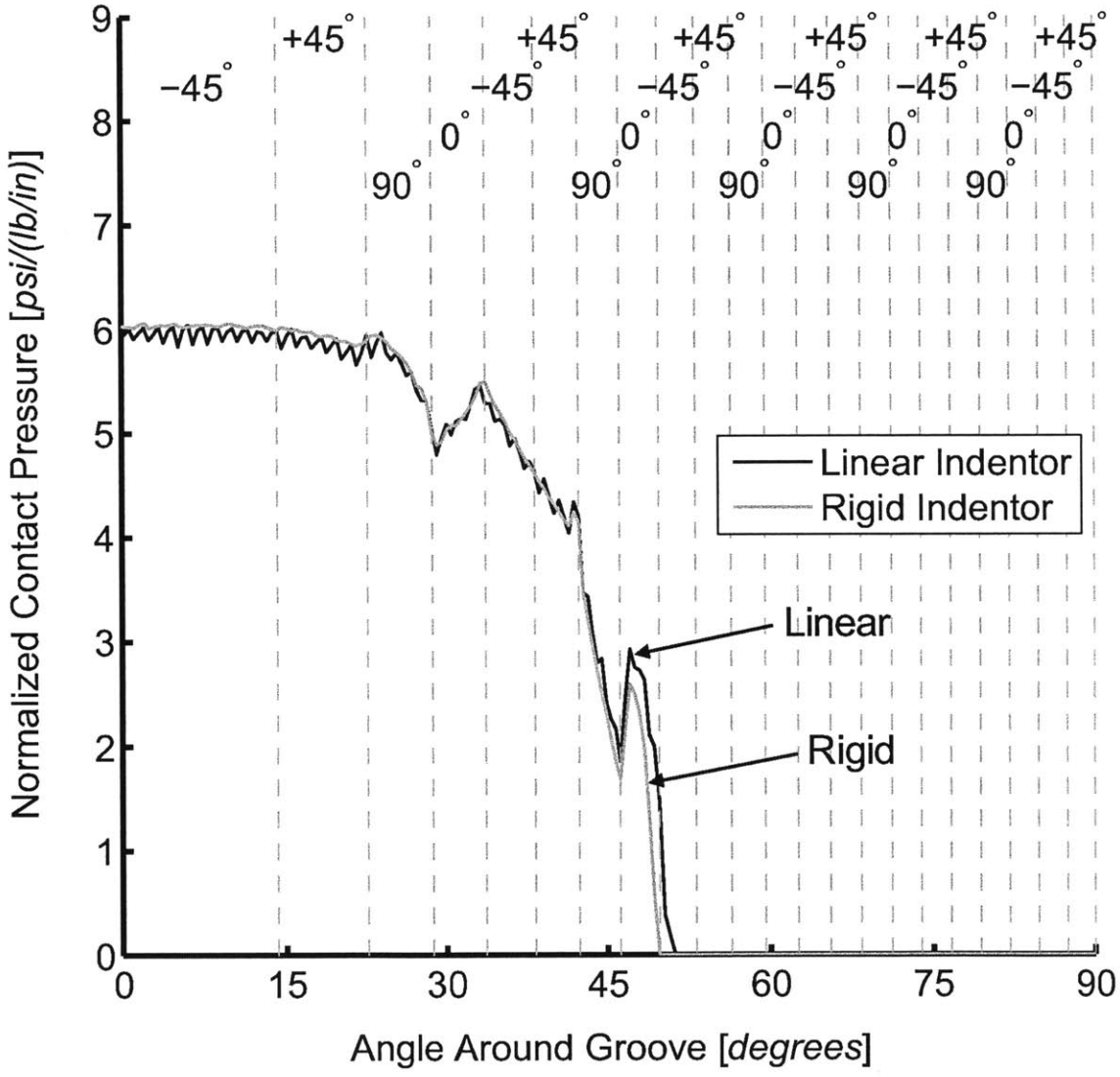

* Note: All pressures normalized by applied load, and given in units of [psi/(lb/in)].

Figure 5.34 Contact pressure for T700/2510 $[\pm 45/0/90]_{10S}$ loaded at 5000 lb/in by a linear elastic indentor and a rigid body indentor.

and σ_C^* occurs at ϕ equal to 43.4°, and r equal to 0.149 inches.

The normalized through-thickness extensional stress, σ_{33}^*, is shown in Figure 5.36. The maximum tensile stress, σ_T^*, is 1.90 psi/(lb/in) and occurs at an angular location of ϕ equal to 50.6° on the groove surface. The maximum compressive stress, σ_C^*, is -5.99 psi/(lb/in) and occurs at the bottom of the groove at ϕ equal to 0.68°. Compared to the model loaded with a rigid indentor, this represents an identical value for σ_T^*, and a decrease of 0.8% for σ_C^*. These stresses occur at similar locations in both models, as in the rigid body model, σ_T^* occurs at ϕ equal to 49.7° on the groove surface, and σ_C^* occurs at ϕ equal to 1.2° on the groove surface.

The normalized shear stress, σ_{13}^*, is shown in Figure 5.37. The maximum shear stress, σ_S^*, is 2.47 psi/(lb/in), and occurs at an angular position of ϕ equal to 41.9° on the groove face. Compared to the model loaded by a rigid indentor, this represents a decrease in shear stress of 1.6%. These stresses occur at similar locations in both models, as in the rigid body model, σ_S^* occurs at ϕ equal to 42.2°, and r equal to 0.126 inches, just under the groove surface.

5.3 Sphere Loading

The three-dimensional model was used to investigate the response of a grooved laminate to loading from a spherical indentor, as detailed in Section 4.2.4. This case is a more complete representation of the grooved composite tube loaded in contact with ball bearings. The case under investigation is a simplification that examines a small section of grooved composite material and a single ball indentor. Due to computational expense, this model uses a vertical plane of symmetry running the length of the groove at the 2-3 plane, and models the indentor as an analytical rigid body. Results from the two-dimensional models presented in the previous section indicate that the assumption of a rigid indentor has a negligible effect on results, as compared to a linear elastic indentor. The laminates studied in the three-dimensional models are the $[\pm\theta/0]_{13S}$ laminate series (θ equal to 15°, 30°, 45°, and 60°), the cross-ply $[90/0]_{20S}$ laminate, and the quasi-isotropic $[\pm 45/0/90]_{10S}$ laminate. All these

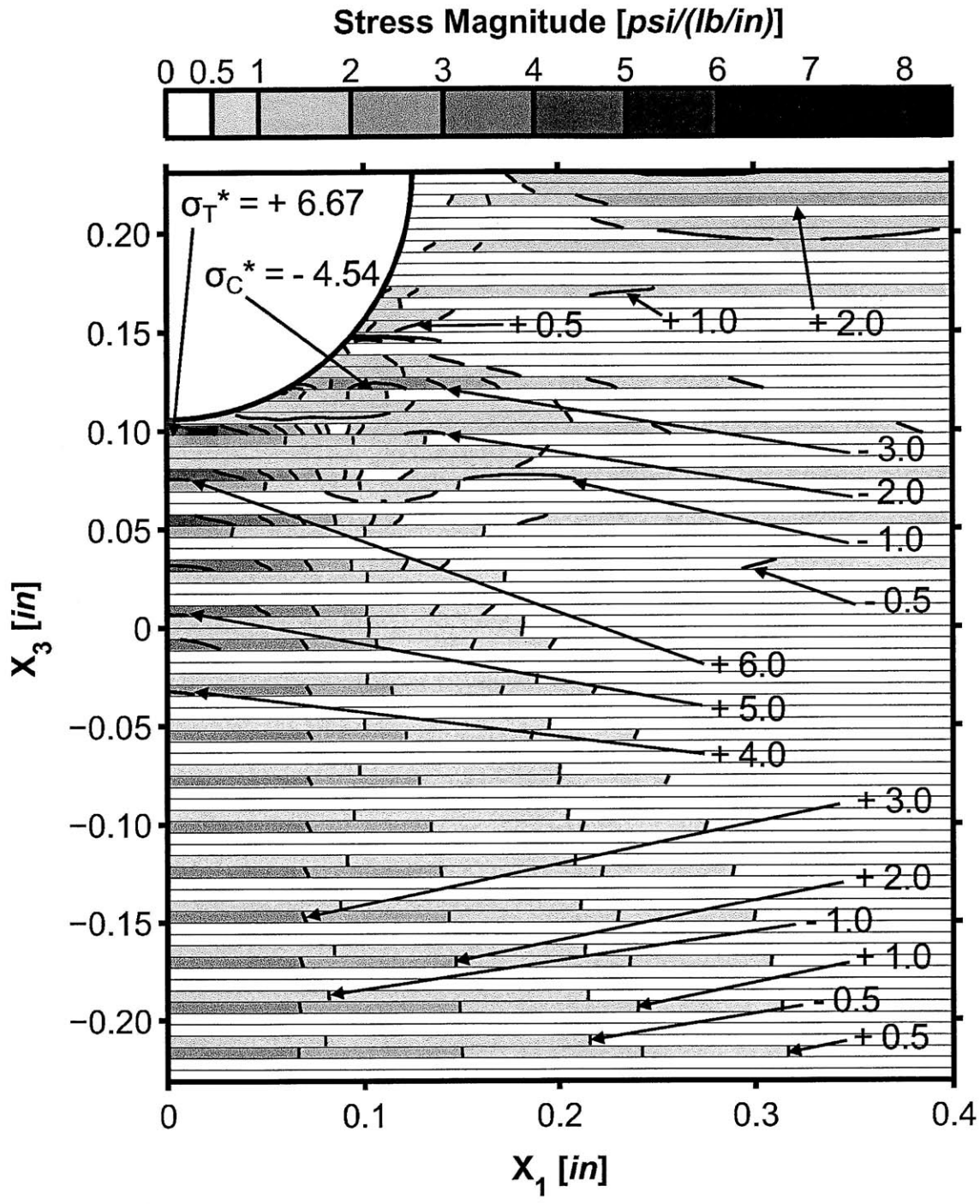

* Note: All stresses normalized by applied load, and given in units of [psi/(lb/in)].

Figure 5.35 Isostress plot of σ_{11}^{*} for the two-dimensional T700/2510 $[\pm 45/0/90]_{10S}$ finite element model with elastic indentor loaded at 5000 lb/in.

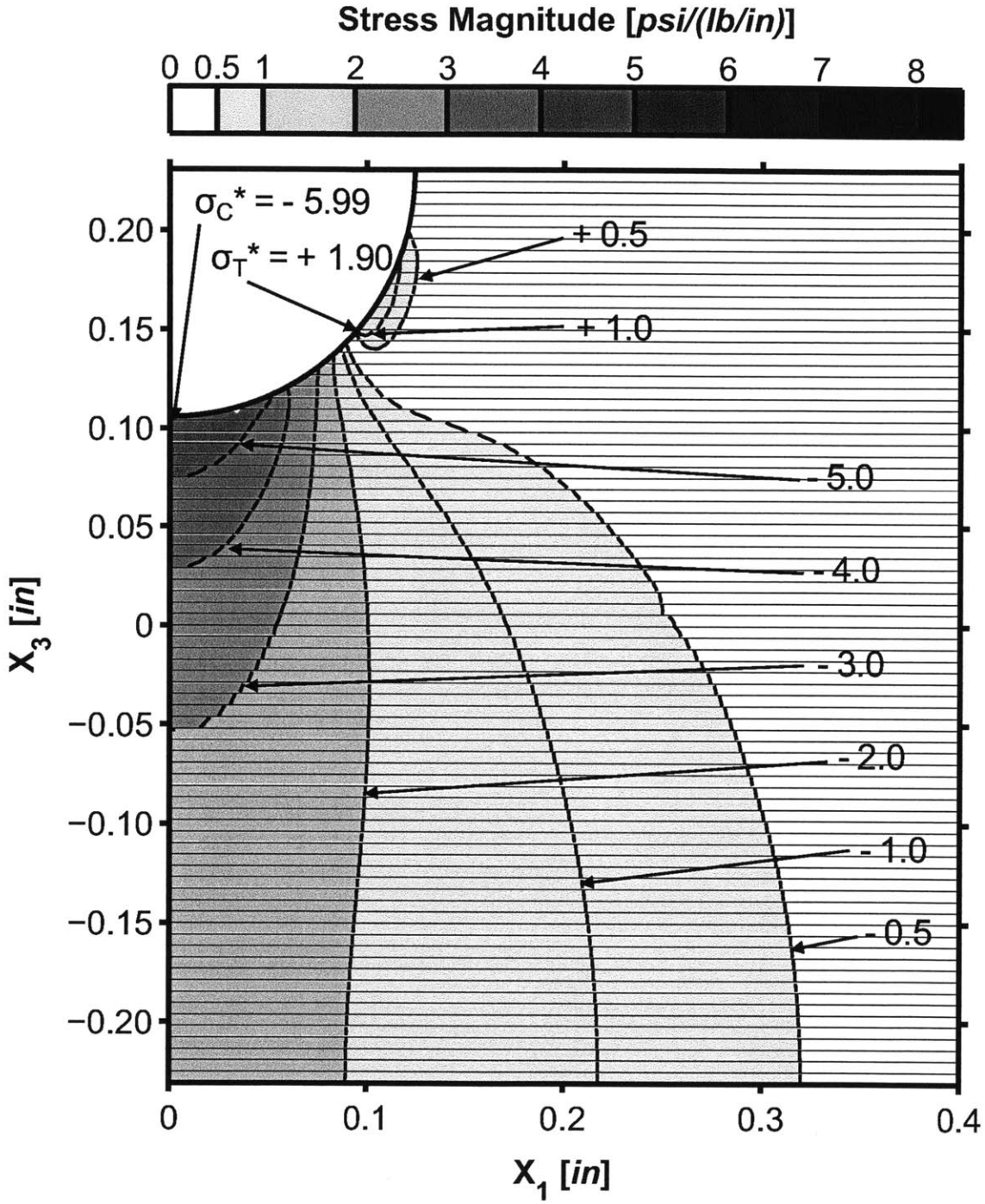

* Note: All stresses normalized by applied load, and given in units of [psi/(lb/in)].

Figure 5.36 Isostress plot of σ_{33}^{*} for the two-dimensional T700/2510 $[\pm 45/0/90]_{10S}$ finite element model with elastic indentor loaded at 5000 lb/in.

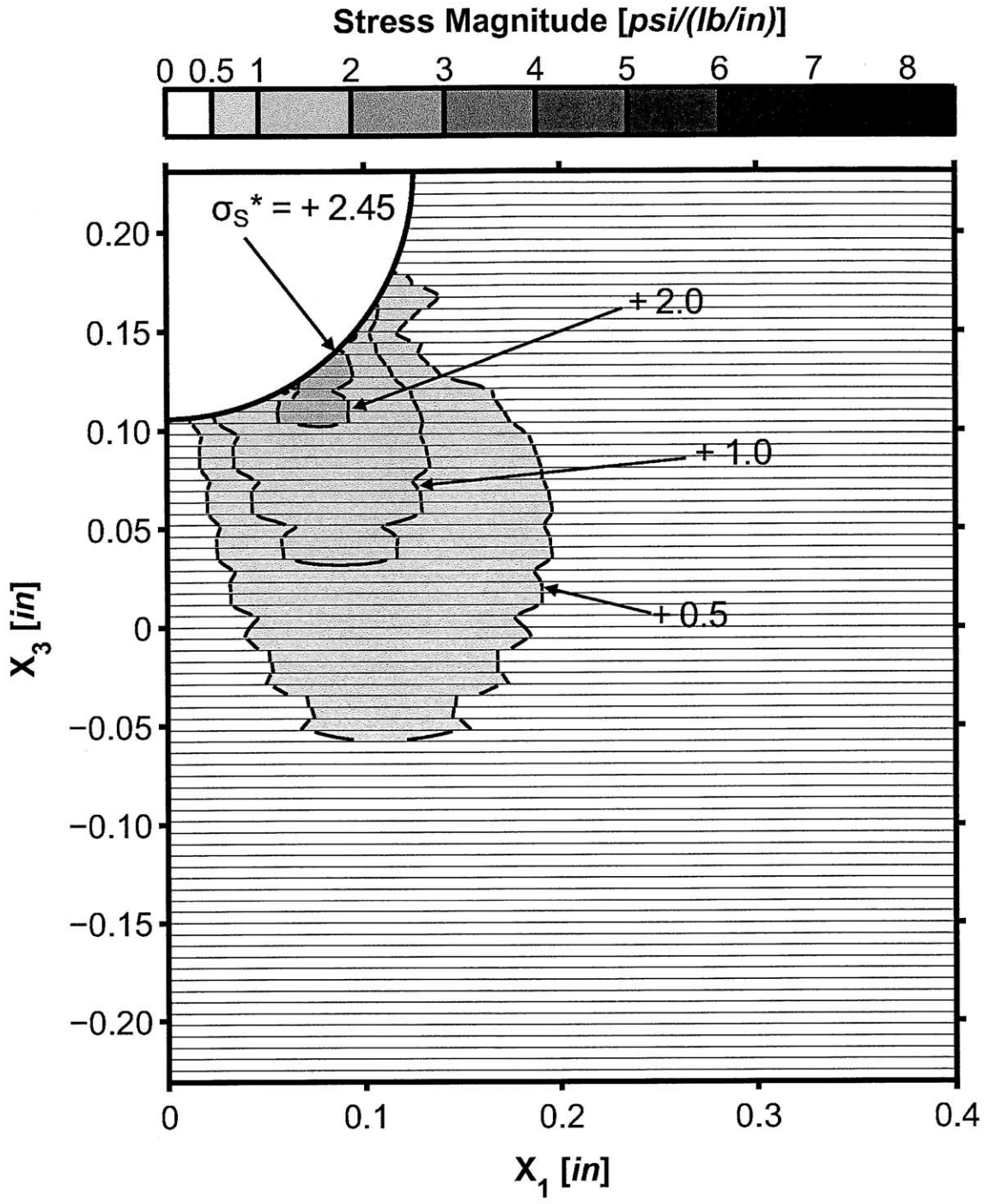

* Note: All stresses normalized by applied load, and given in units of [psi/(lb/in)].

Figure 5.37 Isostress plot of σ^*_{13} for the two-dimensional T700/2510 $[\pm 45/0/90]_{10S}$ finite element model with elastic indentor loaded at 5000 lb/in.

laminates are composed of the T700/2510 material.

5.3.1 Contact Pressure

Loading of the grooved laminate configuration is applied via load on a spherical rigid body indentor. This indentor then contacts and transfers load to the laminate. The distribution of the pressure exerted by the indentor on the laminate is defined as the contact pressure distribution. Contact pressures are normalized by the total applied load. This is similar to the method used for the two-dimensional models, except that the load is in units of [lb] in this case, whereas the two-dimensional case requires loading units of [lb/in], since those models are infinite in the 2-direction. The primary maximum load under investigation in this loading scenario is 300 lbs, as discussed in Section 3.4. For these three-dimensional models, contact pressure results are presented in two formats. The first is a contour plot of the contact pressure distribution on the surface of the groove, with angle around the groove, ϕ, in degrees on the horizontal axis, and the x_2-coordinate in inches as the vertical axis. Contour lines run along points of equal pressure and are presented at intervals of 25 psi/lb. A contour for 0 psi/lb is also presented and represents the furthest extent of contact between the laminate and the indentor. The maximum normalized pressure is noted and its location is presented in the contour plots. The second format is a pressure plot versus angle around the groove, ϕ, with the angle on the horizontal axis, and the normalized contact pressure, p_C^*, on the vertical axis, similar to the contact pressure plots in the two-dimensional case. Cuts through the pressure distribution are presented for intervals of x_2 through the contact region. These cuts are shown for x_2 equal to 0.0, 0.005, 0.010, and 0.015 inches for all cases. This plotting format presents a more detailed picture of how the pressure distribution changes with ϕ, and allows direct comparison with the two-dimensional case. Ply boundaries are denoted in each plot type with dashed gray lines and associated ply angles are noted at the top of each figure. Both of these plotting formats are limited by the discretization of the laminate, as pressure can only be calculated at finite element nodes and interpolation between nodal values is linear.

The normalized contact pressure, p_C^*, contour plots for the $[\pm\theta/0]_{13S}$ laminates are presented in Figures 5.38, 5.40, 5.42, and 5.44 for θ equal to 15°, 30°, 45°, and 60°, respectively. The other presentation of the normalized contact pressure at constant values of x_2 is given in Figures 5.39, 5.41, 5.43, and 5.45 for θ equal to 15°, 30°, 45°, and 60°, respectively. The contour plot of the normalized contact pressure for the cross-ply $[90/0]_{20S}$ laminate is shown in Figure 5.46, and the other presentation showing the pressure at constant values of x_2 is presented in Figure 5.47. The contour plot of the normalized contact pressure for the quasi-isotropic $[\pm 45/0/90]_{10S}$ laminate is given in Figure 5.48, and an alternate view showing pressure at constant values of x_2 is presented in Figure 5.49. The maximum contact pressure for each laminate, along with its location, is presented in Table 5.5.

The contact pressure distributions in the three-dimensional case generally form an elliptical footprint in the presented contour figures. As with an ellipse, the shape and extent of the contact area in the contour plots is defined by the extent of the semi-major axis, a_C, and semi-minor axis, b_C, as indicated by the most extreme point of contact along the ϕ-axis and x_2-axis, respectively. Note that although ϕ, and hence a_C, is an angle with units of degrees, it is treated as a "contact length" to the extent that an ellipse could be mathematically formulated using this variable to fit the contour plots presented on the ϕ-x_2 axes. Also note that a_C can be converted to an actual contact arc length, L_C, that measures the length of contact around the curve of the groove in the 1-3 plane in inches, with r_g also in inches, through the equation:

$$L_C = r_g * a_C * \frac{\pi}{180} \tag{5.3}$$

where r_g is the radius of the groove. However, it is more convenient and intuitive to speak of the contact length as the angle around the groove, ϕ, to which contact is maintained, also defined as $\phi_{contact}$. The contact area for all laminates studied is similar, with all laminates having a semi-major axis, a_C, of approximately 54°, and a semi-minor axis, b_C, of 0.017 inches. These contact area parameters for each laminate are detailed in Table 5.5.

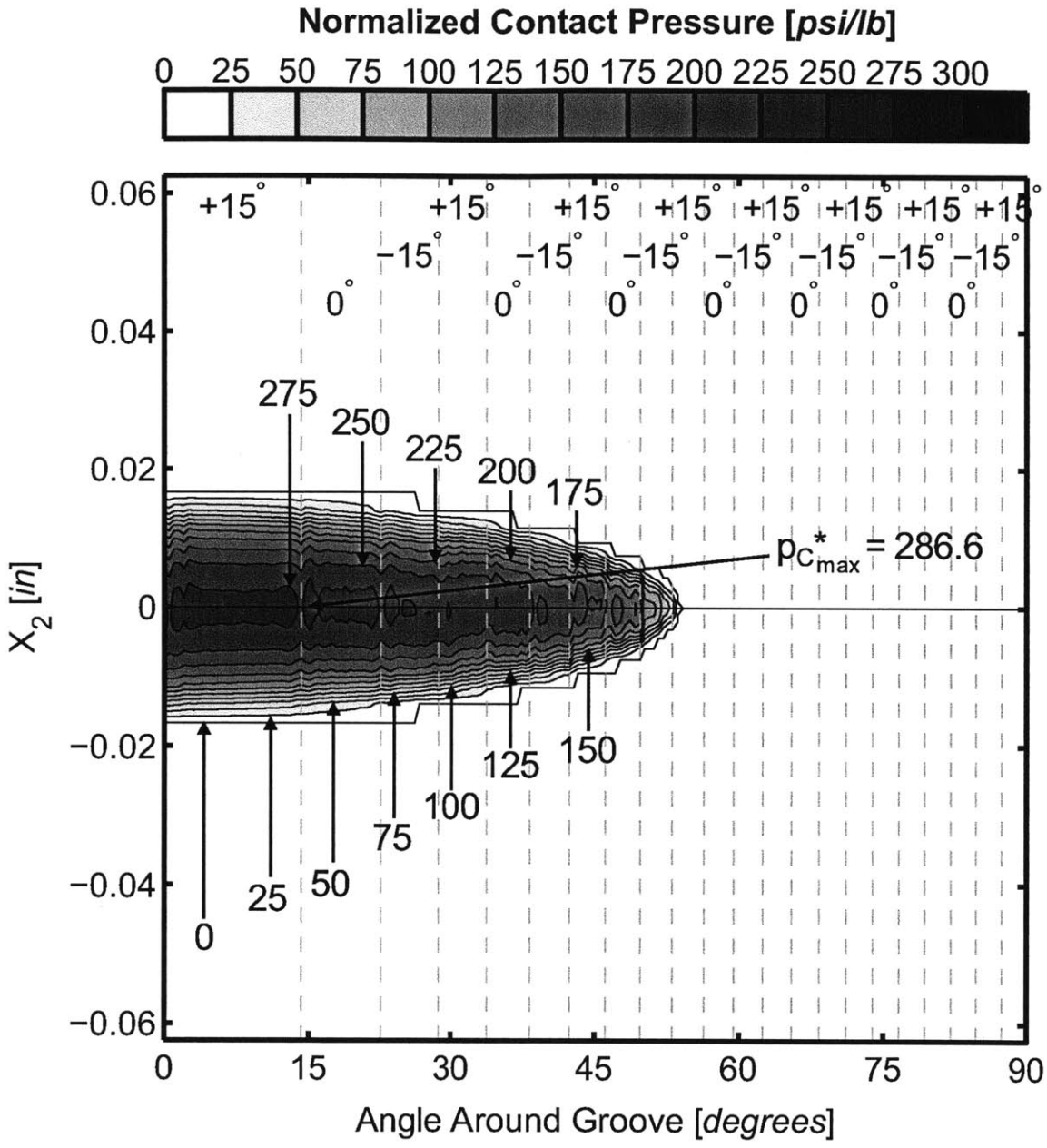

* Note: All pressures normalized by applied load, and given in units of [psi/lb].

Figure 5.38 Normalized contact pressure contour plots for the three-dimensional T700/2510 $[\pm 15/0]_{13S}$ laminate model loaded at 300 lb.

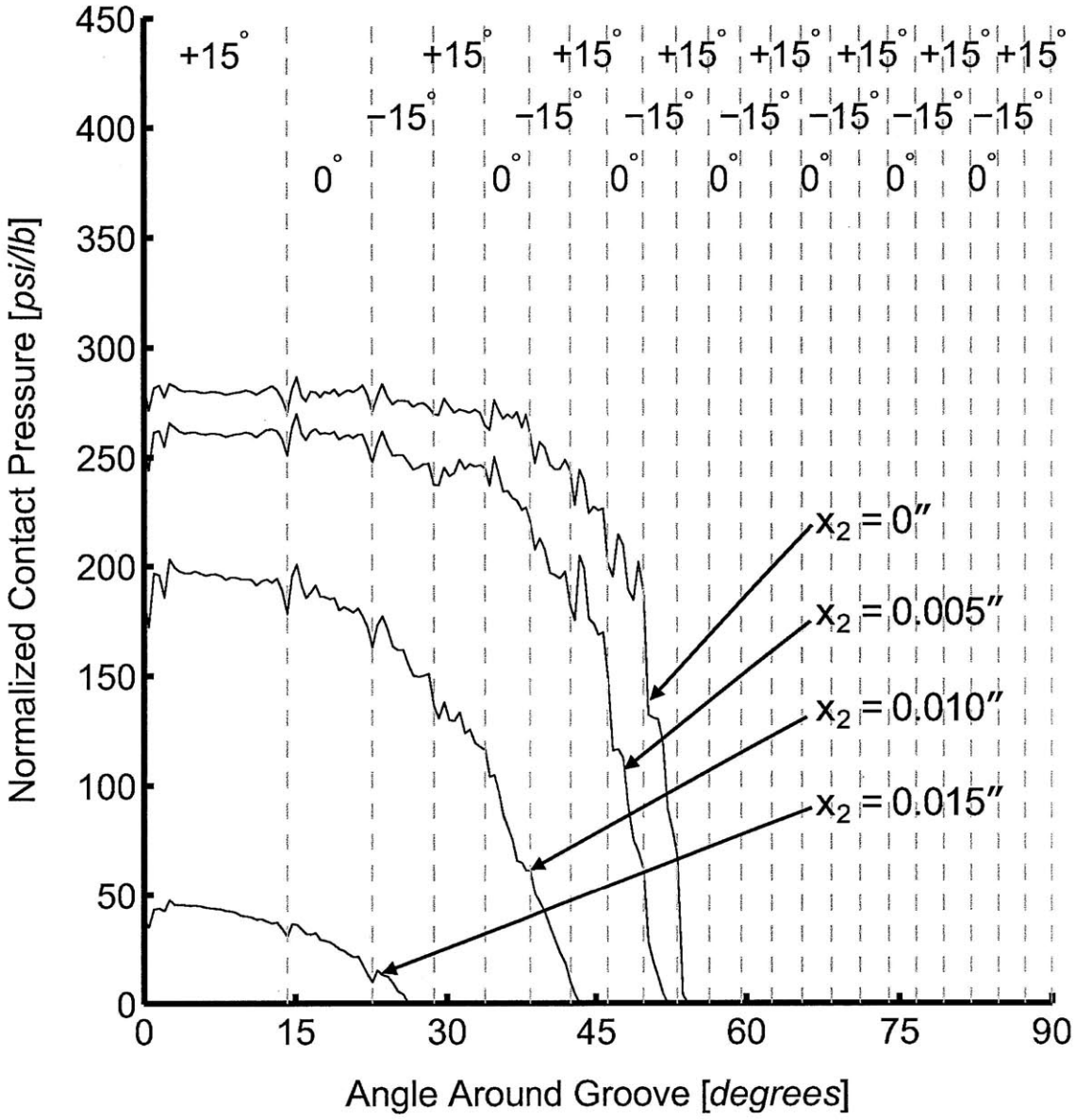

* Note: All pressures normalized by applied load, and given in units of [psi/lb].

Figure 5.39 Normalized contact pressure plots at given values of x_2 for the three-dimensional T700/2510 $[\pm 15/0]_{13S}$ laminate model loaded at 300 lb.

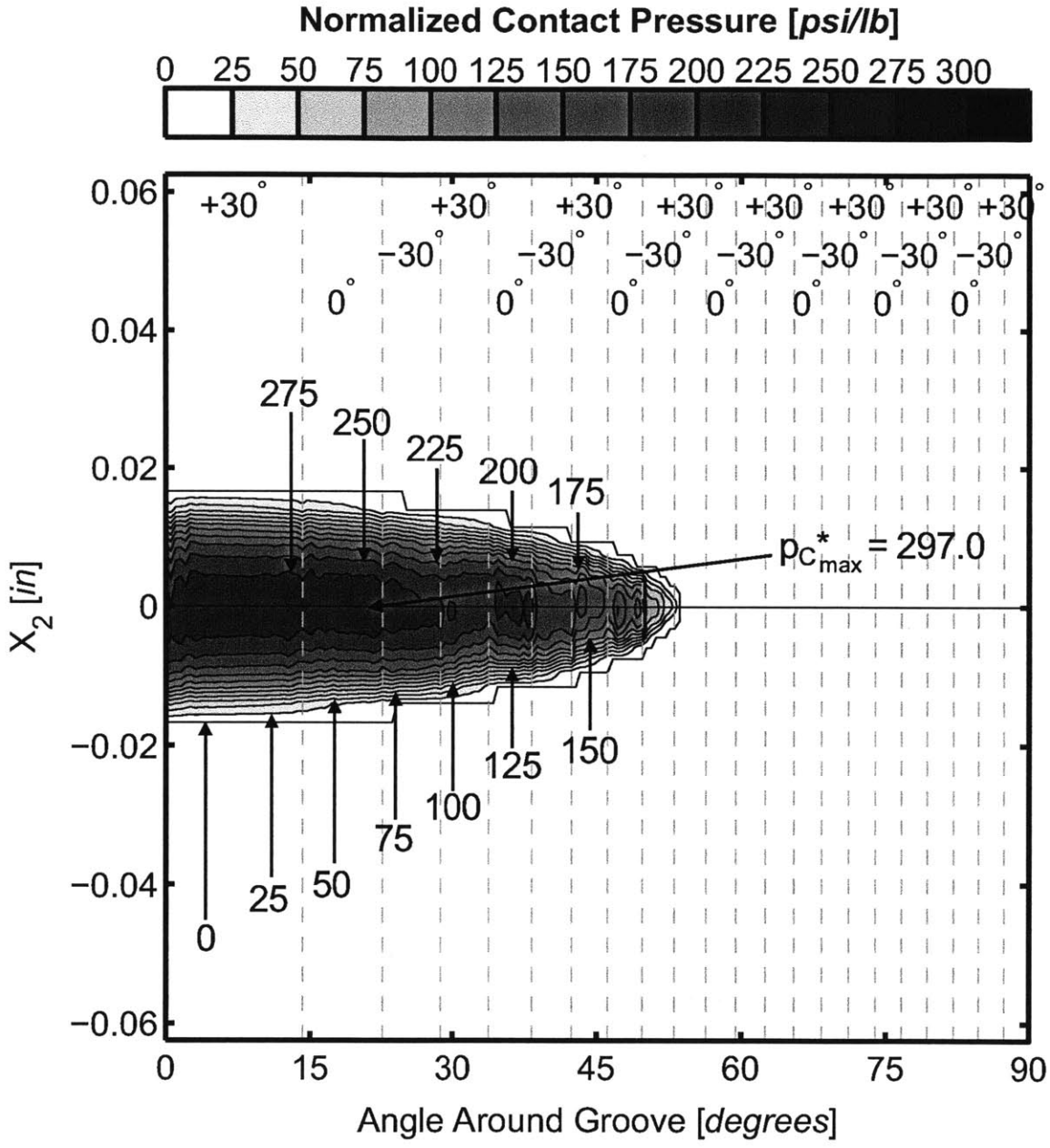

* Note: All pressures normalized by applied load, and given in units of [psi/lb].

Figure 5.40 Normalized contact pressure contour plots for the three-dimensional T700/2510 $[\pm 30/0]_{13S}$ laminate model loaded at 300 lb.

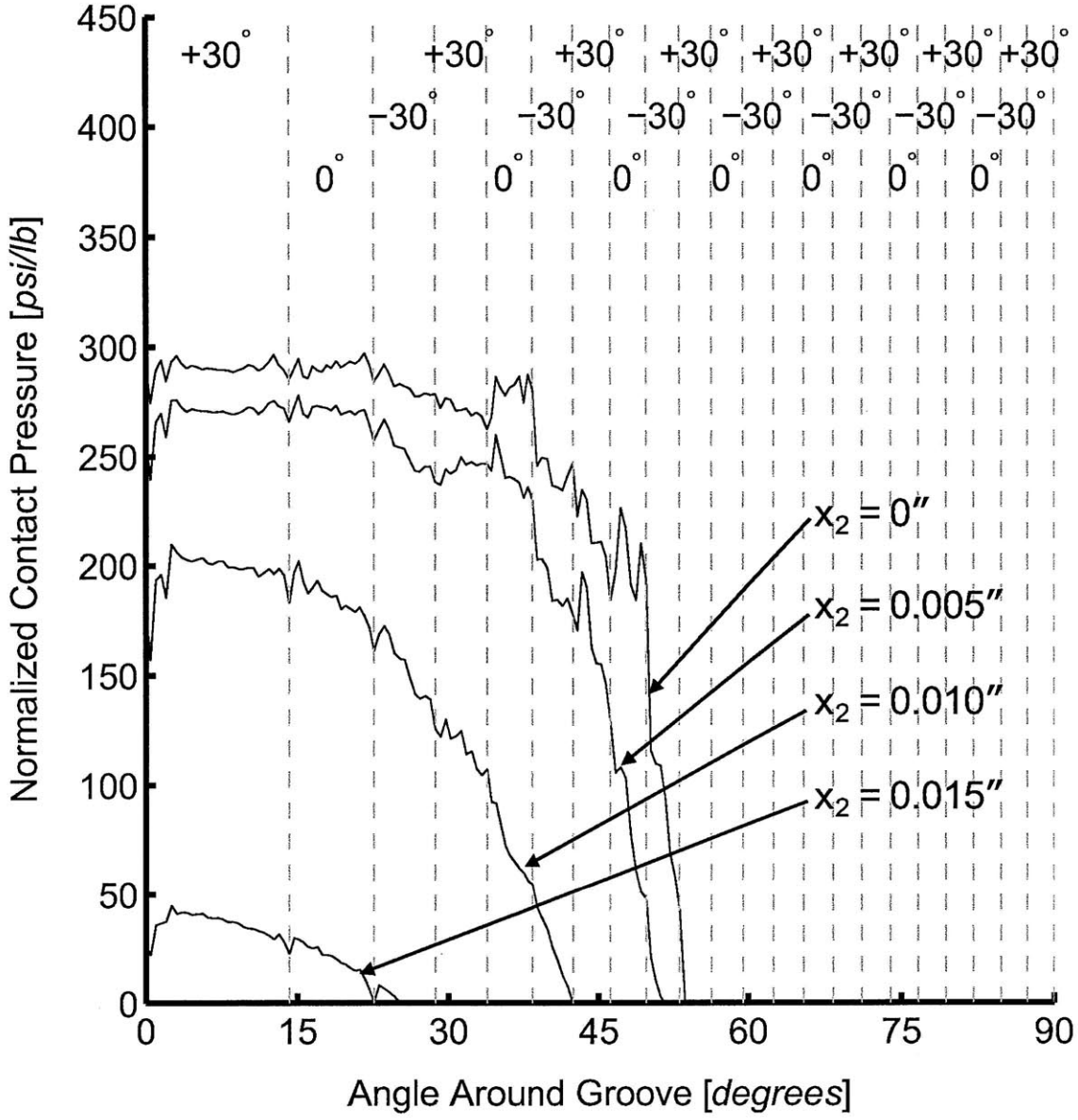

* Note: All pressures normalized by applied load, and given in units of [psi/lb].

Figure 5.41 Normalized contact pressure plots at given values of x_2 for the three-dimensional T700/2510 $[\pm 30/0]_{13S}$ laminate model loaded at 300 lb.

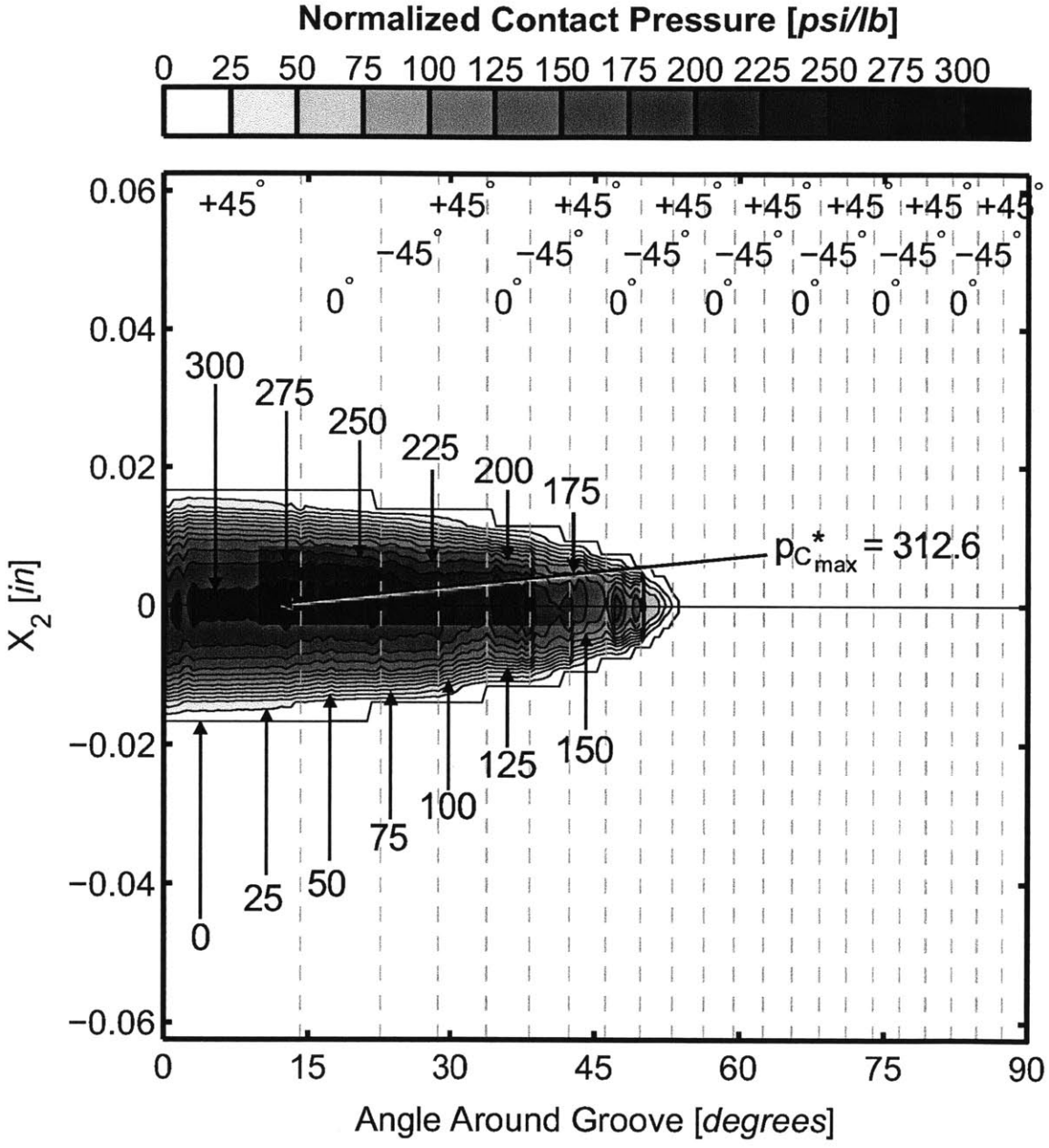

* Note: All pressures normalized by applied load, and given in units of [psi/lb].

Figure 5.42 Normalized contact pressure contour plots for the three-dimensional T700/2510 $[\pm 45/0]_{13S}$ laminate model loaded at 300 lb.

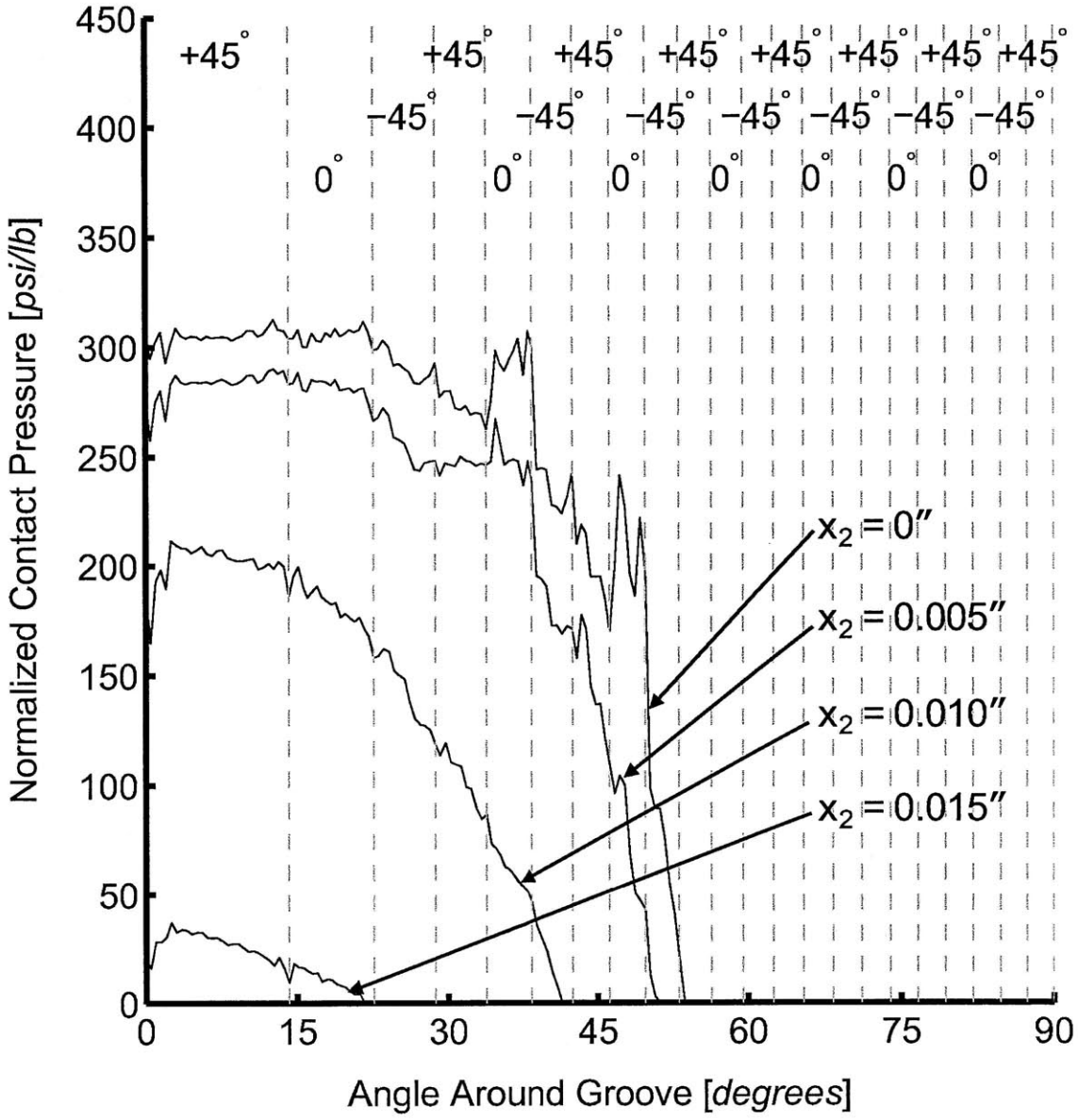

* Note: All pressures normalized by applied load, and given in units of [psi/lb].

Figure 5.43 Normalized contact pressure plots at given values of x_2 for the three-dimensional T700/2510 $[\pm 45/0]_{13S}$ laminate model loaded at 300 lb.

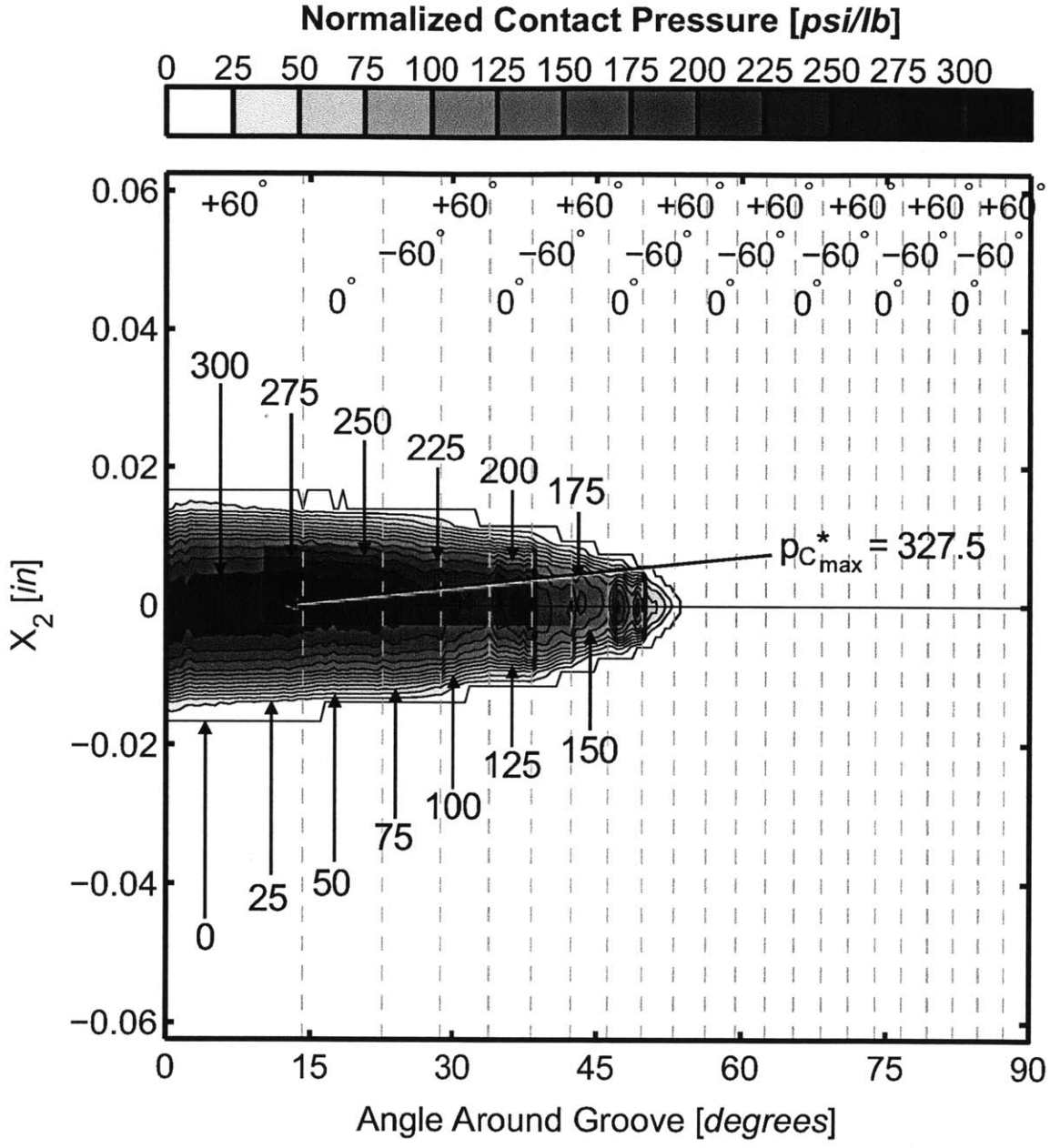

* Note: All pressures normalized by applied load, and given in units of [psi/lb].

Figure 5.44 Normalized contact pressure contour plots for the three-dimensional T700/2510 $[\pm 60/0]_{13S}$ laminate model loaded at 300 lb.

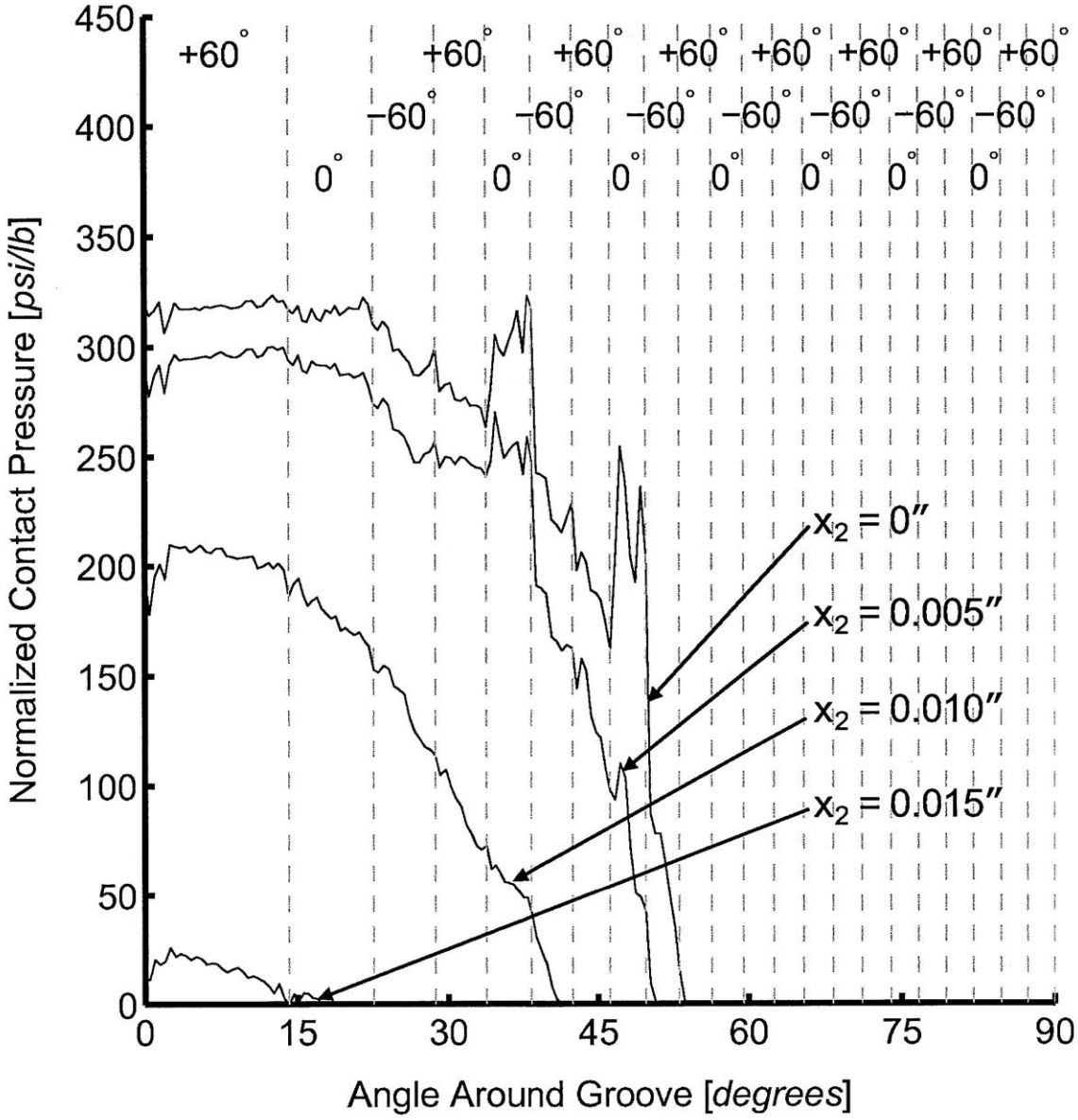

* Note: All pressures normalized by applied load, and given in units of [psi/lb].

Figure 5.45 Normalized contact pressure plots at given values of x_2 for the three-dimensional T700/2510 $[\pm 60/0]_{13S}$ laminate model loaded at 300 lb.

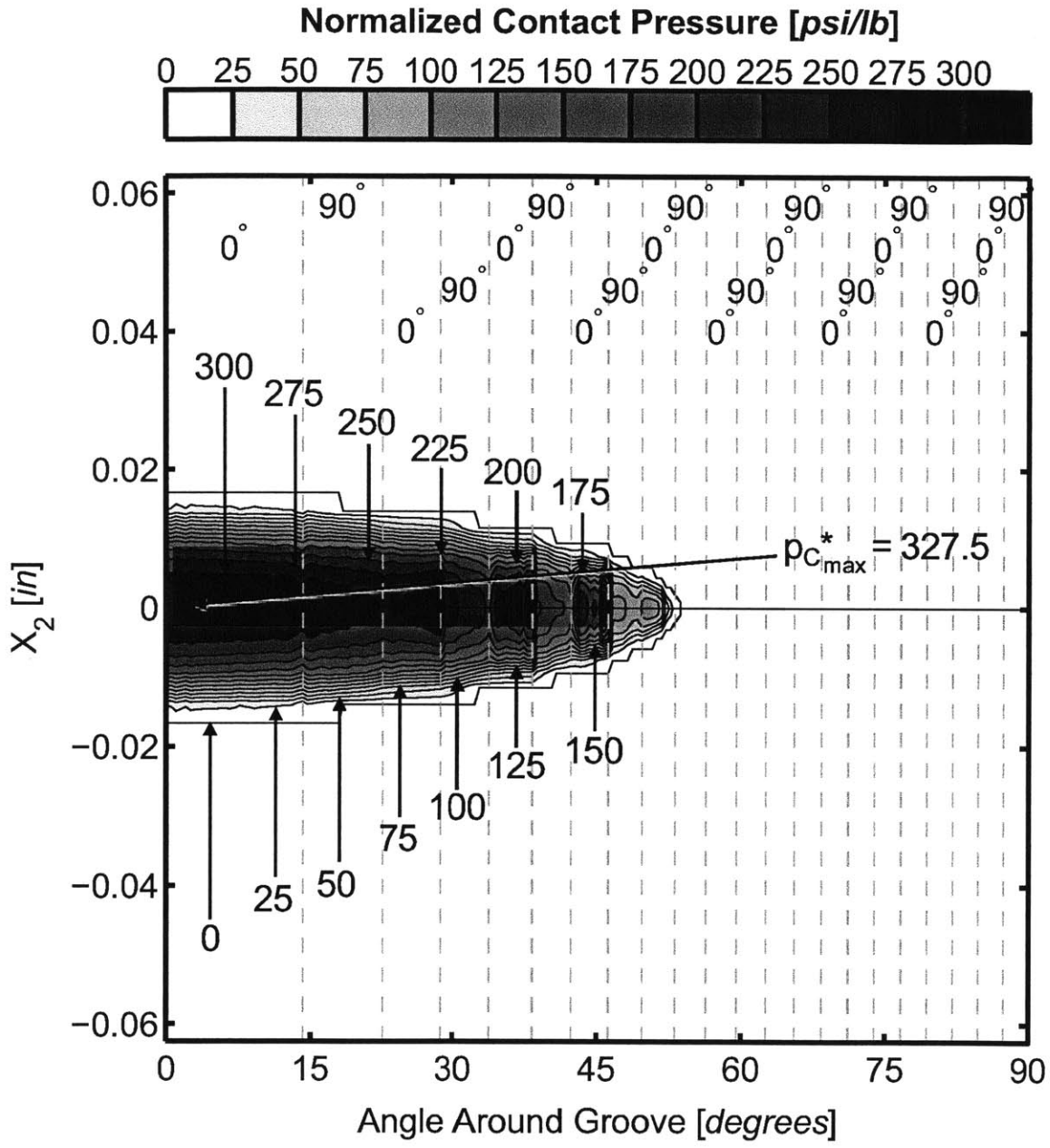

* Note: All pressures normalized by applied load, and given in units of [psi/lb].

Figure 5.46 Normalized contact pressure contour plots for the three-dimensional T700/2510 $[90/0]_{20S}$ laminate model loaded at 300 lb.

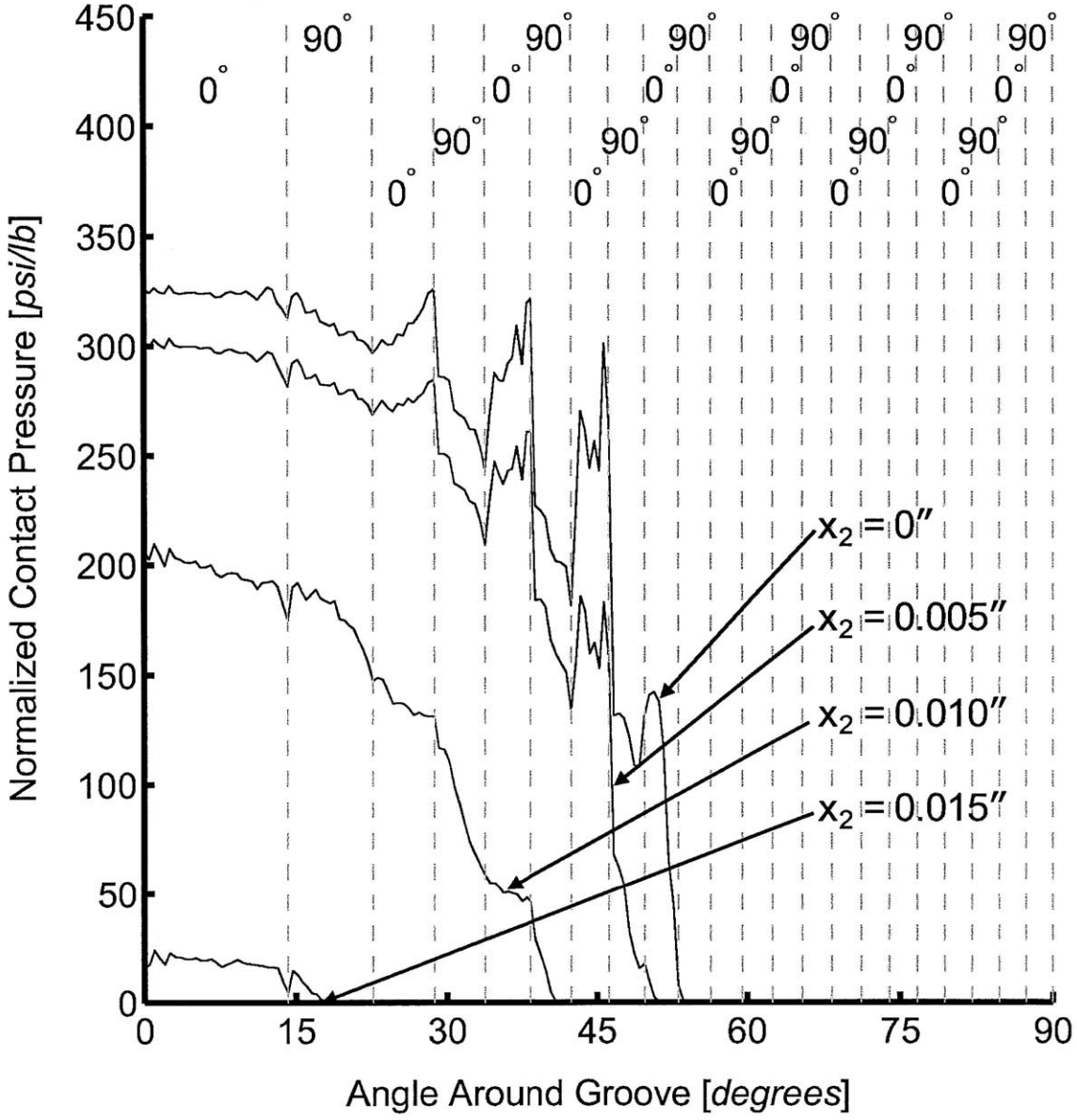

* Note: All pressures normalized by applied load, and given in units of [psi/lb].

Figure 5.47 Normalized contact pressure plots at given values of x_2 for the three-dimensional T700/2510 $[90/0]_{20S}$ laminate model loaded at 300 lb.

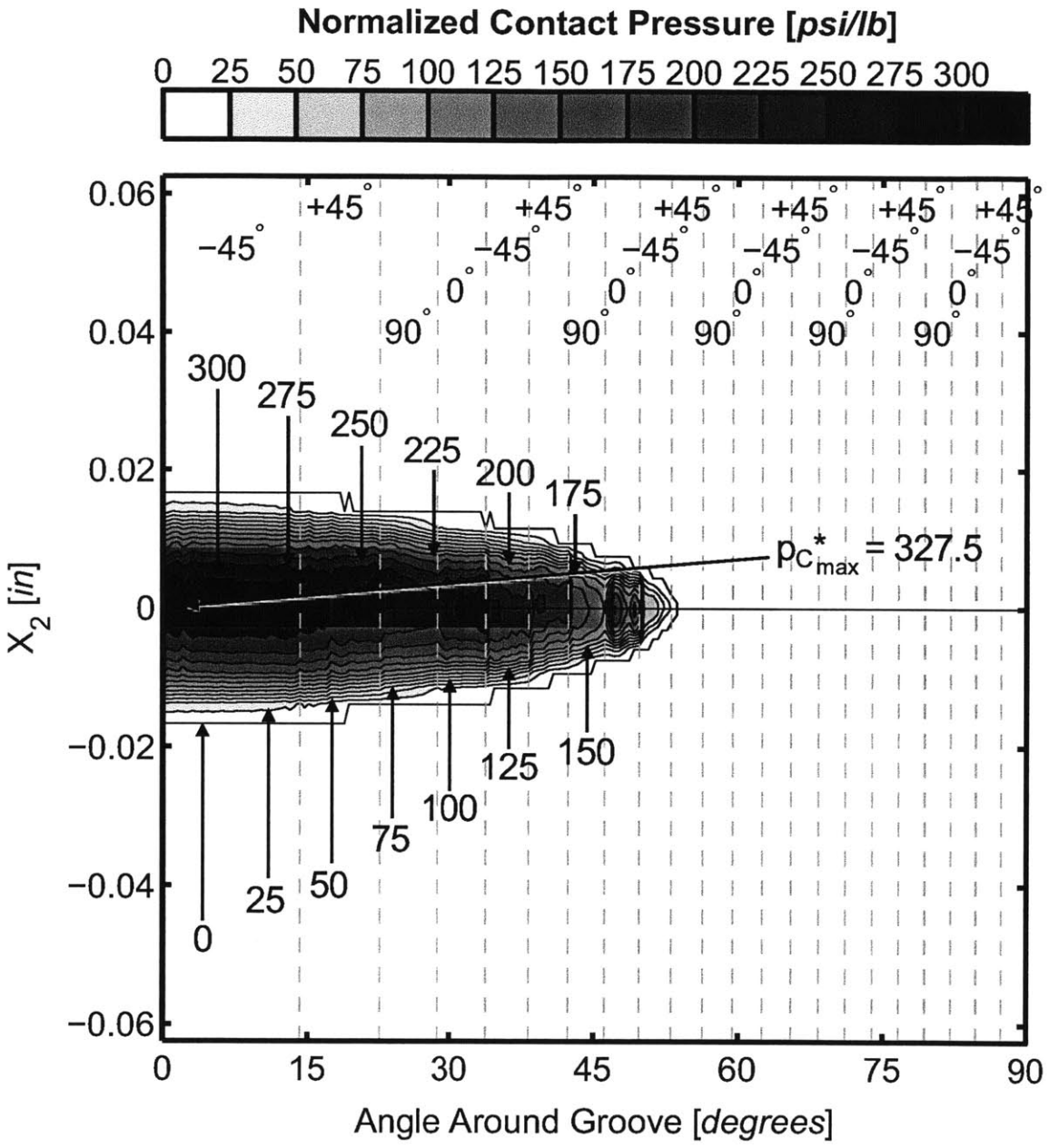

* Note: All pressures normalized by applied load, and given in units of [psi/lb].

Figure 5.48 Normalized contact pressure contour plots for the three-dimensional T700/2510 $[\pm 45/0/90]_{10S}$ laminate model loaded at 300 lb.

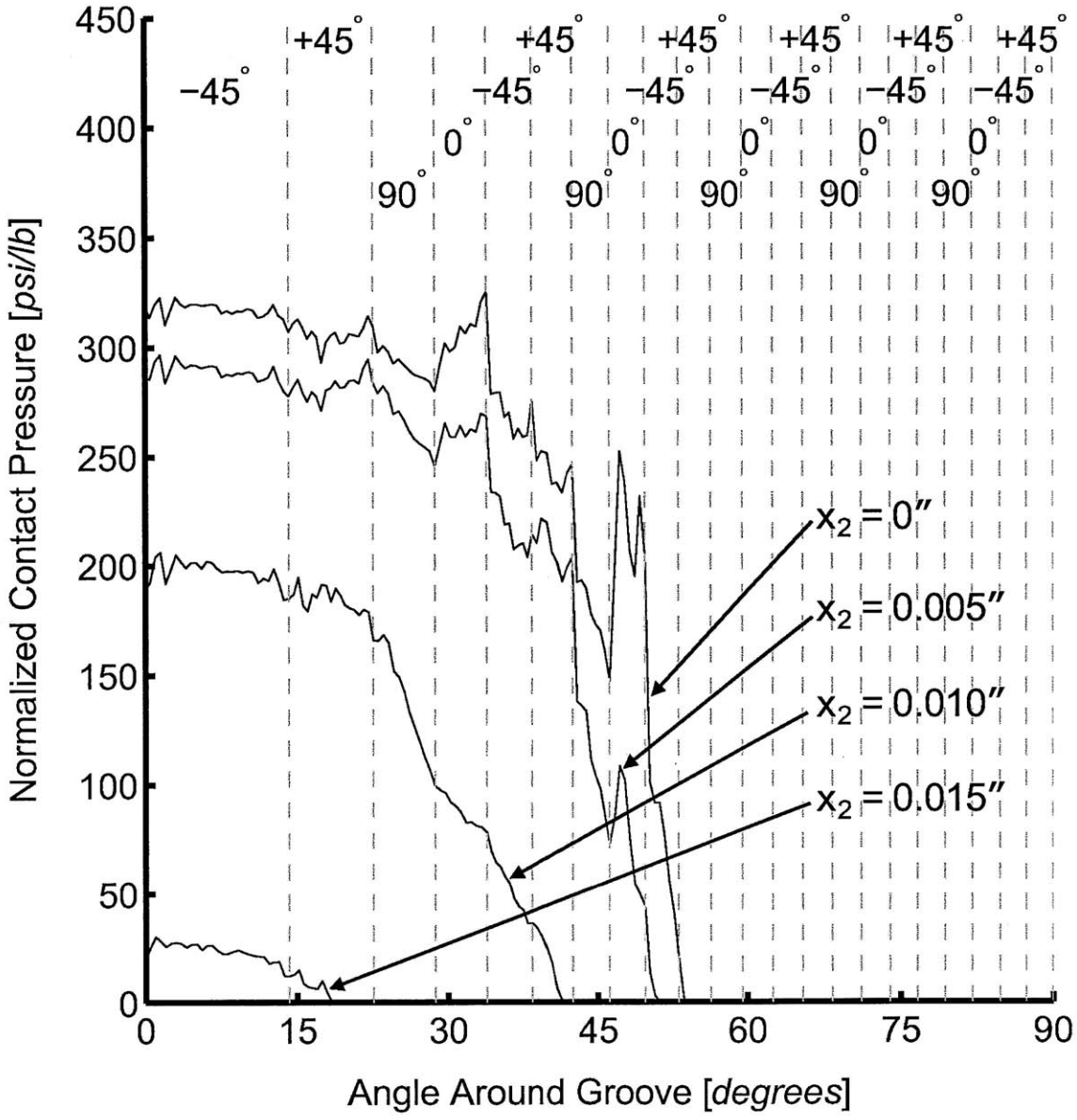

* Note: All pressures normalized by applied load, and given in units of [psi/lb].

Figure 5.49 Normalized contact pressure plots at given values of x_2 for the three-dimensional T700/2510 $[\pm 45/0/90]_{10S}$ laminate model loaded at 300 lb.

Table 5.5 Maximum normalized contact pressure, $p^*_{C_{max}}$, and its location and extent via defined elliptical parameters, a_C and b_C, for three-dimensional models loaded at 300 lb

Laminate		**Contact Pressure**				
Material	Layup	$p^*_{C_{max}}$ $[psi/lb]$	ϕ_P $[deg]$	x_{2_P} $[in]$	a_C $[deg]$	b_C $[in]$
T700/2510	$[\pm 15/0]_{13S}$	287	15.2	0.0	54.2	0.017
T700/2510	$[\pm 30/0]_{13S}$	297	21.7	0.0	53.7	0.017
T700/2510	$[\pm 45/0]_{13S}$	313	12.7	0.0	53.7	0.017
T700/2510	$[\pm 60/0]_{13S}$	324	12.7	0.0	53.7	0.017
T700/2510	$[90/0]_{20S}$	328	2.5	0.0	53.7	0.017
T700/2510	$[\pm 45/0/90]_{10S}$	325	33.8	0.0	53.7	0.017

In addition to a similar contact area shape, all laminates studied share other behavior characteristics. Generally, the change of pressure between plies is related to the difference in ply angle between those plies. For example, pressure increases in 0° plies and decreases in 90° plies. In addition, the change in pressure from one ply to a neighboring ply can be a sharp, discontinuous change, in contrast to the behavior seen in the two-dimensional case, where pressure changes between plies are comparatively smooth. This can best be seen by contrasting the behavior of the $[\pm 45/0/90]_{10S}$ laminate in the two-dimensional case, shown in Figure 5.6, to the three-dimensional case, shown in Figure 5.49. However, as with the two-dimensional case, the magnitude of the pressure change is dependent on the difference in angle between the two plies, and the ϕ-coordinate, with higher pressure changes coming from greater angle differences, and at greater values of ϕ. These effects can compound for a high difference in ply angle at a high value of ϕ yielding an even greater difference in contact pressure between the plies. Finally, all results share a degree of node-to-node variation and jaggedness apparent in the plots, most likely due to discretization of the laminate, and the numerical contact model used. These jagged variations are typically on the order of 4% of the local contact pressure in magnitude, but can be as high as 8%, and span between 1° to 2° on the face of the groove, or 0.002 to 0.004 inches of arc length (2 to 4 elements). Particularly within a ply, there are no geometric features to suggest that the contact pressure distribution should be anything but smooth. In contrast, contact pressure between dissimilar plies could be expected to be discontinuous at the interface due to the material change at the ply boundary, and the modeling of such as an abrupt change.

Of note, in the three-dimensional case, some asymmetries are apparent in the contact pressure distributions for any laminate with angled plies. The crossply $[90/0]_{20S}$ laminate is the only laminate to show no asymmetries about the x_1-axis or ϕ-axis. The asymmetry across the x_1-axis is most pronounced in angled plies, appears in the contact pressure contour plots as a lateral shift in the pressure contours biased toward the angle direction. For example, $+45°$ plies tend to have greater pressure at positive values of x_2, whereas $-45°$ plies tend to have greater pressure at negative values of x_2.

These pressure distributions also become more asymmetric in these angled plies as the angle around the groove, ϕ, increases. The degree of asymmetry is shown in Figure 5.50 by plotting the contact pressure along a constant value of ϕ, showing variation in pressure in the 2-direction, and overlaying the pressures for positive values of x_2 and negative values of x_2. This comparison is presented for two different +45° plies in the $[\pm 45/0/90]_{10S}$ laminate, at values of ϕ of 21.2° and 42.4°. In this example, the maximum variation due to asymmetry at the value of ϕ of 21.2° is 7.6%, and at the value of ϕ of 42.4°, the maximum variation due to asymmetry is 16.6%. Values for other laminates are similar, and vary depending on the ply angle and the groove angle, as discussed. These variations are small, but not insignificant. These trends indicate the cause of the asymmetry is the presence of coefficients of mutual influence in angled plies, by which extensional strains cause shear strains, and the lack of this behavior in the $[90/0]_{20S}$ laminate supports this assertion.

Some further trends are apparent in examining the $[\pm\theta/0]_{13S}$ laminates. For all of these laminates, the contact area remains similar, and the semi-major and semi-minor axes of the elliptical area do not change appreciably. However, there is a noticeable increase in pressure near the center of contact, and a decrease in pressure near the periphery of the contact area, as the value of θ increases. This is noticeable on the contour plots in the narrowing of the contact area in x_2 from ϕ equal to 15° to 45°. It can also be seen in the decrease in the contact pressure curve at x_2 equal to 0.015 inches as θ increases. A similar decrease is notable in the pressure curve for x_2 equal to 0.01 inches at higher values of ϕ. The increase in pressure toward the center of contact is evident for lower values of ϕ in the pressure curves for x_2 equal to 0.0 and 0.005 inches.

The cross-ply $[90/0]_{20S}$ laminate shows the same trends found for the other laminates as presented. The results align particularly well with the $[\pm\theta/0]_{13S}$ laminates with high values of θ, and generally represent an extension of that trend. However, it is notable as being the only contact pressure distribution which is symmetric about the x_1-axis or ϕ-axis. It also has a high maximum contact pressure, comparable with the $[\pm 60/0]_{13S}$ and quasi-isotropic laminates. The quasi-isotropic laminate generally

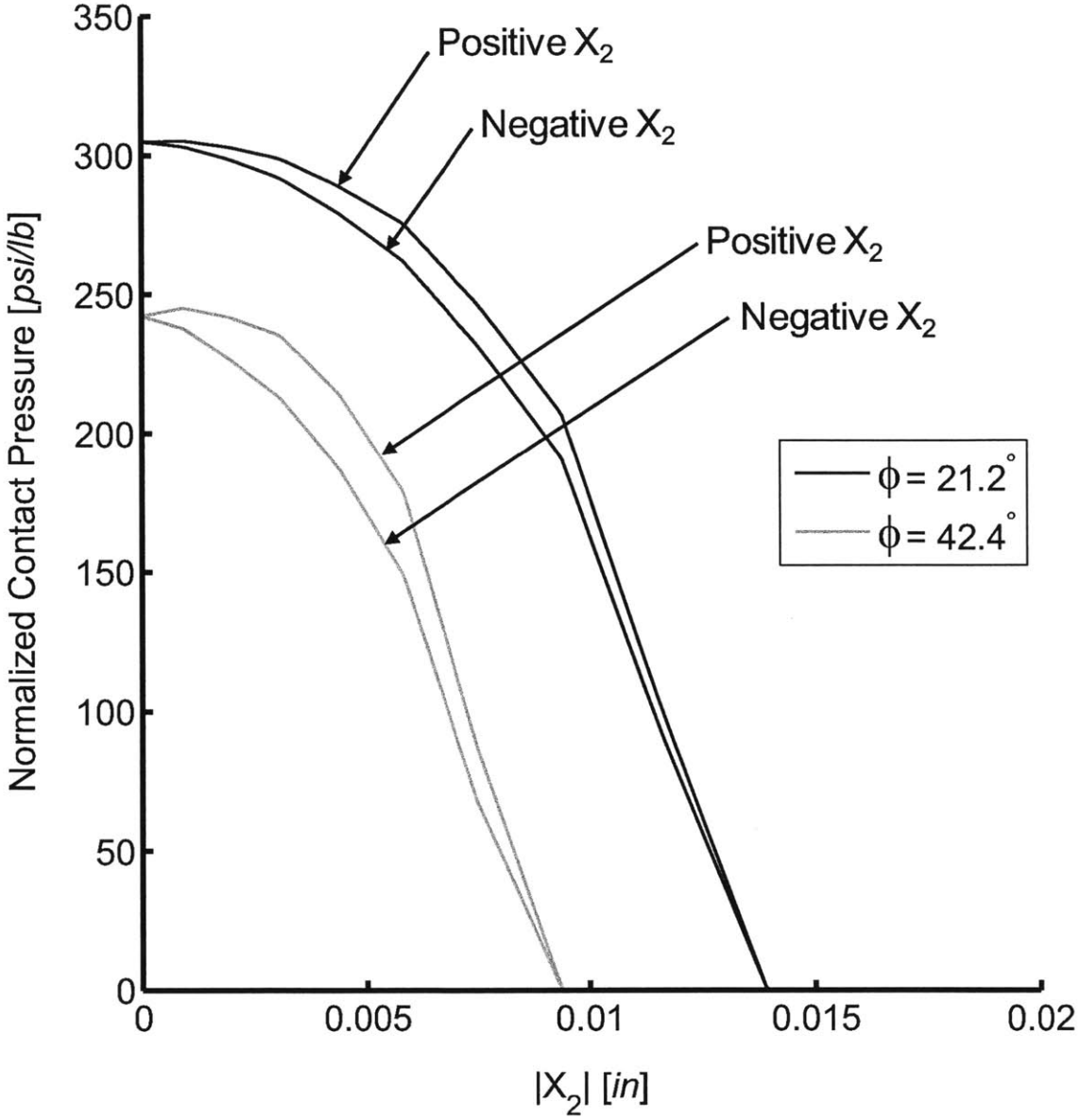

* Note: All pressures normalized by applied load, and given in units of [psi/lb].

Figure 5.50 Normalized contact pressure asymmetry versus distance, x_2, in two $+45°$ plies at values of ϕ of 21.2° and 42.4° for the three-dimensional T700/2510 $[\pm 45/0/90]_{10S}$ laminate model loaded at 300 lb.

amalgamates characteristics from each of the laminates studied, carrying aspects of the $[\pm\theta/0]_{13S}$ laminate in the behavior of the angled $\pm 45°$ plies and some aspects of the $[90/0]_{20S}$ laminate in the behavior of the 0° and 90° plies. The maximum contact pressure here is high, similar to the $[\pm 60/0]_{13S}$ and cross-ply laminates.

5.3.2 Stress Response

The stress response of the laminate for the three-dimensional case is shown using isostress plots of section cuts through the laminate to best show the extent of various stress fields. The locations of these section cuts depends on the stress field under investigation. A section cut through a constant value of x_1 of 0, while valuable in theory, is not used due to the effect of interference from the plane of symmetry detailed in Section 3.4. Due to the concentration of stresses in the region local to the groove, the isostress plots show restricted views of the laminate instead of the full laminate width and length in order to maximize visibility of the isostress lines. The x_1-section cuts show the full height of the laminate, but restrict the visible range in x_2 from -0.2 to $+0.2$ inches. The x_2-section cuts show the full height of the laminate, but restrict the visible range in x_1 from 0.0 to $+0.4$ inches. Stresses are normalized by the applied load, in this case 300 lb, and are presented in units of [psi/lb]. Isostress lines connect points of equal stress at values of ± 5, ± 10, and ± 20 psi/lb, and at higher stress magnitudes at intervals of ± 20 psi/lb up to stress values of ± 180 psi/lb.

Isostress plots for the normalized extensional longitudinal stress, σ_{11}^*, for the T700/2510 $[\pm 15/0]_{13S}$ laminate are shown in Figures 5.51 and 5.52 for the x_1-section cuts at 0.05, and 0.10 inches, respectively. Perpendicular section cuts are shown in Figures 5.53 and 5.54 for values of x_2 of 0.0 and 0.02 inches, respectively. Isostress plots for σ_{11}^* for the T700/2510 $[\pm 30/0]_{13S}$ laminate are shown in Figures 5.55 and 5.56 for the x_1-section cuts at 0.05, and 0.10 inches, respectively. Perpendicular section cuts are shown in Figures 5.57 and 5.58 for values of x_2 of 0.0 and 0.02 inches, respectively. Isostress plots for σ_{11}^* for the T700/2510 $[\pm 45/0]_{13S}$ are shown in Figures 5.59 and 5.60 for the x_1-section cuts at 0.05, and 0.10 inches, respectively. Perpendicular section cuts are shown in Figures 5.61 and 5.62 for values of x_2 of 0.0 and 0.02 inches,

respectively. Isostress plots for σ_{11}^* for the T700/2510 $[\pm 60/0]_{13S}$ laminate are shown in Figures 5.63 and 5.64 for the x_1-section cuts at 0.05, and 0.10 inches, respectively. Perpendicular section cuts are shown in Figures 5.65 and 5.66 for values of x_2 of 0.0 and 0.02 inches, respectively. The isostress plots for σ_{11}^* for the cross-ply $[90/0]_{20S}$ T700/2510 laminate are shown in Figures 5.67 and 5.68 for the x_1-section cuts at 0.05, and 0.10 inches, respectively. Perpendicular section cuts are shown in Figures 5.69 and 5.70 for values of x_2 of 0.0 and 0.02 inches, respectively. The isostress plots for σ_{11}^* for the quasi-isotropic $[\pm 45/0/90]_{10S}$ T700/2510 laminate are shown in Figures 5.71 and 5.72 for the x_1-section cuts at 0.05, and 0.10 inches, respectively. Perpendicular section cuts are shown in Figures 5.73 and 5.74 for values of x_2 of 0.0 and 0.02 inches, respectively. The maximum tensile stresses, σ_T^*, and the respective locations for each laminate are given in Table 5.6. The maximum compressive stresses, σ_C^*, and the respective locations for each laminate are given in Table 5.7.

The response exhibited in the σ_{11}^* stress field is the most complex of the stress fields examined here. Stress magnitude as well as sign is highly dependent on location and ply angle. Neighboring plies of differing angle can frequently have similar stress magnitudes, but opposite signs. Stress within a ply can shift from tension to compression to tension again, all across small length scales. Behavior of plies of similar angle and location can also change from one laminate to another as the overall stress configuration changes with the overall structural stiffness. Despite these complexities, the laminates in the three-dimensional case share general characteristics with the two-dimensional case, so terminology adopted for the two-dimensional case is used here as well in an attempt to clarify the picture.

There are three primary zones of stress in the laminate, as previously shown in Figure 5.8. Moving counterclockwise around the groove from the bottom of the laminate, Zone 1 extends from the bottom of the groove to the bottom of the laminate and contains alternating plies and regions in tension and compression. Zone 2 extends diagonally from the groove wall into the body of the laminate and is primarily in compression. Zone 3 extends from the upper portion of the groove wall to the top face of the laminate and is primarily in tension. The maximum tensile stresses, σ_T^*, occur

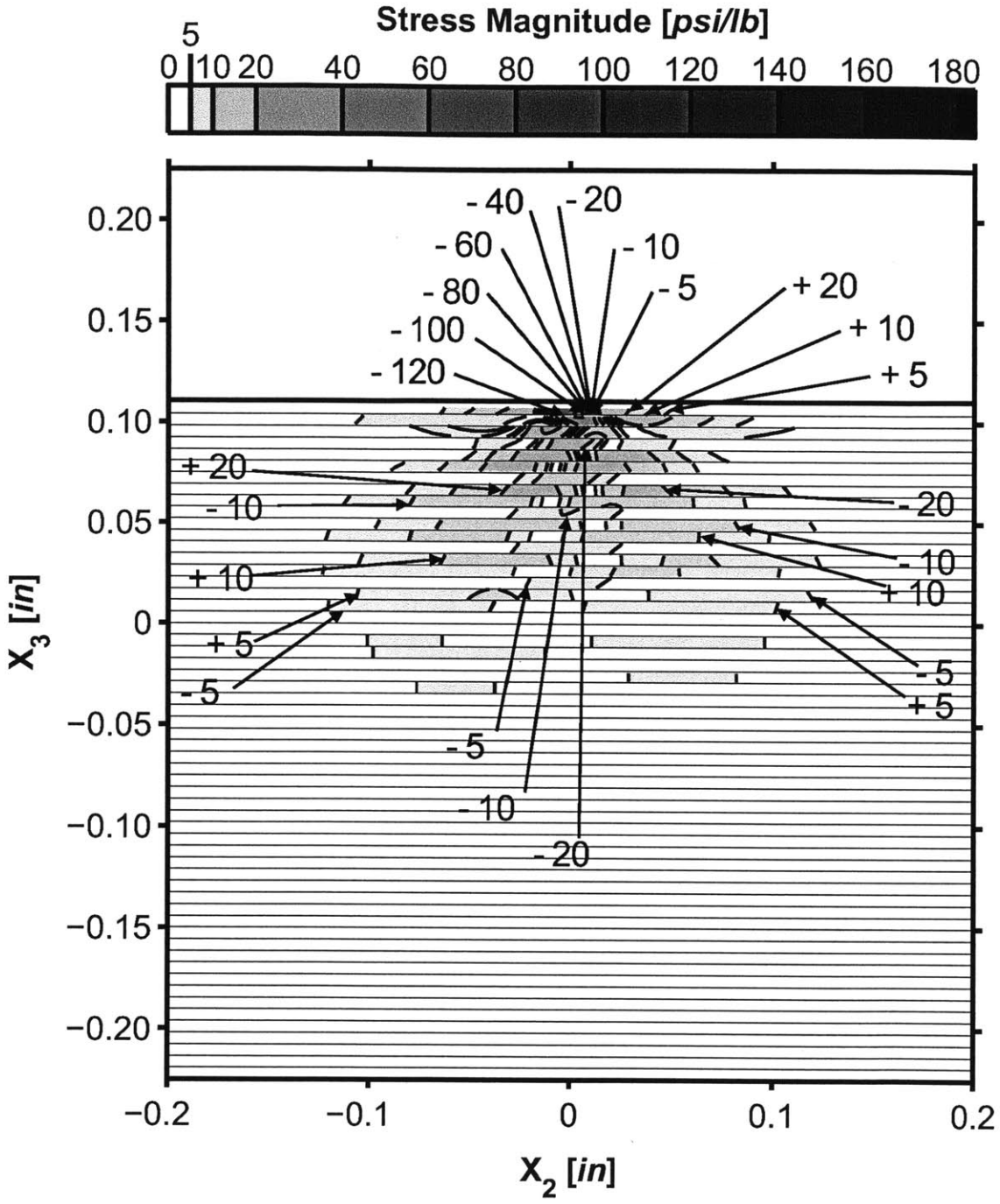

* Note: All stresses normalized by applied load, and given in units of [psi/lb].

Figure 5.51 Isostress plot of σ_{11}^{*} for a section cut at a value of x_1 of 0.05 inches in the three-dimensional T700/2510 $[\pm 15/0]_{13S}$ laminate model loaded at 300 lb.

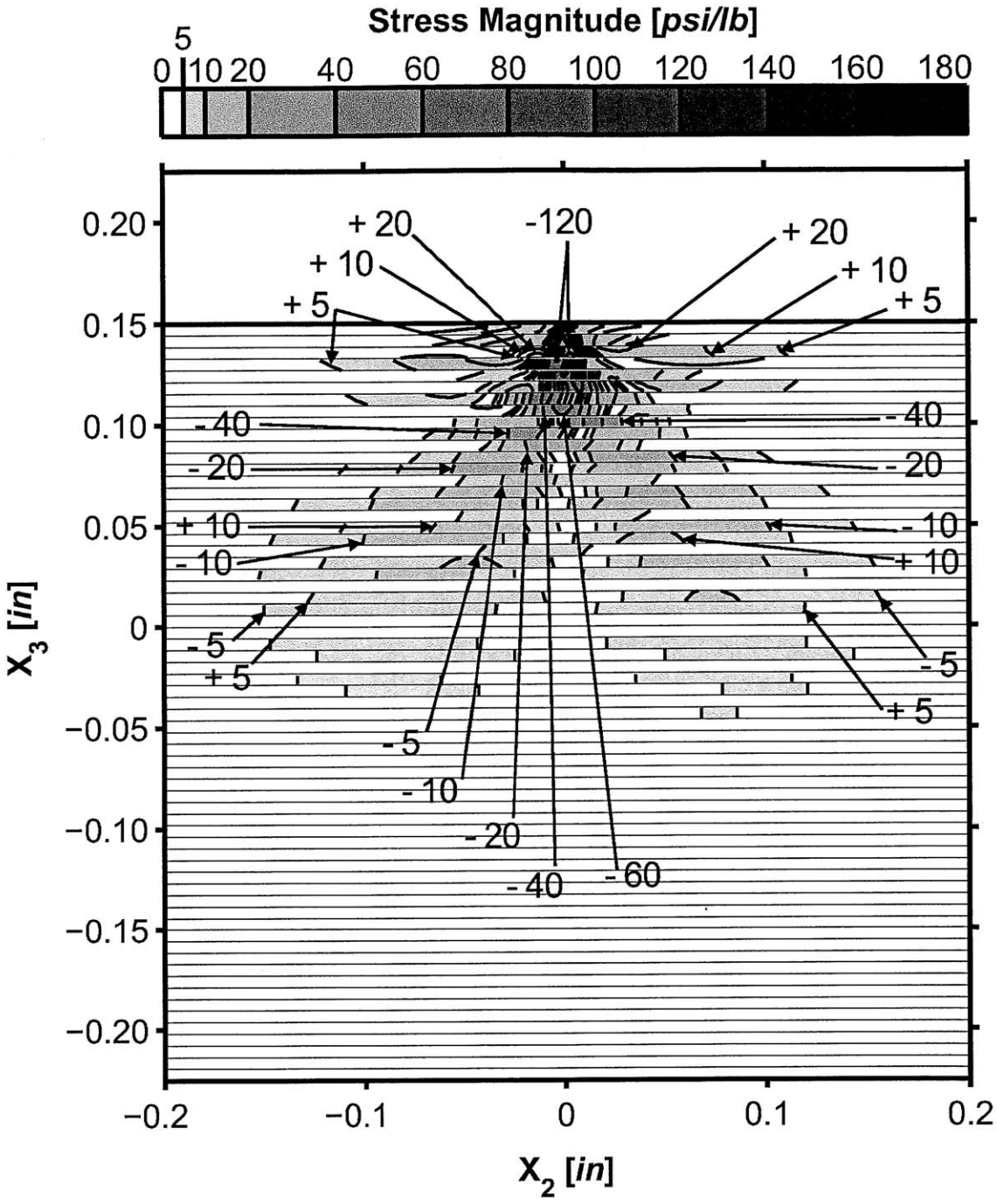

* Note: All stresses normalized by applied load, and given in units of [psi/lb].

Figure 5.52 Isostress plot of σ_{11}^{*} for a section cut at a value of x_1 of 0.10 inches in the three-dimensional T700/2510 $[\pm 15/0]_{13S}$ laminate model loaded at 300 lb.

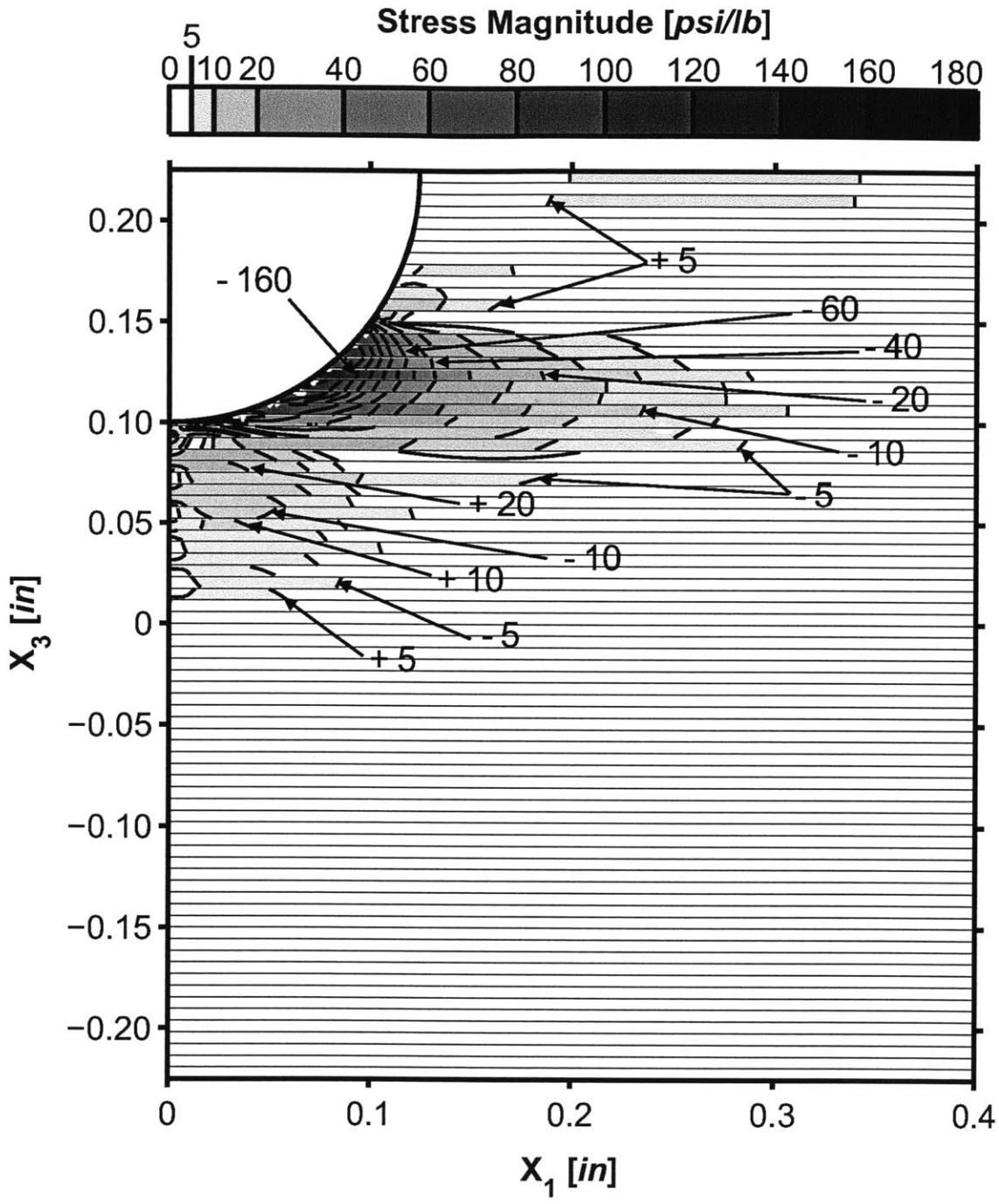

* Note: All stresses normalized by applied load, and given in units of [psi/lb].

Figure 5.53 Isostress plot of σ_{11}^{*} for a section cut at a value of x_2 of 0.0 inches in the three-dimensional T700/2510 $[\pm 15/0]_{13S}$ laminate model loaded at 300 lb.

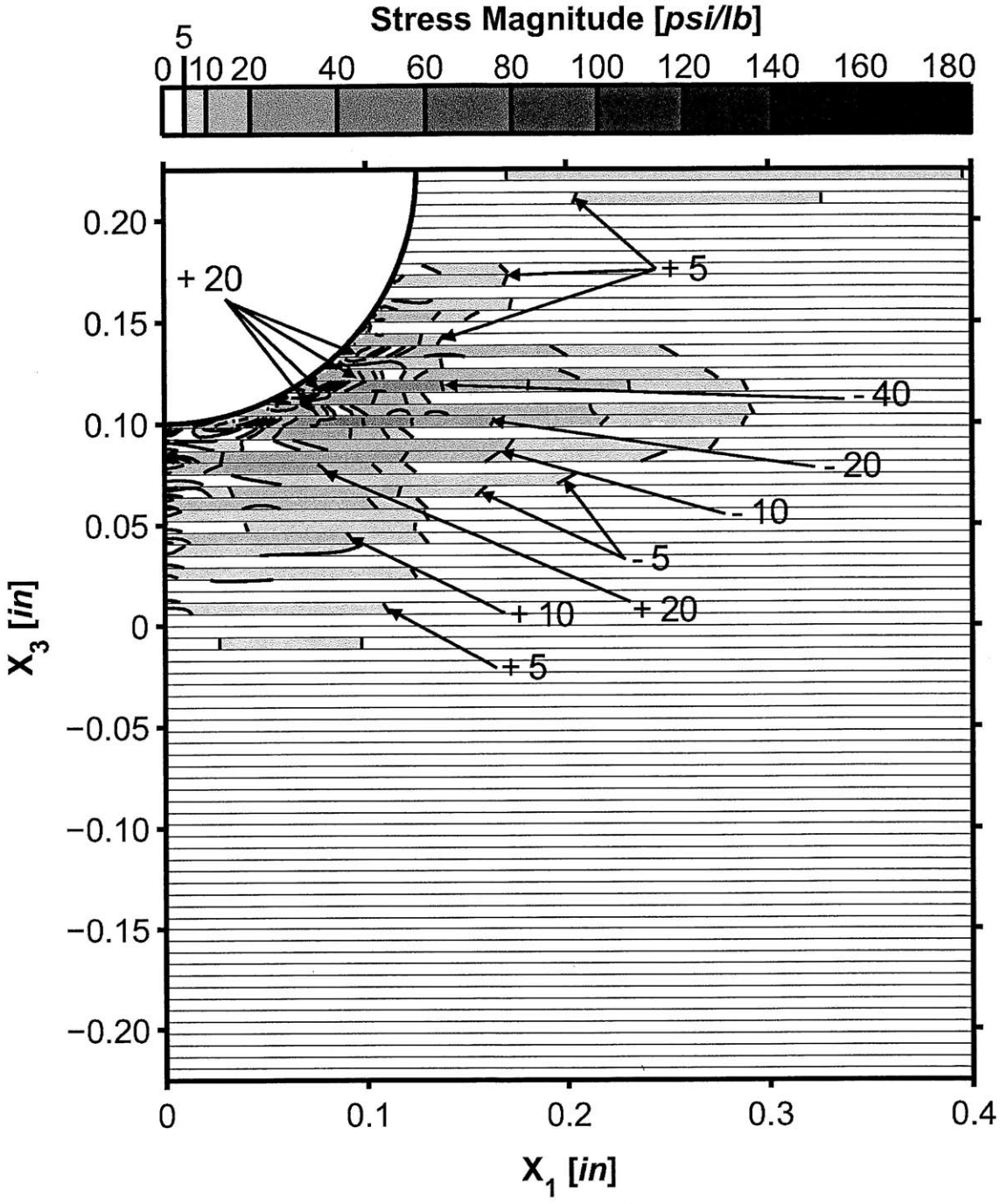

* Note: All stresses normalized by applied load, and given in units of [psi/lb].

Figure 5.54 Isostress plot of σ_{11}^{*} for a section cut at a value of x_2 of 0.02 inches in the three-dimensional T700/2510 $[\pm 15/0]_{13S}$ laminate model loaded at 300 lb.

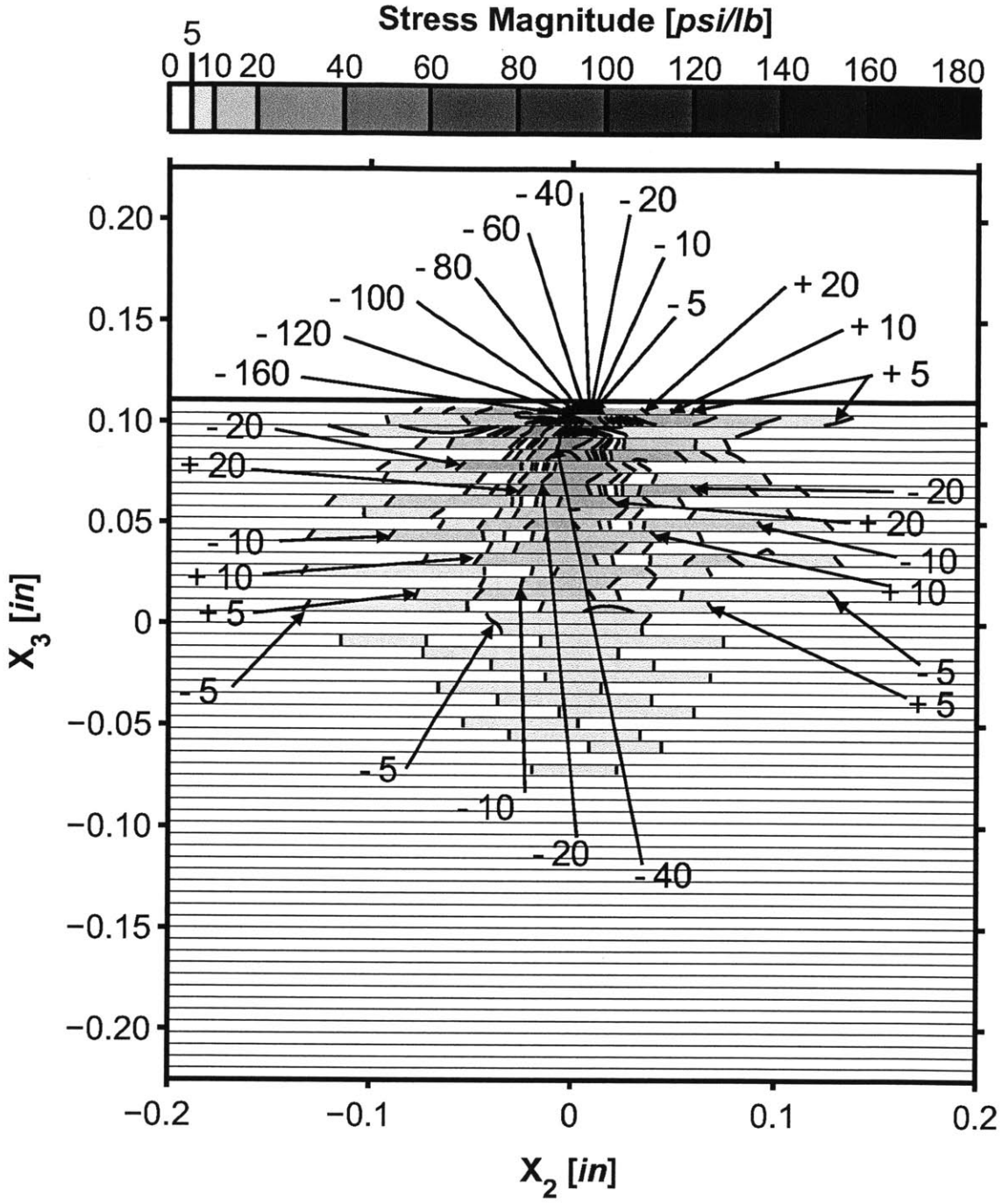

* Note: All stresses normalized by applied load, and given in units of [psi/lb].

Figure 5.55 Isostress plot of σ_{11}^{*} for a section cut at a value of x_1 of 0.05 inches in the three-dimensional T700/2510 $[\pm 30/0]_{13S}$ laminate model loaded at 300 lb.

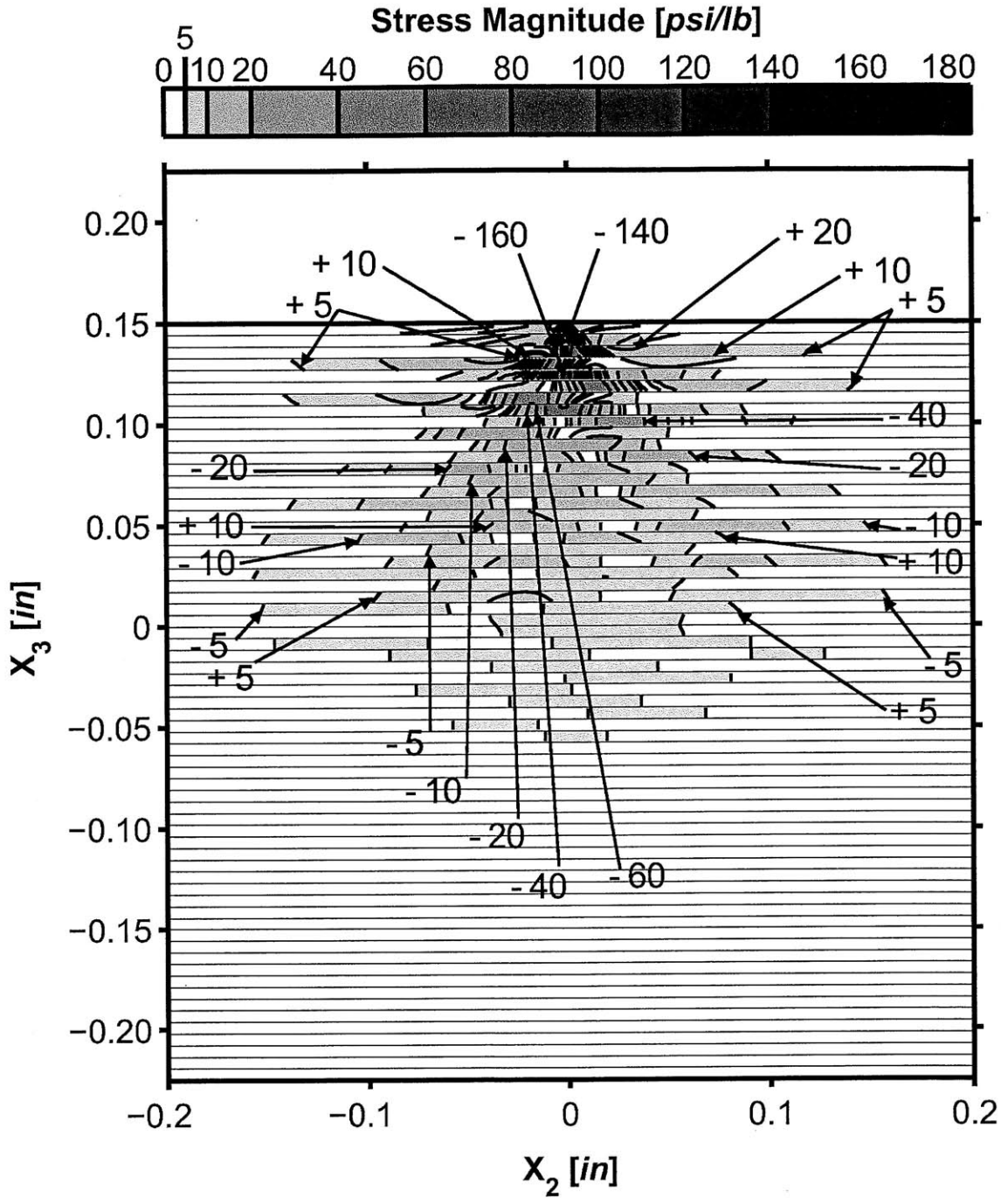

* Note: All stresses normalized by applied load, and given in units of [psi/lb].

Figure 5.56 Isostress plot of σ_{11}^{*} for a section cut at a value of x_1 of 0.10 inches in the three-dimensional T700/2510 $[\pm 30/0]_{13S}$ laminate model loaded at 300 lb.

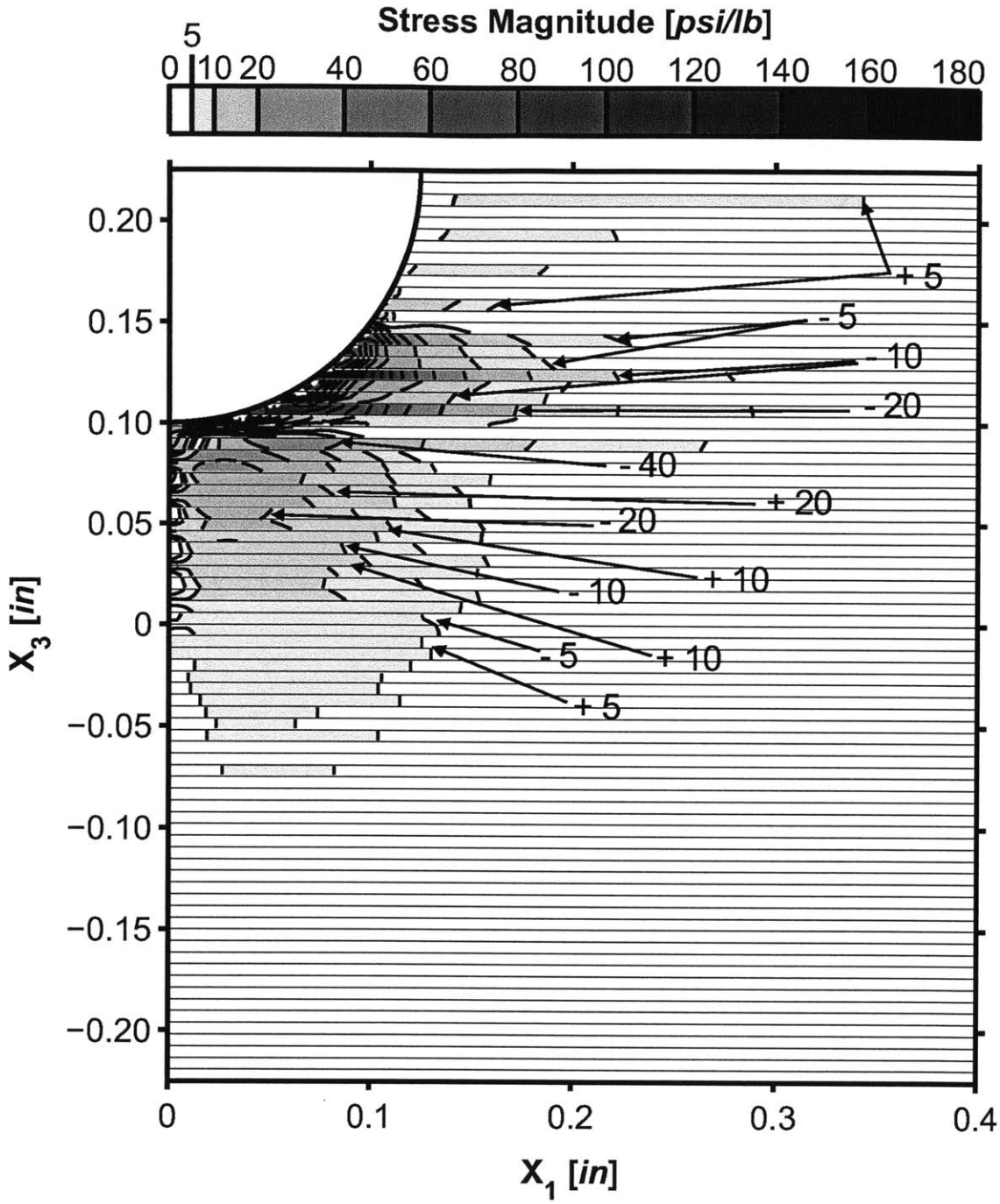

* Note: All stresses normalized by applied load, and given in units of [psi/lb].

Figure 5.57 Isostress plot of σ_{11}^{*} for a section cut at a value of x_2 of 0.0 inches in the three-dimensional T700/2510 $[\pm 30/0]_{13S}$ laminate model loaded at 300 lb.

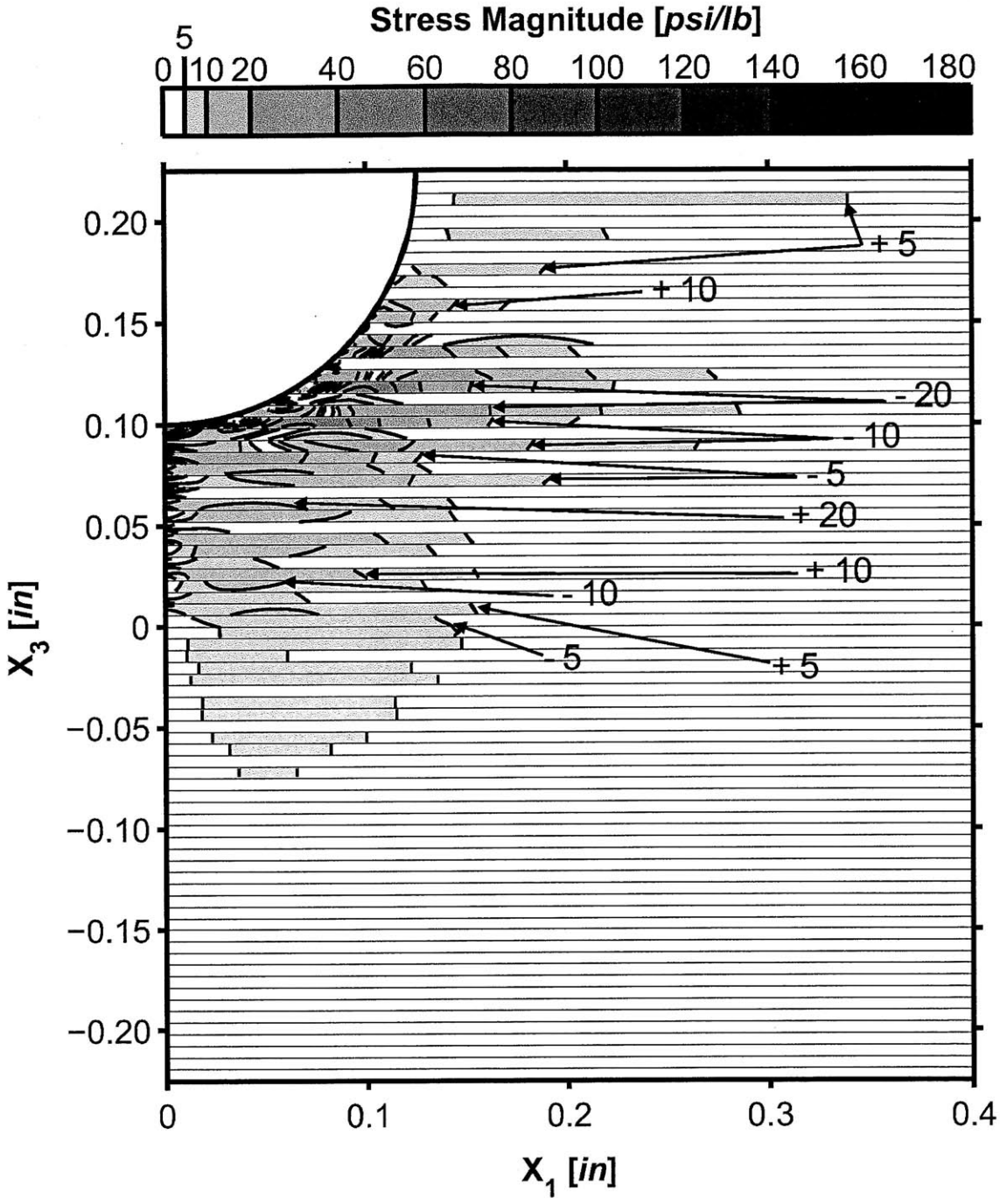

* Note: All stresses normalized by applied load, and given in units of [psi/lb].

Figure 5.58 Isostress plot of σ_{11}^{*} for a section cut at a value of x_2 of 0.02 inches in the three-dimensional T700/2510 $[\pm 30/0]_{13S}$ laminate model loaded at 300 lb.

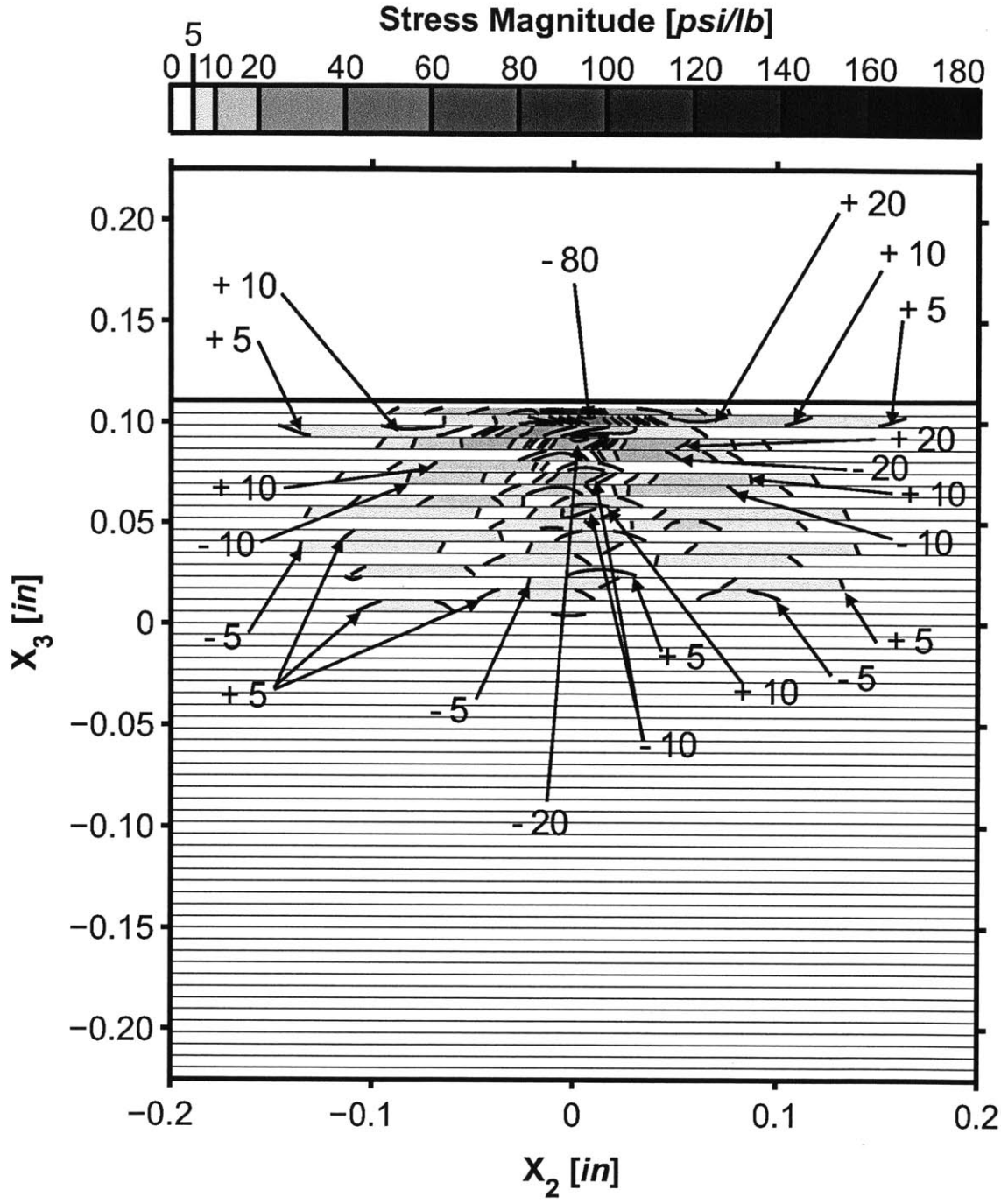

* Note: All stresses normalized by applied load, and given in units of [psi/lb].

Figure 5.59 Isostress plot of σ_{11}^{*} for a section cut at a value of x_1 of 0.05 inches in the three-dimensional T700/2510 $[\pm 45/0]_{13S}$ laminate model loaded at 300 lb.

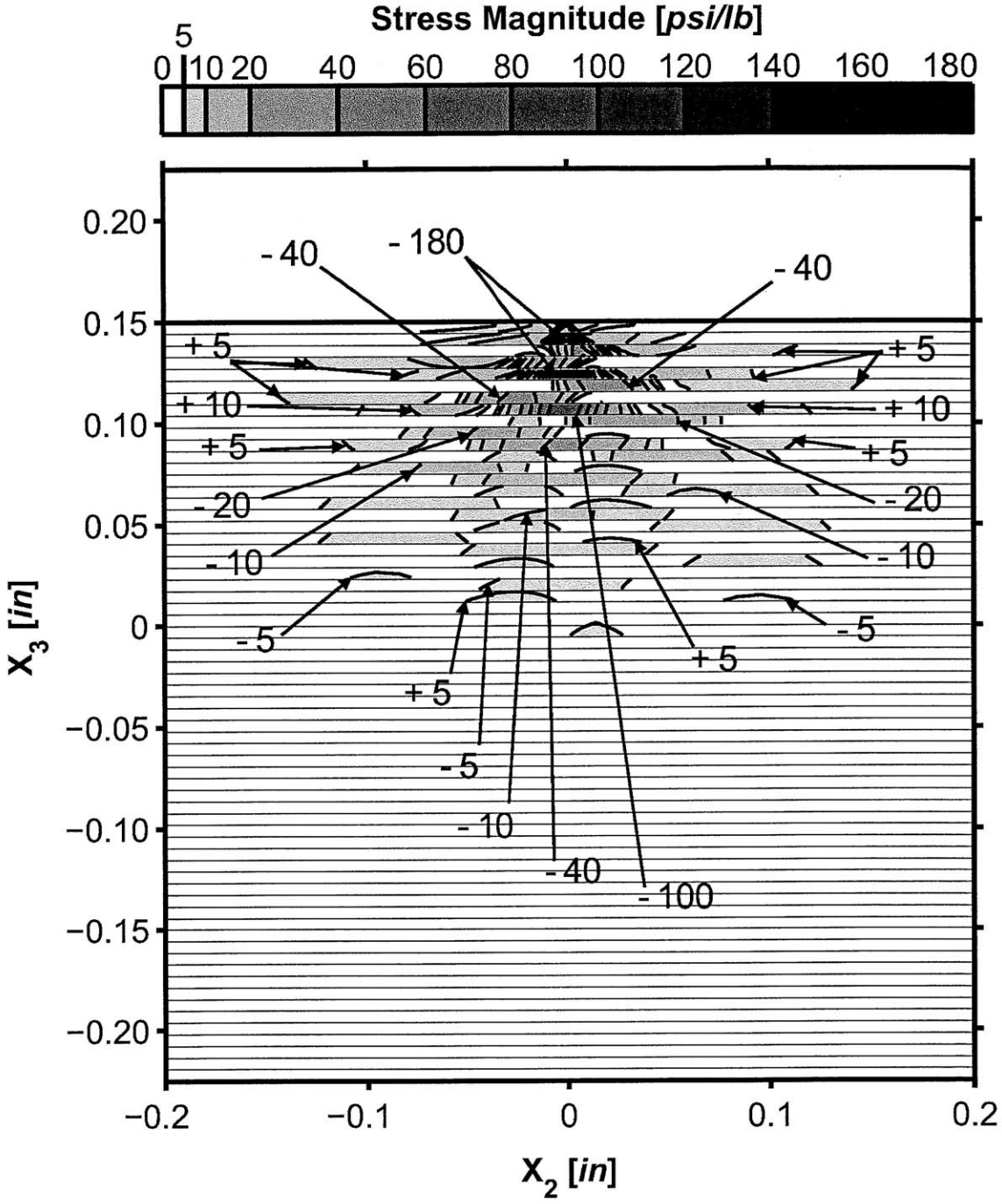

* Note: All stresses normalized by applied load, and given in units of [psi/lb].

Figure 5.60 Isostress plot of σ_{11}^{*} for a section cut at a value of x_1 of 0.10 inches in the three-dimensional T700/2510 $[\pm 45/0]_{13S}$ laminate model loaded at 300 lb.

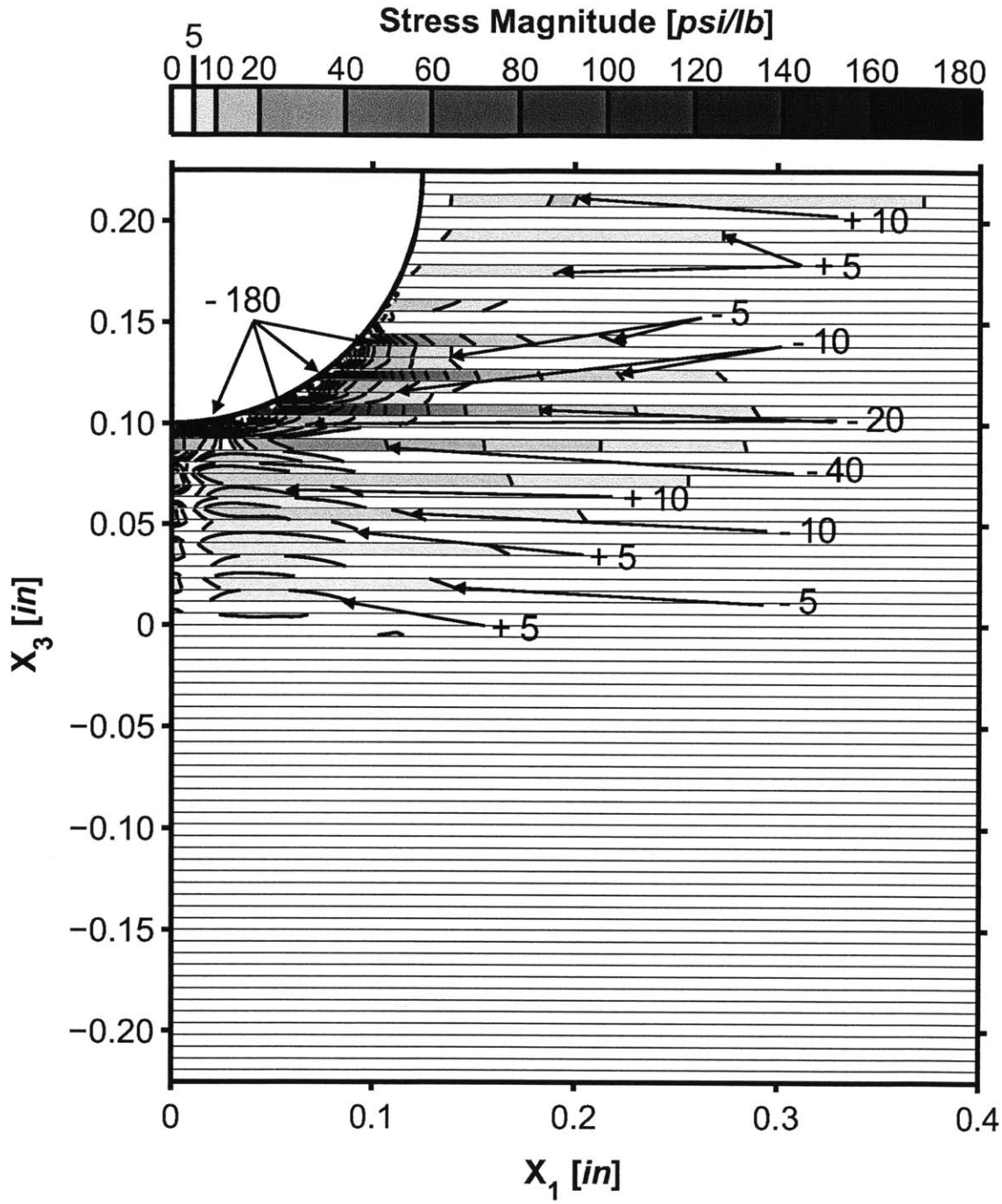

* Note: All stresses normalized by applied load, and given in units of [psi/lb].

Figure 5.61 Isostress plot of σ_{11}^{*} for a section cut at a value of x_2 of 0.0 inches in the three-dimensional T700/2510 $[\pm 45/0]_{13S}$ laminate model loaded at 300 lb.

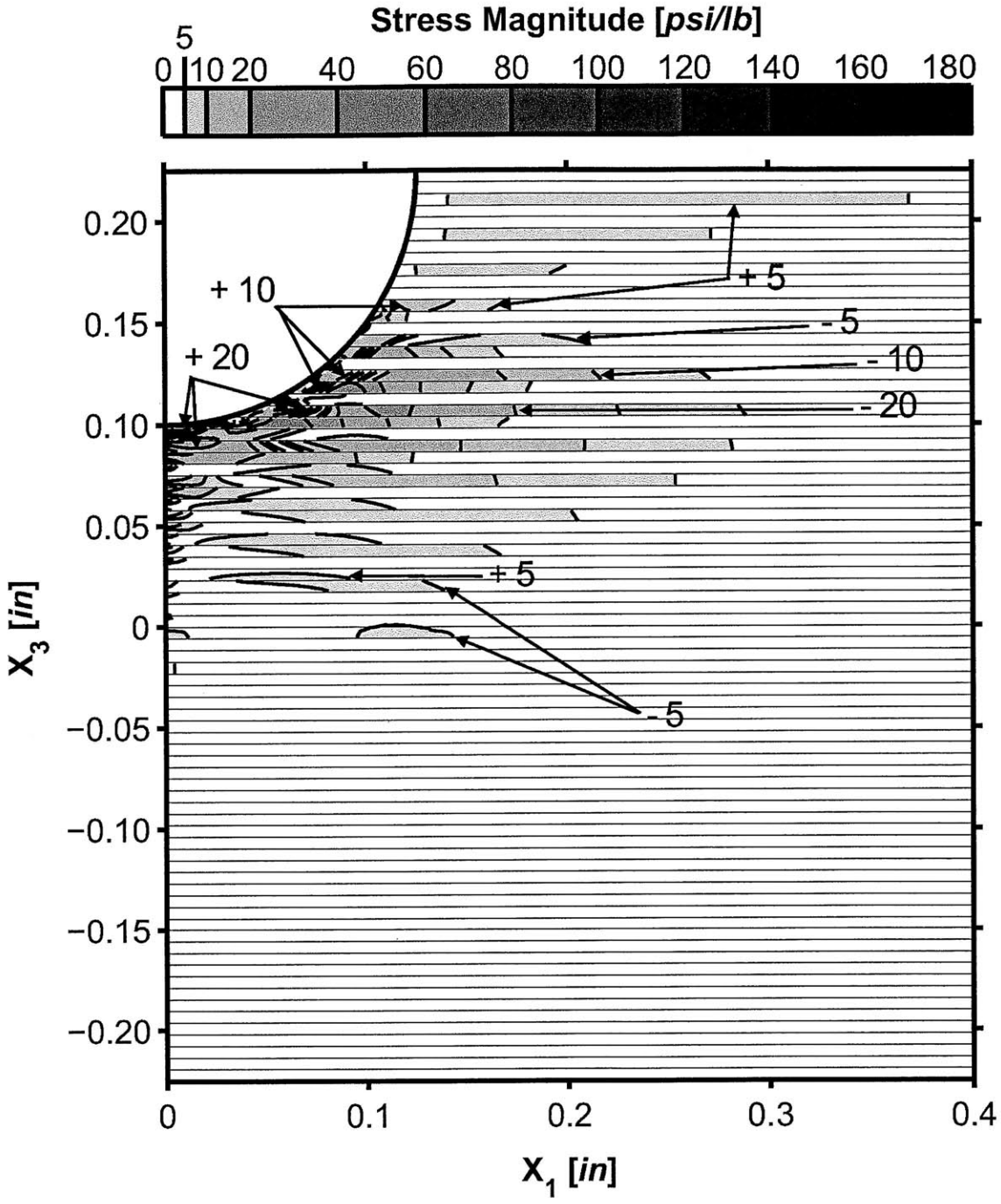

* Note: All stresses normalized by applied load, and given in units of [psi/lb].

Figure 5.62 Isostress plot of σ_{11}^{*} for a section cut at a value of x_2 of 0.02 inches in the three-dimensional T700/2510 $[\pm 45/0]_{13S}$ laminate model loaded at 300 lb.

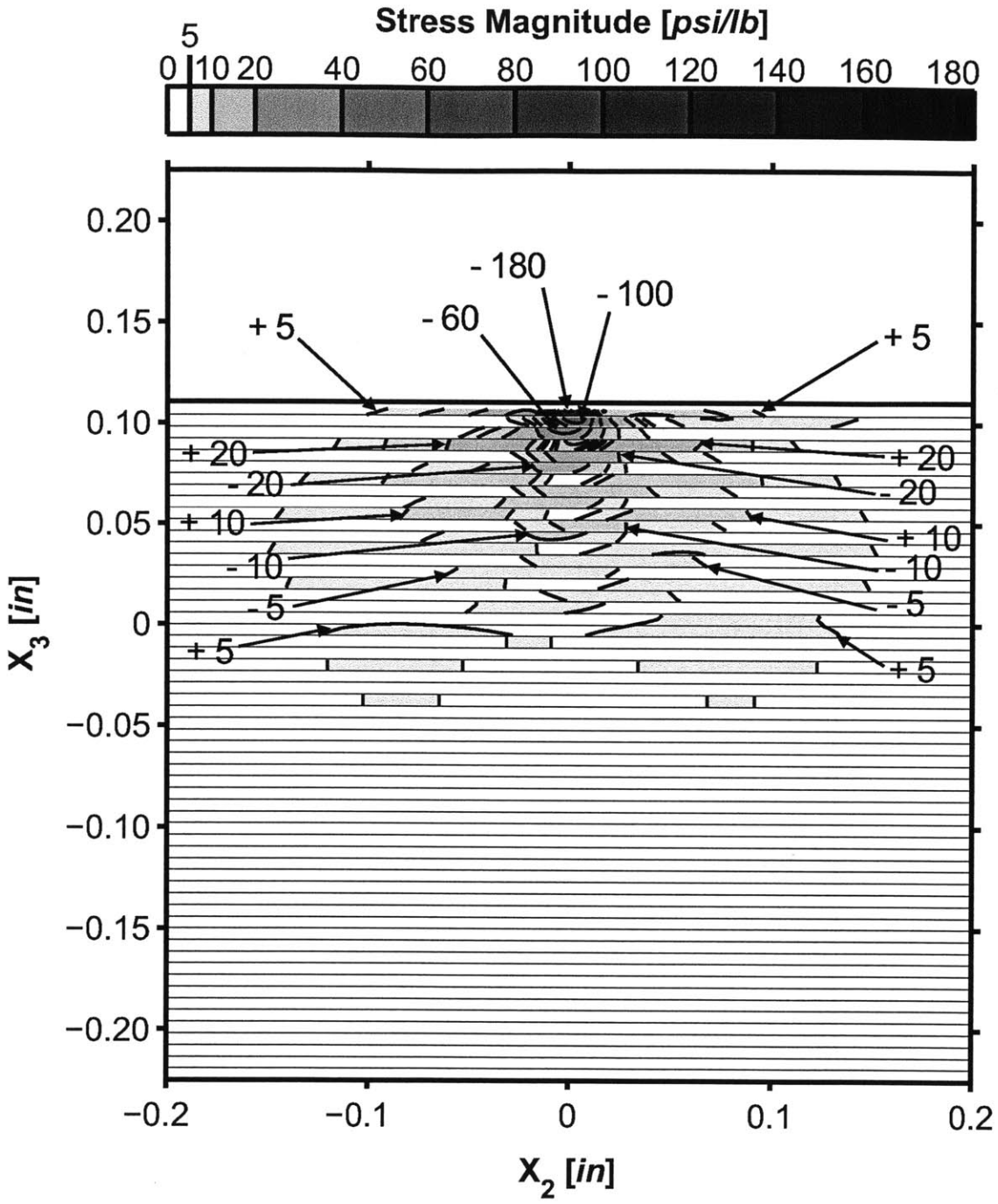

* Note: All stresses normalized by applied load, and given in units of [psi/lb].

Figure 5.63 Isostress plot of σ_{11}^{*} for a section cut at a value of x_1 of 0.05 inches in the three-dimensional T700/2510 $[\pm 60/0]_{13S}$ laminate model loaded at 300 lb.

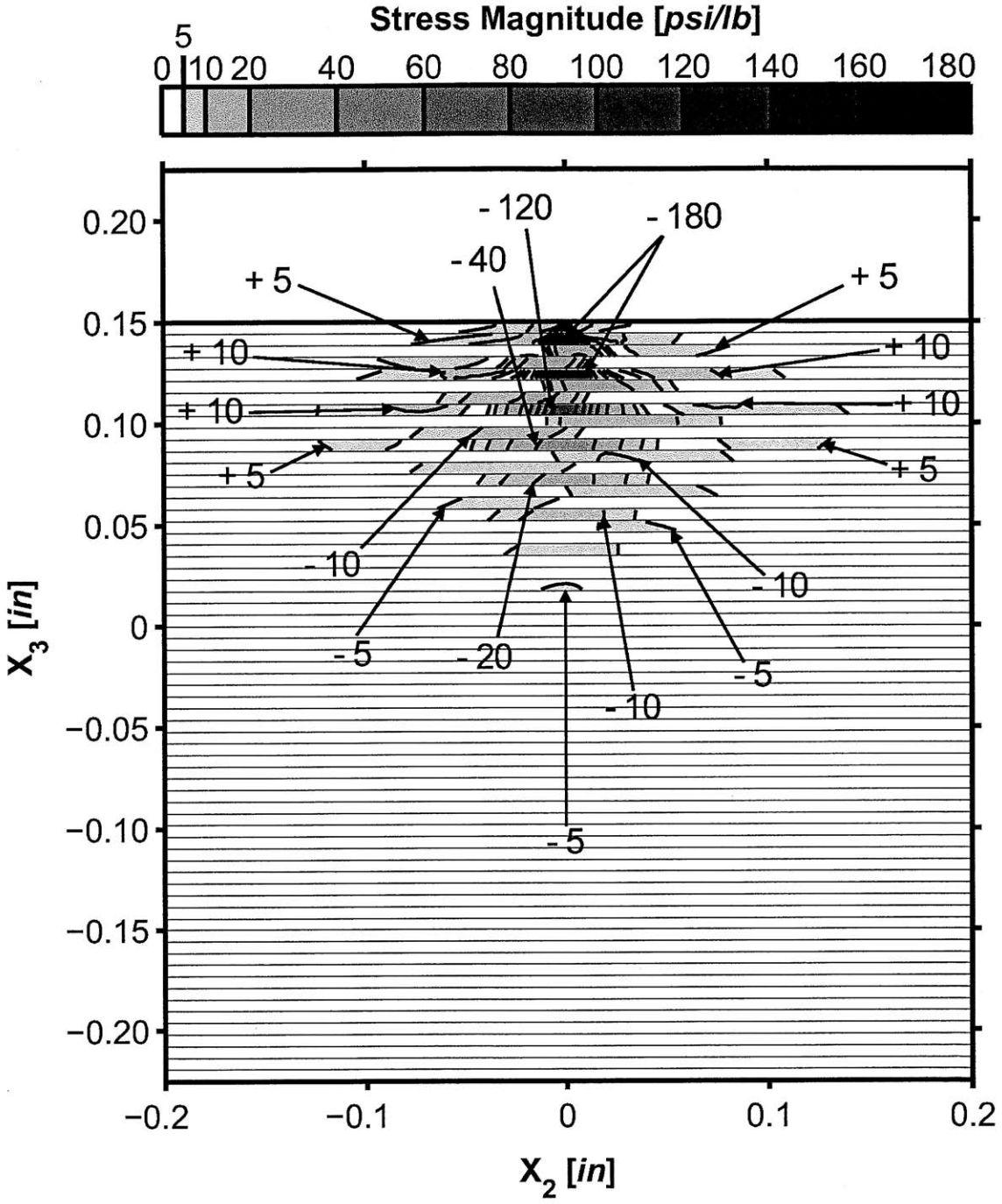

* Note: All stresses normalized by applied load, and given in units of [psi/lb].

Figure 5.64 Isostress plot of σ_{11}^{*} for a section cut at a value of x_1 of 0.10 inches in the three-dimensional T700/2510 $[\pm 60/0]_{13S}$ laminate model loaded at 300 lb.

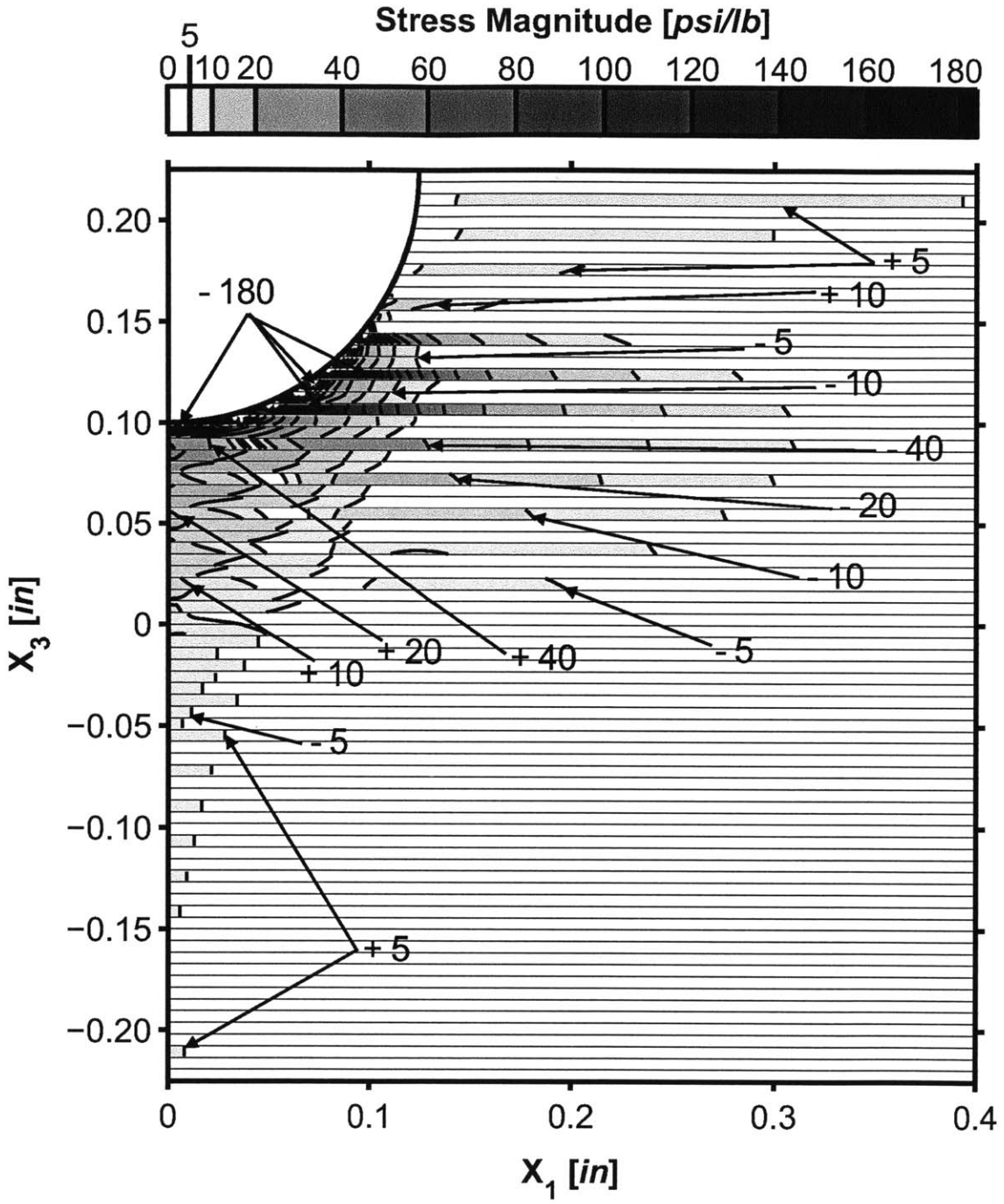

* Note: All stresses normalized by applied load, and given in units of [psi/lb].

Figure 5.65 Isostress plot of σ_{11}^{*} for a section cut at a value of x_2 of 0.0 inches in the three-dimensional T700/2510 $[\pm 60/0]_{13S}$ laminate model loaded at 300 lb.

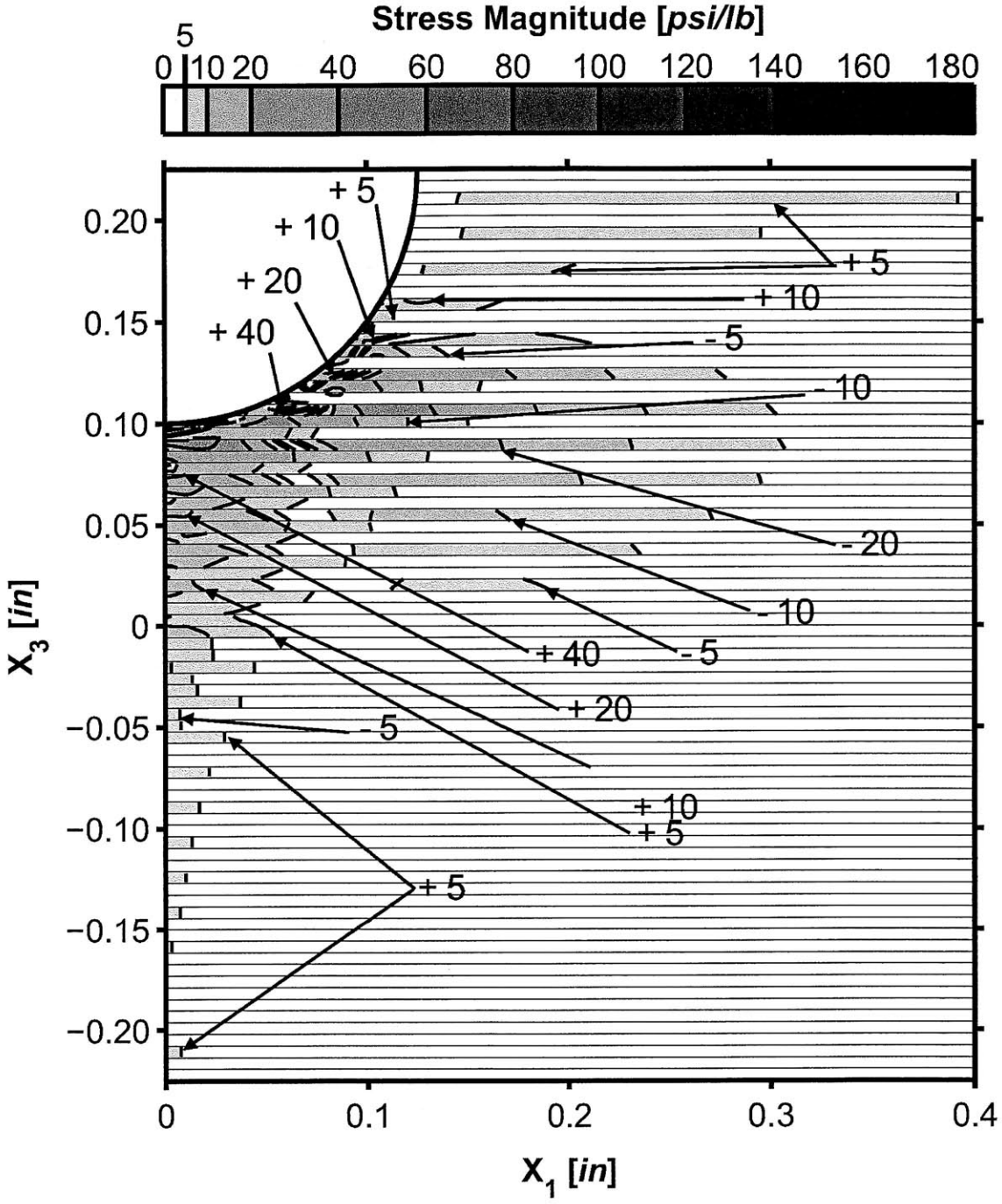

* Note: All stresses normalized by applied load, and given in units of [psi/lb].

Figure 5.66 Isostress plot of σ_{11}^{*} for a section cut at a value of x_2 of 0.02 inches in the three-dimensional T700/2510 $[\pm 60/0]_{13S}$ laminate model loaded at 300 lb.

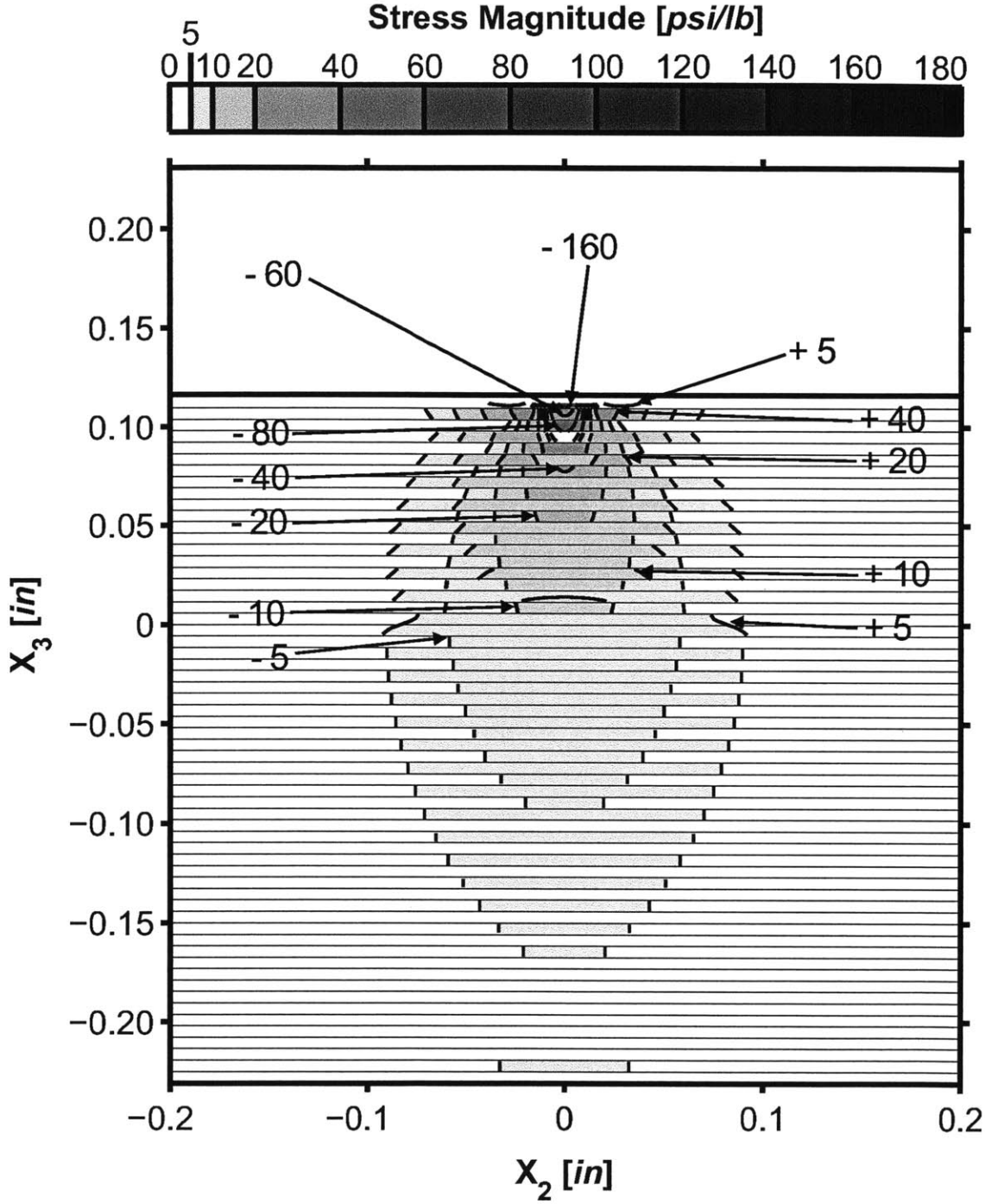

* Note: All stresses normalized by applied load, and given in units of [psi/lb].

Figure 5.67 Isostress plot of σ_{11}^{*} for a section cut at a value of x_1 of 0.05 inches in the three-dimensional T700/2510 $[90/0]_{20S}$ laminate model loaded at 300 lb.

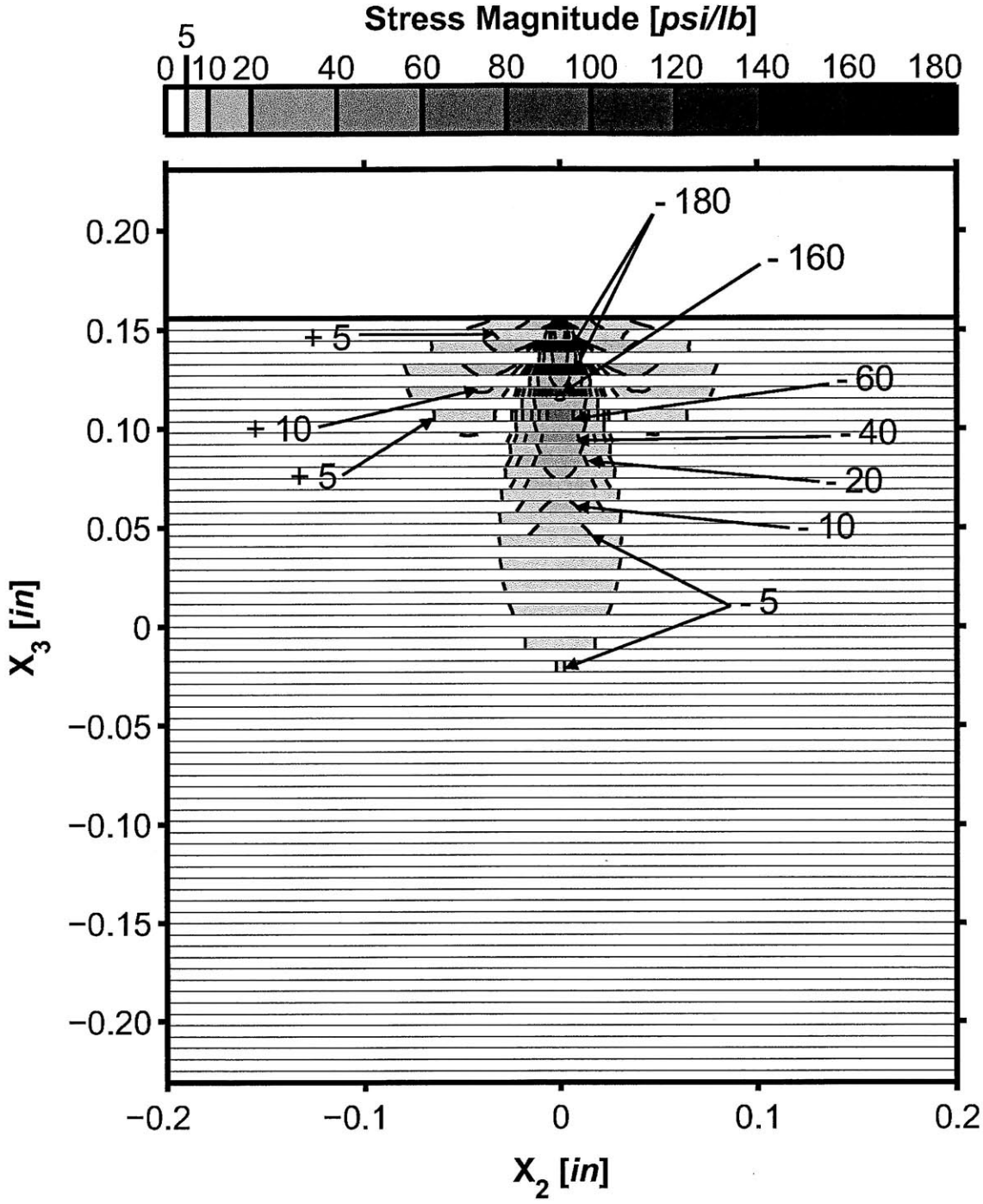

* Note: All stresses normalized by applied load, and given in units of [psi/lb].

Figure 5.68 Isostress plot of σ_{11}^{*} for a section cut at a value of x_1 of 0.10 inches in the three-dimensional T700/2510 $[90/0]_{20S}$ laminate model loaded at 300 lb.

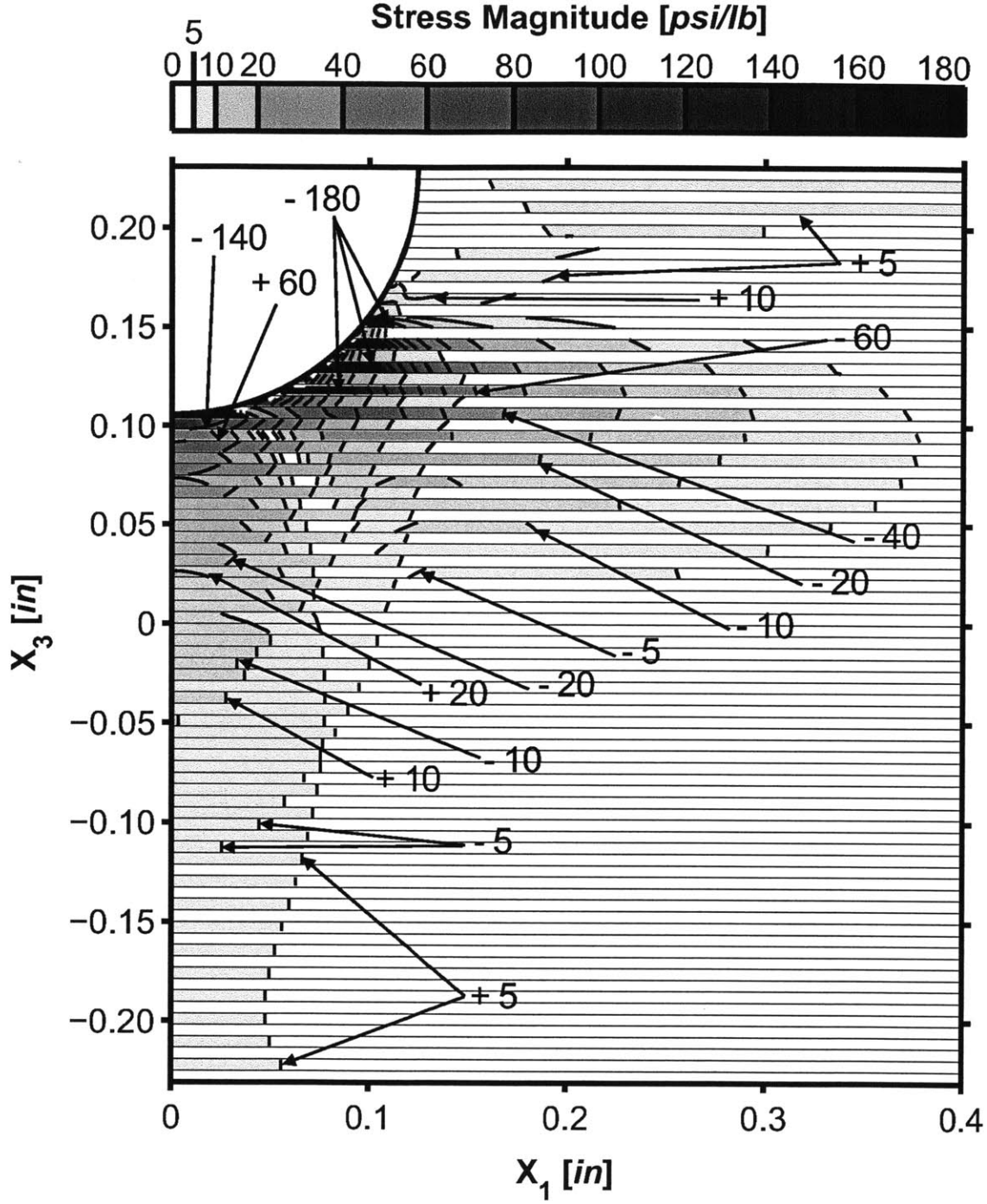

* Note: All stresses normalized by applied load, and given in units of [psi/lb].

Figure 5.69 Isostress plot of σ_{11}^{*} for a section cut at a value of x_2 of 0.0 inches in the three-dimensional T700/2510 $[90/0]_{20S}$ laminate model loaded at 300 lb.

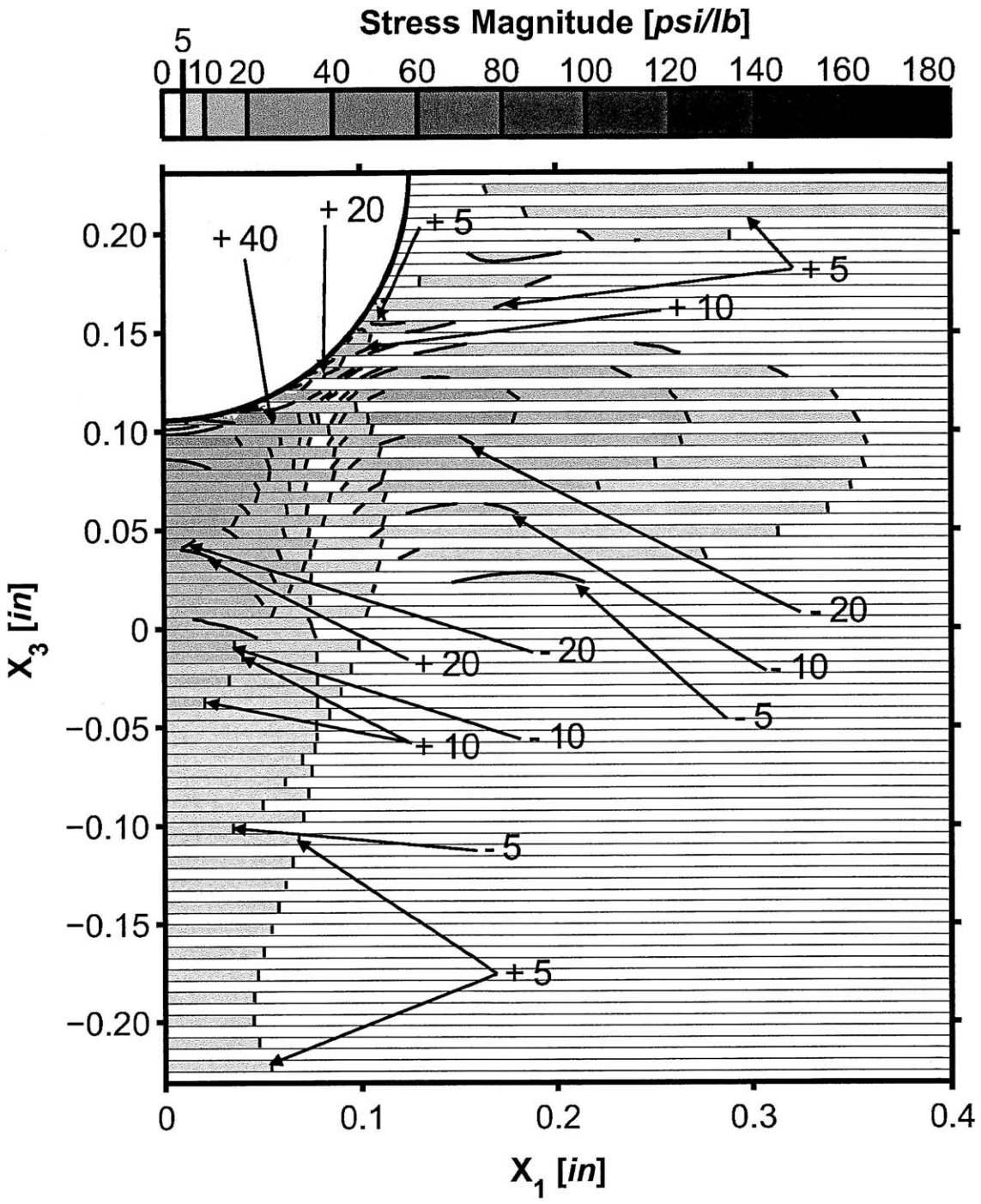

* Note: All stresses normalized by applied load, and given in units of [psi/lb].

Figure 5.70 Isostress plot of σ_{11}^{*} for a section cut at a value of x_2 of 0.02 inches in the three-dimensional T700/2510 $[90/0]_{20S}$ laminate model loaded at 300 lb.

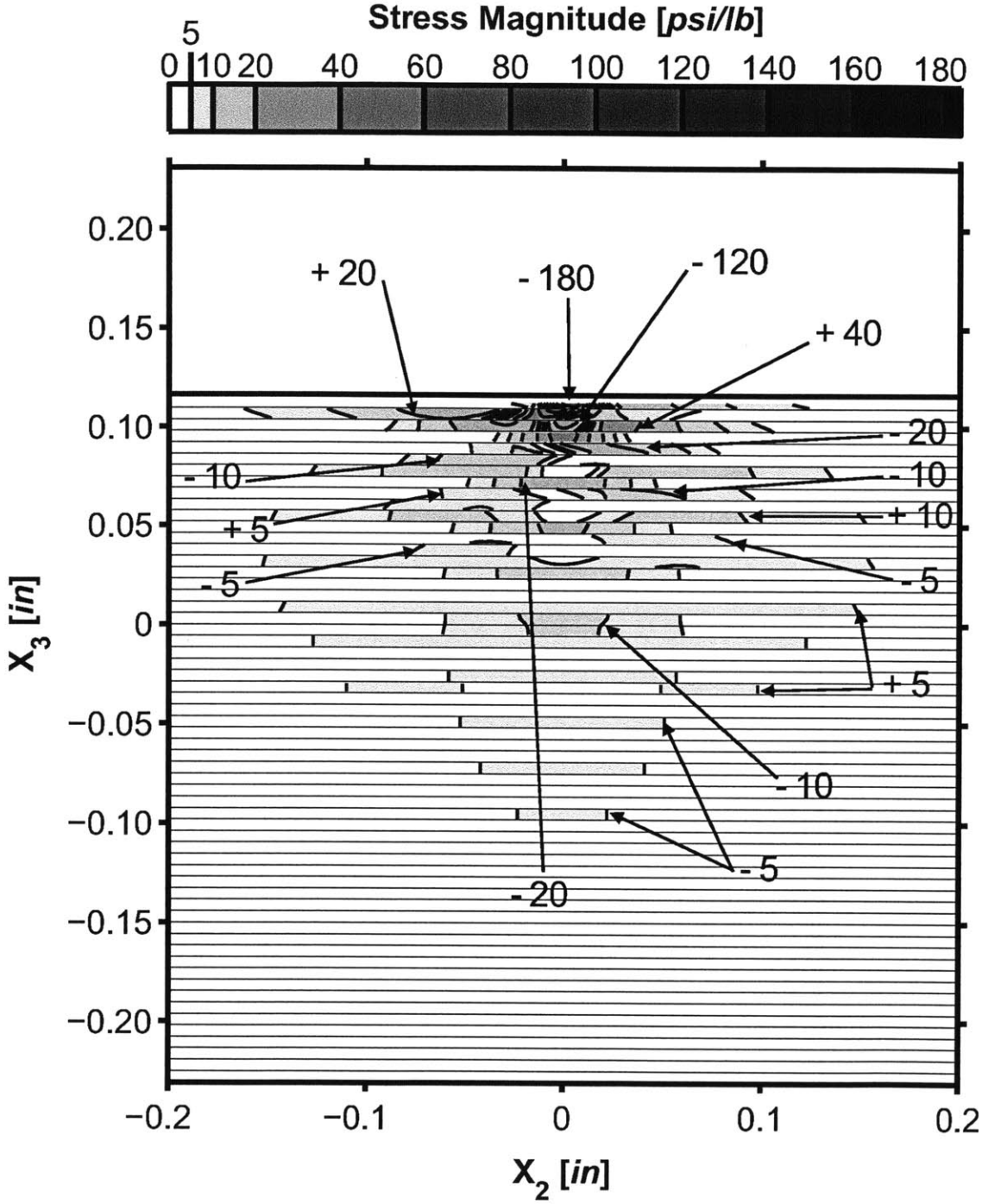

* Note: All stresses normalized by applied load, and given in units of [psi/lb].

Figure 5.71 Isostress plot of σ_{11}^{*} for a section cut at a value of x_1 of 0.05 inches in the three-dimensional T700/2510 $[\pm 45/0/90]_{10S}$ laminate model loaded at 300 lb.

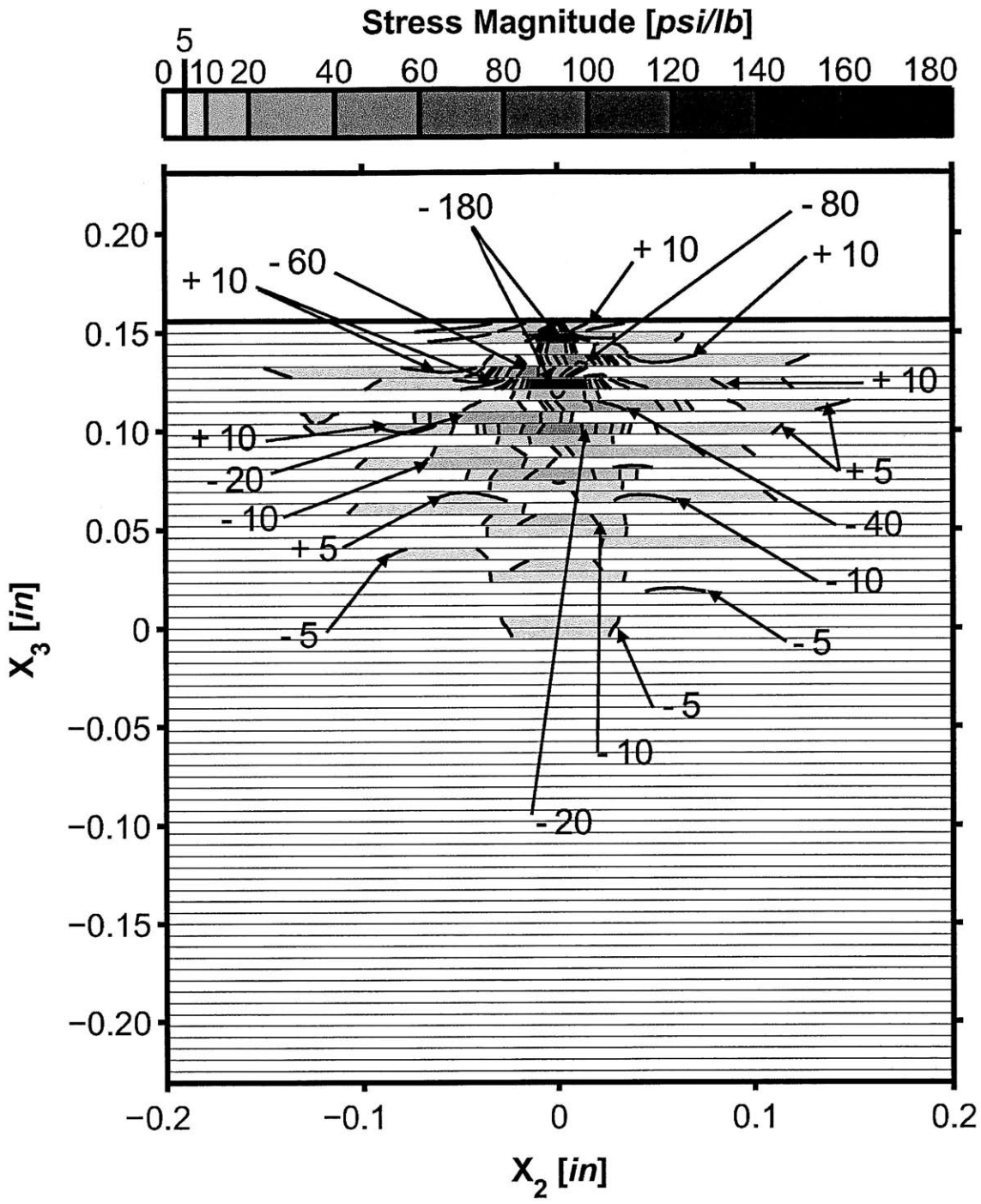

* Note: All stresses normalized by applied load, and given in units of [psi/lb].

Figure 5.72 Isostress plot of σ_{11}^{*} for a section cut at a value of x_1 of 0.10 inches in the three-dimensional T700/2510 $[\pm 45/0/90]_{10S}$ laminate model loaded at 300 lb.

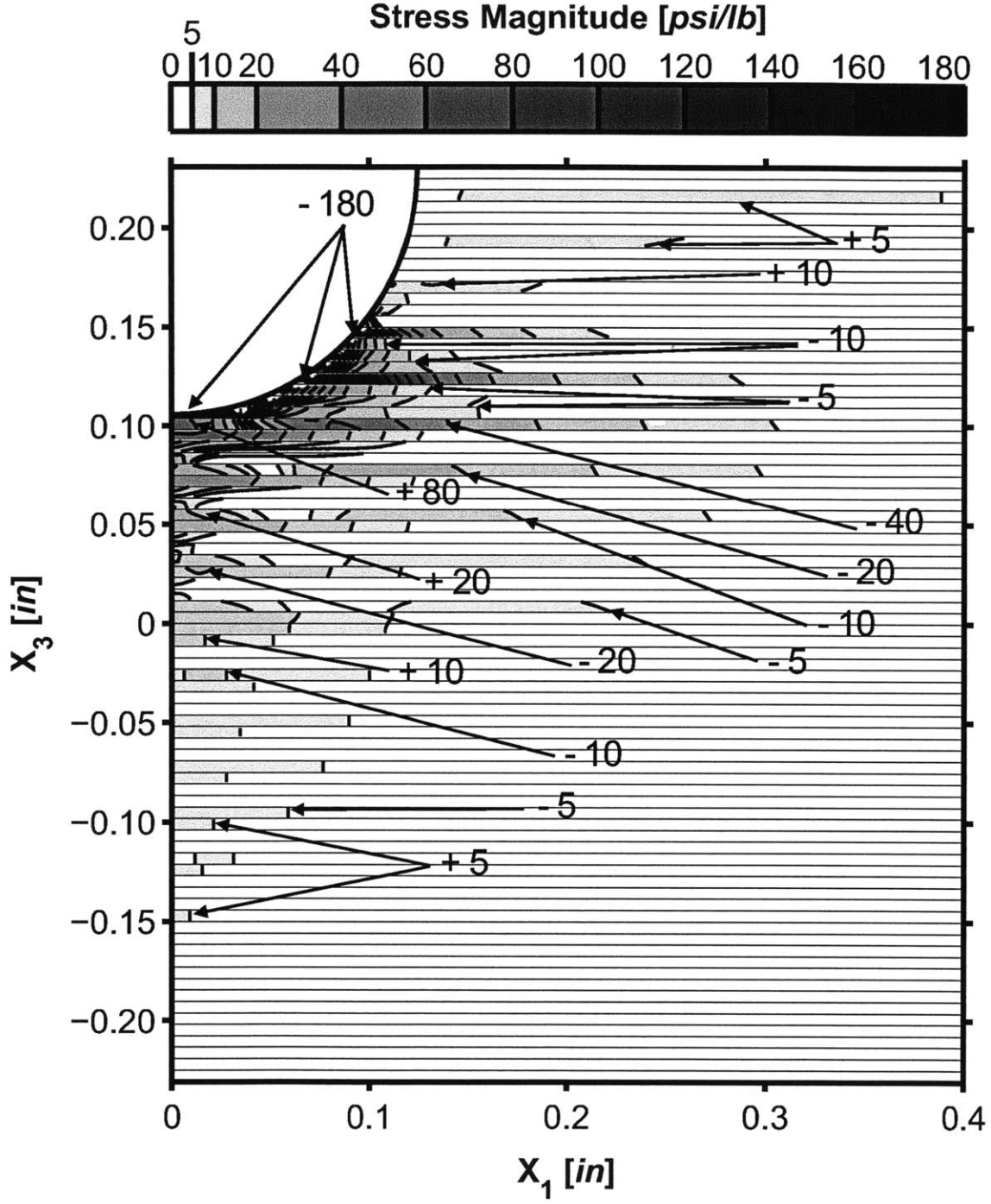

* Note: All stresses normalized by applied load, and given in units of [psi/lb].

Figure 5.73 Isostress plot of σ_{11}^{*} for a section cut at a value of x_2 of 0.0 inches in the three-dimensional T700/2510 $[\pm 45/0/90]_{10S}$ laminate model loaded at 300 lb.

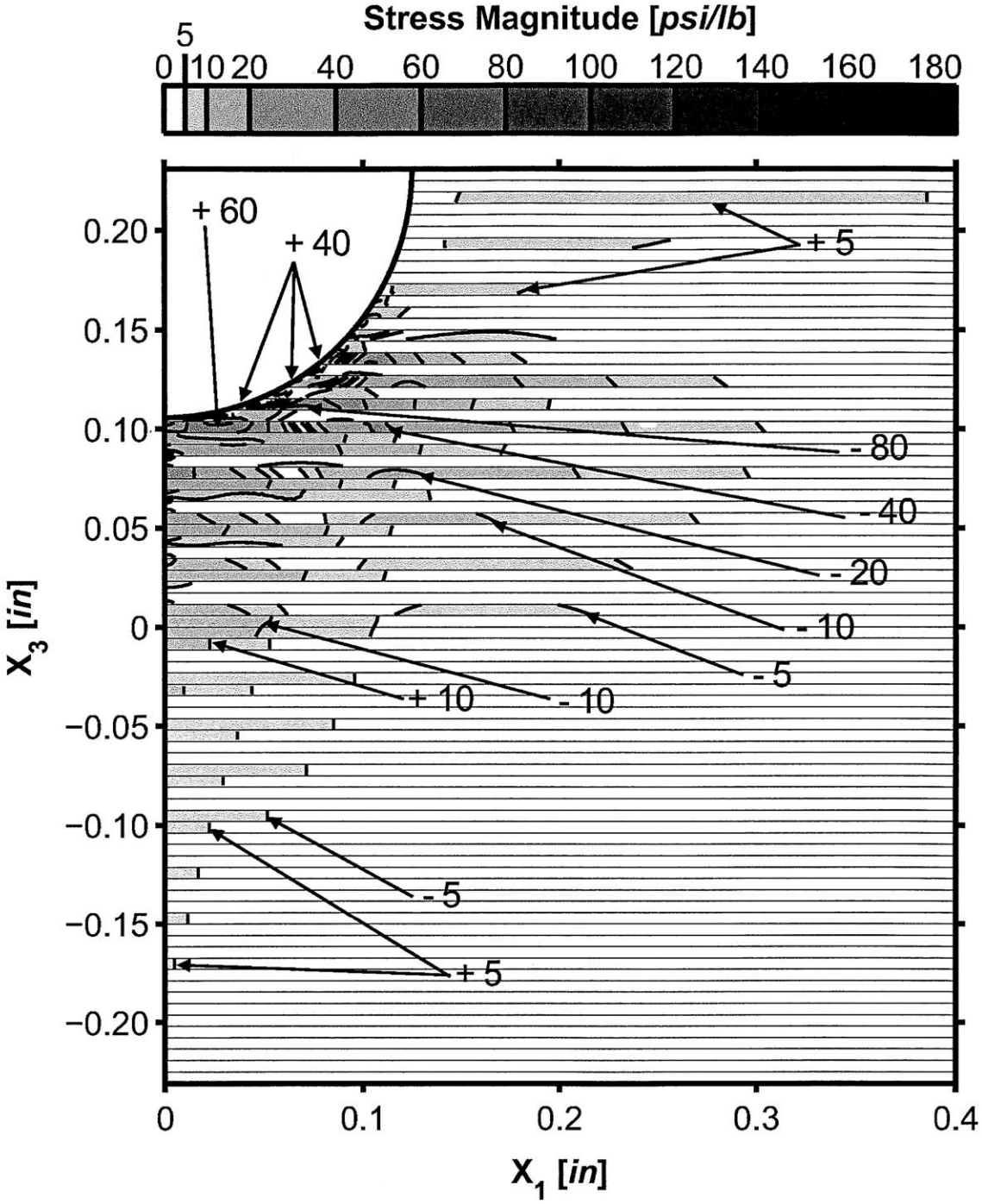

* Note: All stresses normalized by applied load, and given in units of [psi/lb].

Figure 5.74 Isostress plot of σ_{11}^{*} for a section cut at a value of x_2 of 0.02 inches in the three-dimensional T700/2510 $[\pm 45/0/90]_{10S}$ laminate model loaded at 300 lb.

Table 5.6 Maximum magnitudes of tensile normalized stress values, σ_{11}^{*}, and locations in cylindrical coordinates for three-dimensional models loaded at 300 lb

Laminate		**Tension**			
Material	Layup	σ_T^* $[psi/lb]$	ϕ_T $[deg]$	r_T $[in]$	x_{2_T} $[in]$
T700/2510	$[\pm 15/0]_{13S}$	101	3.6	0.125	0.017
T700/2510	$[\pm 30/0]_{13S}$	112	14.2	0.125	-0.017
T700/2510	$[\pm 45/0]_{13S}$	141	0.0	0.139	-0.014
T700/2510	$[\pm 60/0]_{13S}$	147	14.2	0.125	-0.017
T700/2510	$[90/0]_{20S}$	244	0.0	0.125	0.0
T700/2510	$[\pm 45/0/90]_{10S}$	102	5.1	0.127	0.012

Table 5.7 Maximum magnitudes of compressive normalized stress values, σ_{11}^{*}, and locations in cylindrical coordinates for three-dimensional models loaded at 300 lb

Laminate		**Compression**			
Material	Layup	σ_C^* $[psi/lb]$	ϕ_C $[deg]$	r_C $[in]$	x_{2_C} $[in]$
T700/2510	$[\pm 15/0]_{13S}$	-179	39.1	0.134	-0.002
T700/2510	$[\pm 30/0]_{13S}$	-224	39.1	0.134	0.0
T700/2510	$[\pm 45/0]_{13S}$	-260	37.8	0.132	0.0
T700/2510	$[\pm 60/0]_{13S}$	-279	37.8	0.132	0.0
T700/2510	$[90/0]_{20S}$	-257	39.1	0.139	0.0
T700/2510	$[\pm 45/0/90]_{10S}$	-264	39.1	0.134	0.0

beneath the bottom of the groove in Zone 1 in 0° plies. The maximum compressive stresses, σ_C^*, occur along the groove face in Zone 2 at a consistent angular location, ϕ, between 37.8 and 39.1°.

In Zone 1, the primary driver of stress is most likely the Poisson's effect from high compressive strains in the 3-direction from the indentor. In this zone, positive angled plies are in compression towards positive values of x_2, and in tension towards negative values of x_2. For negative angled plies, this trend is reversed, with the plies in compression towards negative values of x_2 and tension towards positive values of x_2. These regions are not evenly split at the centerline of x_2 equal to zero. There is some overlap, with the compressive regions most frequently being larger, and the tensile regions tending to shrink and even disappear as ply angle increases. Behavior of the 0° plies in Zone 1 is dependent on the laminate. These plies generally have a region of compressive stress near the x_3-axis, and roughly symmetric regions of tension on either side of the x_3-axis. The relative sizes and intensities of these compressive and tensile regions in the 0° plies is the factor that is dependent on the laminate. In the $[\pm 15/0]_{13S}$ laminate, the 0° plies in this zone are almost entirely in compression, whereas, in the $[90/0]_{20S}$ laminate, these plies are almost entirely in tension. The rest of the laminates fall along this spectrum of behavior with the split of tension and compression, as described, of varying ratios depending on the laminate. Stresses in this zone are largest in magnitude immediately beneath the groove, and decrease in intensity toward the laminate backface. The highest stresses are in the 0° plies immediately beneath the groove.

In Zone 2, the primary driver of stress is most likely the lateral forces applied by the indentor pushing apart the walls of the groove. This zone is in compression. In x_2, this zone is localized to the area of contact near x_2 equal to 0.0. In x_1, this zone extends from the lower half of the groove, where contact occurs, horizontally out into the laminate toward positive values of x_1 and down toward the laminate backface. The exact angle and dispersion of stress depends on the particular laminate. In this zone, stress is concentrated in the 0° plies for all laminates investigated. The magnitude of stress in other plies in this region is proportional to the stiffness of that

ply in the 1-direction. The stresses of the largest magnitude in this zone are along the groove face, particularly in the 0° plies.

In Zone 3, the primary driver of stress is the stiffness of the laminate as a structure balanced against the deformation of the local region of indentation. This zone is primarily in tension, and wraps around Zone 2 to either side in the 2-direction and above in 3-direction. Stresses in this zone are carried primarily in the 0° plies, while the magnitude of stress in the other plies in this zone is proportional to the stiffness of that ply in the 1-direction. The stresses of largest magnitude in this zone are on the groove face, close to Zone 2 and the area of contact.

Examining the $[\pm\theta/0]_{13S}$ laminates, a few trends are notable. In Zone 1, the 0° plies change from being primarily in compression for θ equal to 15°, to being primarily in tension as θ increases to 60°. The $\pm\theta$ plies change from being almost equally in tension and compression at a θ value of 15°, to being entirely in compression as θ increases to 60°. In Zone 2, stresses decrease in $\pm\theta$ plies, and increase in 0° plies as θ increases. In Zone 3, there is not a significant change as θ changes. Overall, the magnitude of the maximum tensile stress, σ_T^*, increases by approximately 37% from 101 psi/lb to 147 psi/lb as θ increases from 15° to 60°. The maximum compressive stress, σ_C^*, increases in magnitude by 43% from -179 psi/lb to -279 psi/lb as θ increases from 15° to 60°.

Isostress plots for the normalized through-thickness extensional stress, σ_{33}^*, for the $[\pm 15/0]_{13S}$ laminate are provided in Figures 5.75 and 5.76 for the x_1-section cuts at 0.05 and 0.10 inches, respectively. A perpendicular section cut is shown in Figure 5.77 for a value of x_2 of 0.0. Isostress plots for σ_{33}^* for the $[\pm 30/0]_{13S}$ laminate are shown in Figures 5.78 and 5.79 for the x_1-section cuts at 0.05 and 0.10 inches, respectively. A perpendicular section cut is shown in Figure 5.80 for a value of x_2 of 0.0. Isostress plots for σ_{33}^* for the $[\pm 45/0]_{13S}$ laminate are shown in Figures 5.81 and 5.82 for the x_1-section cuts at 0.05 and 0.10 inches, respectively. A perpendicular section cut is shown in Figure 5.83 for a value of x_2 of 0.0. Isostress plots for σ_{33}^* for the $[\pm 60/0]_{13S}$ laminate are presented in Figures 5.84 and 5.85 for the x_1-section cuts at 0.05 and 0.10 inches, respectively. A perpendicular section cut is shown in Figure 5.86 for a

value of x_2 of 0.0. Isostress plots for σ_{33}^* for the cross-ply $[90/0]_{20S}$ laminate are given in Figures 5.87 and 5.88 for the x_1-section cuts at 0.05 and 0.10 inches, respectively. A perpendicular section cut is shown in Figure 5.89 for a value of x_2 of 0.0. Isostress plots for σ_{33}^* in the quasi-isotropic $[\pm 45/0/90]_{10S}$ laminate are given in Figures 5.90 and 5.91 for the x_1-section cuts at 0.05 and 0.10 inches, respectively. A perpendicular section cut is shown in Figure 5.92 for a value of x_2 of 0.0. The maximum tensile stress, σ_T^*, for each laminate and its location relative to the groove is presented in Table 5.8. The same data for the maximum compressive stress, σ_C^*, is presented in Table 5.9.

In this three-dimensional, sphere-loaded case, the distribution of the normalized through-thickness extensional stress, σ_{33}^*, is similar to the two-dimensional, cylinder loaded case. In addition, the stress distribution is similar across all laminates studied, with a nearly identical shape in each. There are two major features in this stress distribution. The primary feature is a large region of compressive stress extending from the bottom of the groove to the bottom of the laminate, concentrated local to the area of contact, and expanding out in the 1-direction and 2-direction as depth increases. The secondary feature is a smaller region of tensile stress along the upper wall of the groove, concentrated adjacent to the area of contact and partially wrapping around the primary region of compressive stress. For σ_{33}^*, there is almost no variation within the stress distribution from ply-to-ply due to ply angle, thus the stress field remains mostly continuous between the plies.

The primary compressive region of stress is concentrated beneath the area of contact and is driven by the compressive strain from the loaded indentor. High compressive stresses occur local to this region, but drop off quickly, particularly compared to the two-dimensional case, leading to high gradients. As stress drops with distance from the groove, the stress gradients also decrease. The maximum compressive stress occurs on the groove face near the bottom of the groove, regardless of ply angle or laminate.

The smaller region of tensile stress is wrapped around the upper end of the region of compressive stress, along the upper groove wall. The stresses here are likely due

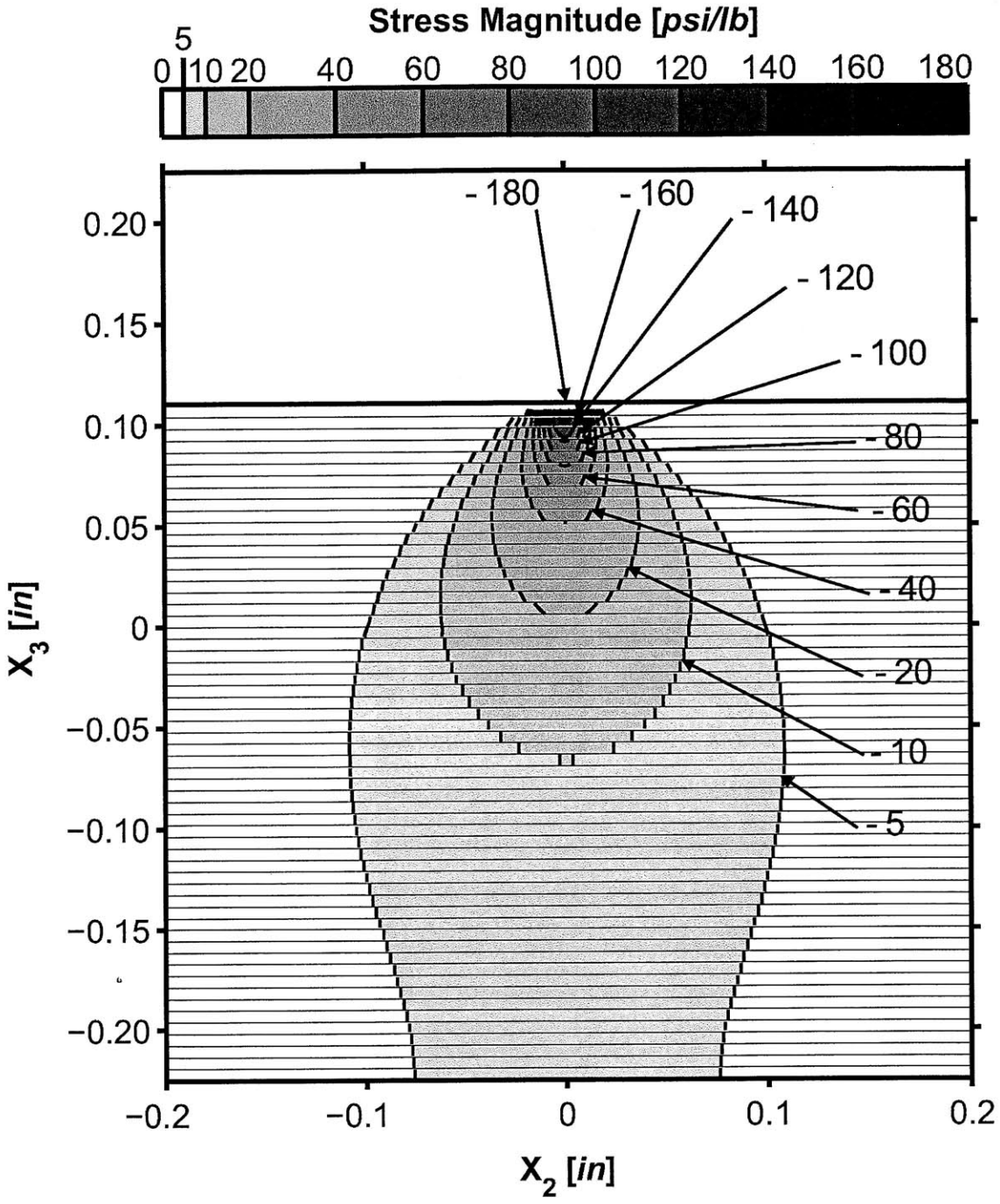

* Note: All stresses normalized by applied load, and given in units of [psi/lb].

Figure 5.75 Isostress plot of σ^*_{33} for a section cut at a value of x_1 of 0.05 inches in the three-dimensional T700/2510 $[\pm 15/0]_{13S}$ laminate model loaded at 300 lb.

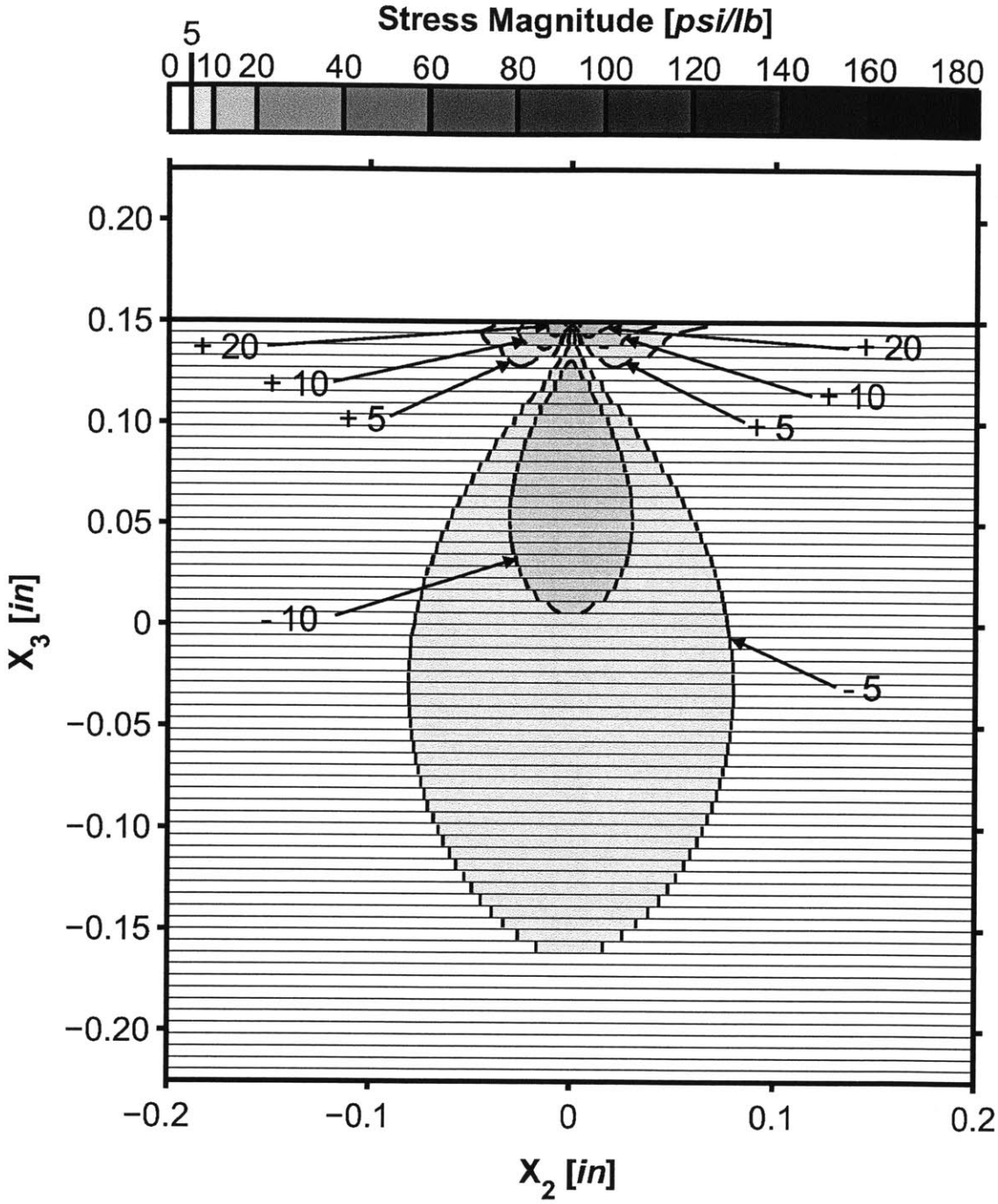

* Note: All stresses normalized by applied load, and given in units of [psi/lb].

Figure 5.76 Isostress plot of σ^*_{33} for a section cut at a value of x_1 of 0.10 inches in the three-dimensional T700/2510 $[\pm 15/0]_{13S}$ laminate model loaded at 300 lb.

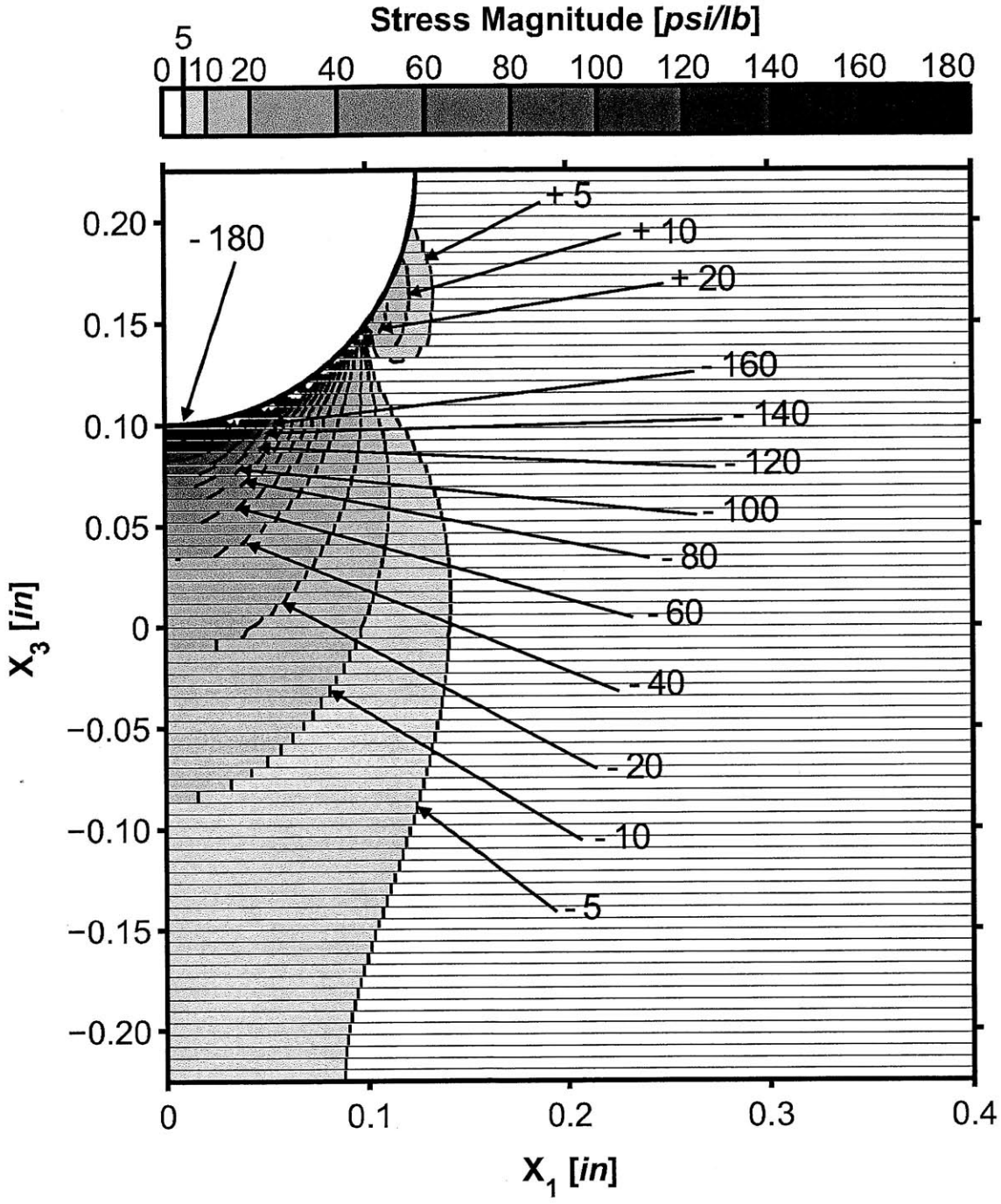

* Note: All stresses normalized by applied load, and given in units of [psi/lb].

Figure 5.77 Isostress plot of σ_{33}^{*} for a section cut at a value of x_2 of 0.0 inches in the three-dimensional T700/2510 $[\pm 15/0]_{13S}$ laminate model loaded at 300 lb.

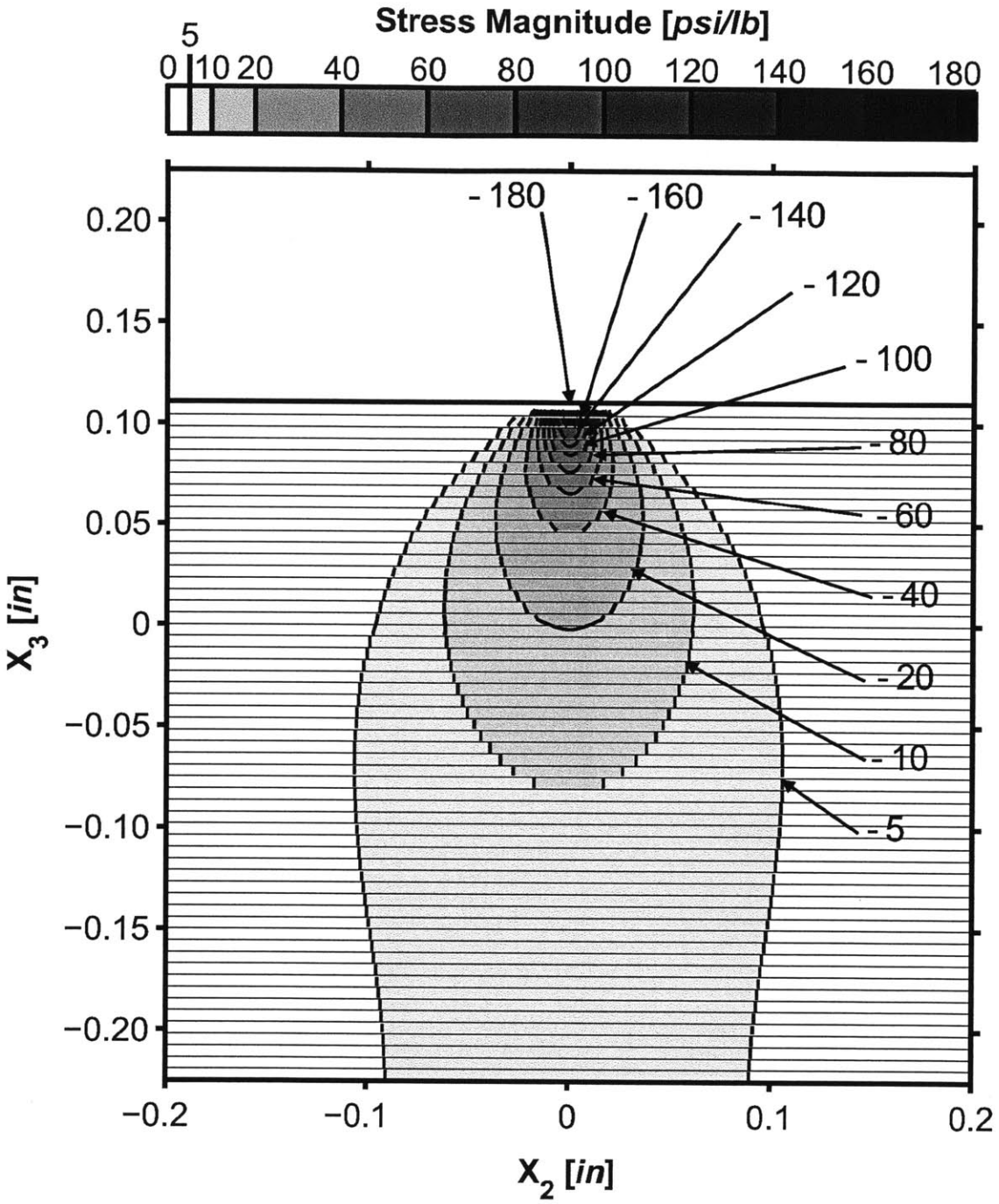

* Note: All stresses normalized by applied load, and given in units of [psi/lb].

Figure 5.78 Isostress plot of σ^*_{33} for a section cut at a value of x_1 of 0.05 inches in the three-dimensional T700/2510 $[\pm 30/0]_{13S}$ laminate model loaded at 300 lb.

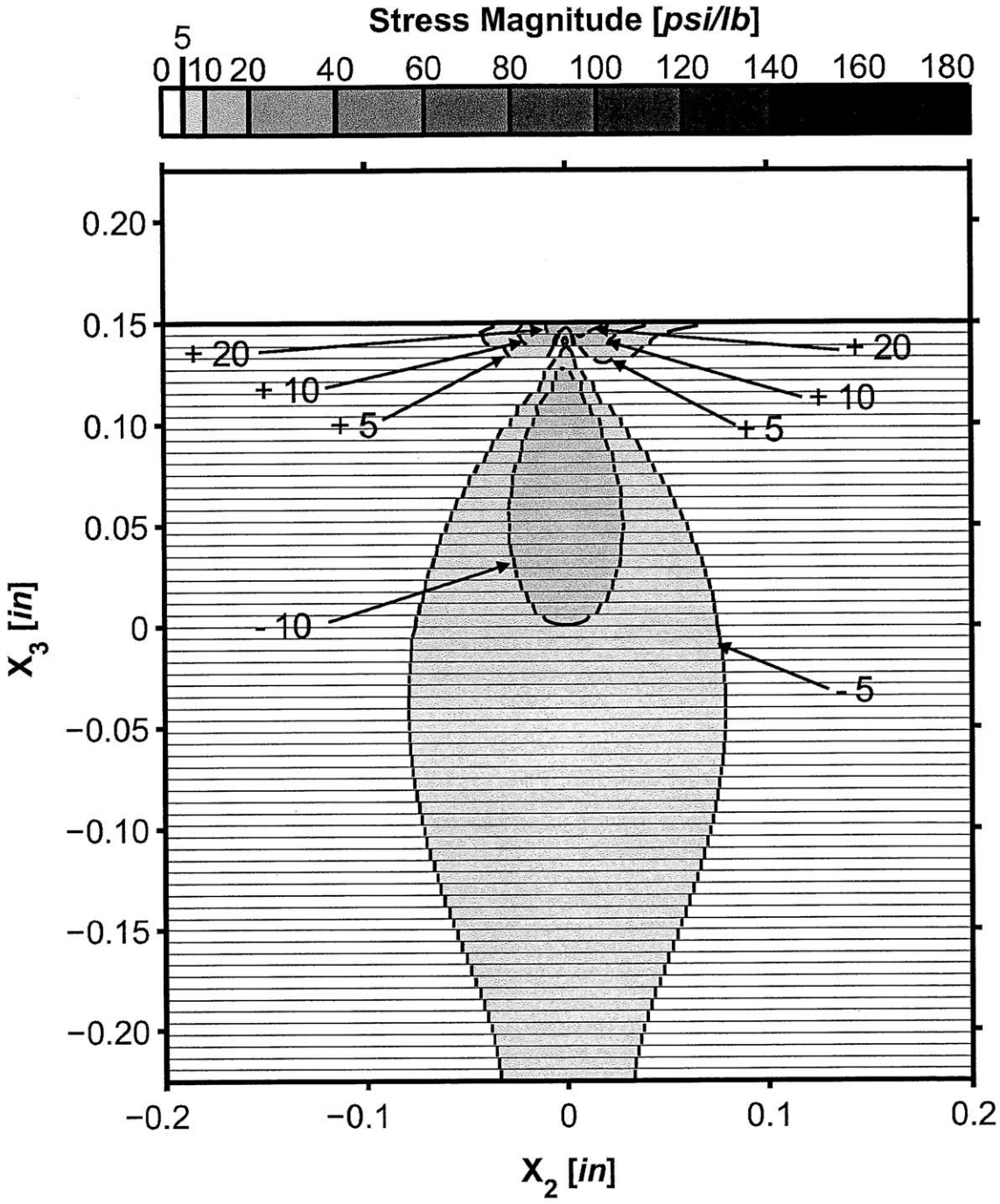

* Note: All stresses normalized by applied load, and given in units of [psi/lb].

Figure 5.79 Isostress plot of σ_{33}^{*} for a section cut at a value of x_1 of 0.10 inches in the three-dimensional T700/2510 $[\pm 30/0]_{13S}$ laminate model loaded at 300 lb.

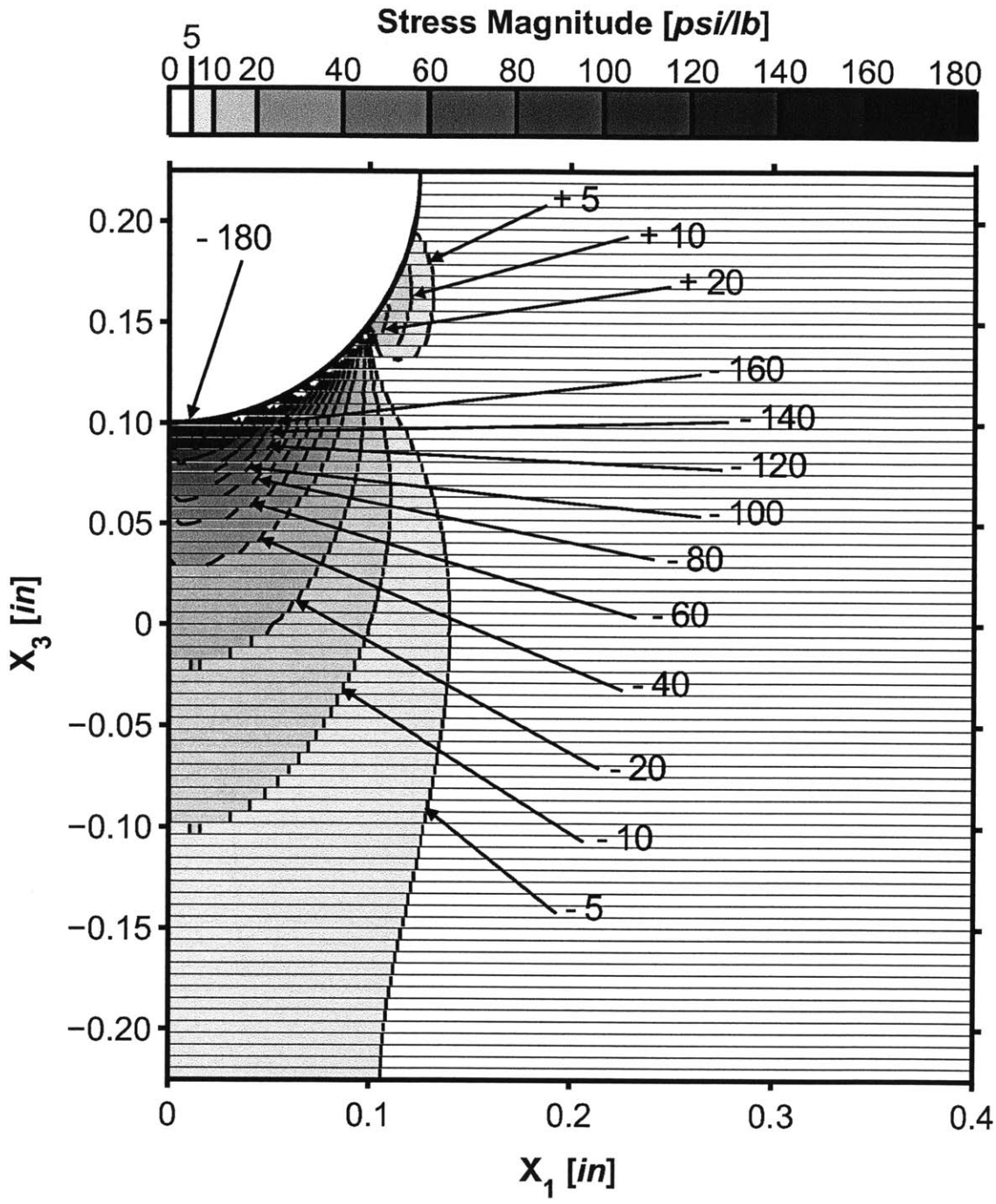

* Note: All stresses normalized by applied load, and given in units of [psi/lb].

Figure 5.80 Isostress plot of σ^*_{33} for a section cut at a value of x_2 of 0.0 inches in the three-dimensional T700/2510 $[\pm 30/0]_{13S}$ laminate model loaded at 300 lb.

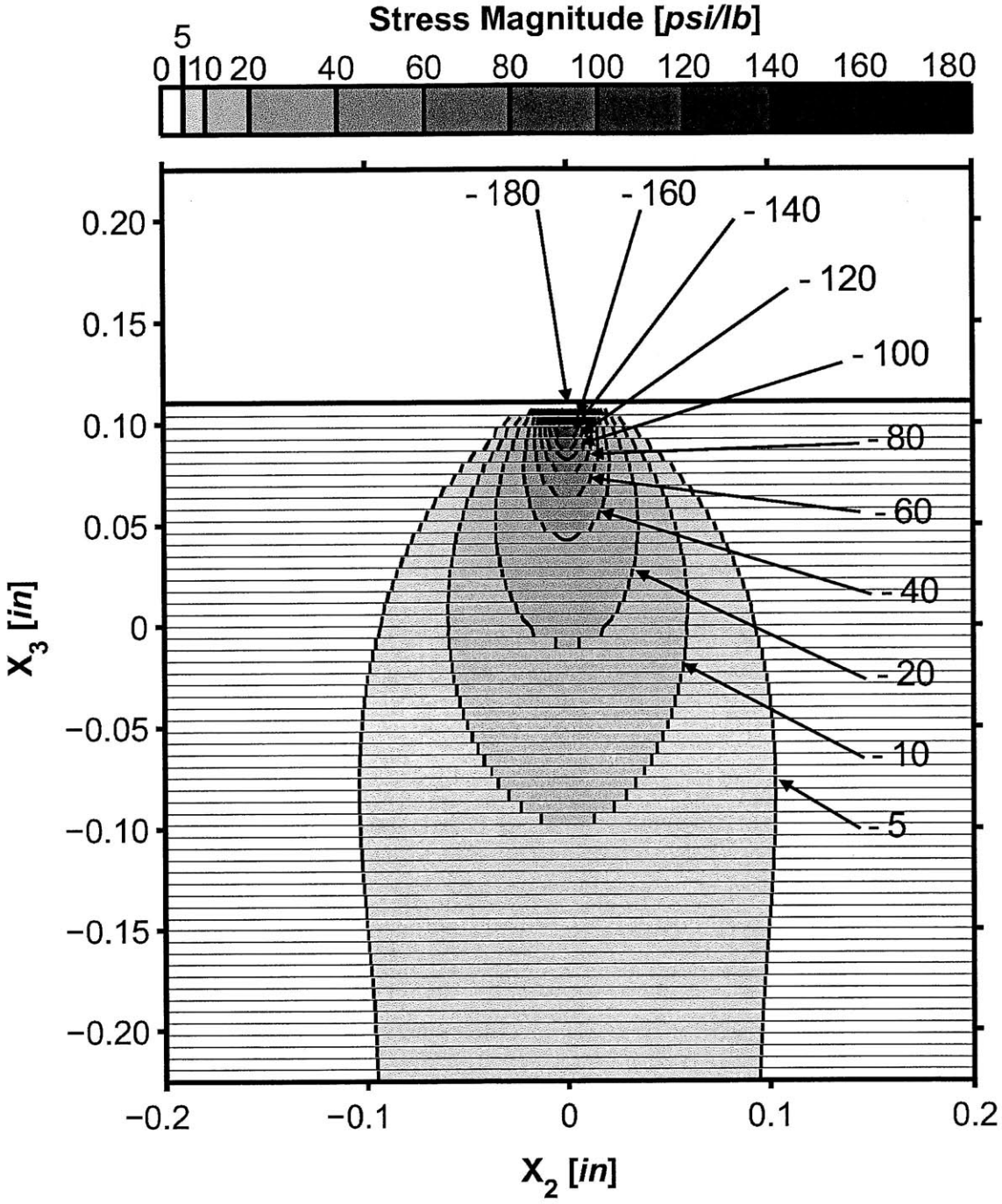

* Note: All stresses normalized by applied load, and given in units of [psi/lb].

Figure 5.81 Isostress plot of σ^*_{33} for a section cut at a value of x_1 of 0.05 inches in the three-dimensional T700/2510 $[\pm 45/0]_{13S}$ laminate model loaded at 300 lb.

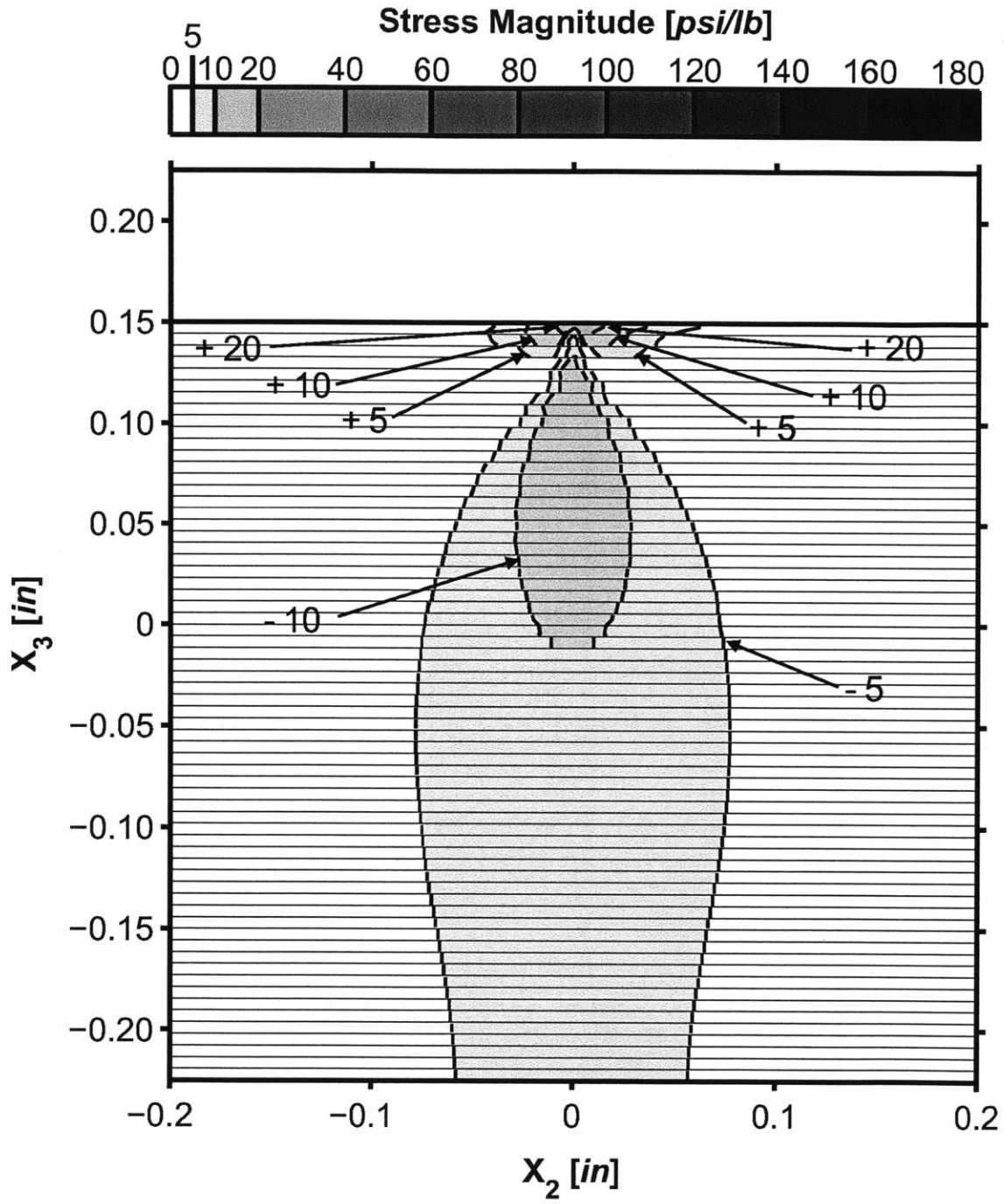

* Note: All stresses normalized by applied load, and given in units of [psi/lb].

Figure 5.82 Isostress plot of σ^*_{33} for a section cut at a value of x_1 of 0.10 inches in the three-dimensional T700/2510 $[\pm 45/0]_{13S}$ laminate model loaded at 300 lb.

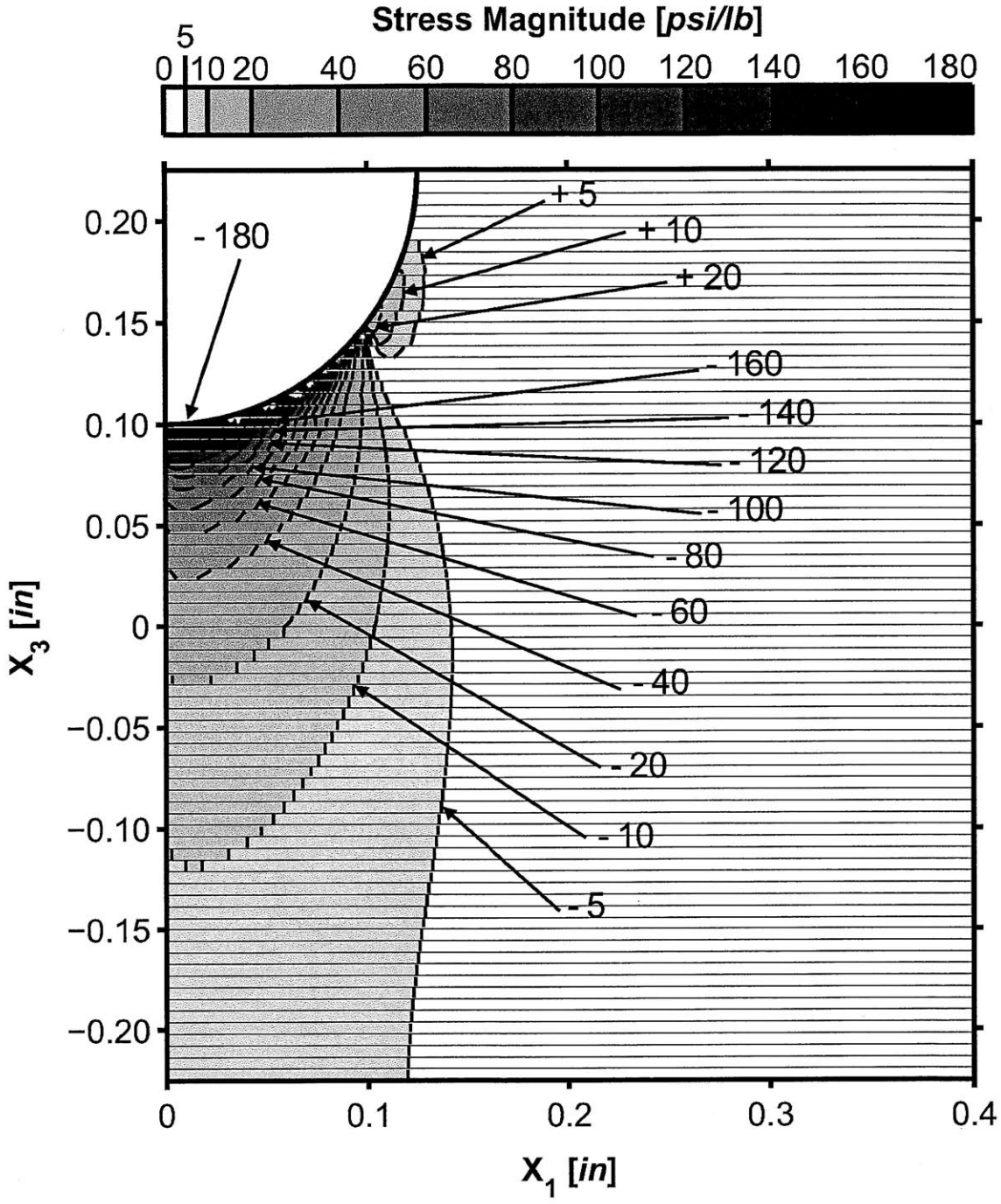

* Note: All stresses normalized by applied load, and given in units of [psi/lb].

Figure 5.83 Isostress plot of σ^*_{33} for a section cut at a value of x_2 of 0.0 inches in the three-dimensional T700/2510 $[\pm 45/0]_{13S}$ laminate model loaded at 300 lb.

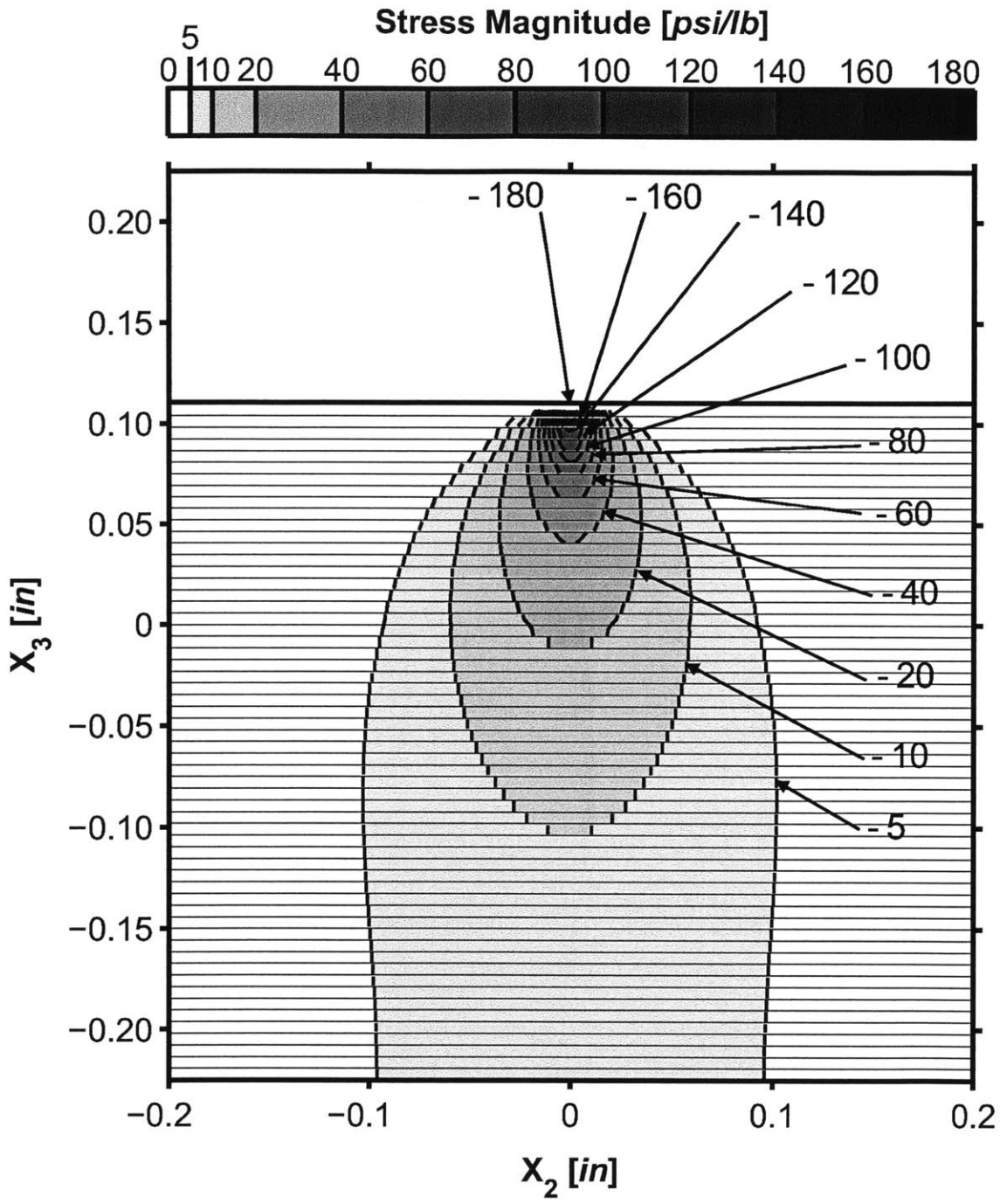

* Note: All stresses normalized by applied load, and given in units of [psi/lb].

Figure 5.84 Isostress plot of σ^*_{33} for a section cut at a value of x_1 of 0.05 inches in the three-dimensional T700/2510 $[\pm 60/0]_{13S}$ laminate model loaded at 300 lb.

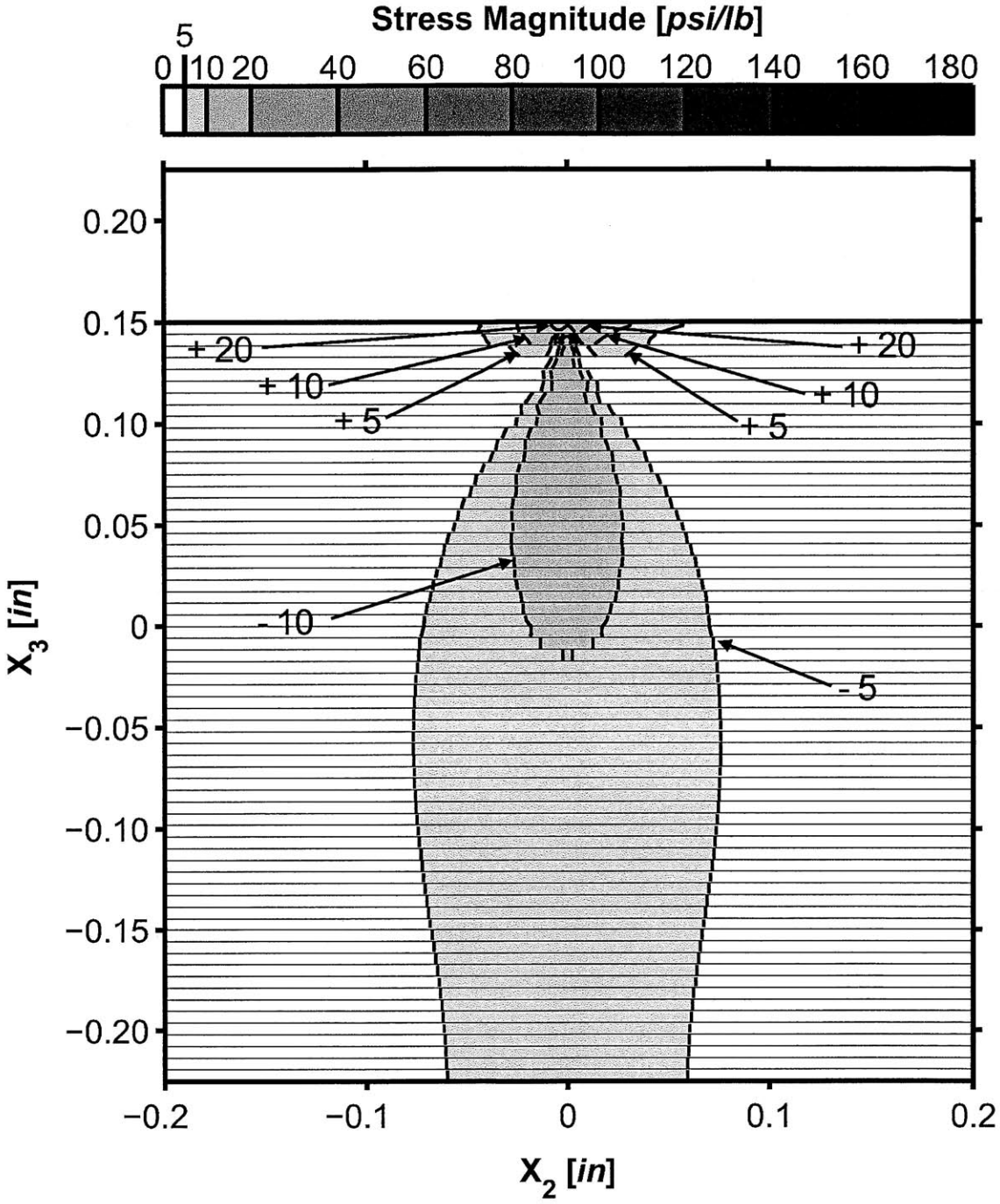

* Note: All stresses normalized by applied load, and given in units of [psi/lb].

Figure 5.85 Isostress plot of σ_{33}^{*} for a section cut at a value of x_1 of 0.10 inches in the three-dimensional T700/2510 $[\pm 60/0]_{13S}$ laminate model loaded at 300 lb.

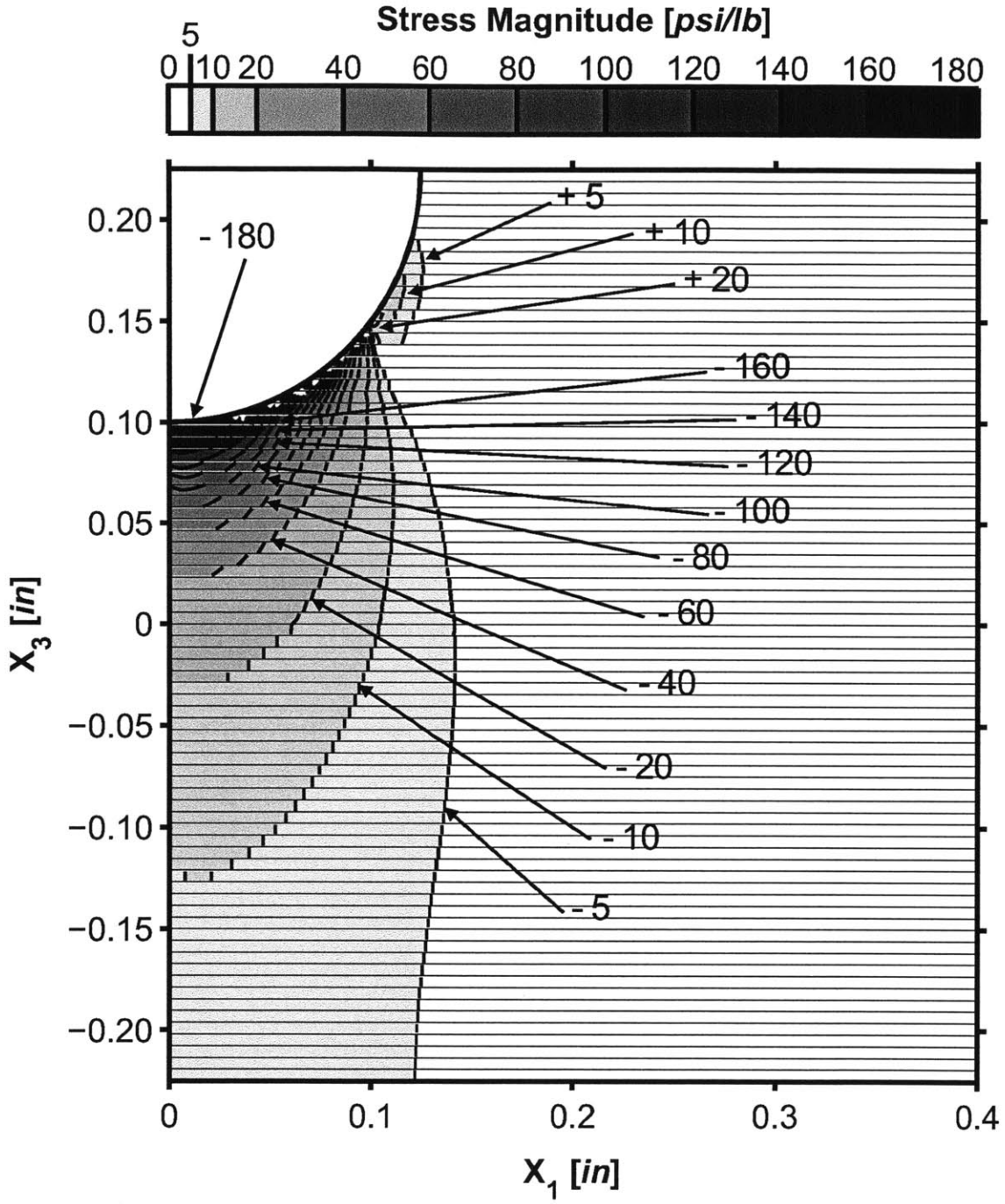

* Note: All stresses normalized by applied load, and given in units of [psi/lb].

Figure 5.86 Isostress plot of σ^*_{33} for a section cut at a value of x_2 of 0.0 inches in the three-dimensional T700/2510 $[\pm 60/0]_{13S}$ laminate model loaded at 300 lb.

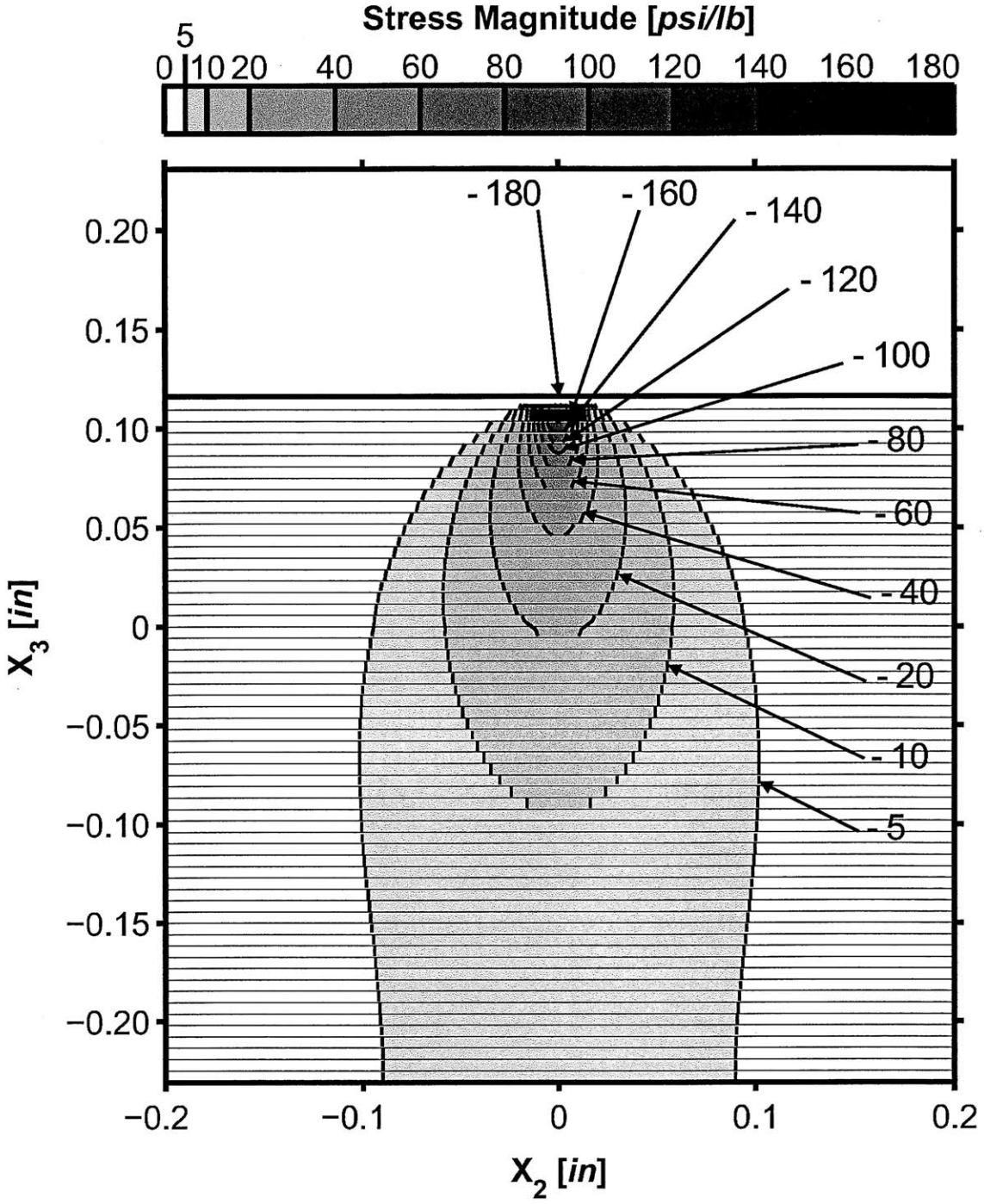

* Note: All stresses normalized by applied load, and given in units of [psi/lb].

Figure 5.87 Isostress plot of σ^*_{33} for a section cut at a value of x_1 of 0.05 inches in the three-dimensional T700/2510 $[90/0]_{20S}$ laminate model loaded at 300 lb.

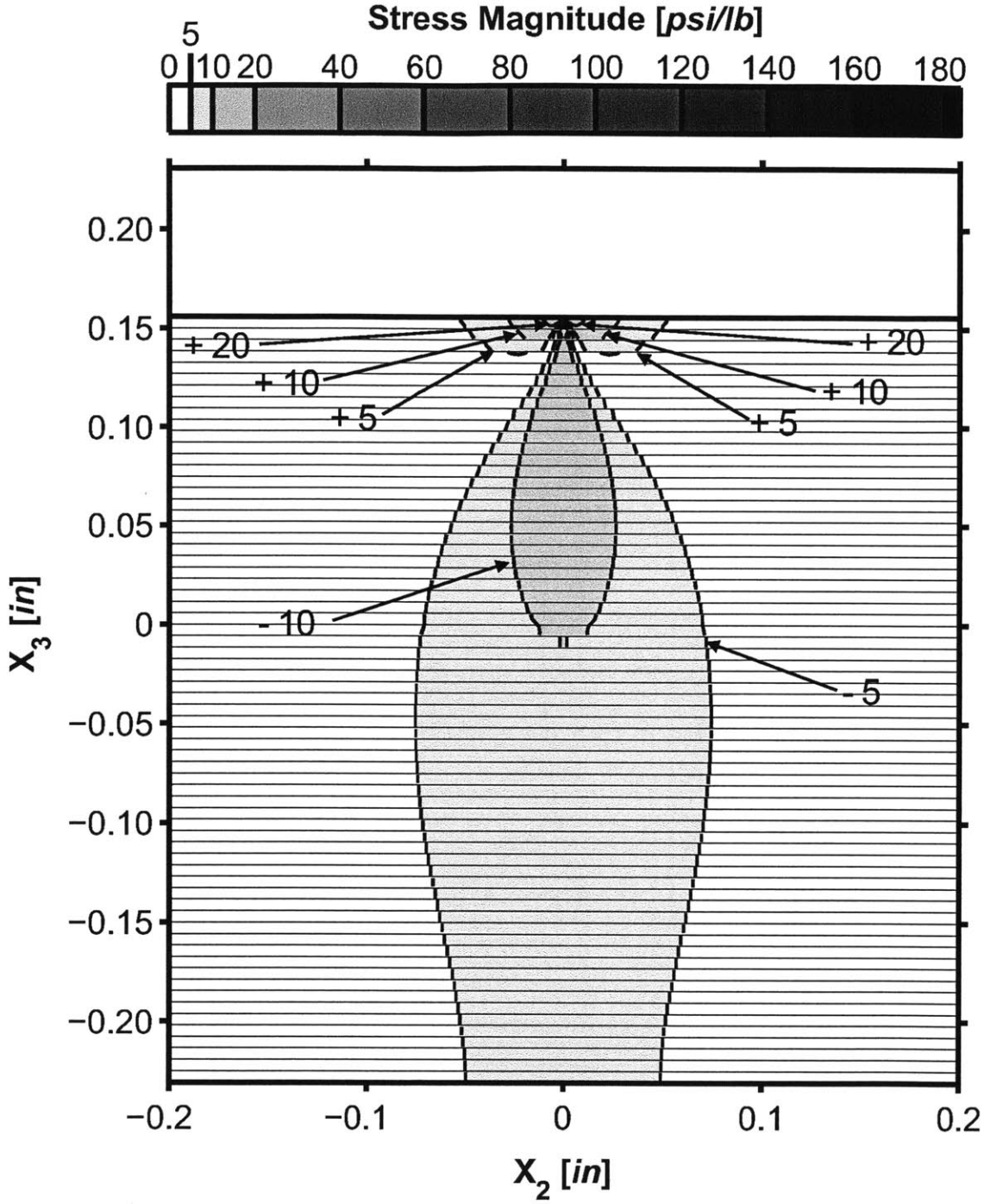

* Note: All stresses normalized by applied load, and given in units of [psi/lb].

Figure 5.88 Isostress plot of σ^*_{33} for a section cut at a value of x_1 of 0.10 inches in the three-dimensional T700/2510 $[90/0]_{20S}$ laminate model loaded at 300 lb.

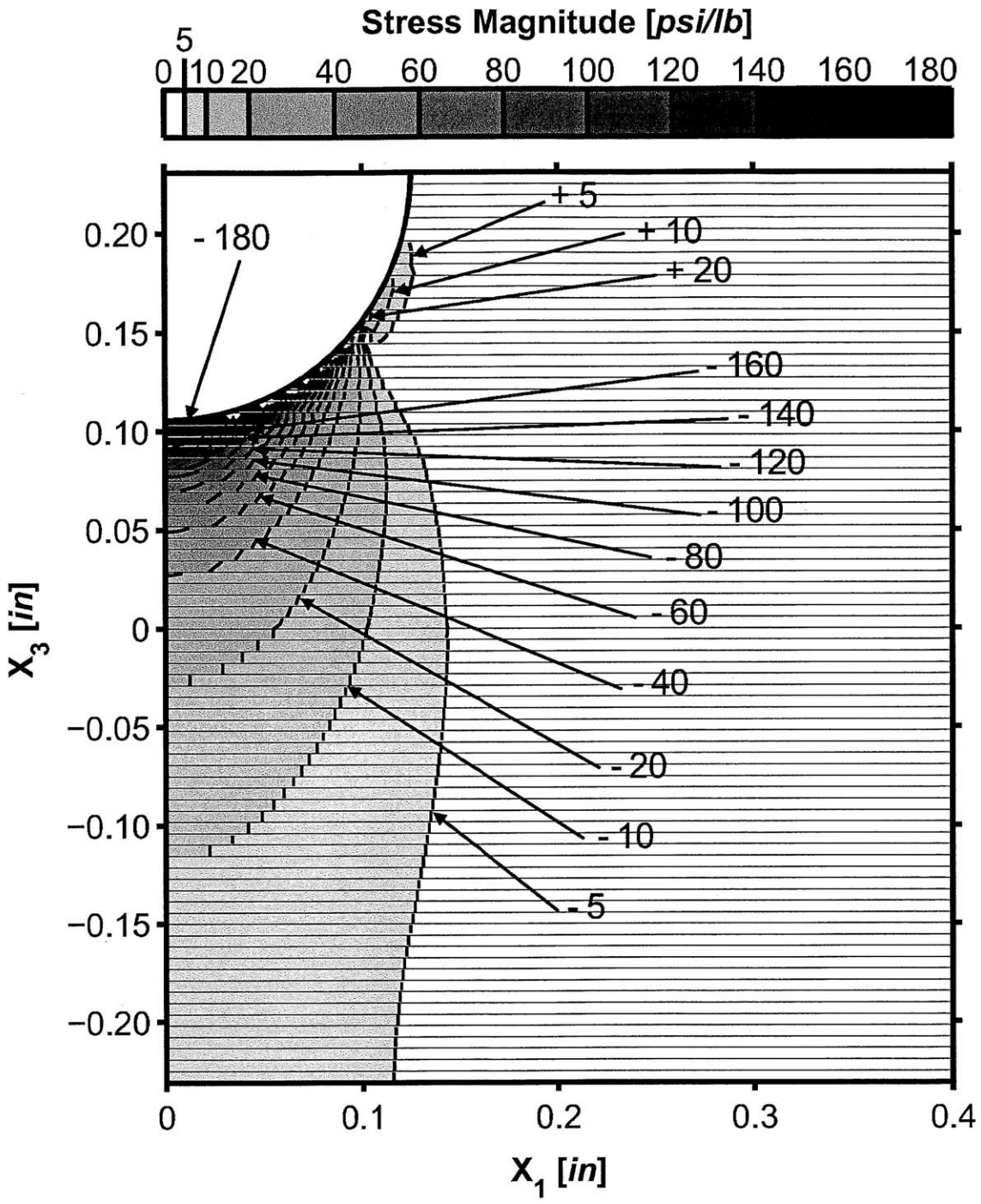

* Note: All stresses normalized by applied load, and given in units of [psi/lb].

Figure 5.89 Isostress plot of σ_{33}^{*} for a section cut at a value of x_2 of 0.0 inches in the three-dimensional T700/2510 $[90/0]_{20S}$ laminate model loaded at 300 lb.

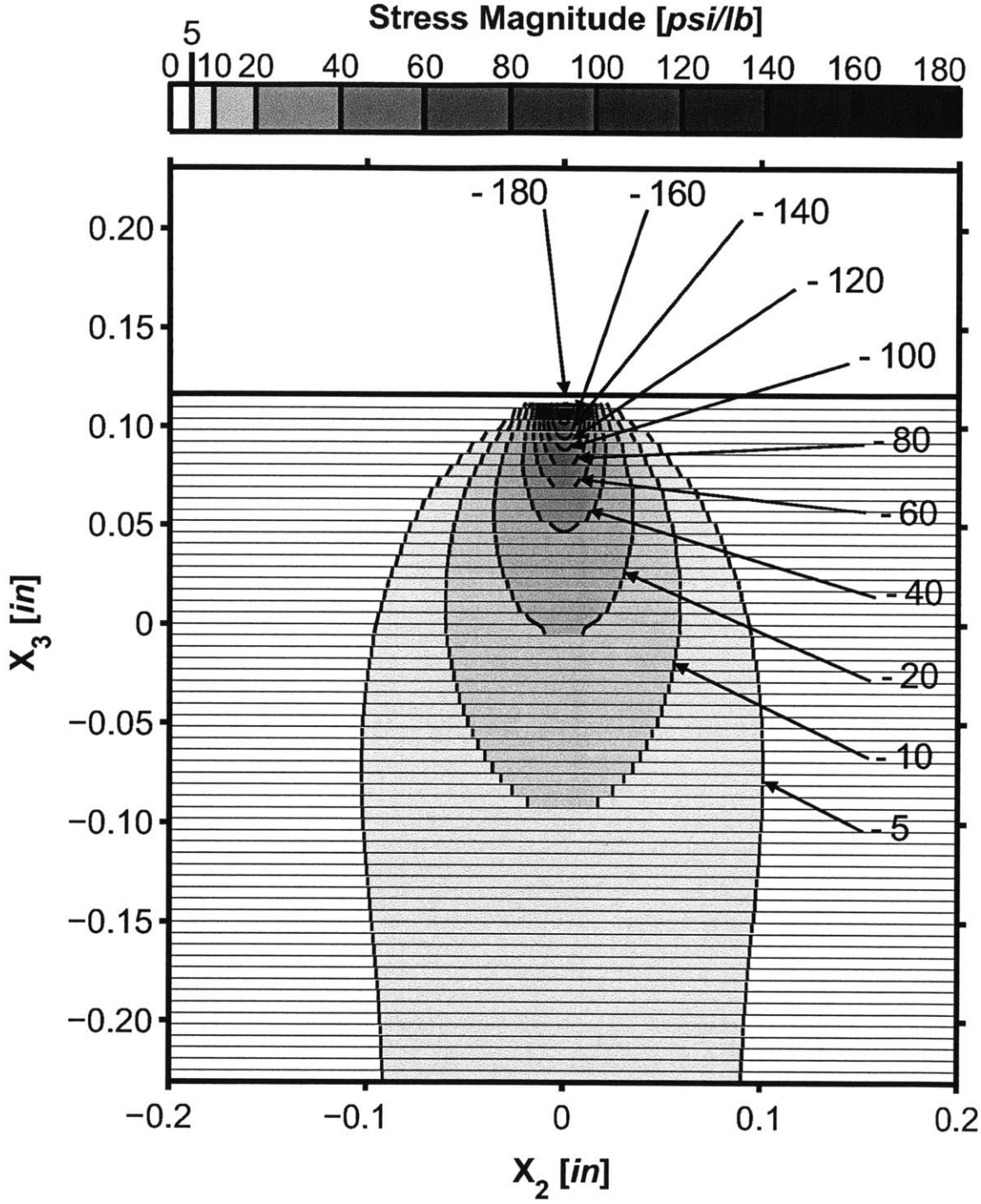

* Note: All stresses normalized by applied load, and given in units of [psi/lb].

Figure 5.90 Isostress plot of σ^*_{33} for a section cut at a value of x_1 of 0.05 inches in the three-dimensional T700/2510 $[\pm 45/0/90]_{10S}$ laminate model loaded at 300 lb.

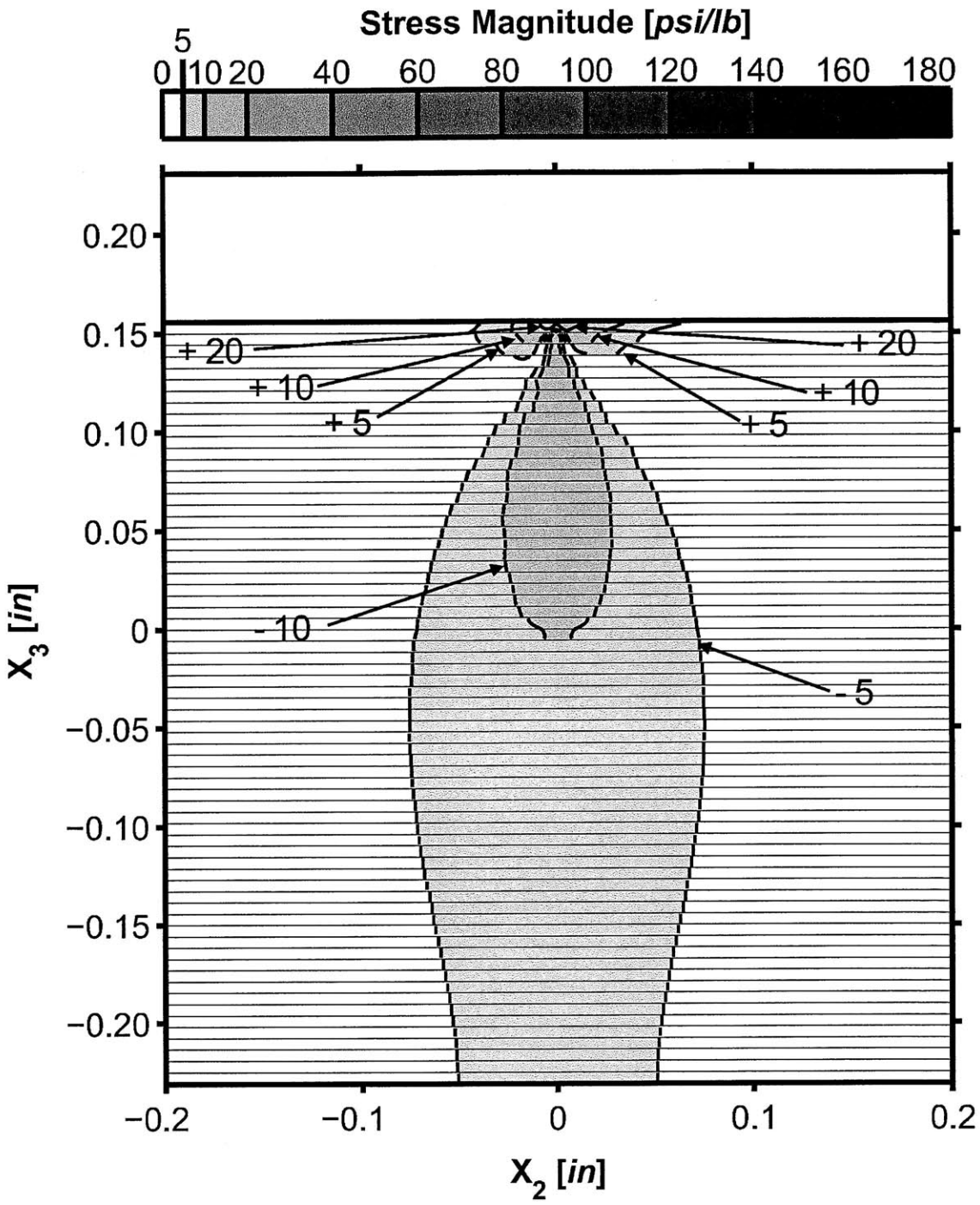

* Note: All stresses normalized by applied load, and given in units of [psi/lb].

Figure 5.91 Isostress plot of σ_{33}^{*} for a section cut at a value of x_1 of 0.10 inches in the three-dimensional T700/2510 $[\pm 45/0/90]_{10S}$ laminate model loaded at 300 lb.

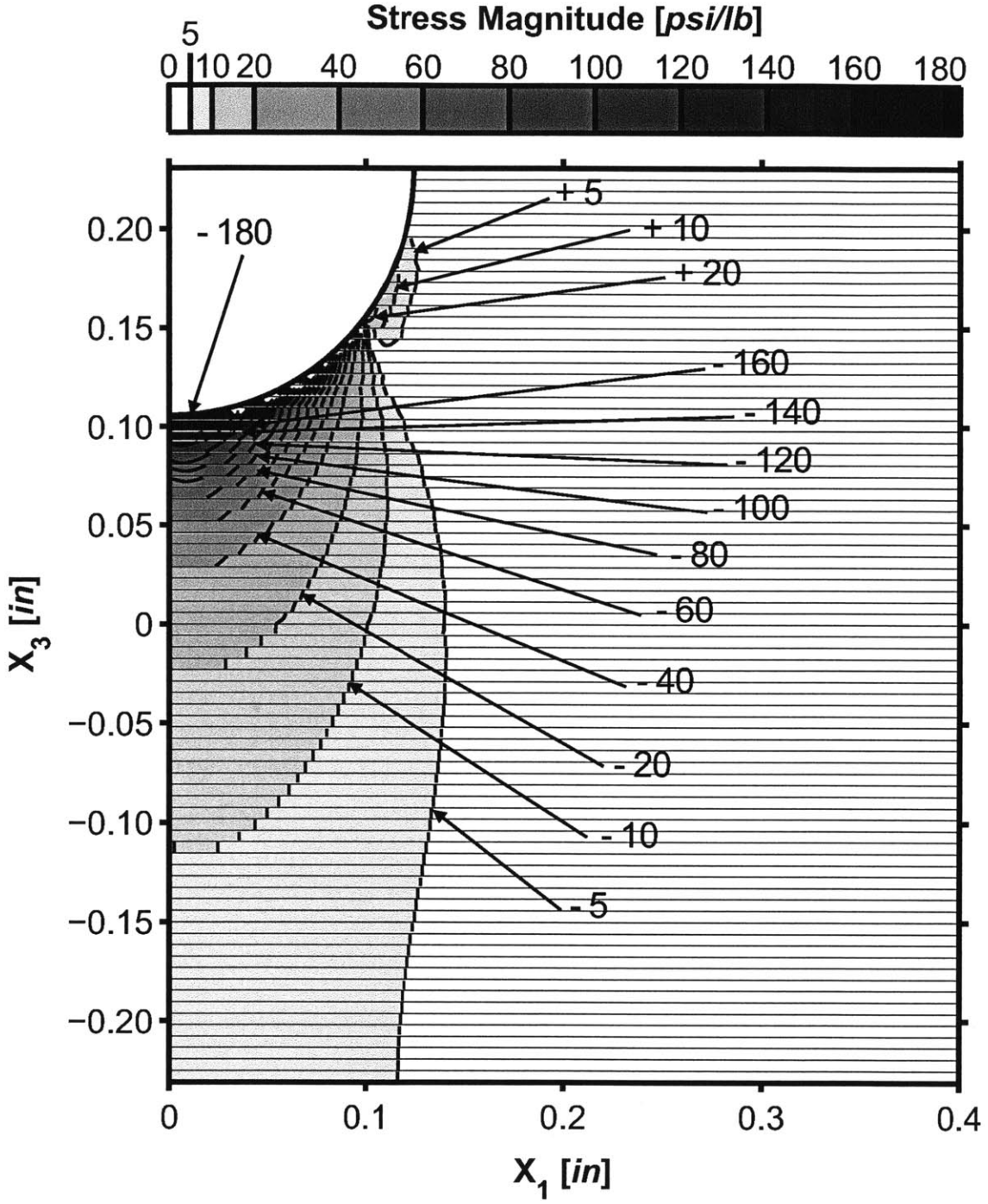

* Note: All stresses normalized by applied load, and given in units of [psi/lb].

Figure 5.92 Isostress plot of σ^*_{33} for a section cut at a value of x_2 of 0.0 inches in the three-dimensional T700/2510 $[\pm 45/0/90]_{10S}$ laminate model loaded at 300 lb.

Table 5.8 Maximum magnitudes of tensile normalized stress values, σ^*_{33}, and locations in cylindrical coordinates for three-dimensional models loaded at 300 lb

Laminate		**Tension**			
Material	Layup	σ^*_T $[psi/lb]$	ϕ_T $[deg]$	r_T $[in]$	x_{2_T} $[in]$
T700/2510	$[\pm 15/0]_{13S}$	49	53.1	0.125	0.0
T700/2510	$[\pm 30/0]_{13S}$	45	52.2	0.125	-0.003
T700/2510	$[\pm 45/0]_{13S}$	39	50.7	0.125	-0.004
T700/2510	$[\pm 60/0]_{13S}$	33	50.7	0.125	-0.004
T700/2510	$[90/0]_{20S}$	36	52.2	0.125	-0.003
T700/2510	$[\pm 45/0/90]_{10S}$	36	50.7	0.125	-0.004

Table 5.9 Maximum magnitudes of compressive normalized stress values, σ^*_{33}, and locations in cylindrical coordinates for three-dimensional models loaded at 300 lb

Laminate		**Compression**			
Material	Layup	σ^*_C $[psi/lb]$	ϕ_C $[deg]$	r_C $[in]$	x_{2_C} $[in]$
T700/2510	$[\pm 15/0]_{13S}$	-278	2.5	0.125	0.0
T700/2510	$[\pm 30/0]_{13S}$	-289	2.5	0.125	0.0
T700/2510	$[\pm 45/0]_{13S}$	-300	3.0	0.125	0.0
T700/2510	$[\pm 60/0]_{13S}$	-313	10.2	0.125	0.0
T700/2510	$[90/0]_{20S}$	-319	1.0	0.125	0.0
T700/2510	$[\pm 45/0/90]_{10S}$	-316	3.0	0.125	0.0

to the elastic resistance of the laminate to the deformation from the indentor. While the indentor depresses a local area of the laminate in the groove, the remainder of the structure maintains the stiffness and position of the laminate topface, leading to the tension between the two regions. The maximum tensile stress occurs in a relatively consistent region between an angular location of ϕ of 50.7° and 53.1° on the surface of the groove.

There is little variation from laminate to laminate in the stress field of σ^*_{33}, although some differences are apparent on close examination of the $[\pm\theta/0]_{13S}$ laminates. Generally, as θ increases, the compressive stresses increase, while the tensile stresses decrease. The increase in compressive stress is apparent upon close examination of the section cuts, particularly those at a value of x_1 of 0.05 inches and of x_2 of 0.0 inches, with the isostress lines slightly increasing in range across the 1-direction, increasing in depth in the 3-direction, and slightly thinning in the 2-direction. The decrease in tensile stress is apparent on examining the section cuts at a value of x_1 of 0.10 inches and of x_2 of 0.0 inches. The maximum normalized compressive stress, σ^*_C, similarly increases by approximately 12% from -278 psi/lb to -313 psi/lb as θ increases from $[\pm15/0]_{13S}$ to $[\pm60/0]_{13S}$. The maximum normalized tensile stress, σ^*_T, decreases by approximatley -36% from 49 psi/lb to 33 psi/lb, as θ increases from 15° to 60° in the $[\pm\theta/0]_{13S}$ laminates.

The distribution of normalized shear stress, σ^*_{13}, for the $[\pm15/0]_{13S}$ laminate is shown in Figures 5.93 and 5.94 for the section cuts at a value of x_1 of 0.10 inches and a value of x_2 of 0.0 inches, respectively. Isostress plots for σ^*_{13} for the $[\pm30/0]_{13S}$ laminate are shown in Figures 5.95 and 5.96 for the section cuts at a value of x_1 of 0.10 inches and a value of x_2 of 0.0 inches, respectively. Isostress plots for σ^*_{13} for the $[\pm45/0]_{13S}$ laminate are shown in Figures 5.97 and 5.98 for the section cuts at a value of x_1 of 0.10 inches and a value of x_2 of 0.0 inches, respectively. Isostress plots for σ^*_{13} for the $[\pm60/0]_{13S}$ laminate are presented in Figures 5.99 and 5.100 for the section cuts at a value of x_1 of 0.10 inches and a value of x_2 of 0.0 inches, respectively. Isostress plots for σ^*_{13} for the cross-ply $[90/0]_{20S}$ laminate are shown in Figures 5.101 and 5.102 for the section cuts at a value of x_1 of 0.10 inches and a

value of x_2 of 0.0 inches, respectively. Isostress plots for σ_{13}^* for the quasi-isotropic $[\pm 45/0/90]_{10S}$ laminate are provided in Figures 5.103 and 5.104 for the section cuts at a value of x_1 of 0.10 inches and a value of x_2 of 0.0 inches, respectively. Values and locations for the maximum normalized shear stress, σ_S^*, are given in Table 5.10 for all laminates studied. Locations for maximum shear stress are provided in the cylindrical coordinate system of the groove.

The shape of the normalized shear stress distribution, σ_{13}^*, is consistent across all laminates. The shear stress is most likely driven by the shear strain caused by the loaded indentor. The stress distribution consists of a single lobe of positive shear stress extending into the laminate from the bottom and sides of the groove. The shear stress is concentrated on the groove face along the area of contact and particularly near an angular location, ϕ, of approximately 40°. The shear stress difference from ply-to-ply is relatively small, resulting in a mostly continuous stress distribution for most laminates investigated. It is apparent that the small difference in stress between plies is dependent on the difference in angle between the plies, with greater angles resulting in greater differences in stress. Generally, the smaller the ply angle, the lower the shear stress.

Examining the $[\pm\theta/0]_{13S}$ laminates, a few trends are apparent. As mentioned above, as θ increases, the difference in stress between neighboring plies of different angles increases. This is evident in the waviness of the isostress lines from one ply to the next. Generally, as θ increases, the maximum shear stress, σ_{13}^*, increases slightly as well, with the exception of the $[\pm 15/0]_{13S}$ laminate, which has a higher maximum shear stress than the $[\pm 30/0]_{13S}$ laminate. The change from least to greatest maximum shear stress is approximately 8%. The location of maximum shear stress remains relatively consistent across all laminates, lying on the face of the groove at an x_2 value of 0.0 and between an angular location, ϕ, of 38.3° and 43.3°.

5.3.3 Effect of Load Magnitude

The linearity of the response is investigated by changing the magnitude of the load applied to the indentor. As with the two-dimensional, cylinder-loaded case,

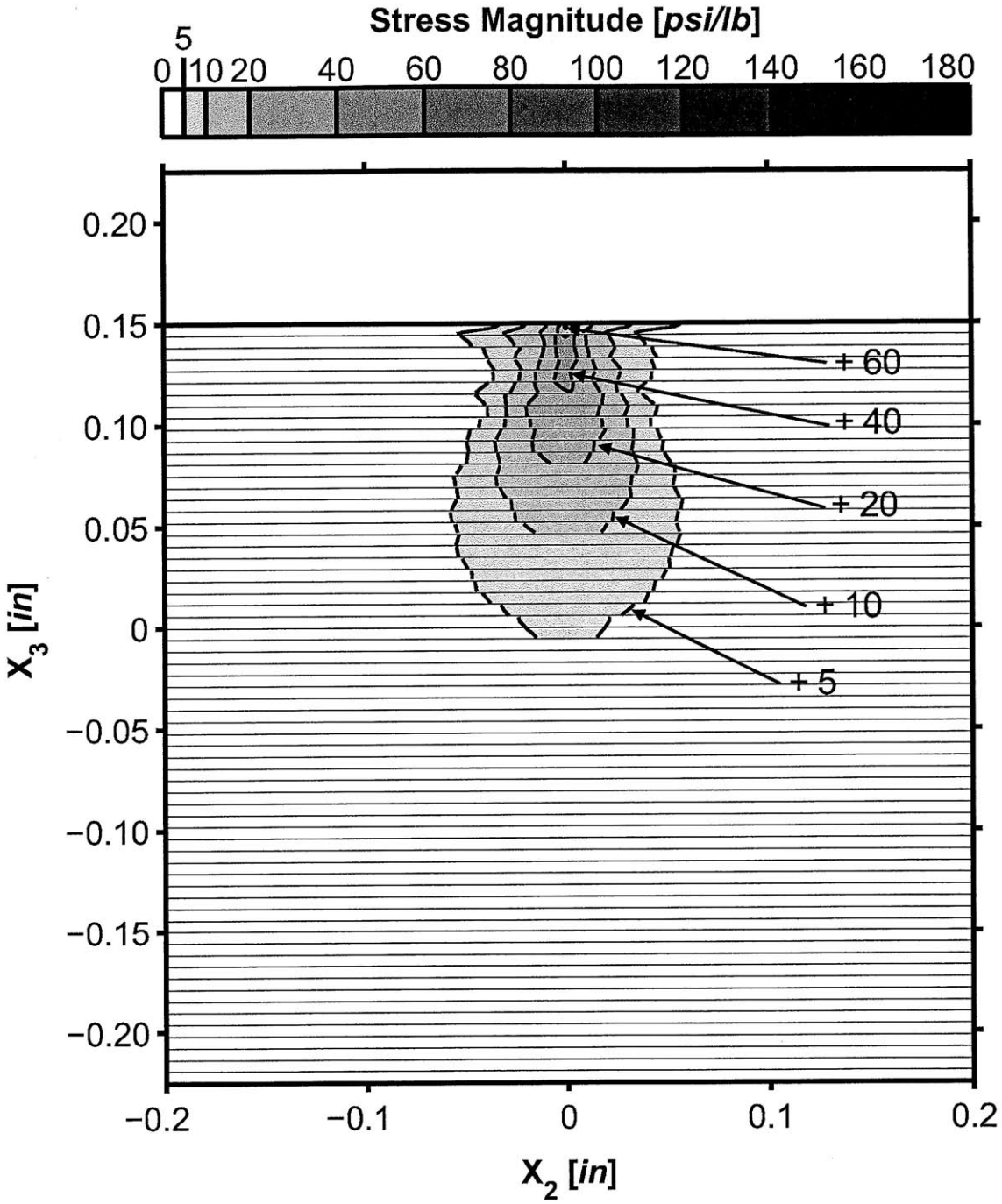

* Note: All stresses normalized by applied load, and given in units of [psi/lb].

Figure 5.93 Isostress plot of σ^*_{13} for a section cut at a value of x_1 of 0.10 inches in the three-dimensional T700/2510 $[\pm 15/0]_{13S}$ laminate model loaded at 300 lb.

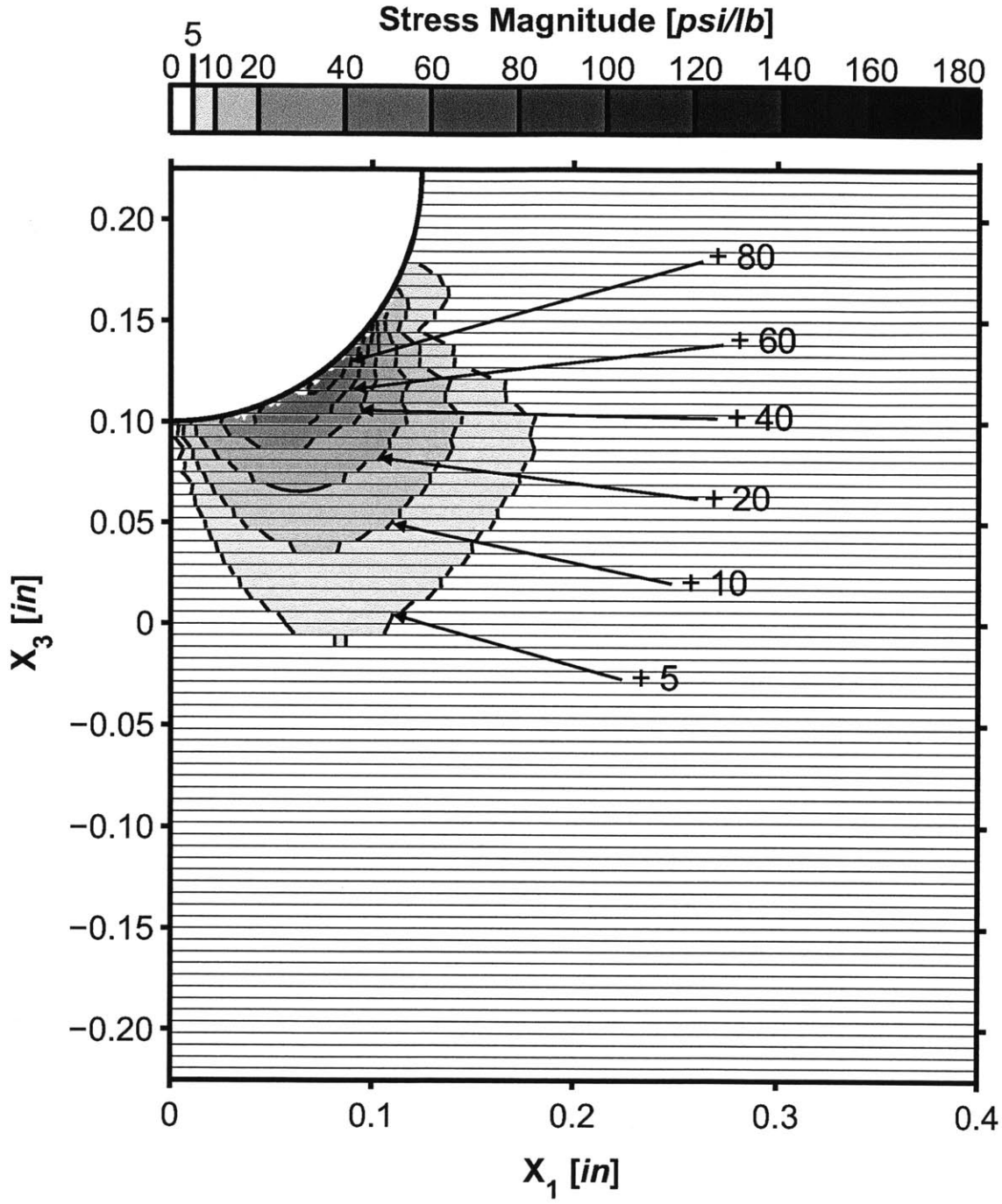

* Note: All stresses normalized by applied load, and given in units of [psi/lb].

Figure 5.94 Isostress plot of σ^*_{13} for a section cut at a value of x_2 of 0.0 inches in the three-dimensional T700/2510 $[\pm 15/0]_{13S}$ laminate model loaded at 300 lb.

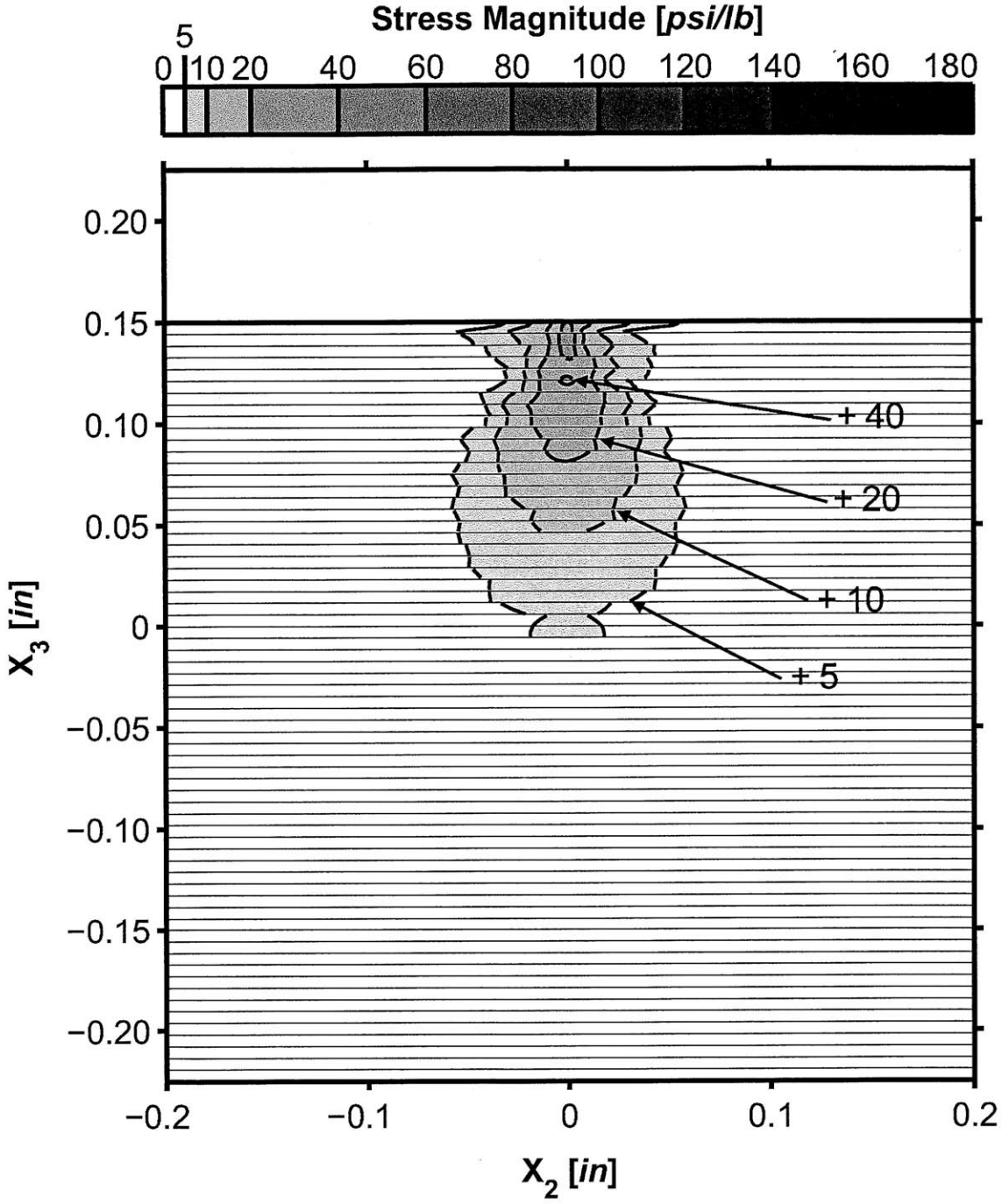

* Note: All stresses normalized by applied load, and given in units of [psi/lb].

Figure 5.95 Isostress plot of σ^*_{13} for a section cut at a value of x_1 of 0.10 inches in the three-dimensional T700/2510 $[\pm 30/0]_{13S}$ laminate model loaded at 300 lb.

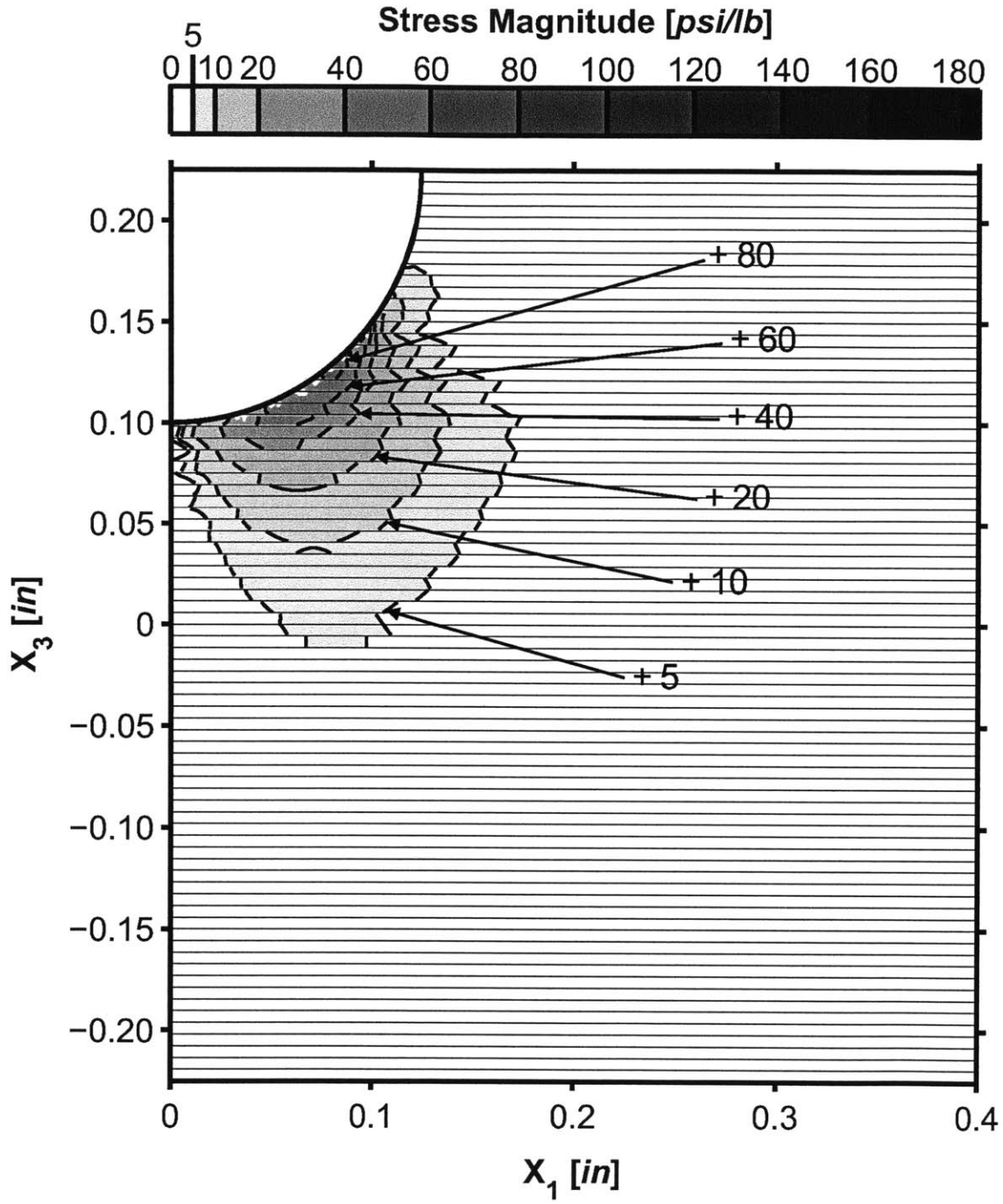

* Note: All stresses normalized by applied load, and given in units of [psi/lb].

Figure 5.96 Isostress plot of σ^*_{13} for a section cut at a value of x_2 of 0.0 inches in the three-dimensional T700/2510 $[\pm 30/0]_{13S}$ laminate model loaded at 300 lb.

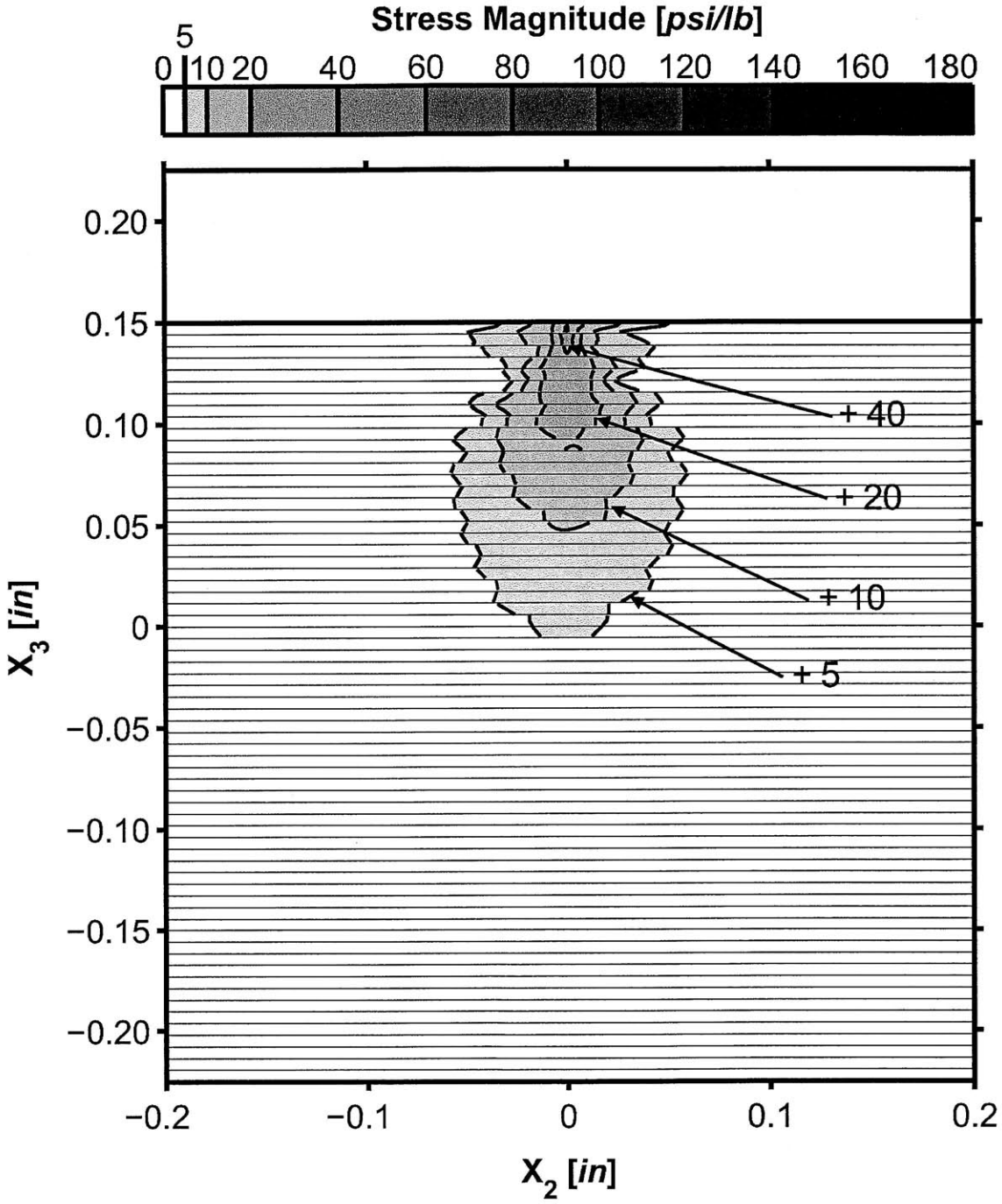

* Note: All stresses normalized by applied load, and given in units of [psi/lb].

Figure 5.97 Isostress plot of σ^*_{13} for a section cut at a value of x_1 of 0.10 inches in the three-dimensional T700/2510 $[\pm 45/0]_{13S}$ laminate model loaded at 300 lb.

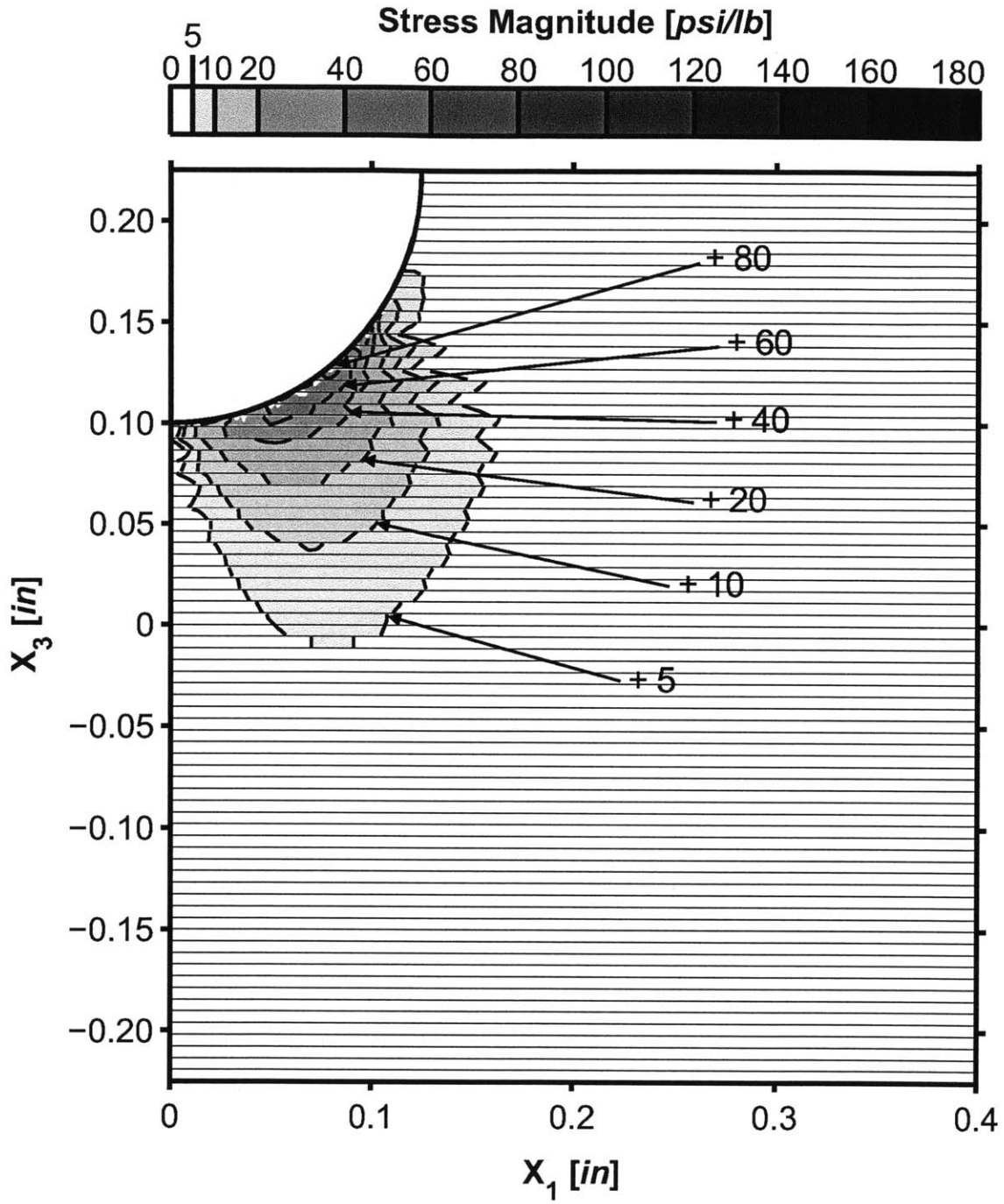

* Note: All stresses normalized by applied load, and given in units of [psi/lb].

Figure 5.98 Isostress plot of σ^*_{13} for a section cut at a value of x_2 of 0.0 inches in the three-dimensional T700/2510 $[\pm 45/0]_{13S}$ laminate model loaded at 300 lb.

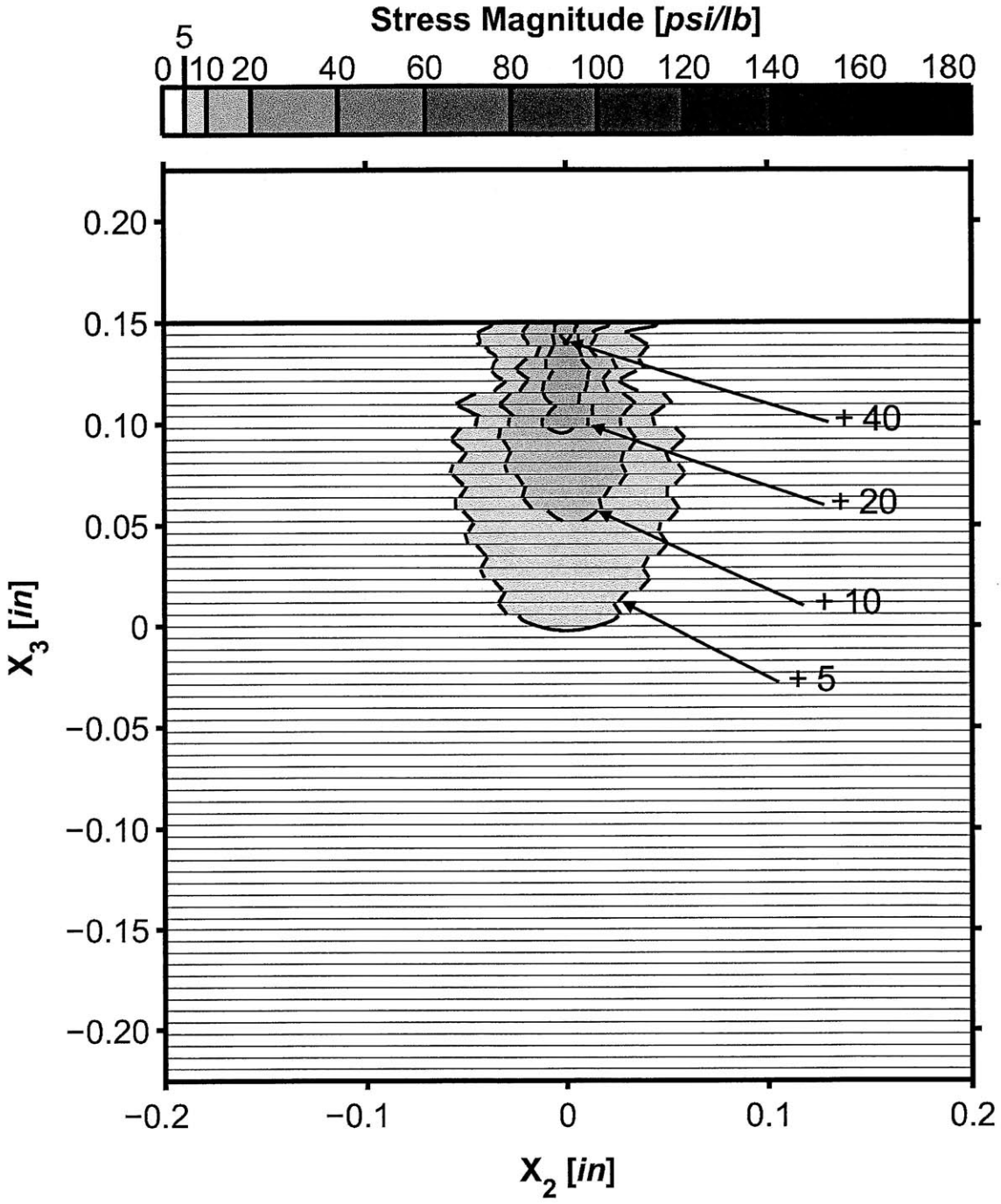

* Note: All stresses normalized by applied load, and given in units of [psi/lb].

Figure 5.99 Isostress plot of σ_{13}^{*} for a section cut at a value of x_1 of 0.10 inches in the three-dimensional T700/2510 $[\pm 60/0]_{13S}$ laminate model loaded at 300 lb.

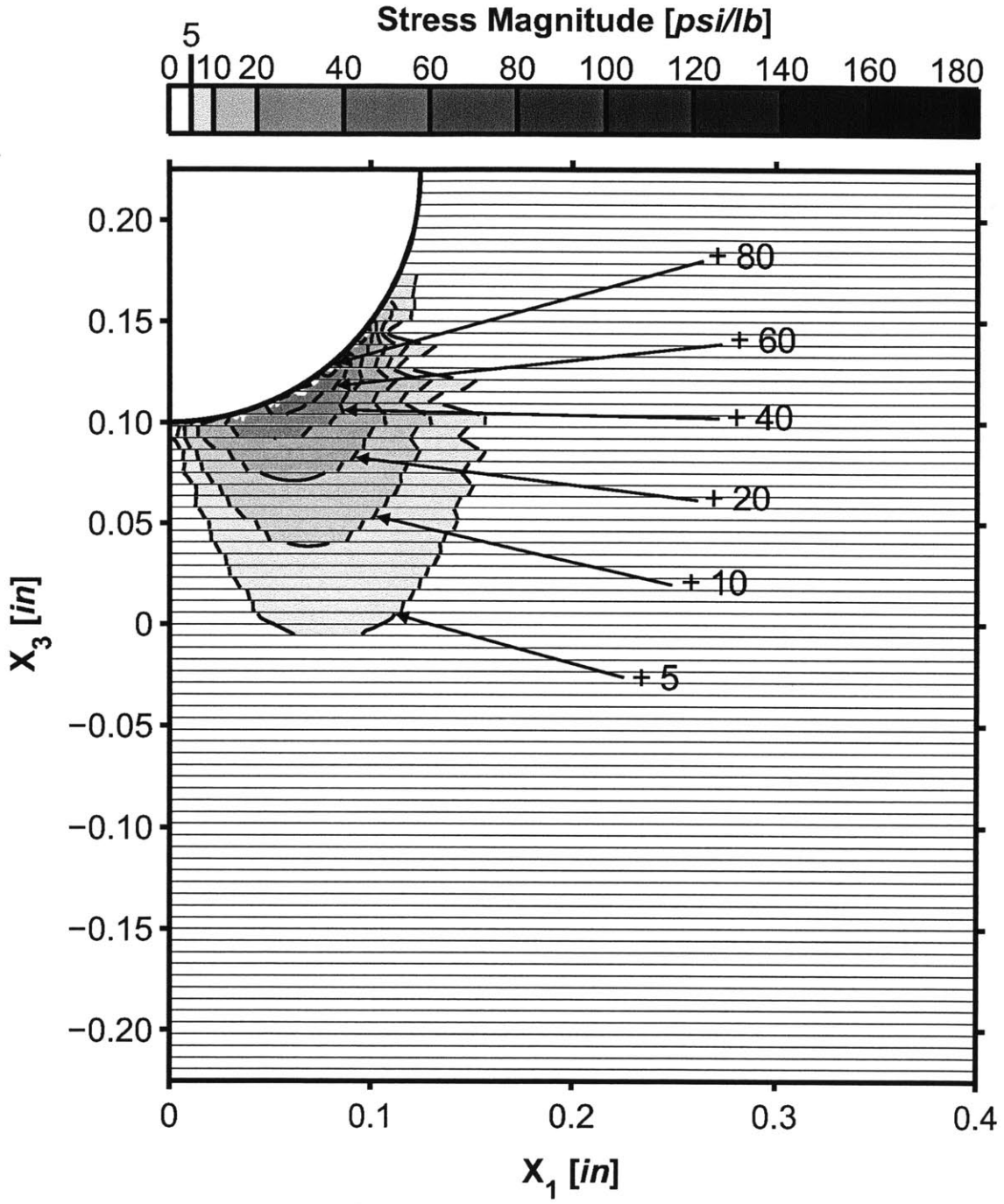

* Note: All stresses normalized by applied load, and given in units of [psi/lb].

Figure 5.100 Isostress plot of σ_{13}^{*} for a section cut at a value of x_2 of 0.0 inches in the three-dimensional T700/2510 $[\pm 60/0]_{13S}$ laminate model loaded at 300 lb.

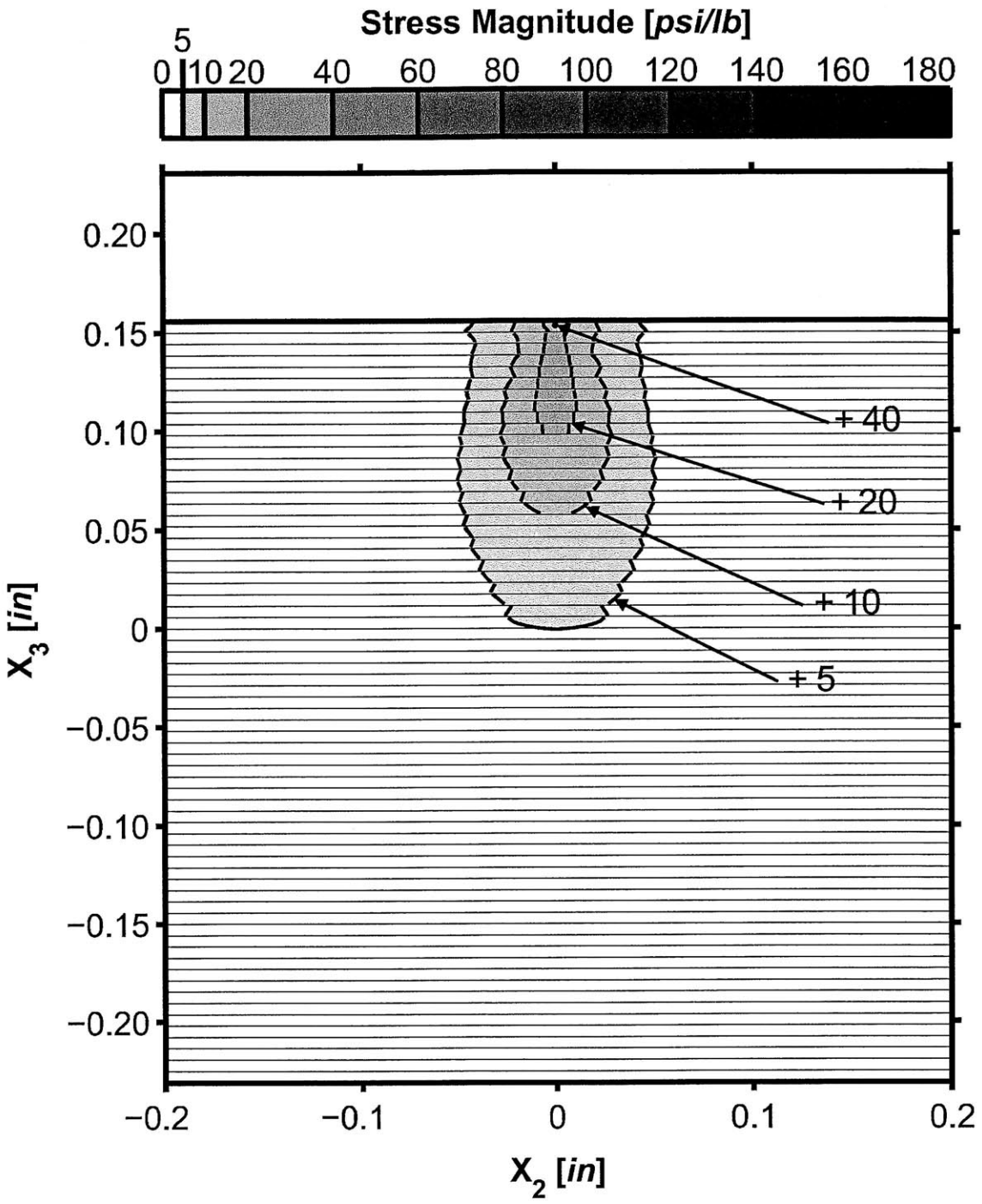

* Note: All stresses normalized by applied load, and given in units of [psi/lb].

Figure 5.101 Isostress plot of σ^*_{13} for a section cut at a value of x_1 of 0.10 inches in the three-dimensional T700/2510 $[90/0]_{20S}$ laminate model loaded at 300 lb.

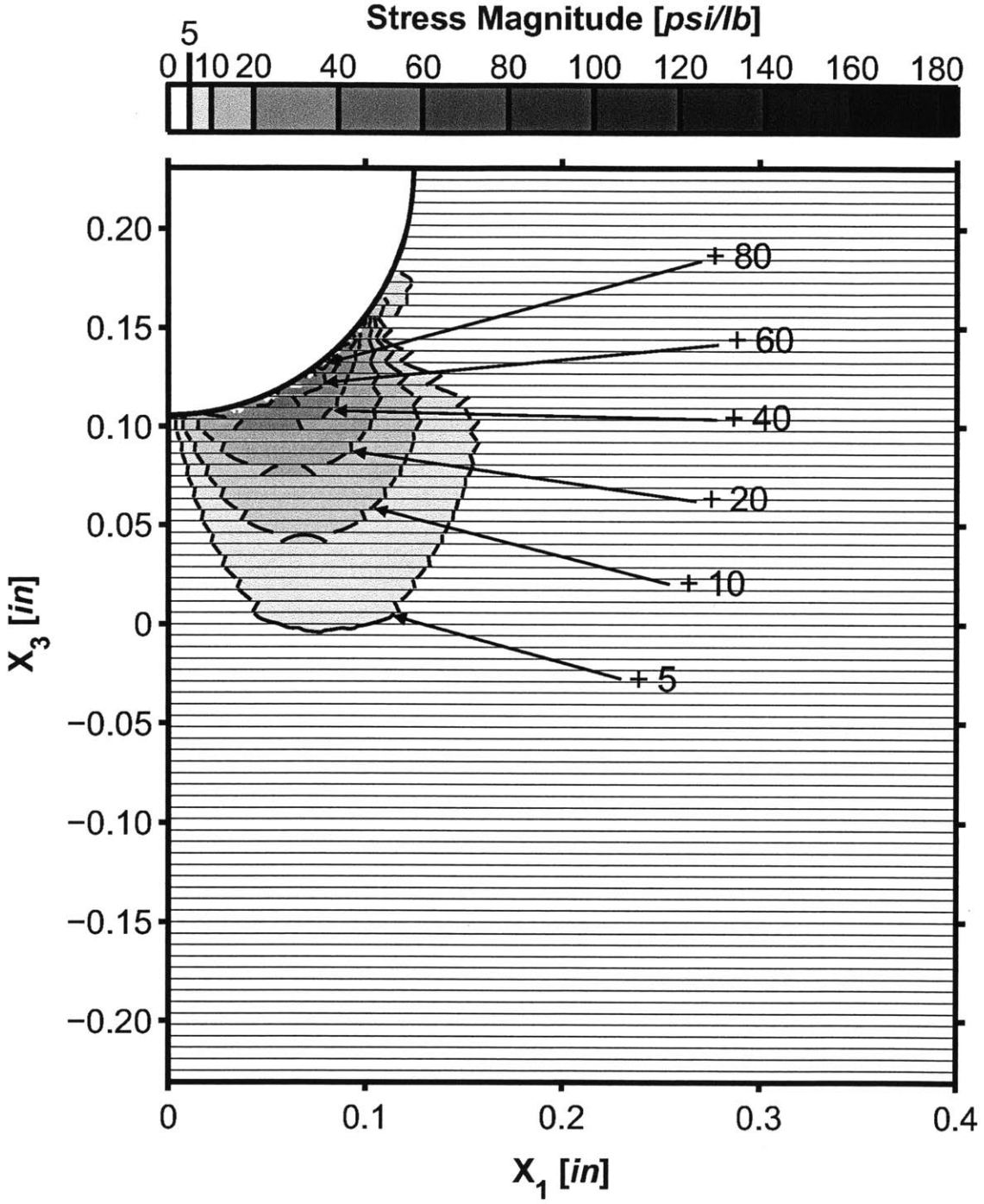

* Note: All stresses normalized by applied load, and given in units of [psi/lb].

Figure 5.102 Isostress plot of σ^*_{13} for a section cut at a value of x_2 of 0.0 inches in the three-dimensional T700/2510 $[90/0]_{20S}$ laminate model loaded at 300 lb.

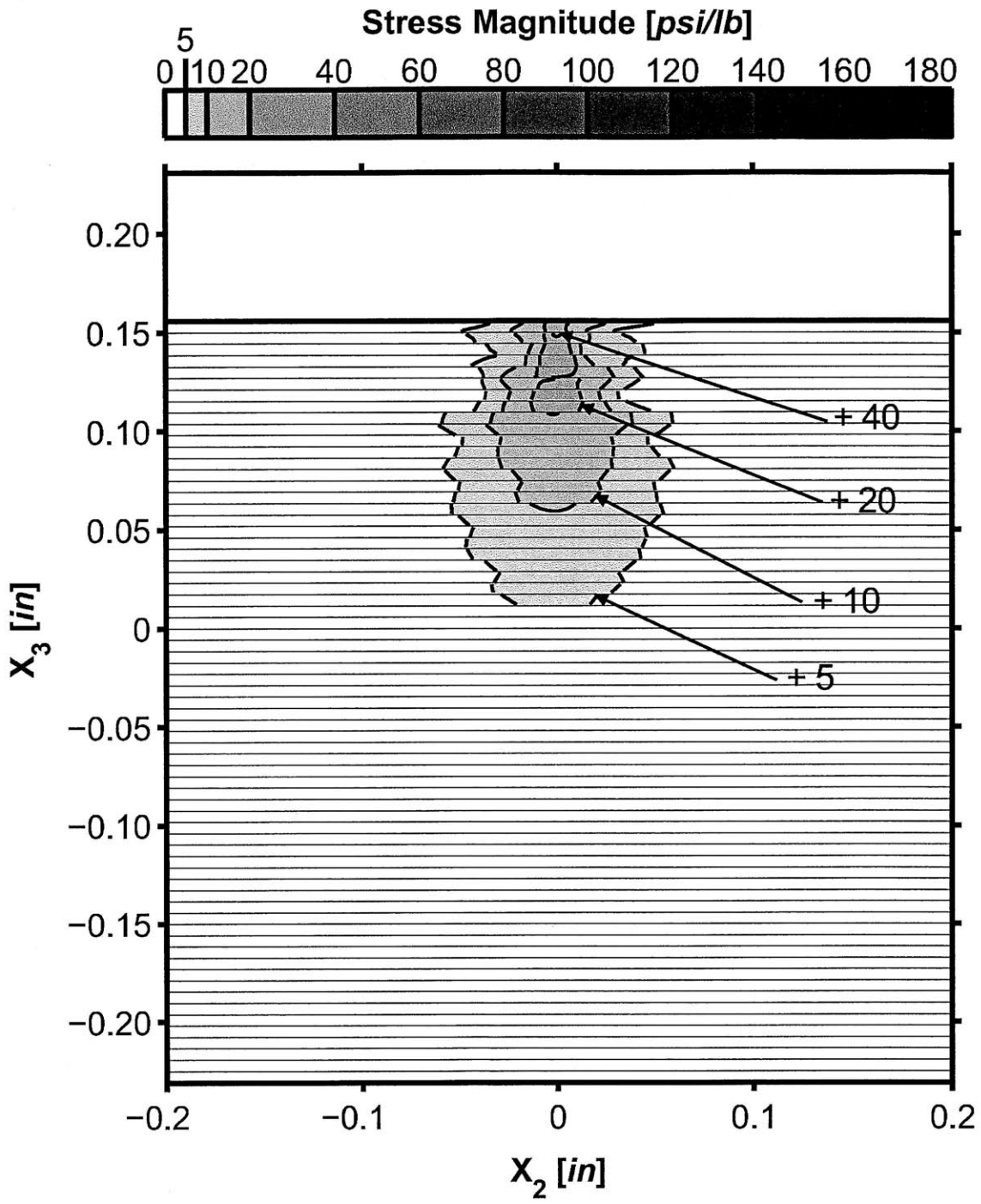

* Note: All stresses normalized by applied load, and given in units of [psi/lb].

Figure 5.103 Isostress plot of σ^*_{13} for a section cut at a value of x_1 of 0.10 inches in the three-dimensional T700/2510 $[\pm 45/0/90]_{10S}$ laminate model loaded at 300 lb.

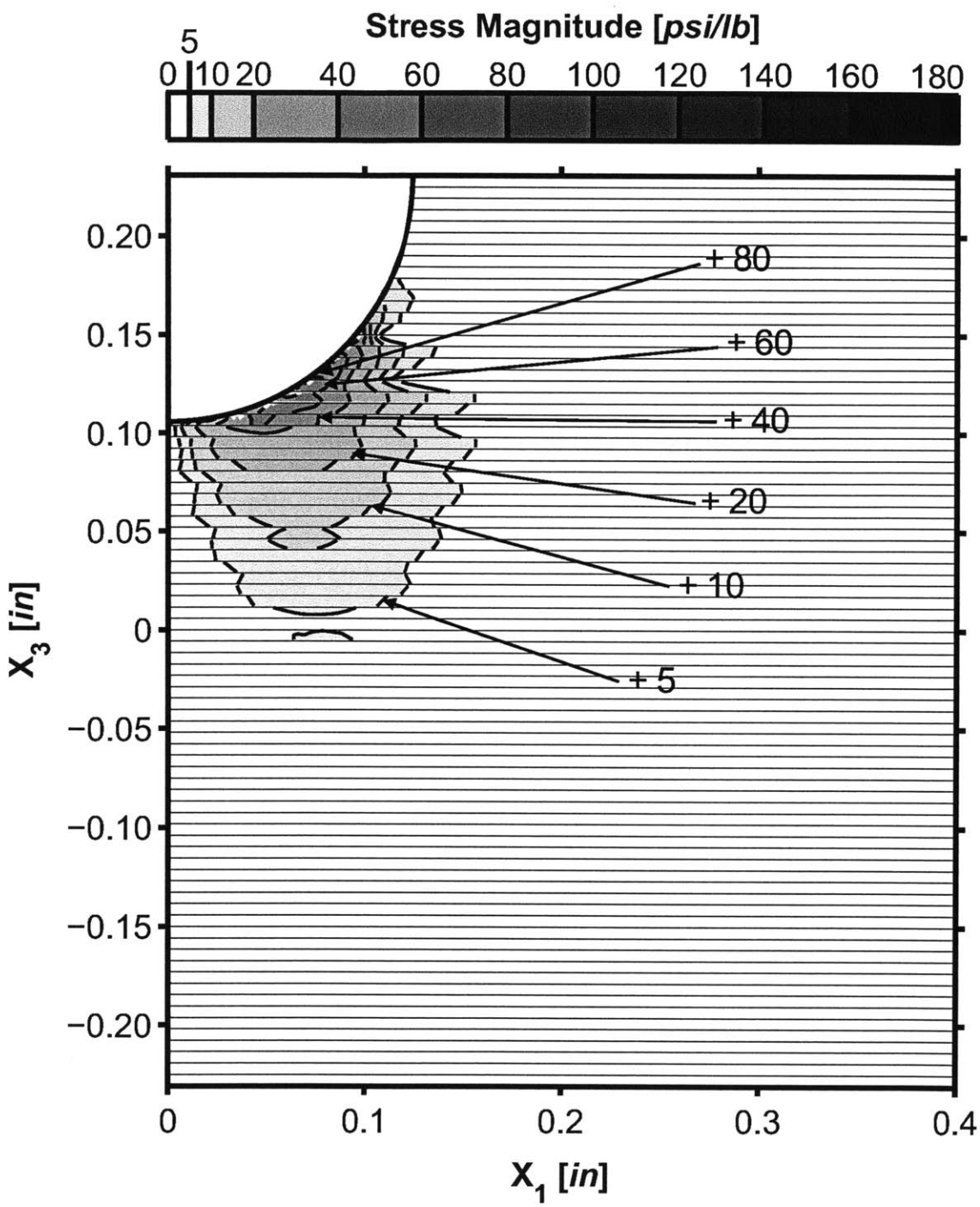

* Note: All stresses normalized by applied load, and given in units of [psi/lb].

Figure 5.104 Isostress plot of σ^*_{13} for a section cut at a value of x_2 of 0.0 inches in the three-dimensional T700/2510 $[\pm 45/0/90]_{10S}$ laminate model loaded at 300 lb.

Table 5.10 Maximum magnitudes of normalized shear stress values, σ^*_{13}, and locations in cylindrical coordinates for three-dimensional models loaded at 300 lb

Laminate		**Shear**			
Material	Layup	σ^*_S $[psi/lb]$	ϕ_S $[deg]$	r_S $[in]$	x_{2_S} $[in]$
T700	$[\pm 15/0]_{13S}$	95	43.3	0.125	0.0
T700	$[\pm 30/0]_{13S}$	94	38.3	0.125	0.0
T700	$[\pm 45/0]_{13S}$	98	38.3	0.125	0.0
T700	$[\pm 60/0]_{13S}$	101	38.3	0.125	0.0
T700	$[90/0]_{20S}$	99	46.2	0.125	0.0
T700	$[\pm 45/0/90]_{10S}$	90	33.8	0.125	0.0

the contact pressure and stress response are studied at a lower load in an effort to determine the linearity of the system. Since both contact pressure and stress results are normalized by the applied load, results would be identical for a system of linear behavior. Different results would indicate a nonlinear response. All laminates were examined at various load magnitudes. However, the effect of load magnitude on response is presented for only the quasi-isotropic T700/2510 $[\pm 45/0/90]_{10S}$ laminate. The response of this laminate is characteristic of all of the laminates investigated, allowing presentation of the response in 0°, 90° and angled plies in one set of results. The load used in this case is 60 lb, or 20% of the original load of 300 lb.

As with the previous three-dimensional results, the contact pressure is presented in two figures: one is a contour plot illustrating the footprint of the indentor-laminate contact, the other is a plot of contact pressure versus groove angle along constant select values of x_2. The contact pressure contour plot for the quasi-isotropic T700/2510 $[\pm 45/0/90]_{10S}$ laminate loaded at 60 lb is presented in Figure 5.105. Contour pressure curves from the case of 60 lb loading are shown in Figure 5.106 at values of x_2 of 0.0, 0.05, 0.10 and 0.15 inches. These are shown in black, and the same contact pressure curves from the 300 lb loading are overlaid in gray. Note that for the contour plot, all contour levels and color indicators are a factor of three larger than their counterparts from the case of 300 lb loading, and in the pressure curve plot the curves along values of x_2 of 0.010 and 0.015 inches do not exist since there is no contact at these locations in the case of the 60 lb loading.

For the case of 60 lb loading, the area of contact is much smaller, with much higher normalized pressures, compared to the case of 300 lb loading. The maximum normalized contact pressure, $p^*_{C_{max}}$, is 872 psi/lb, and occurs at an angular location, ϕ, of 1.5°, along the x_2 equals 0.0 centerline. This value is 268% of the maximum normalized contact pressure of 325 psi/lb in the case of 300 lb loading, and in a different location. Similarly, all normalized pressures in the distribution are significantly higher and with higher gradients than in the case of 300 lb loading. This is most likely due to the need to distribute the load from the indentor over a smaller contact area. While the shape of the contact contours in the case of 60 lb loading remains a

similar semi-ellipsoid, the area on the plot is much smaller, with a semi-major axis, a_C, of 37.0° and a semi-minor axis, b_C, of 0.009 inches, as compared with the values of 53.7° and 0.017 inches for a_C and b_C, respectively, in the case of the 300 lb loading. This smaller contact area is due to the groove of the laminate conforming less to the indentor because of the lower load.

The normalized longitudinal extensional stress, σ_{11}^*, for the quasi-isotropic T700/2510 $[\pm 45/0/90]_{10S}$ laminate loaded at 60 lb is shown in Figures 5.107 and 5.108 for the x_1-section cuts at 0.05 and 0.10 inches. The perpendicular x_2-section cuts at 0.0 and 0.02 inches are shown in Figures 5.109 and 5.110. Little difference is seen here in the behavior of each ply as compared to the case of 300 lb loading. The trends outlined in Section 5.3.2 for the σ_{11}^* distribution still hold true, with three zones of stress apparent. Zone 1 is beneath the groove and consists of alternating regions of tension and compression. Zone 2 extends diagonally from the bottom of the groove into the laminate from the area of contact and is in compression. Zone 3 extends around Zone 2 in the 2-direction and in the 3-direction from the top of the groove toward the top of the laminate and is in tension. Zones 1 and 2 are slightly closer in the case of 60 lb loading than in the case of 300 lb loading, with Zone 3 extending. This reflects the smaller contact area and higher concentration of relative load in that smaller area close to the bottom of the groove. However, it is apparent that normalized stresses of σ_{11}^* in the case of 60 lb loading are larger than in the case of 300 lb loading. This results in higher stress gradients, particularly local to the groove. The maximum normalized tensile stress, σ_T^*, is 210 psi/lb, or 206% of that for the case of 300 lb loading, and occurs on the groove face at an angular location, ϕ, of 10.2°, and a location of x_2 of -0.009 inches. The maximum normalized compessive stress, σ_C^*, is -828 psi/lb, or 313% of that of the case of 300 lb loading, and occurs on the groove face at an angular location, ϕ, of 10.2°, and a location of x_2 of 0.002 inches.

The normalized through-thickness extensional stress, σ_{33}^*, for the quasi-isotropic T700/2510 $[\pm 45/0/90]_{10S}$ laminate loaded at 60 lb is shown in Figures 5.111 and 5.112 for the x_1-section cuts at 0.05 and 0.10 inches. The perpendicular x_2-section cut at 0.0 is shown in Figure 5.113. The general form of the stress field at the 60 lb load

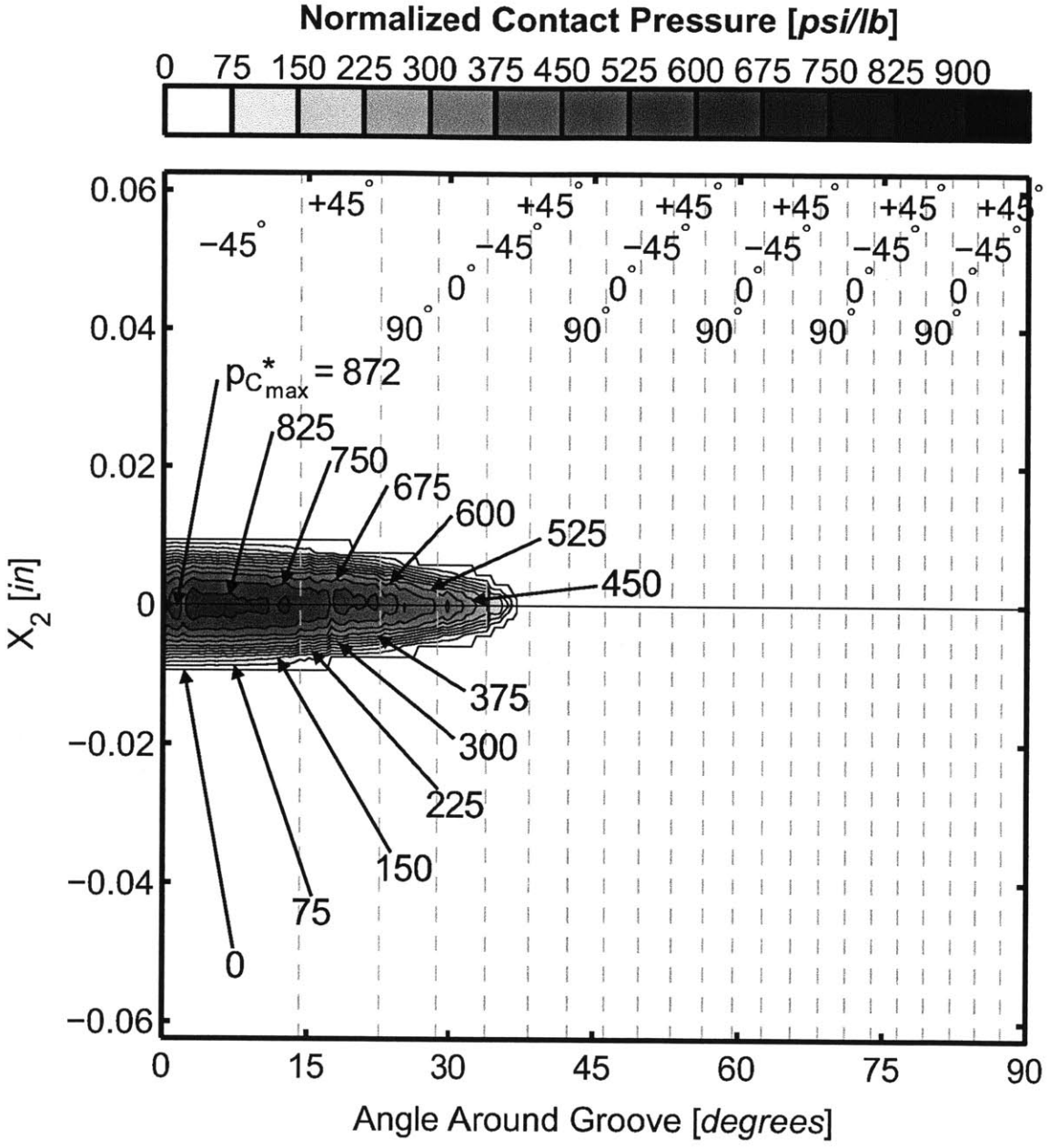

* Note: All stresses normalized by applied load, and given in units of [psi/lb].

Figure 5.105 Normalized contact pressure contour plots for the three-dimensional T700/2510 $[\pm 45/0/90]_{10S}$ laminate model loaded at 60 lb.

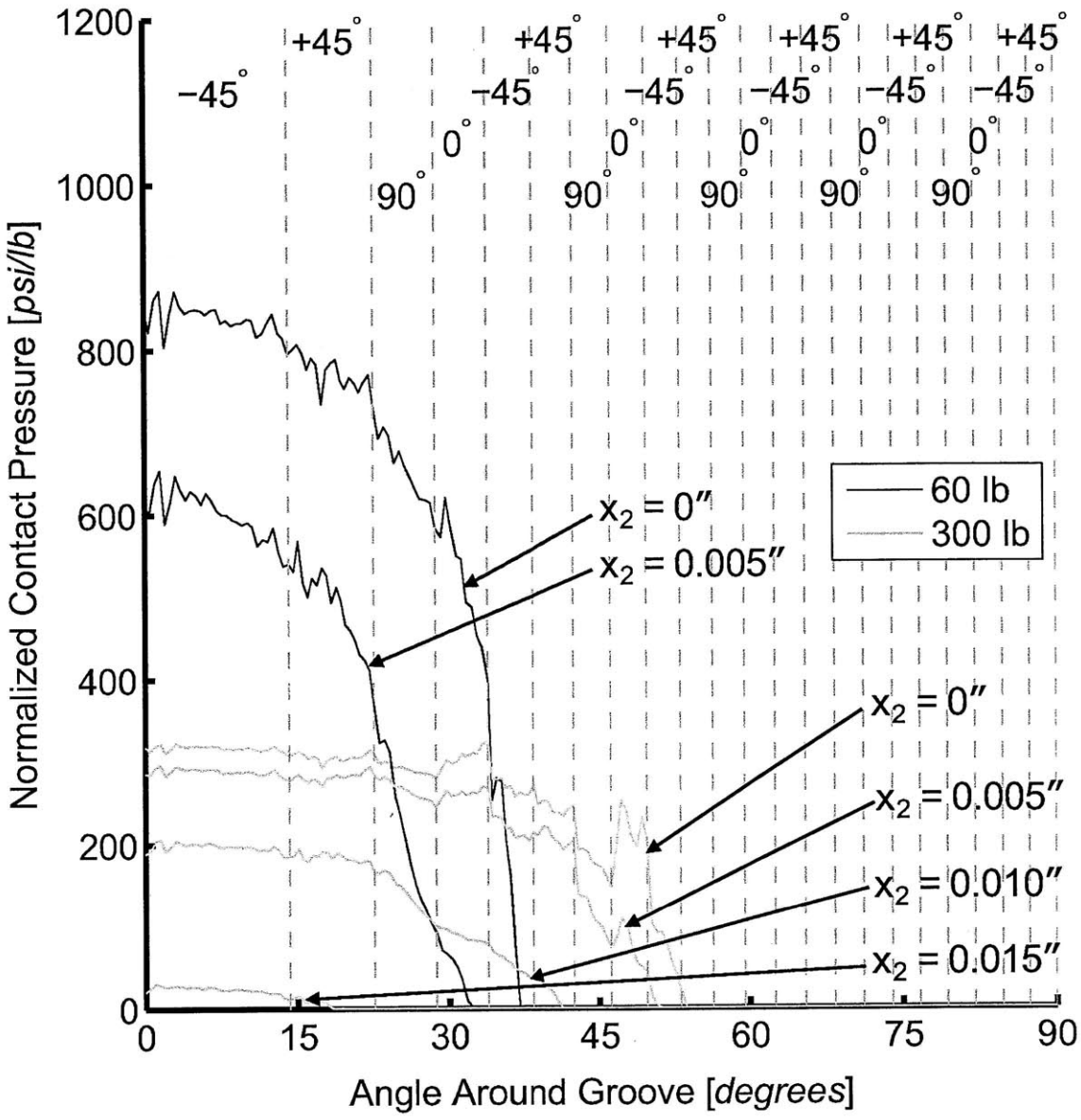

* Note: All pressures normalized by applied load, and given in units of [psi/lb].

Figure 5.106 Normalized contact pressure curves along given values of x_2 for the three-dimensional T700/2510 $[\pm 45/0/90]_{10S}$ laminate model loaded at 60 lb and 300 lb.

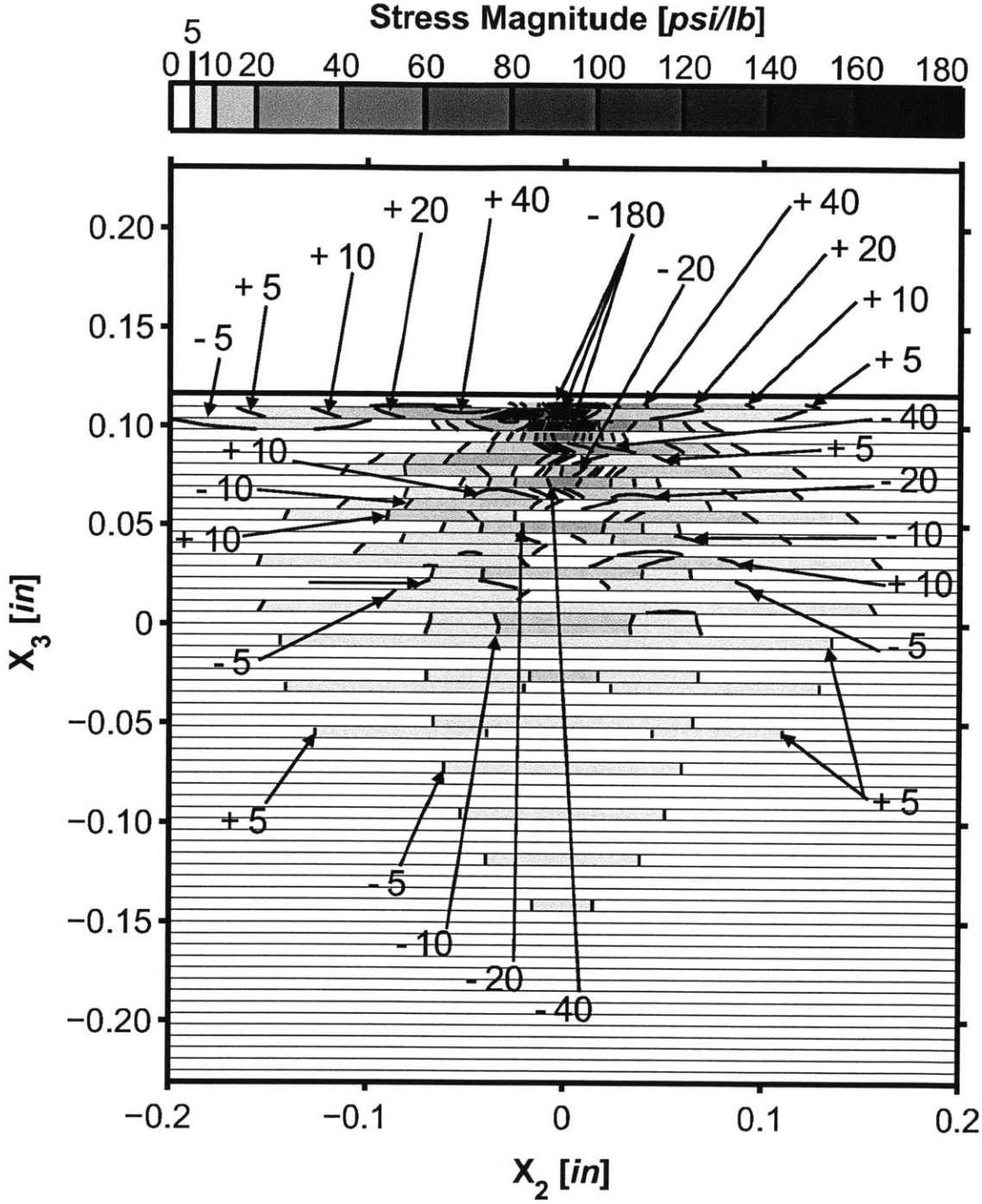

* Note: All stresses normalized by applied load, and given in units of [psi/lb].

Figure 5.107 Isostress plot of σ_{11}^{*} for a section cut at a value of x_1 of 0.05 inches in the three-dimensional T700/2510 $[\pm 45/0/90]_{10S}$ laminate model loaded at 60 lb.

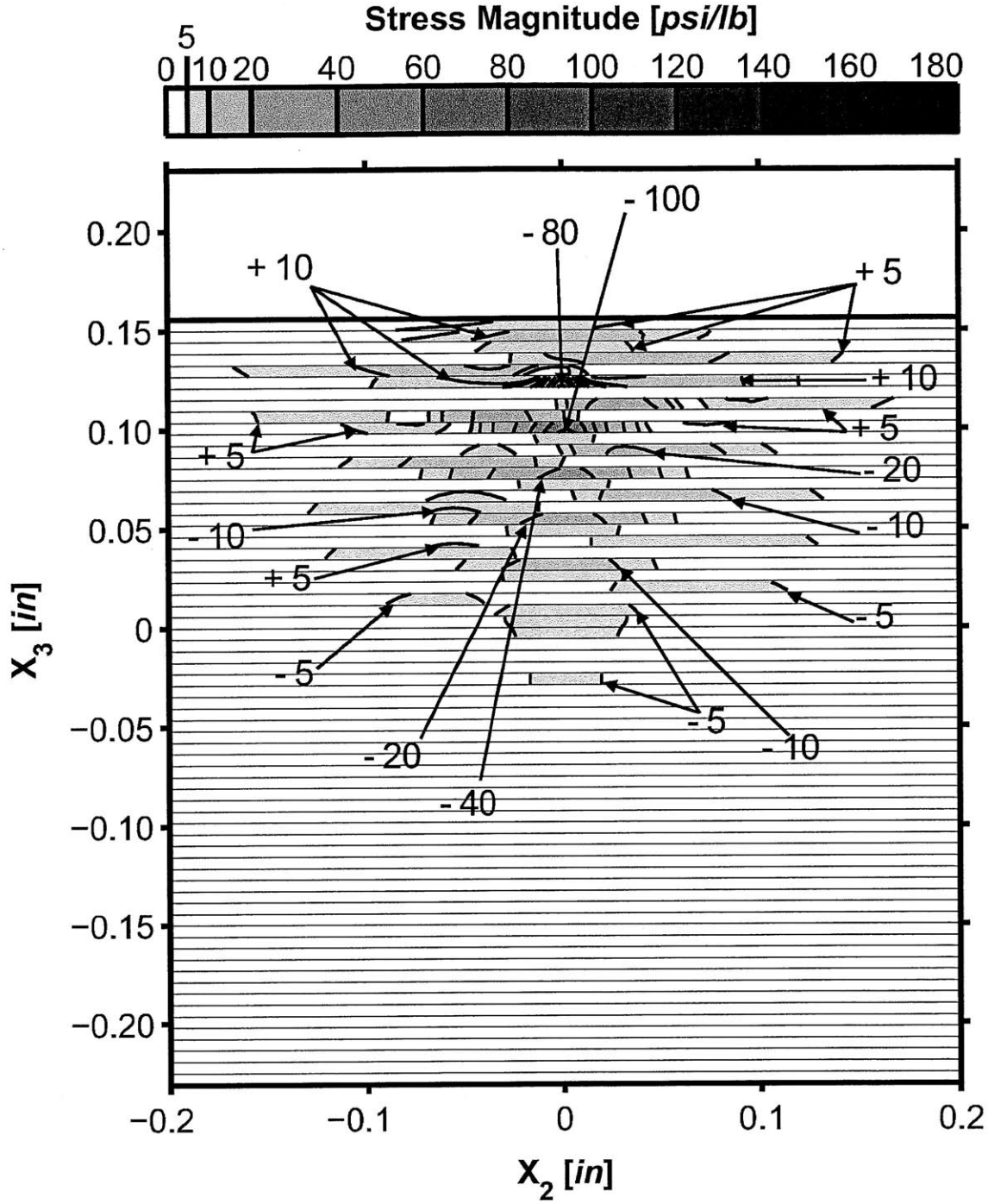

* Note: All stresses normalized by applied load, and given in units of [psi/lb].

Figure 5.108 Isostress plot of σ_{11}^{*} for a section cut at a value of x_1 of 0.10 inches in the three-dimensional T700/2510 $[\pm 45/0/90]_{10S}$ laminate model loaded at 60 lb.

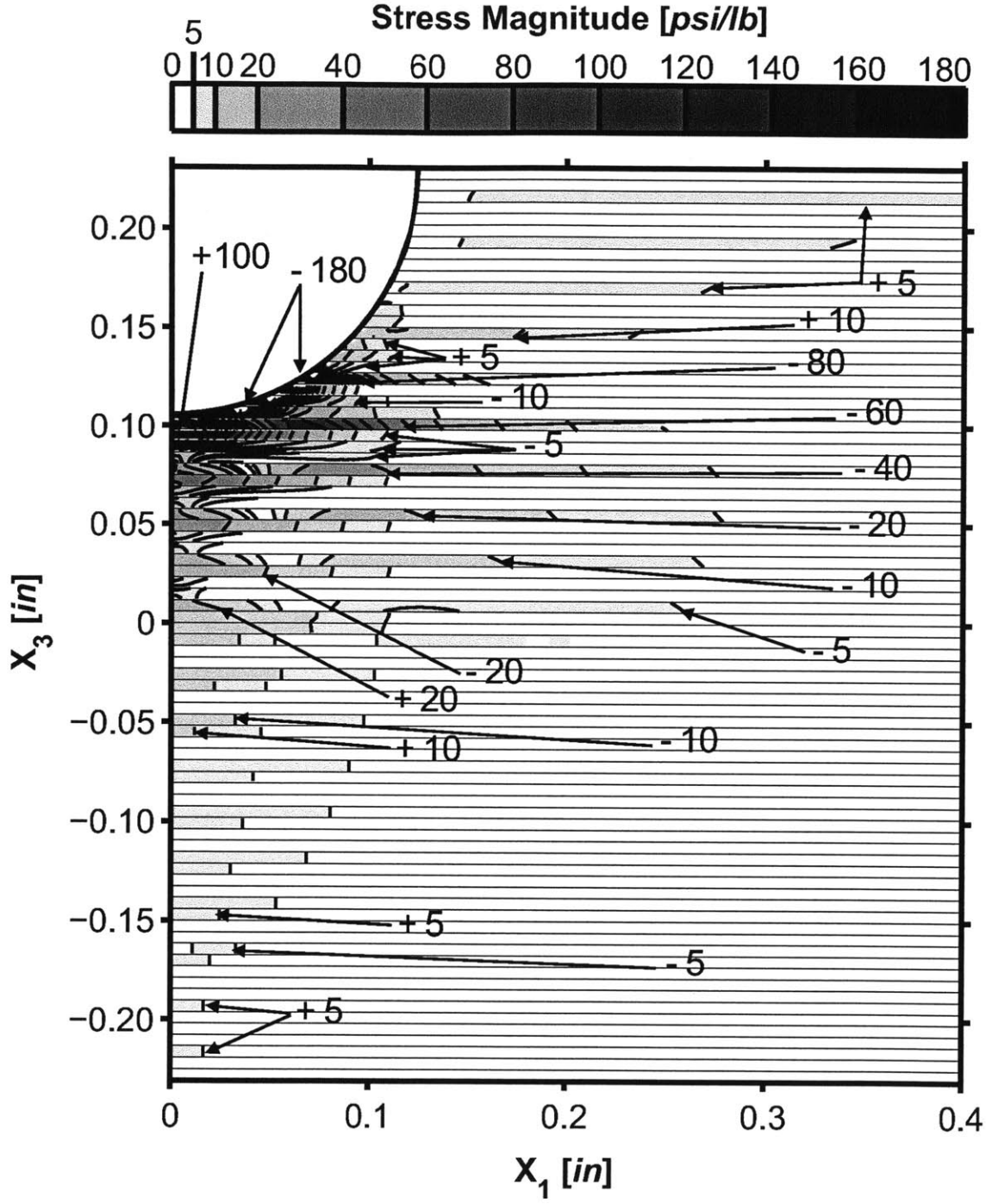

* Note: All stresses normalized by applied load, and given in units of [psi/lb].

Figure 5.109 Isostress plot of σ_{11}^{*} for a section cut at a value of x_2 of 0.0 inches in the three-dimensional T700/2510 $[\pm 45/0/90]_{10S}$ laminate model loaded at 60 lb.

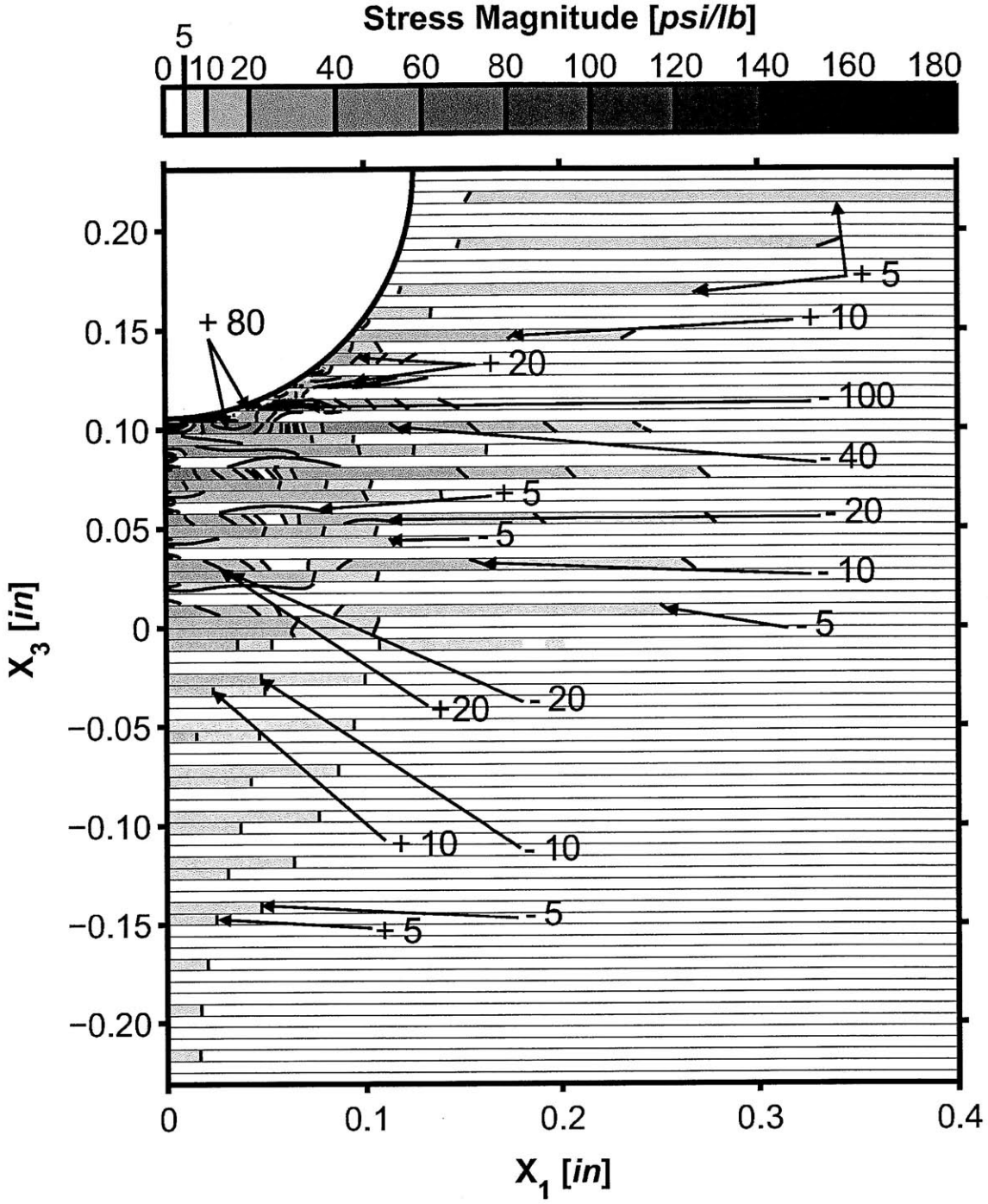

* Note: All stresses normalized by applied load, and given in units of [psi/lb].

Figure 5.110 Isostress plot of σ_{11}^{*} for a section cut at a value of x_2 of 0.02 inches in the three-dimensional T700/2510 $[\pm 45/0/90]_{10S}$ laminate model loaded at 60 lb.

again remains similar to the case of the 300 lb load. The stress distribution consists of one large area of compressive stress under the groove, and a smaller lobe of tensile stress along the groove wall and wrapping slightly around the area of compressive stress. In comparison to the higher loading, the stress distribution for the 60 lb loading shows a higher normalized stress and stress concentration in the compressive area. This area is slightly larger at the bottom of the laminate, and slightly narrower near the bottom of the groove, but the stresses near the base of the groove are much higher with higher gradients than in the case of the 300 lb loading. The tensile area of stress is significantly larger, making up for the shrinking of the compressive stress area in this region, although tensile stress magnitudes are not significantly larger. The maximum normalized tensile stress, σ_T^*, is 45 psi/lb, or 125% of that of the case of the 300 lb loading, and occurs on the groove face at an angular location, ϕ, of 35.2°, and a location of x_2 of -0.003 inches. The maximum normalized compessive stress, σ_C^*, is -845 psi/lb, or 268% of that of the case of the 300 lb loading, and occurs on the groove face at an angular location, ϕ, of 1.0°, and a location of x_2 of 0.0 inches.

The normalized shear stress, σ_{13}^*, for the quasi-isotropic T700/2510 $[\pm 45/0/90]_{10S}$ laminate loaded at 60 lb is shown in Figure 5.112 for the x_1-section cut at 0.10 inches. The perpendicular x_2-section cut at 0.0 is shown in Figure 5.113. Again, the general shape of the stress field remains similar as for the case of higher loading, and the trends noted for the higher loading in Section 5.3.2 still hold. The stress distribution has changed shape slightly, moving closer to the plane of x_1 equal to zero, in accordance with the shrinking contact area. This is most easily seen in the cross-section of x_1 equal to 0.10 inches. In the case of 300 lb loading, this is near the widest point of the stress distribution and the highest stresses. However, for the 60 lb loading, the stress in this area has decreased considerably due to the shift in stress location. In general, the stress field extends farther into the laminate in the 2-direction and the 3-direction, and not as far in the 1-direction, as compared to the case of 300 lb loading. The stresses and stress gradients are also higher than in the case of 300 lb loading. The maximum normalized shear stress, σ_S^*, is -169 psi/lb, or 188% of that of the case of 300 lb loading, and occurs beneath the groove face at a

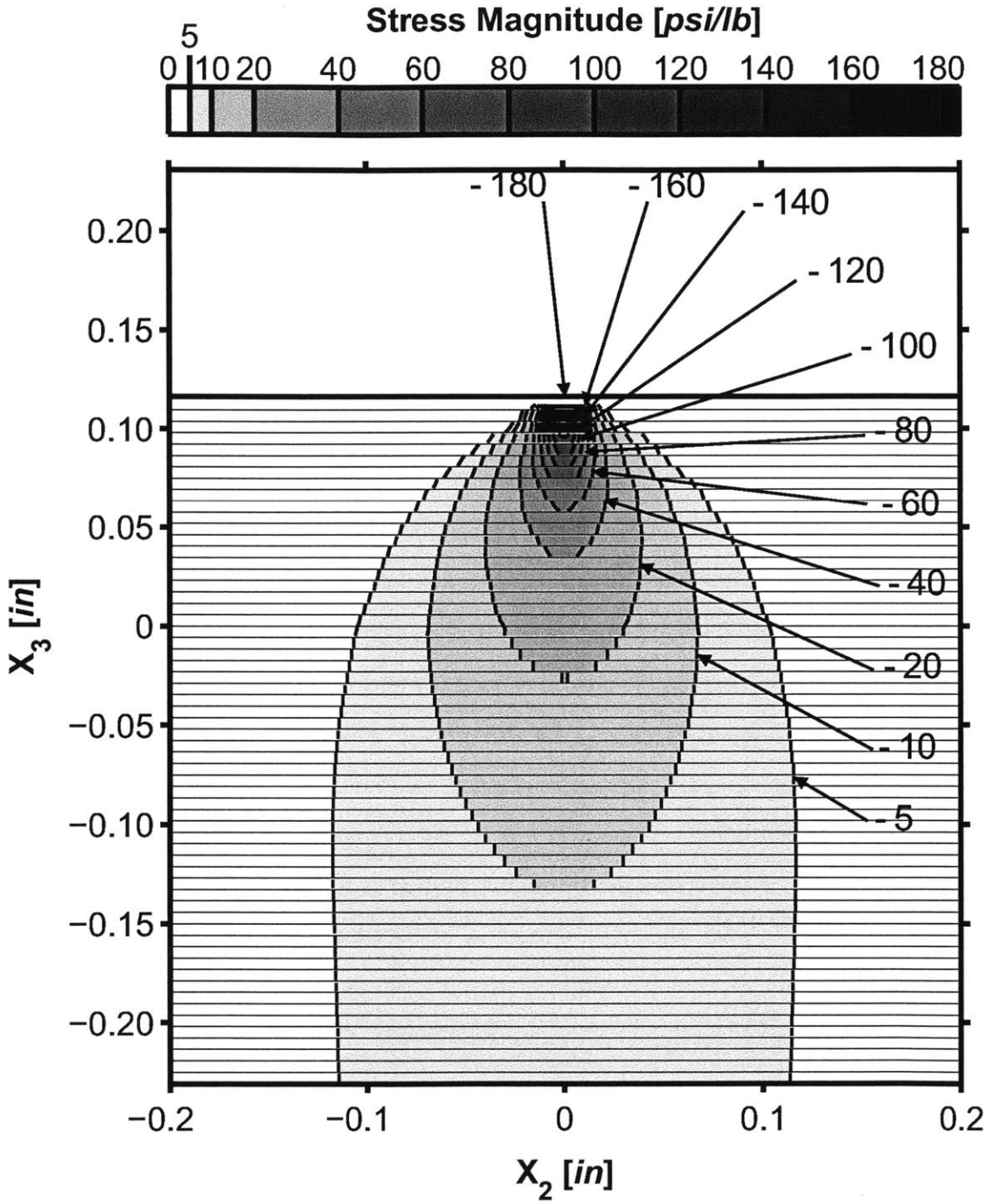

* Note: All stresses normalized by applied load, and given in units of [psi/lb].

Figure 5.111 Isostress plot of σ^*_{33} for a section cut at a value of x_1 of 0.05 inches in the three-dimensional T700/2510 $[\pm 45/0/90]_{10S}$ laminate model loaded at 60 lb.

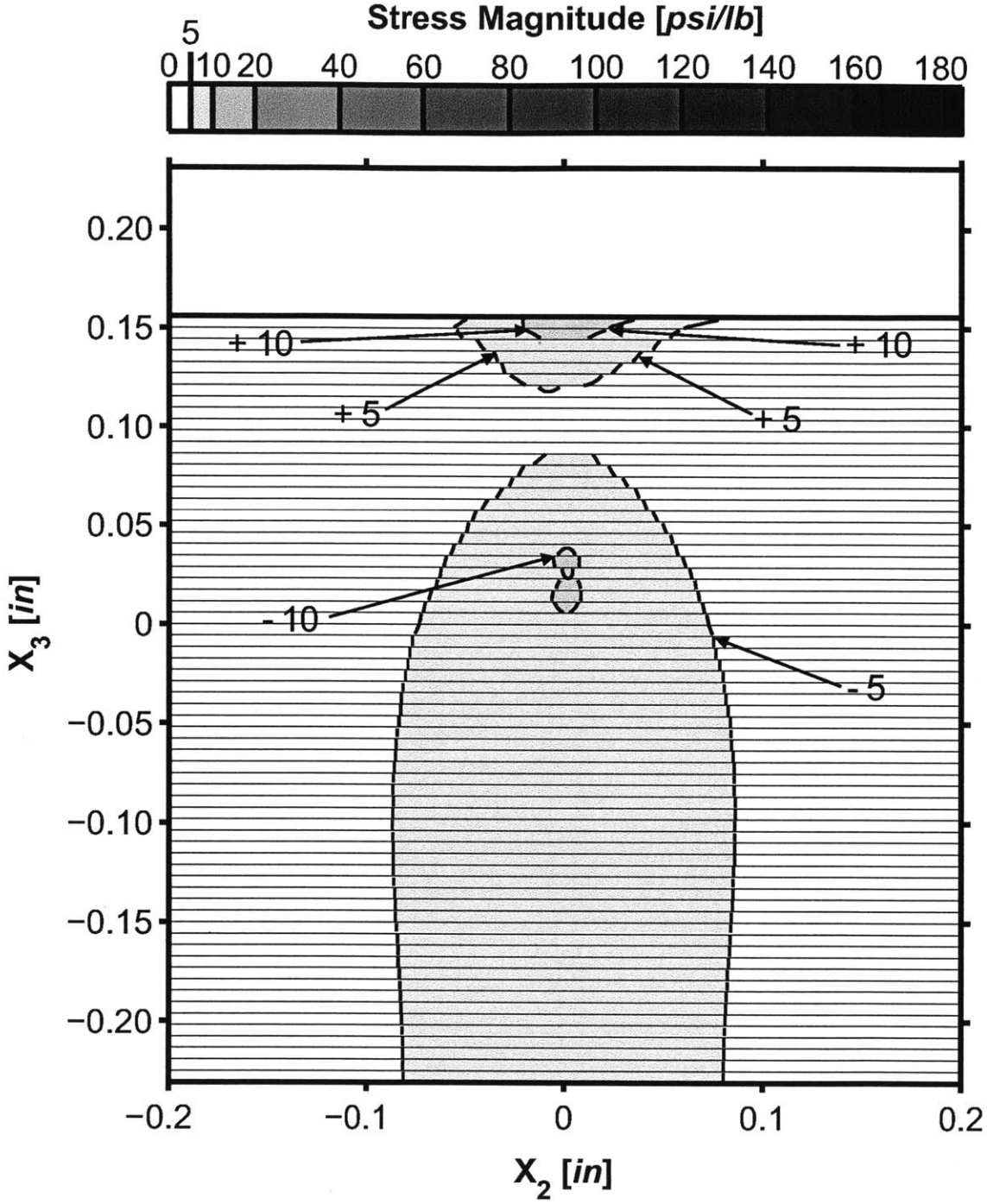

* Note: All stresses normalized by applied load, and given in units of [psi/lb].

Figure 5.112 Isostress plot of σ^*_{33} for a section cut at a value of x_1 of 0.10 inches in the three-dimensional T700/2510 $[\pm 45/0/90]_{10S}$ laminate model loaded at 60 lb.

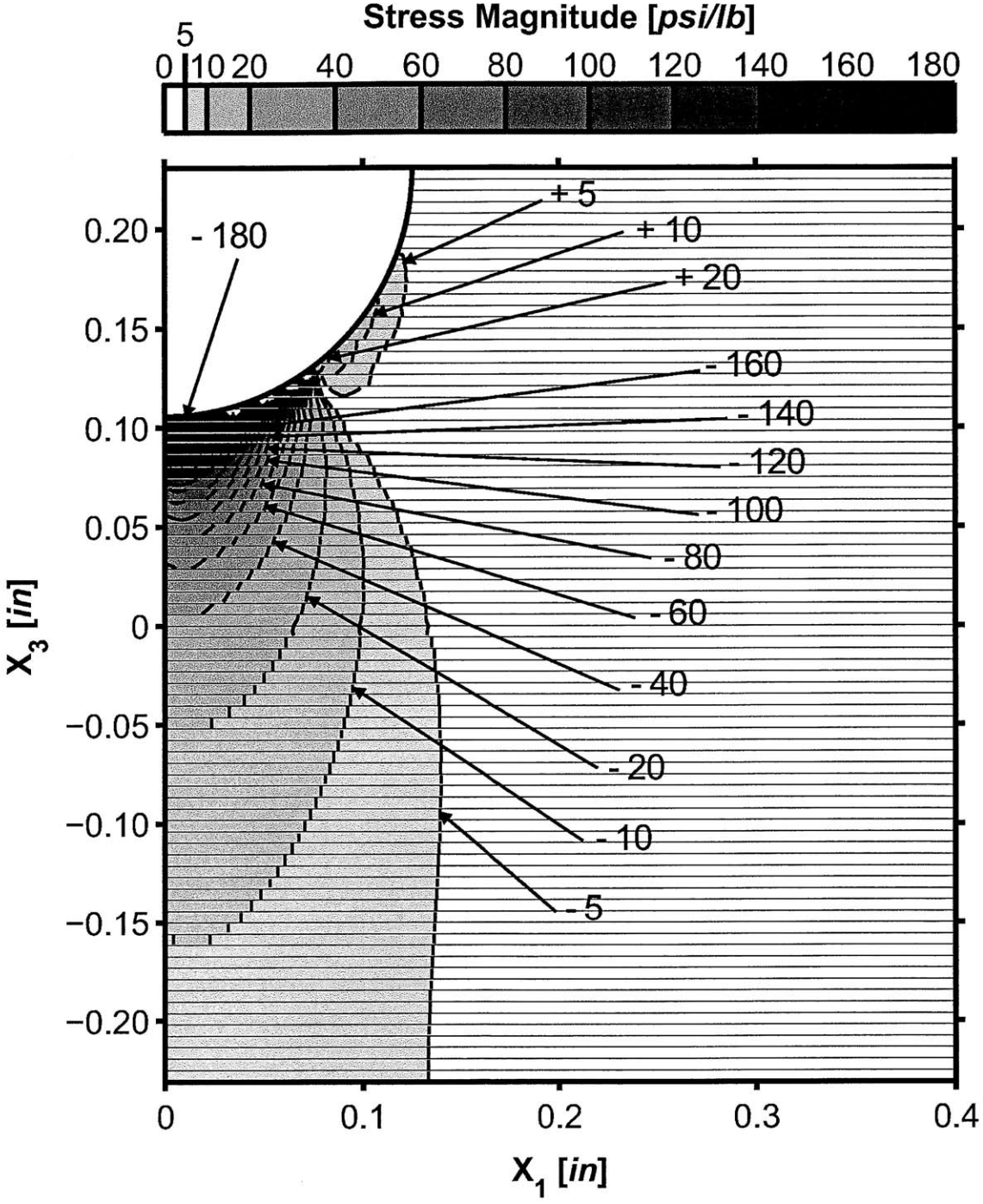

* Note: All stresses normalized by applied load, and given in units of [psi/lb].

Figure 5.113 Isostress plot of σ^*_{33} for a section cut at a value of x_2 of 0.0 inches in the three-dimensional T700/2510 $[\pm 45/0/90]_{10S}$ laminate model loaded at 60 lb.

radius, r, of 0.131 inches, at an angular location, ϕ, of 22.1°, and a location of x_2 of 0.0 inches.

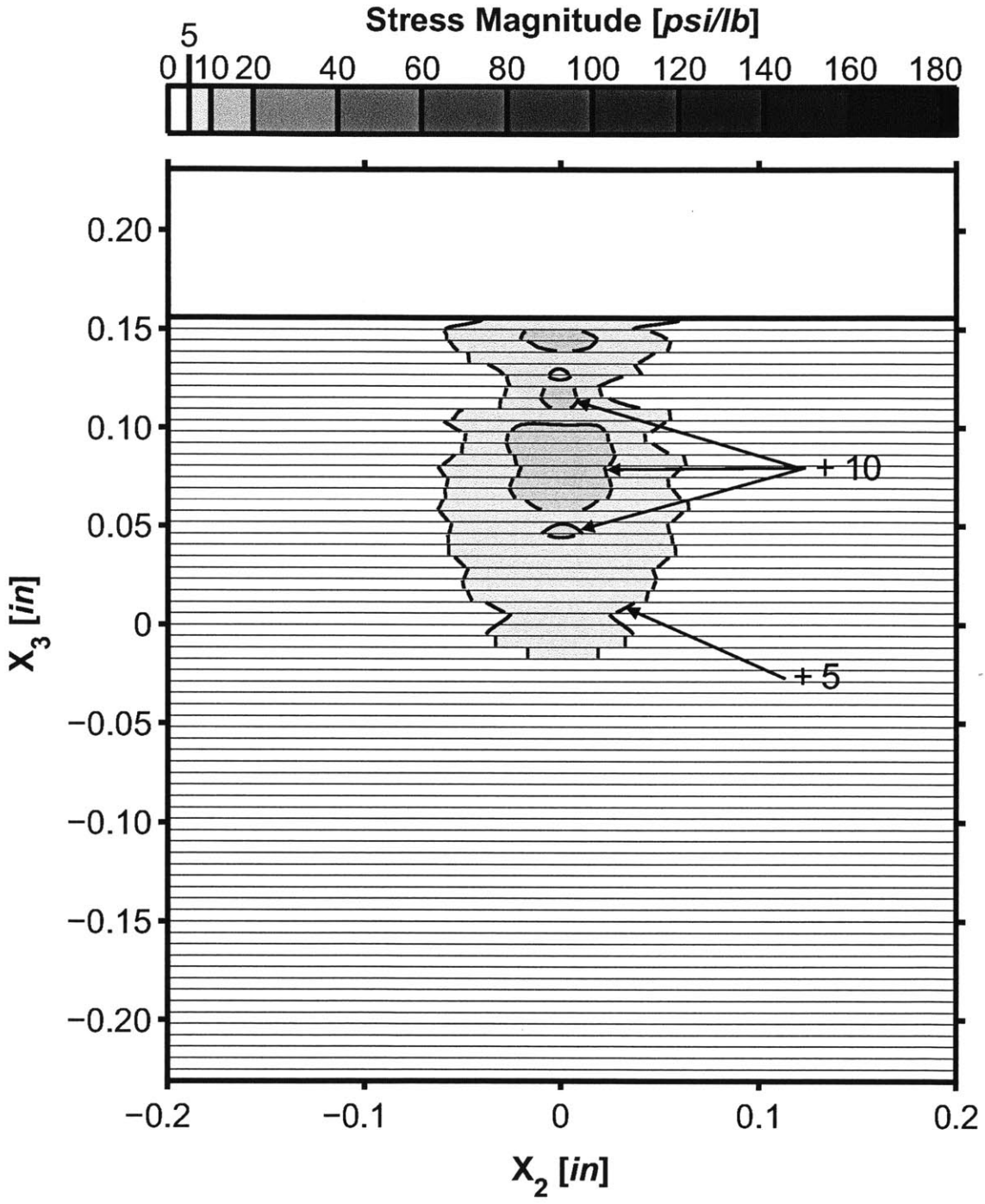

* Note: All stresses normalized by applied load, and given in units of [psi/lb].

Figure 5.114 Isostress plot of σ^*_{13} for a section cut at a value of x_1 of 0.10 inches in the three-dimensional T700/2510 $[\pm 45/0/90]_{10S}$ laminate model loaded at 60 lb.

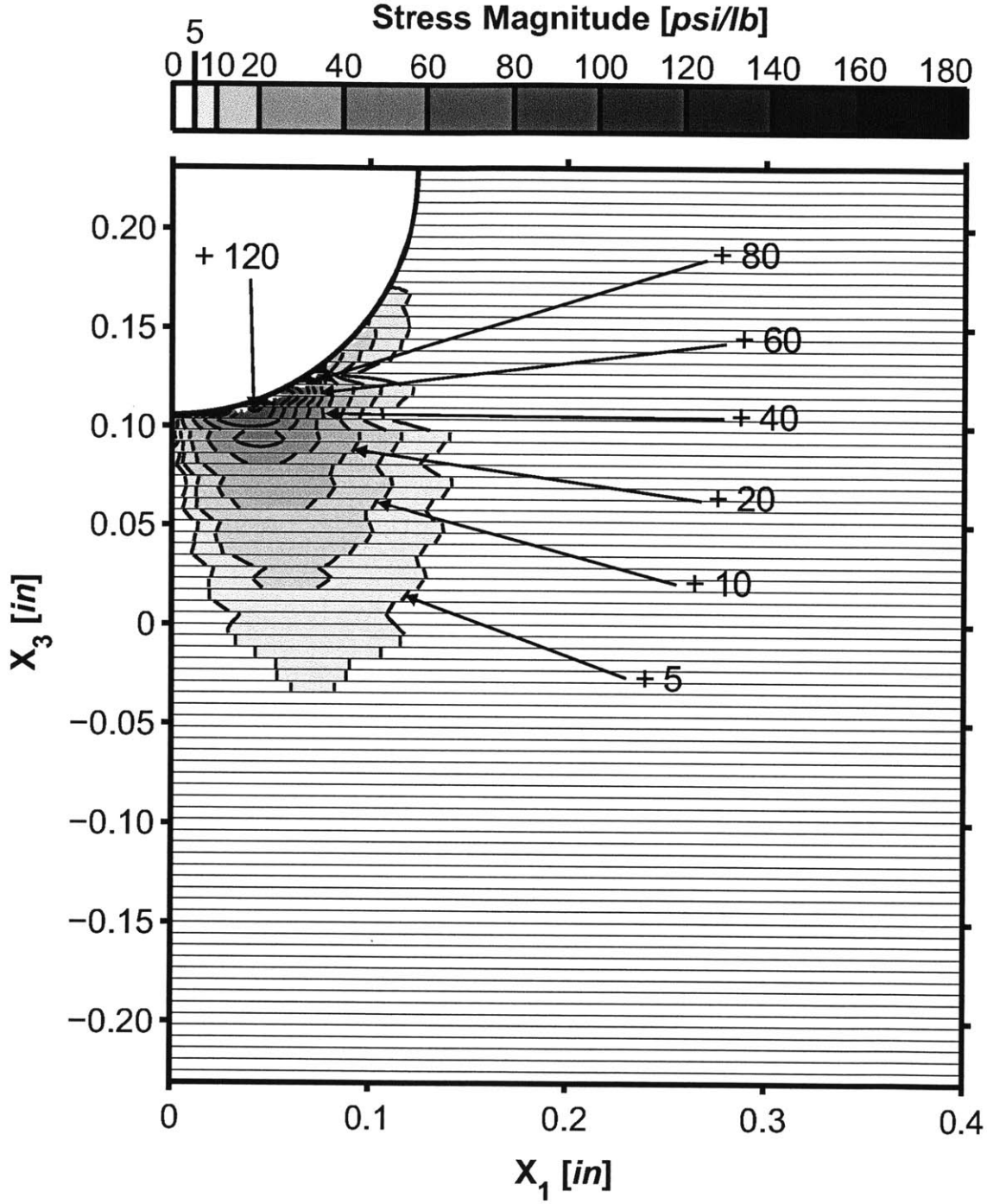

* Note: All stresses normalized by applied load, and given in units of [psi/lb].

Figure 5.115 Isostress plot of σ_{13}^{*} for a section cut at a value of x_2 of 0.0 inches in the three-dimensional T700/2510 $[\pm 45/0/90]_{10S}$ laminate model loaded at 60 lb.

Chapter 6

DISCUSSION

The primary goal of the current work is to examine the response of a grooved composite laminate to out-of-plane conformal contact loading through the use of finite element modeling, with particular focus on the area local to the groove. In addition, the influence of ply angle and orthotropy is assessed across various laminates, and the linearity of the response to the loading factor is studied to assess the importance of these features in the modeling of grooved laminates. These objectives also necessitated investigation into best modeling practices for grooved laminates. The contact pressure determined in this work is compared to the Hertzian distribution used to model contact in previous work [5]. The effectiveness of using a rigid body for the indentor as an approximation to a linear elastic body is studied. The applicability of a two-dimensional model to the full three-dimensional case is examined. These items are discussed in this chapter, referencing the results obtained in the current investigation and reported in Chapter 5.

6.1 Modeling Effects

In discussing the results from Chapter 5, it is important to note those effects or limitations that arise due to the specific modeling techniques used in this investigation, rather than due to any physical manifestation. Particularly, the use of finite element modeling in this investigation, and the specific implementation used in the modeling

of the current investigation, as detailed in Chapter 4, has a number of effects on the observed results. These effects have three main origins: discretization of the laminates using the finite element method, the contact model employed, and, in the three-dimensional case, the boundary condition of symmetry.

For this investigation, displacement-based finite elements were used to model the grooved composite laminate. The use of linear finite elements in this implementation requires the discretization of the structure into individual elements, defined by a set of nodes and the straight edges connecting them. Finite element analysis is then used to calculate the displacements at the nodes for a given set of loads and boundary conditions. These displacements are used by ABAQUS to calculate the stresses at the nodes, which are then reported and output to MATLAB for viewing. Linear interpolation was used to calculate and display stresses between nodes. This process inherently limits the current analysis to determining the stresses at the nodes only, and using linear approximations for the stresses between nodes. This means that maximum stress magnitudes can only occur at nodes, as linear interpolation cannot reach a maximum or minimum between two nodes. Thus, maximum stresses are only approximations in both location and magnitude, and are limited in error by the minimum distance between nodes in the region local to the maximum stress location.

For this investigation, the discretization of the laminates was performed as detailed in Section 4.2. The distance between nodes, and hence the possible error in location of maximum stress magnitudes, can be best determined by examining the mesh seeds for the relevant region of the laminate in that section. For the two-dimensional models, this distance is between 0.001 inches on the groove face, and 0.002 inches in the body of the laminate in Region 1, the region where all maximum stress magnitudes occur. For the three-dimensional models, this distance is between 0.0011 inches on the groove face, and 0.0037 inches in the part of Region 1 where the maximum stress magnitudes occur.

As discussed in Section 4.2, the discretization of the laminates did not employ symmetry about any of the laminate planes, although the geometry of the grooved laminate structure is symmetric across the 1-3 plane and across the 2-3 plane. While

there is generally little effect from the lack of symmetry in the finite element mesh, some small discrepancies are apparent, particularly in the locations and values of maximum stresses. In the two-dimensional model, the geometry, as well as the material properties, loading, and boundary conditions, are symmetric across the 2-3 plane. This implies that the structural response should similarly be symmetric across this plane. However, the finite element discretization is not symmetric. This generates some small asymmetries in the structural response. For example, in the normalized shear stress response, σ_{13}^{*}, for the T700/2510 $[\pm 45/0/90]_{10S}$ laminate, the maximum shear stress magnitude should be identical on either side of the x_3-axis due to symmetry. However, maximum shear stress magnitudes are 2.50 psi/(lb/in) for positive x_1, and 2.52 psi/(lb/in) for negative x_1. This is a difference of 1.1%. Similar minor differences in magnitude are seen for the other stress fields, and in the other laminates investigated. While these differences are small, and perhaps negligible, they arise from the asymmetry in the finite element discretization, and are not inherent to the system.

Note that the asymmetries seen in the three-dimensional models are not a result of the minor asymmetries arising from the asymmetric mesh. The material properties in the three-dimensional case give rise to an asymmetry across the 1-3 plane due to the inherent directionality of the orthotropic composite material. These asymmetries are due specifically to material properties that appear in the three-dimensional models, but not in the two-dimensional models, such as coefficients of mutual influence and the Poisson's ratios involving the 2-direction. Thus, the asymmetries seen across this plane in the three-dimensional case are due to actual physical asymmetries. The modeling issues arising from the 2-3 plane of symmetry employed in the three-dimensional finite element models is discussed in Section 6.7.

The two remaining effects due to modeling are discussed in the following sections, as appropriate. General limitations arising from the contact models employed are presented in Section 6.3, and specific limitations of the contact model implementation in the case of the linear elastic indentor is presented in Section 6.5.

6.2 Comparison to Hertzian Loading

Previous work in the modeling of grooved laminates [5] has used the Hertzian method to approximate the pressure distribution between the laminate and the indentor, since this is the foremost analytical method for determining the details of contact between two curved bodies. Unfortunately, the Hertzian method can only solve contact between two isotropic bodies. The extension by Willis to anisotropic bodies is limited to anisotropic half-spaces, and cannot be used for the curved surface of the groove with its piecewise defined orthotropic properties due to the laminated nature of the material. Currently, the only method for defining contact between the grooved laminate and the round indentor is the numerical method, for example the finite element method used in this work. Even this method has its limitations, as described in Sections 6.1 and 6.3.

For consistency, all finite element results for this comparison are presented for the AS1/3501-6 $[0/\pm 45/90]_{15S}$ laminate, the same as that used in previous work [5]. The Hertzian distribution is determined by three primary factors: the curvature of the contacting bodies, the material properties of the contacting bodies, and the applied load. The result is an ellipsoidal pressure distribution defined over x_1 with the parameters of maximum pressure, σ_{max}, and projected contact length along x_1, a_H, given in the equation:

$$p_C = \sigma_{max}\left[1 - \left(\frac{x_1}{a_H}\right)^2\right]^{\frac{1}{2}} \tag{6.1}$$

In order to compare the accuracy of the Hertzian distribution as implemented by Bastien [5], a Hertzian distribution must first be generated following the method used in that work which matches the applied load in this work. Following Bastien's method, and using the same material properties and curvature values, a pressure distribution for the 5000 lb/in loading was found to require a value of σ_{max} of 43,700 psi, and a value of a_H of 0.0728 inches.

The resulting Hertzian distribution is plotted along with the numerical contact

pressure determined via a two-dimensional finite element model for a rigid body indentor in Figure 6.1. The differences between the two pressure curves are apparent. The Hertzian distribution maintains contact to a much lower groove angle, 35.6°, as compared to the maximum contact angle of 48.2° from the numerical contact solution. Due to the resulting smaller contact area, the pressure in the Hertzian distribution must be higher near the bottom of the groove in order to maintain both the shape of the curve and the same total load as the numerical result. The obvious discrepancy between the Hertzian distribution and that from the numerical model implies that the Hertzian distribution is a poor approximation of the contact pressure generated in a true case of conformal contact loading. This particular distribution is inaccurate due to the inaccurate contact angle.

Of the three inputs to determining the Hertzian distribution, the curvature of the contacting bodies and the applied load are both accurate, as the geometry of the configuration is explicit, and the applied load is defined. By process of elimination, this leaves the material properties of the contacting bodies as the primary source of error in this approximation. This is logical, as the Hertzian contact model requires both contacting bodies to be modeled as isotropic bodies, whereas in this investigation, the primary body under investigation is an orthotropic laminate. In order to approximate the laminate as an isotropic body, Bastien [5] used an averaging method to determine appropriate values of Young's modulus, E_{avg}, and Poisson's ratio, ν_{avg}. To do this, the three Young's moduli from the single ply AS1/3501-6 properties were averaged, yielding a value of E_{avg} of 7.36 Msi, and the two in-plane Poisson's ratios, yielding a value of ν_{avg} of 0.28. It is these values that Figure 6.1 shows to be inaccurate.

In order to determine the best accuracy achievable with the Hertzian contact model, an alternate formulation is used that bypasses the material properties, and explicitly defines the projected contact length, a_H, to be equal to the contact length determined by the numerical model. The contact angle, $\phi_{contact}$, in the numerical case is 48.2° or a value of a_H of 0.09317 inches in x_1. Maintaining the desired total vertical load at 5000 lb/in, as per Equation 6.1, yields a maximum pressure, σ_{max}, of 34,200 psi. The resulting ideal Hertzian pressure distribution using these derived

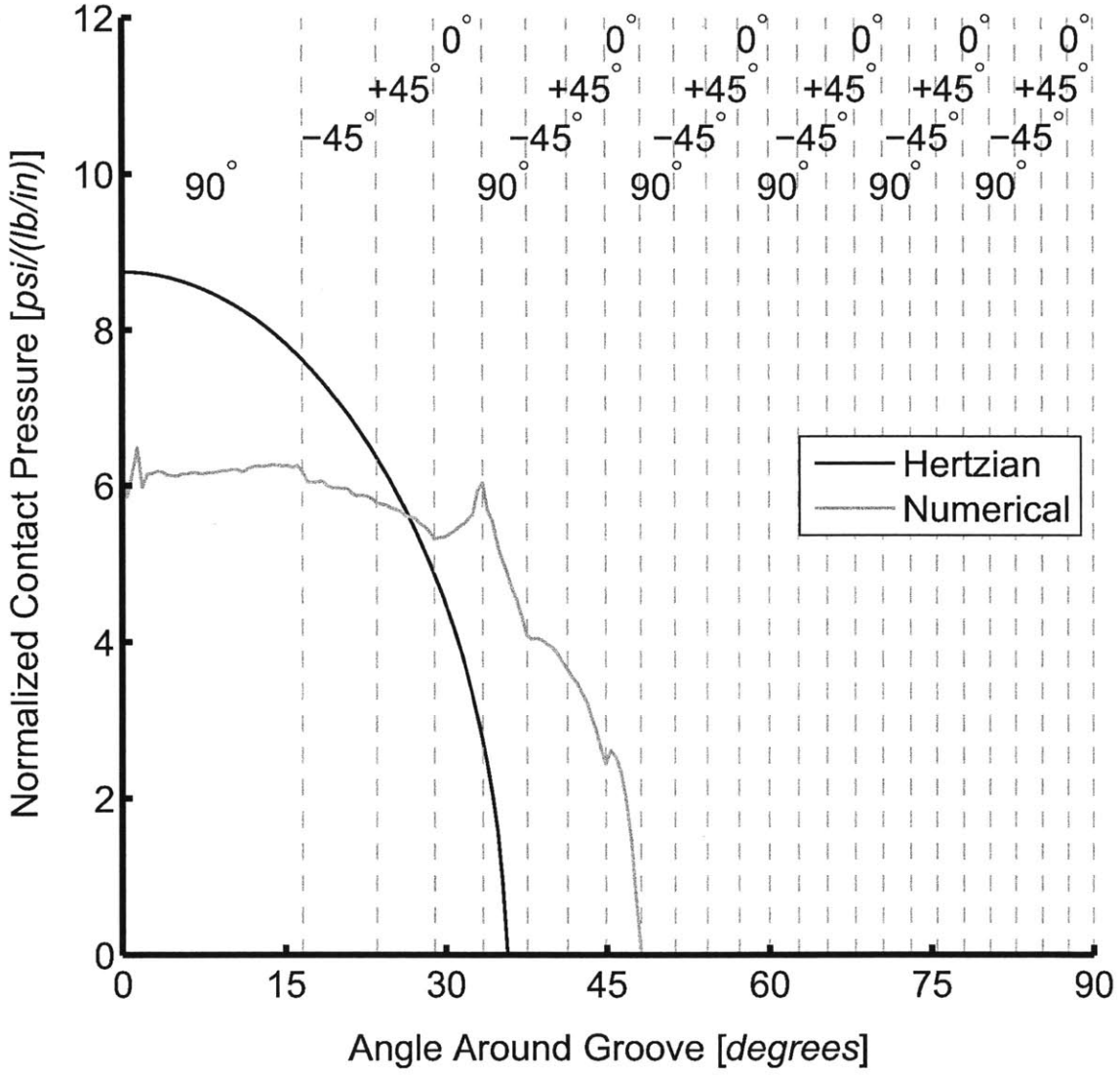

* Note: All pressures normalized by applied load, and given in units of [psi/(lb/in)].

Figure 6.1 Hertzian pressure distribution determined via Bastien method [5] compared to contact pressure distribution determined numerically by finite element analysis for two-dimensional model of AS1/3501-6 $[0/\pm 45/90]_{15S}$ laminate loaded at 5000 lb/in.

values of a_H and σ_{max} is plotted against the contact pressure distribution from the numerical model in Figure 6.2 in order to directly compare the shapes of pressure curves in the best case approximation. It should be noted that the vertical load is identical for both contact models. The smooth curve of the Hertzian distribution is a contrast to the more jagged form of the contact pressure in the numerical case. The Hertzian distribution generally follows a similar shape to the contact pressure distribution from the numerical model, but misses many of the finer points that arise due to the varying stiffnesses of the laminated plies. This occurs, even in this case of ideally matched contact lengths, because the Hertzian distribution assumes the body under contact is uniformly isotropic, and therefore cannot account for the variation in material properties between plies. Notably, the contact pressure near the bottom of the groove is much lower in the 90° ply for the numerical contact distribution as compared to the Hertzian model, but much higher in the 0° and 90° plies farther along the groove wall near a value of ϕ of 30°.

In progressing along the groove wall at higher values of ϕ, in the ±45° plies, the contact pressure from the finite element model is higher than the Hertzian contact pressure in the same location. This can be attributed to a simple cause. As discussed, the Hertzian distribution assumes an isotropic body, but the laminated body is not isotropic. More than that, on average, the stiffness of the composite material is significantly lower in the 3-direction than it is in the 1-direction. Any ply angle lower than 90° will raise the average stiffness in the 1-direction, and this laminate has a large number of 0° and ±45° plies. This results in the laminate having a higher stiffness in the 1-direction.

This principle can similarly be applied to the Poisson's ratio. No matter what averaging process is used, the eventual need to have one Young's Modulus and one Poisson's ratio to define the material of the contacted body for the Hertzian model will eventually require some compromise in accurately portraying the contact pressure for a laminate. As seen in this case, this means that the stiffness at the bottom of the groove will be overestimated, where the low stiffness of the laminate in the 3-direction rules, yielding too great a contact pressure in the Hertzian case. Farther up the groove

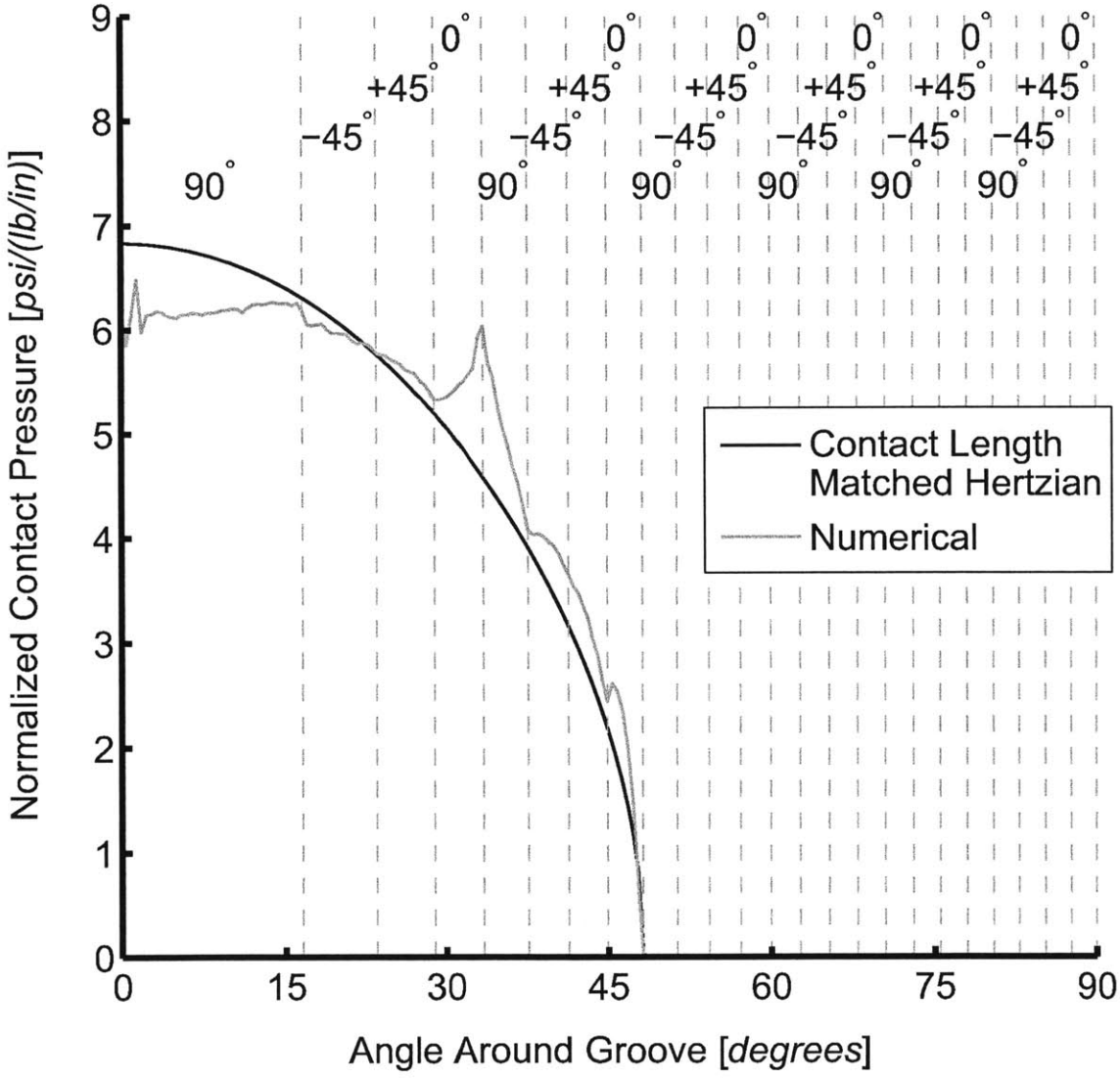

* Note: All pressures normalized by applied load, and given in units of [psi/(lb/in)].

Figure 6.2 Hertzian pressure distribution with matched contact lengths and loads compared to contact pressure distribution determined numerically by finite element analysis for two-dimensional model of AS1/3501-6 $[0/\pm 45/90]_{15S}$ laminate loaded at 5000 lb/in.

wall, as stiffness in the 1-direction becomes more of a factor, the Hertzian distribution will underestimate the average stiffness, yielding too low a contact pressure.

Crucially, by using the contact length found with the numerical model, the Hertzian distribution shown will be the most accurate possible approximation using the Hertzian form. In general, a solution of this accuracy cannot be determined *a priori* because the contact length will not be known. Thus, most solutions using the Hertzian method for grooved laminates must make a "best guess" approximation of the material properties in an attempt to find the most accurate contact length. As shown previously in Figure 6.1, these approximations most often fail to determine the appropriate contact length, which, as is discussed in Section 6.6, is a critical factor in determining the contact pressure and the stress response of the laminate.

6.3 Contact Pressure

Contact pressure is a critical component of this investigation, as it represents the details of the loading of the grooved laminate. This contact pressure, the pressure applied by the loaded indentor to the grooved laminate, is determined numerically via the finite element method using ABAQUS. Some trends are found in the contact pressure distributions across all laminates and cases investigated by observing the results presented in Chapter 5. As seen in Section 6.2, the contact pressure distribution from the numerical analysis is rarely smooth, unless the laminate plies are oriented in a similar direction to give similar material properties along the entirety of the groove, as in the case of the $[\pm 15/0]_{13S}$ laminate. Generally, contact pressure increases in 0° plies, and decreases in 90° plies, with the change in contact pressure from one ply to the next being dependent on the difference in angle between them. These ply-to-ply variations are manifested as superpositions over the basic form of a semi-elliptical pressure curve, reminiscent of the Hertzian distribution.

Before discussing contact pressure trends further, some particular effects that appear due to the discretization and contact model used in the current implementation are discussed. Two contact models were used, one for the finite element models

employing a rigid indentor, and another for the finite element models employing a deformable, linear elastic indentor. Both contact models are subject to limitations arising from the discretization of the laminate, and finite element basis of the models. Thus, the contact pressure, as with the stresses in the laminate, can only be determined and applied at element nodes. In this case, these are the nodes on the groove surface. The contact model employed for the rigid indentor, as described in Section 4.1, considers the indentor as a mathematically described smooth surface. However, contact can still only occur at nodes on the laminate surface. Due to discretization of that surface, some bumps and small ridges do occur in these contact pressure distributions, even within a ply. For example, this is noticeable in the two-dimensional contact pressure distribution for the T700/2510 $[\pm 60/0]_{13S}$ laminate in Figure 5.4 near the $+60°/0°$ ply boundary at a location of ϕ of 15°. Similar features appear in the other laminates as well. This is particularly apparent in many of the contact pressure distributions from the three-dimensional models. These features tend to span on the order of 1° to 2° on the face of the groove, or 0.002 to 0.004 inches of arc length (2 to 4 elements), and represent a change in contact pressure as great as 8%. The contact pressure curves from the two-dimensional models are less jagged than those from the three-dimensional models, with the two-dimensional models generally seeing less than 1% variation, with few exceptions. For example, the contact pressure curves for the T700/2510 $[\pm 45/0/90]_{10S}$ laminate can be contrasted for the two-dimensional model and the three-dimensional model in Figures 5.6 and 5.49, respectively. Ideally, all contact pressure distributions should consist of smooth curves within each ply, as there are no sharp features of geometry, material property, or loading at this length scale to justify such sharp features within a ply. However, the contact pressure from one ply to a neighboring ply would be expected to be discontinuous given the discontinuous change in material properties due to the change in ply angle. The effects of contact model used for the linear indentor are considered in Section 6.5.

The contact pressure is essentially determined by applying a given load to the indentor, which in turn causes a displacement along the groove surface. This causes stresses within the laminate equal to the contact pressure at the surface. This analysis

cycle continues until equilibrium is achieved. The displacement of the nodes along the face of the groove is continuous and follows the contours of the indenting body. This is particularly true for the rigid indentor, although it applies to the elastic indentor as well through a more complicated joint deformation of the indentor and the groove. Since the surface of the groove must deform smoothly, following the geometry of the stiffer indentor, the stiffness of a ply necessarily plays an important role in how much a ply will resist that deformation. The higher the resistance to deformation, the greater the magnitude of the corresponding contact pressure. The relevant stiffness of the ply must be considered in the direction of the applied pressure, in this case normal to the groove surface. Due to the orthotropic nature of the composite material, this is not a trivial consideration, as the angle at which the pressure is applied changes continuously around the groove, while the material orientation, and thus material response, changes from ply to ply as well. Furthermore, in the three-dimensional case, the additional modeling dimension creates complex coupling behavior due to the presence of coefficients of mutual influence and out-of-plane Poisson's ratios. The effects specific to the three-dimensional case are given further consideration in Section 6.7.

Generally, the stiffness of the material in the 3-direction is nearly identical for all ply orientations, since the material is being rotated about the 3-axis. Thus, based on this observation alone, the difference in contact pressure near the bottom of the groove, at low values of the groove angle, ϕ, would not depend significantly on ply orientation. The stiffness of the material in the 1-direction varies significantly, and is highly dependent on ply orientation. The lower the ply angle, the higher the stiffness in the 1-direction, consistent with the direction of the carbon fibers in the composite material. As the angle around the groove, ϕ, increases, the stiffness of plies in the 1-direction becomes more of a factor as displacement from the indentor, and hence the contact pressure, begin to act increasingly in the 1-direction. Thus, as ϕ increases, contact pressure begins to depend increasingly on the ply orientation.

This is not the only consideration in the complex system that results in the observed contact pressures. The stiffness and response of the material beneath the

groove surface, and even the stiffness of the entire structure, are likely to have some influence on the contact pressure as well. Plies that lie beneath the ply in contact offer some supporting stiffness, or potentially lack thereof, which in turn is likely to have an effect on the apparent stiffness at the groove surface, and hence the contact pressure. This stacking of plies, and the influence of subplies, can be likened to a system of springs in series where the stiffness of the individual springs represents the stiffness of various plies. This effect would be most evident, for example, where the displacement of the indentor works at an angle to the groove on a given ply, as it is not only the properties of that ply that determine the contact pressure. In these cases, the contact pressure also depends to some degree on the ply beneath the ply under consideration. This is illustrated in Figure 6.3. This is a likely cause of the gradual increase or decrease in contact pressure in some plies. An example of such is the gradual increase in pressure in the 0° ply in the quasi-isotropic T700/2510 $[\pm 45/0/90]_{10S}$ laminate near a groove angle, ϕ, of 30°, as seen in Figures 5.6 and 5.49 for the two-dimensional case and three-dimensional case, respectively.

In this work, the effect of varying ply angles was investigated using the $[\pm\theta/0]_{13S}$ laminate family with values of θ of 15°, 30°, 45°, and 60°. By comparing the contact pressure distributions across the range of θ values, it is possible to see a number of trends. In contact pressure, the pressures on 0° plies increase as θ increases, and the maximum contact pressure increases as θ increases as well. A visual comparison of the contact pressure distribution for each value of θ is presented for the two-dimensional case in Figure 6.4, and in the three-dimensional case in Figure 6.5 along the center of the laminate for an x_2 value of 0.0. The maximum contact pressures can be compared in Tables 5.1 and 5.5, respectively.

The overlaid comparison of the contact pressures also highlights some of the less obvious effects of varying ply angle. It is clear that at low values of ϕ, along the bottom of the groove, contact pressure increases as θ increases in both the two-dimensional and three-dimensional cases. In the three-dimensional case, this happens regardless of the ply angle. In the two-dimensional case, the pressure increases in $\pm\theta$ plies and decreases in 0° plies. At higher values of ϕ, this trend changes, with contact

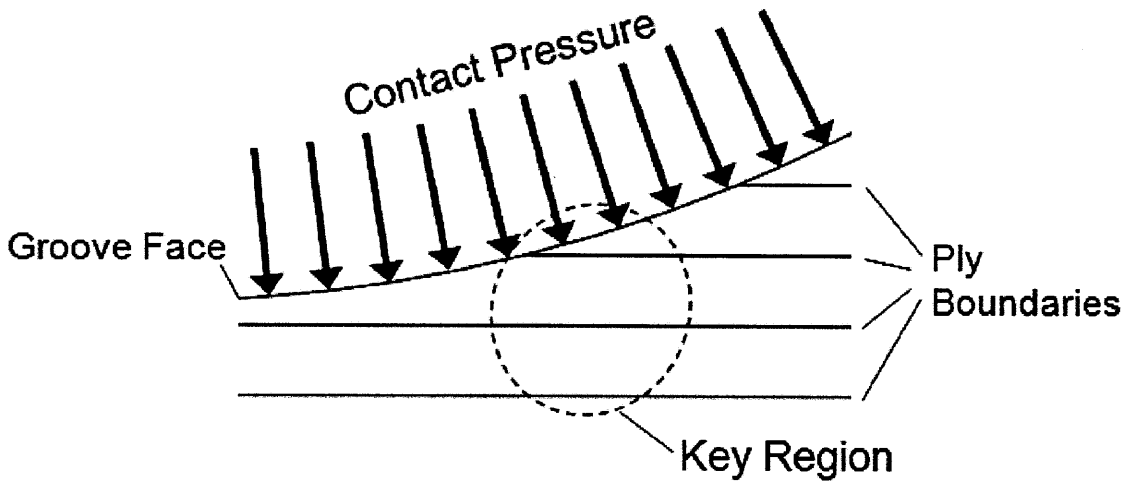

Figure 6.3 Illustration of a region in which contact pressure is most likely to be influenced by properties of the ply beneath the contacted ply.

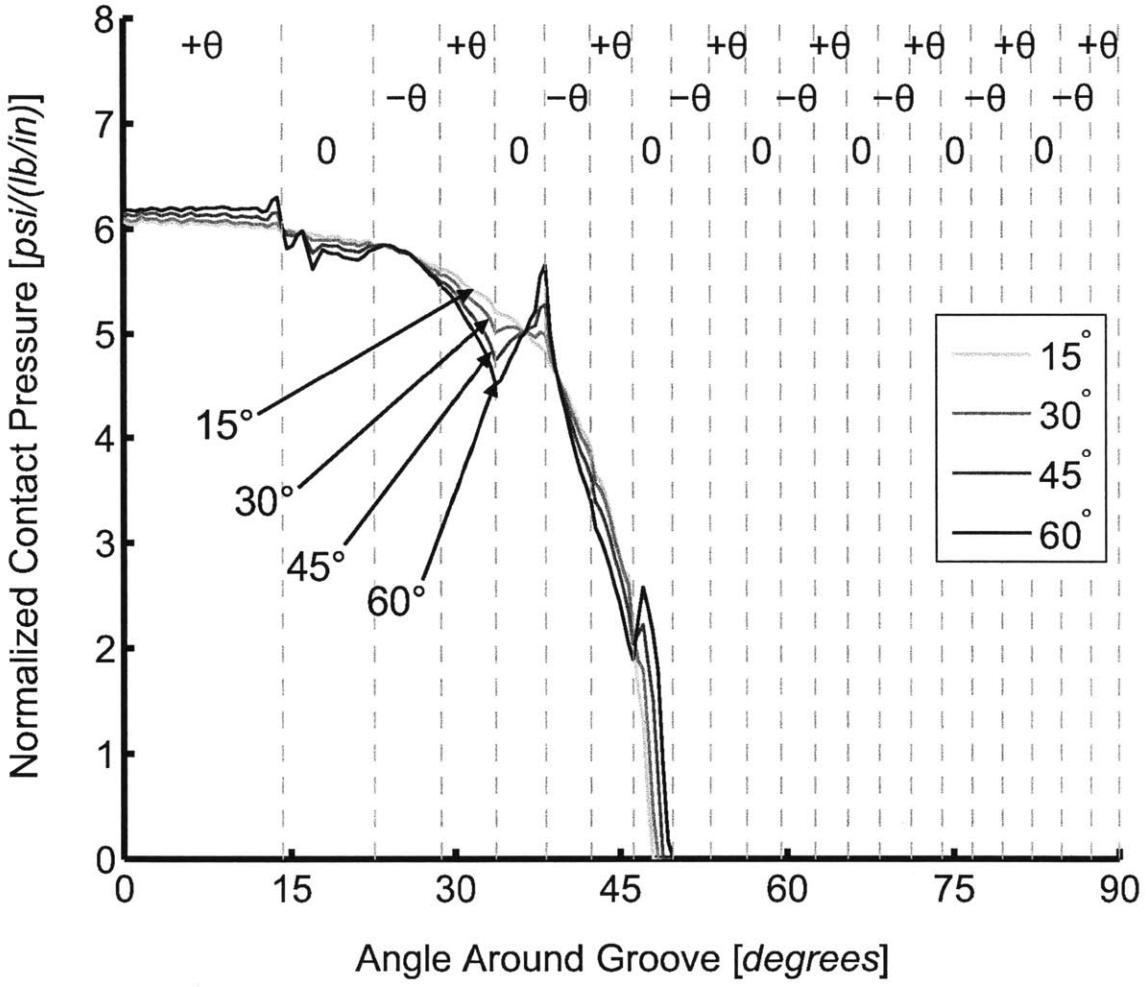

* Note: All pressures normalized by applied load, and given in units of [psi/(lb/in)].

Figure 6.4 Comparison of contact pressure distributions for each of the two-dimensional models of T700/2510 $[\pm\theta/0]_{13S}$ laminates loaded at 5000 lb/in.

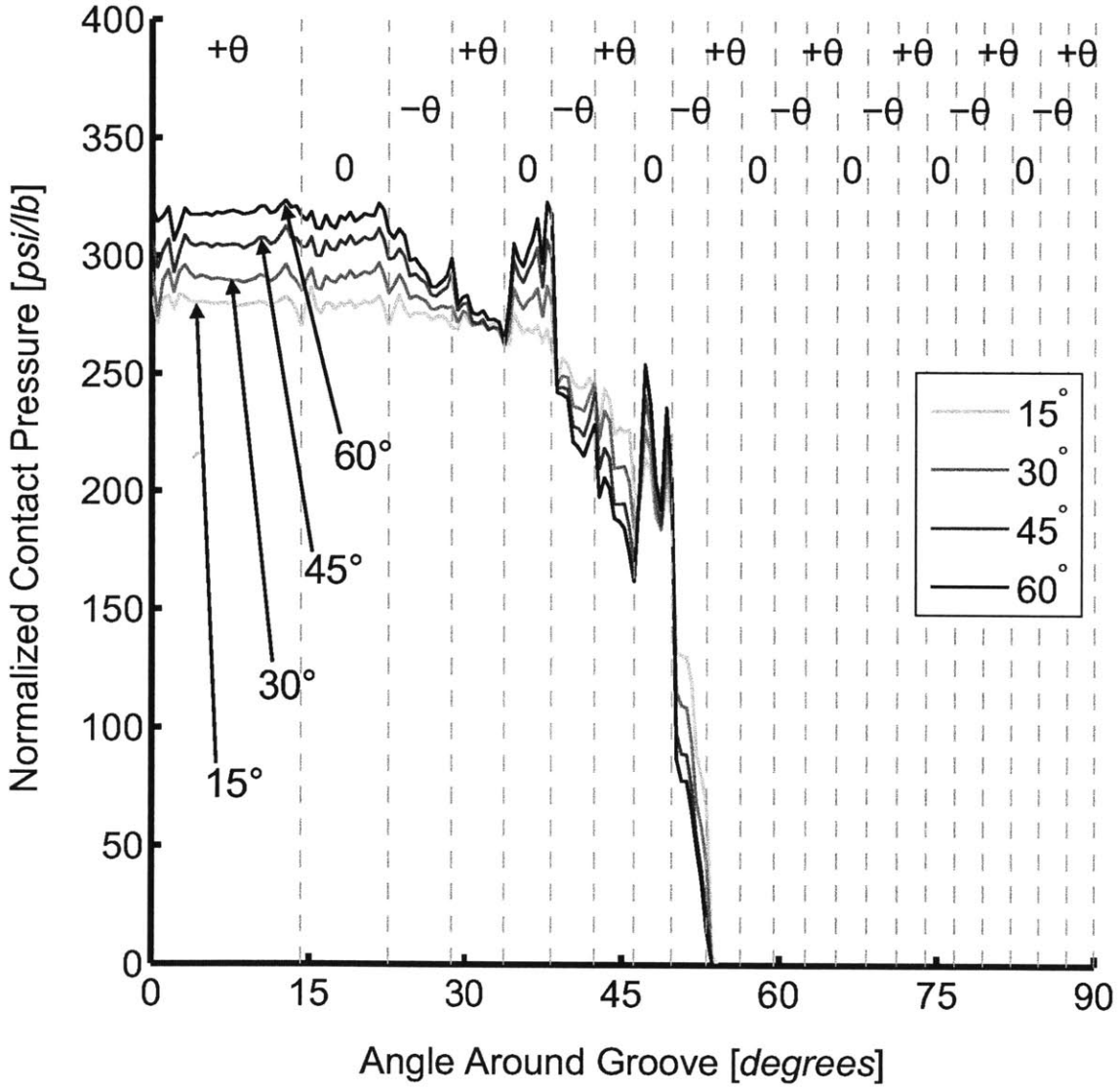

* Note: All pressures normalized by applied load, and given in units of [psi/(lb/in)].

Figure 6.5 Comparison of contact pressure distributions at x_2 equal to 0.0 for each of the three-dimensional models of T700/2510 $[\pm\theta/0]_{13S}$ laminates loaded at 300 lb.

pressure dropping in $\pm\theta$ plies and increasing in 0° plies in both the two-dimensional and three-dimensional cases.

The effects of ply angle on the contact pressure arise from two primary factors: relative stiffness of the angled plies to the 0° plies, and overall "groove stiffness". This concept of "groove stiffness" is defined as the resistance of the surface of the groove to changes in geometry due to the applied loading. This behavior is a consequence of the stiffness of the laminate in the 1-direction and the geometry of the configuration, among other factors. As θ increases, the relative stiffness of the angled plies in the 1-direction and in shear drops considerably. This leads to the 0° plies taking up considerable amounts of the load, particularly at higher groove angles, since the stiffness of these plies is not changing, and is thus relatively higher. In addition, as θ increases, the overall stiffness of the grooved composite structure is dropping, particularly the groove stiffness, which is dependent on the 1-direction stiffness of the material, given its orientation. This causes the groove stiffness to decrease for greater values of θ, allowing the indentor to spread the walls of the groove with less force, and allowing the indentor to settle more fully on the bottom of the groove, and impose a greater pressure there.

6.4 Stress Response

In this work, the stress response of the grooved laminate to contact loading is investigated. The rigid backface boundary condition selected in Section 3.4 allows the effects of the contact loading to be largely isolated from effects of boundary conditions of the overall structural configuration. As a result, the stresses observed are a direct result of the applied contact pressure. By examining the response of the various laminates investigated, trends become apparent relating to the laminated nature of the body, and the particular ply angles involved in the layup. Comparison of the $[\pm\theta/0]_{13S}$ laminates, with values of θ of 15°, 30°, 45°, and 60°, is particularly useful in determining stress variations that are due to variations in ply angle. Three stresses are examined in the results, the longitudinal extensional stress, σ_{11}, the through-

thickness extensional stress, σ_{33}, and the shear stress, σ_{13}. In most cases, these stresses have been normalized by the applied loading. Such stresses are denoted by an asterisk: σ^*_{ij}.

The trends in stress described in this section are presented with examples from the two-dimensional finite element models, as these results are more intuitive. The conclusions hold for the three-dimensional models as well, but additional effects from the third modeling dimension make the discussed trends less obvious. This includes coupling via the coefficients of mutual influence, and out-of-plane Poisson's ratios. Further consideration for the difference between the two-dimensional case and the three-dimensional case are given in Section 6.7.

The longitudinal extensional stress, σ_{11}, is the stress field most heavily influenced by ply angle. An example of common behavior of this normalized stress field in the simpler two-dimensional case in the quasi-isotropic $[\pm 45/0/90]_{10S}$ laminate is shown in Figure 5.14. All the laminates investigated in this work show a great deal of variability in σ_{11} from ply to ply. This ply-to-ply variation appears to be dependent on the difference in ply angle between the neighboring plies. For example, in the two-dimensional case, the $[\pm 15/0]_{13S}$ laminate shows little variation from ply to ply in Figure 5.9 as compared to the $[\pm 60/0]_{13S}$ laminate, which shows larger variation from ply to ply in Figure 5.12. In the two-dimensional case, it is also apparent that neighboring positive and negative angled plies show a much more continuous stress behavior from ply to ply, supporting the assertion that the stress variation is due to ply angle, as positive and negative angled plies have identical material properties for a given angle in the two-dimensional case. Most variation within a ply occurs horizontally, and there is usually little variation vertically within a ply.

The variation in σ_{11} between plies is caused for the most part by the difference in 1-direction stiffness between plies of various angles. For example, the stiffness of 0° plies in the 1-direction is 18.8 Msi, while the stiffness of 90° plies in the 1-direction is 1.94 Msi. Thus, even with identical strains, the longitudinal stress will be higher in the 0° plies. The effect of this decrease in stiffness of higher angled plies can also be observed in the trends of the two-dimensional isostress plots of σ^*_{11} for the $[\pm\theta/0]_{13S}$ laminates,

shown in Figures 5.9, 5.10, 5.11, and 5.12 for values of θ of 15°, 30°, 45°, and 60°, respectively. As the ply angle, θ, increases, the laminates become more compliant in the 1-direction, and thus these stresses decrease in the θ plies while increasing in the 0° plies. It is this behavior that leads to the high variation in maximum normalized stresses amongst the laminates. The variation amongst the laminates for the maximum normalized tensile stress, σ_T^*, is 1.99 psi/(lb/in) to 8.52 psi/(lb/in), or 330%, and the variation in the values of maximum normalized compressive stress, σ_C^*, is 2.29 psi/(lb/in) to 4.43 psi/(lb/in), or 98%.

The ply-to-ply variations make picking out the details of the stress field of σ_{11} difficult. However, it is apparent that there are three primary stress zones, as shown in Figure 5.8, that arise from various causes. Zone 1 is immediately beneath the groove, and is mostly in tension. Stresses in this zone most likely arise from the Poisson's effect from high compressive strains in the 3-direction from the indentor coupled with stresses arising from differential equilibrium considerations. Zone 2 is to the side of the groove, and is mostly in compression. Stresses in this zone most likely arise from the component of pressure from the indentor that is applied to the groove parallel to the 1-direction. Zone 3 extends from the upper wall of the groove, from the point where contact with the indentor ends, to along the top of the laminate, and is primarily in tension. Stresses in this zone most likely arise from the stiffness of the laminate as a structure balanced against the deformation of the local region of indentation, as no load is directly applied to this zone. Of these zones, Zone 1 tends to have the highest tensile stresses, and Zone 2 tends to have the highest compressive stresses. The boundaries of these zones of stress in the laminates are often muddled due to the highly varying stresses from ply to ply.

The through-thickness extensional stress, σ_{33}, remains very consistent across all laminates investigated and is mostly continuous within a laminate, even from ply to ply. This can be seen by comparing the normalized isostress plots of σ_{33}^* from any of the two-dimensional models in Figures 5.16, 5.17, 5.18, 5.19, 5.20 and 5.21. The variation between stress fields is so minor that most isostress plots of this stress field are indistinguishable from one laminate to another. The variations between laminates

become more obvious in the list of maximum stress magnitudes for σ_{33}^* for each of the laminates, given in Table 5.3. In this table, it can be seen that the variation amongst all the laminates in the maximum normalized compressive stress, σ_C^*, is from 6.04 psi/(lb/in) to 6.19 psi/(lb/in), or 2.5%, and the variation in the maximum normalized tensile stress, σ_T^*, is 1.75 psi/(lb/in) to 2.33 psi/(lb/in), or 33%.

The lack of variation in the σ_{33} isostress plots is not surprising, since the material stiffness in the 3-direction remains constant, regardless of ply angle. This explains the lack of ply-to-ply variation within any given laminate, as well as the lack of variation over the laminates as a whole. The variations that are apparent in the list of maximum stress magnitudes is then most likely due to changes in the stiffness of the overall grooved laminate configuration. For example, again considering the $[\pm\theta/0]_{13S}$ laminates, as θ increases, the stiffness of the laminate in the 1-3 plane of modeling decreases since stiffness in the 1-direction decreases with increased ply angle, and stiffness in the 3-direction remains constant regardless of ply angle. Thus, the overall stiffness of the configuration decreases. This results in an increase in contact pressure concentration at the bottom of the groove, as described in Section 6.3, and thus an increase in compressive stress, σ_{33}, beneath the groove. As the stiffness of the structure decreases with increased ply angle, the stiffness of the upper surface of the laminate decreases as well, and its ability to support the downward deformation of the groove is limited, thus decreasing the tensile stress, σ_{33}, from the stretching of the upper wall of the groove. However, as compared to the variation in the longitudinal stress, σ_{11}, the variation in the through-thickness stress, σ_{33}, is relatively minor.

The shear stress, σ_{13}, also remains very consistent across all laminates investigated, and is mostly continuous within a laminate, even from ply to ply. Small variations between neighboring plies become more apparent as the orientation angle between the plies increases. For example, in the $[\pm 15/0]_{13S}$ laminate, the isostress lines for σ_{13}^* are relatively smooth, as seen in Figure 5.23, whereas in the $[\pm 60/0]_{13S}$ laminate, the path of the isostress lines is significantly more variable, but not discontinuous, as seen in Figure 5.26. A minor variation from laminate to laminate is also apparent in the maximum shear stress magnitudes, σ_S^*, shown in Table 5.4, where the variation

in σ_S^* amongst all the laminates is from 2.49 psi/(lb/in) to 2.81 psi/(lb/in), or 12.9%.

The variations in shear stress from ply to ply and laminate to laminate is relatively minor. For the most part, these variations are driven by the change in shear stiffness in the 1-3 plane that are dependent on ply angle. Relative to changes in 1-direction stiffness, these variations in shear stiffness are moderate. For example, shear stiffness in the 0° plies is 0.613 Msi, while shear stiffness in the 90° plies is 0.399 Msi.

6.5 Effect of Elastic Indentor

The majority of the analysis in this work was conducted using a rigid body as an approximation for a steel indentor. A second analysis was conducted using a more physically accurate linear elastic body as an indentor in the two-dimensional case in an effort to judge the validity of the rigid body approximation. The rationale behind the rigid body approximation is that the stiffness of the high strength steel used in the indentor is much greater than the stiffness of the carbon fiber composite laminate in the through-thickness direction, by a factor of approximately 25. Thus, compared to the laminate, the indentor is approximately rigid. However, this approximation becomes less valid when comparing the stiffness of the indentor to the stiffness of the composite along the axis of the fibers. In that case, the stiffness of the steel only varies from the stiffness of the composite by a factor of 1.68. Thus, where the indentor is pressing mostly in the 3-direction, near the bottom of the groove, the rigid body approximation should be very good. However, as the angle around the groove increases, such that more force is applied in the 1-direction, the approximation will become less accurate. This analysis with a linear elastic indentor was conducted with all of the laminates investigated, but results are presented here for the case of the T700/2510 $[\pm 45/0/90]_{10S}$ laminate, as this case is representative of findings from all laminates studied.

Before discussing the results from the models with a linear elastic indentor, consideration must be given to effects observed in the results that are due to the contact model used in this implementation, rather than any physical manifestation. The

analysis using the linear elastic indentor was initially thought to be the ideal solution, most similar to the physical reality of the configuration, since it modeled the material properties of the indentor. There is a known drawback to this method, as it requires the discretization of the indentor using the finite element method, and thus compromises the accuracy of the geometry. The contact model employed for the deformable, elastic indentor allows for the discretization of both the groove surface and the indentor, as described in Section 4.1. This method relies on matching nodes on the indentor surface to nodes on the groove surface, and determining the appropriate pressure the interaction of the two surfaces would generate on each node. However, since both of the interacting surfaces are discretized, local pressure concentrations are likely to occur. The contact scheme used with the deformable indentor, the "Surface-to-Surface" contact scheme, is meant to more accurately distribute the load over the nodes on the groove surface and minimize these local pressure concentrations. To do this, smoothing settings were used through the contact scheme to minimize this node-to-node variation in the form of averaging the impact on one node across many other local nodes. However, these models still suffer from more error in the results due to discretization than the models with rigid body indentors. This error takes the form of jagged oscillations superposed on previously discussed trends in contact pressure, and are a result of the discretization of both the groove surface and indentor surface. It should be noted that any additional smoothing may lessen this effect. However, this could potentially introduce inaccuracies from oversmoothing if averaged over too large of an area. This would need to be addressed if there were to be a desire to approach a more exact solution. While the jagged features seen in this case appear to be similar to those found in the rigid body contact model and discussed previously, their origin and details are different. The features in the contact distribution for the deformable model are more abundant, occur at regular intervals, and are larger in magnitude, as can be seen in the comparison presented in Figure 5.34. These jagged oscillations occur along the entire length of the contact pressure distribution, and with magnitude of the variations of approximately 3% of the base pressure and with a consistent wavelength of three element lengths, or a groove angle

of approximately 1.4°, and are the result of the sharp features created on the faces of the two ideally smooth bodies of the groove and the indentor due to the discretization of these surfaces.

The results of the analysis largely confirm the rigid body approximation. The contact pressure results for the linear elastic indentor as compared to the rigid body indentor for a two-dimensional laminate of T700/2510 $[\pm 45/0/90]_{10S}$ loaded at 5000 lb/in are shown in Figure 5.34. The comparison confirms that the results are largely similar for low values of ϕ, near the bottom of the groove up to a value of ϕ of approximately 40°. In this region, the maximum difference in contact pressure is approximately 3%. There is increasing discrepancy as ϕ increases above a value of 40° up to the end of the region of contact. In this region, the maximum difference is approximately 12%, but the load is also lower. Overall, these two pressure distributions are very similar, despite the differences. The two pressure distributions follow the same trends in ply-to-ply variation, and differences in pressure between the models are minimal for the majority of the range of contact angle, averaging less than 1.4% at values of ϕ of 45° and below, and reasonable for the rest of the range, averaging less than 8.8% from a value of ϕ of 45° to $\phi_{contact}$ equal to 51.2°. The difference in total contact angle from the rigid body model to the linear elastic model is similarly only 3%. These similarities are attributable to the ±45° and 90° plies within the laminate. While the longitudinal stiffness of a unidirectional ply is much more comparable to the stiffness of the steel indentor, only one in four plies approaches that stiffness. For example, in the 1-direction, the stiffness of 45° plies is only 32% of that of a 0° ply, and a 90° ply is only 10.3% as stiff as a 0° ply. In addition, none of the plies are loaded directly along the 1-direction, but all more of a combination of the 1-direction and the 3-direction, as required by the normal to the groove surface. Thus, on average, the approximation still holds, even at higher groove angles. It should be noted that the variation should be expected to increase for even higher contact angles, and that the variation is still greatest in the 0° plies. Thus, a stiffer laminate or a stiffer material will further affect the validity of the rigid body approximation. Conversely, a lower load, yielding a lower contact angle with the majority of contact near the bottom of

the groove, should increase the validity of the rigid body approximation.

The difference in the stress response is a direct function of the difference in the contact loading, all else (material, layup, boundary conditions) being constant between the two models. The stress response can be compared by examining the isostress plots, and the maximum compressive and tensile stresses, for the models with the rigid indentor and the models with the linear elastic indentor. The normalized longitudinal extensional stress, σ_{11}^*, is presented in Figures 5.14 and 5.35 for the models with the rigid indentor and the linear elastic indentor, respectively. The normalized through-thickness extensional stress, σ_{33}^*, is presented in Figures 5.21 and 5.36 for the models with the rigid indentor and the linear elastic indentor, respectively. The normalized shear stress, σ_{13}^*, is presented in Figures 5.28 and 5.37 for the models with the rigid indentor and the linear elastic indentor, respectively. The maximum compressive and tensile stresses for each of these stress fields and the percentage difference between the two is summarized in Table 6.1. The locations of maximum stress are shown in the preceding figures and variation in these locations between the two model types is minimal, with the maximum difference in angular location being 1.6° and the maximum difference in radial location being 0.004 inches.

As can be seen from a comparison of the isostress figures, the stress fields for both the model with the rigid indentor and the model with the linear elastic indentor are nearly identical. It should be noted that the first isostress lines on all plots represent the smallest increases in stress, representing increases of only 0.5 psi/(lb/in), compared to the 1.0 psi/(lb/in) of the higher isostress lines at stresses of 1.0 psi/(lb/in) and greater. Thus, the positions of the 0.5 psi/(lb/in) isostress lines are particularly susceptible to small variations in stress. The largest differences between the two models are seen in the plots for σ_{11}^*, particularly in the 0° plies. Even here, the variation in the position of isostress lines tends to be on the order of one element length, or approximately 0.002 inches. Stresses are not consistently greater or less, but the difference depends on location and ply. For example, the table of stresses shows that the maximum tensile stress increases, while the maximum compressive stress decreases. The isostress plots for the stress fields of σ_{33}^* and σ_{13}^* are nearly

Table 6.1 Maximum normalized stress values for two-dimensional models of a rigid body indentor and of a linear elastic indentor on the T700/2510 $[\pm 45/0/90]_{10S}$ laminate loaded at 5000 lb/in.

Stress Type	**Indentor Model**		**% Difference**
	Elastic *[psi/(lb/in)]*	Rigid *[psi/(lb/in)]*	
Tensile σ_{11}	6.67	6.50	-2.5%
Compressive σ_{11}	4.32	4.43	2.5%
Tensile σ_{33}	1.90	1.90	0.0%
Compressive σ_{33}	5.99	6.04	0.8%
Shear σ_{13}	2.42	2.49	2.9%

identical between the two models, with isostress lines being coincident, or nearly so, in all cases. This same trend can be seen in the maximum stresses where the tensile stress of σ_{33}^{*} is identical in both cases, while the compressive stress is slightly lower in the model of the linear elastic case. The shear stress sees a more significant decrease in stress, but still only of 2.9% in the model of the linear elastic case as compared to the model of the rigid case.

Overall, the rigid body approximation is deemed sufficiently accurate to model the steel indentor in the current work. There are some discrepancies between the results from the model of the rigid body case as compared to the model of the linear elastic case, but these discrepancies are are small, most frequently less than 3%. The difference in the stress response of the laminate between the two indentor models is negligible, and difficult to discern even when overlaid. However, there is also some question as to the accuracy of the linear elastic model as implemented here. As discussed previously, the contact model employed to handle the two discretized surfaces resulted in a jagged oscillation in the contact pressure. This variation in smoothness likely introduces other minor inaccuracies into the models that utilize the linear elastic indentor, specific to this implementation. Given this, the minimal variation in stress and contact pressure between the two models, and the significantly higher computational cost of using a discretized linear elastic indentor, the rigid body indentor is seen as a suitable engineering approximation. Thus, the rigid body indentor was used in the majority of the models in this work.

6.6 Effect of Load Magnitude

The effect of load magnitude on the response of the grooved laminate was investigated by applying various loadings to the indentor and examining the effects on the contact pressure distribution and the stress fields. Although this investigation was conducted using all of the laminates investigated, results for this discussion are presented for the quasi-isotropic T700/2510 $[\pm 45/0/90]_{10S}$ laminate as a representative case. Since results of the contact pressure and all of the stresses are normalized

by the applied load, yielding units of [psi/(lb/in)] in the two-dimensional case and [psi/lb] in the three-dimensional case, the effect of the load magnitude on the response is easily seen. In both the two-dimensional case and three-dimensional case, two primary loadings are compared: a full load, P, and a lower loading that is 20% of the magnitude of the full load. For the two-dimensional case, these loads are 5000 lb/in for the full load and 1000 lb/in for the lower load, with the results presented in Section 5.1.3. For the three-dimensional case, the loads are 300 lb for the full load and 60 lb for the lower load, with the results presented in Section 5.3.3. The numerical contact solution requires establishing contact at incremental load levels, and the contact pressures for these additional loads are presented here as well to show the continuation of the trends established in the results shown in Chapter 5. A plot comparing normalized contact pressure at additional loadings for the two-dimensional case is presented in Figure 6.6. A plot comparing normalized contact pressure along the centerline of x_2 equal to 0.0 at additional loadings for the three-dimensional case is presented in Figure 6.7. Footprints of the contact area at these same loadings are shown in Figure 6.8.

The contact pressure distributions for the two loadings are compared in the two-dimensional case in Figures 5.30 and 6.6, and in the three-dimensional case in Figures 5.106 and 6.7. In both instances, it is apparent that the magnitude of the load has a profound effect on the response. If the response of the laminate was linearly scalable by the magnitude of the load, the contact pressure curves would be coincident since they are normalized by the applied loading. This is clearly not the case for either the two-dimensional or three-dimensional cases. The primary cause of this nonlinearity is the variability in contact area. As increasing load is applied, the rigid indentor causes the laminate to conform to the indentor as it is pressed into the laminate to an increasing degree such that contact area increases. This behavior occurs due to the curved nature of the surfaces that allow for an increasing area of contact as indentor descends, and the laminate deforms. Complex behavior, such as pinching of the indentor by the groove walls, will affect the contact area as well. Nonlinear behavior such as this makes accurately predicting the contact area inherently difficult.

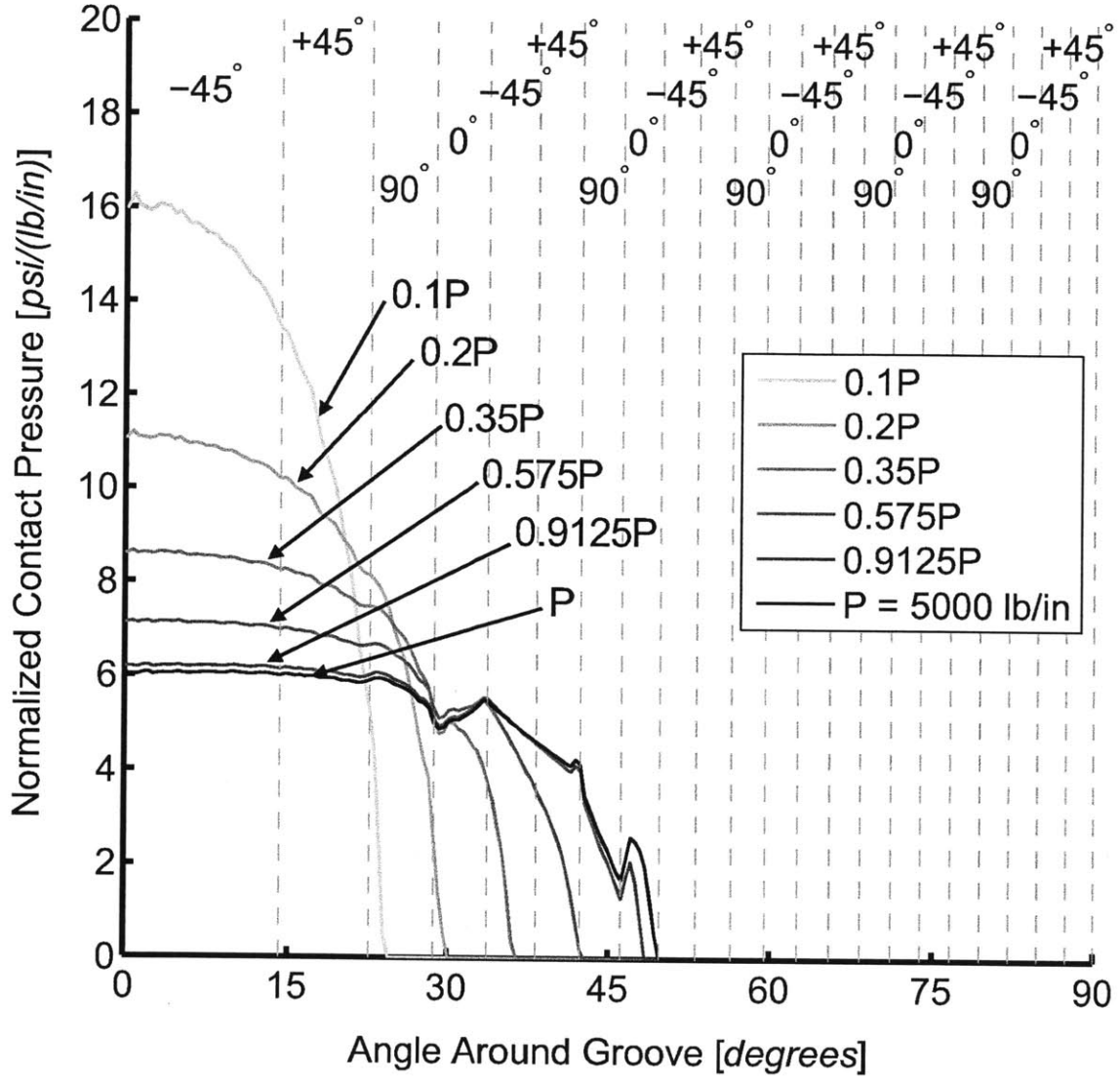

* Note: All pressures normalized by applied load, and given in units of [psi/(lb/in)].

Figure 6.6 Normalized contact pressure for two-dimensional model of T700/2510 $[\pm 45/0/90]_{10S}$ laminate loaded at 10%, 20%, 35%, 57.5%, 91.25%, and 100% of the maximum load of 5000 lb/in.

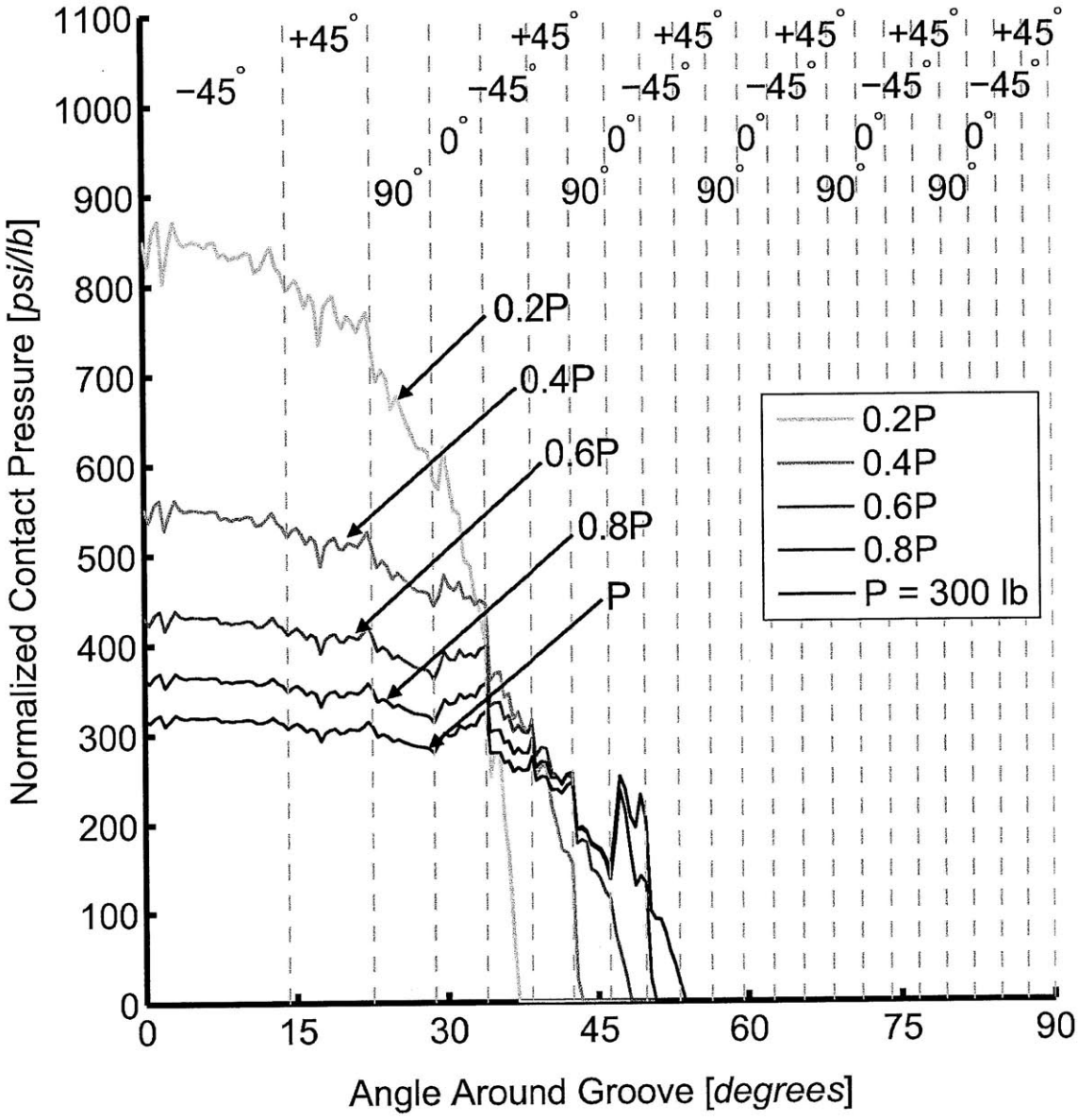

* Note: All pressures normalized by applied load, and given in units of [psi/(lb/in)].

Figure 6.7 Normalized contact pressure along x_2 equal to 0.0 for three-dimensional model of T700/2510 $[\pm 45/0/90]_{10S}$ laminate loaded at 20%, 40%, 60%, 80%, and 100% of the maximum load of 300 lb.

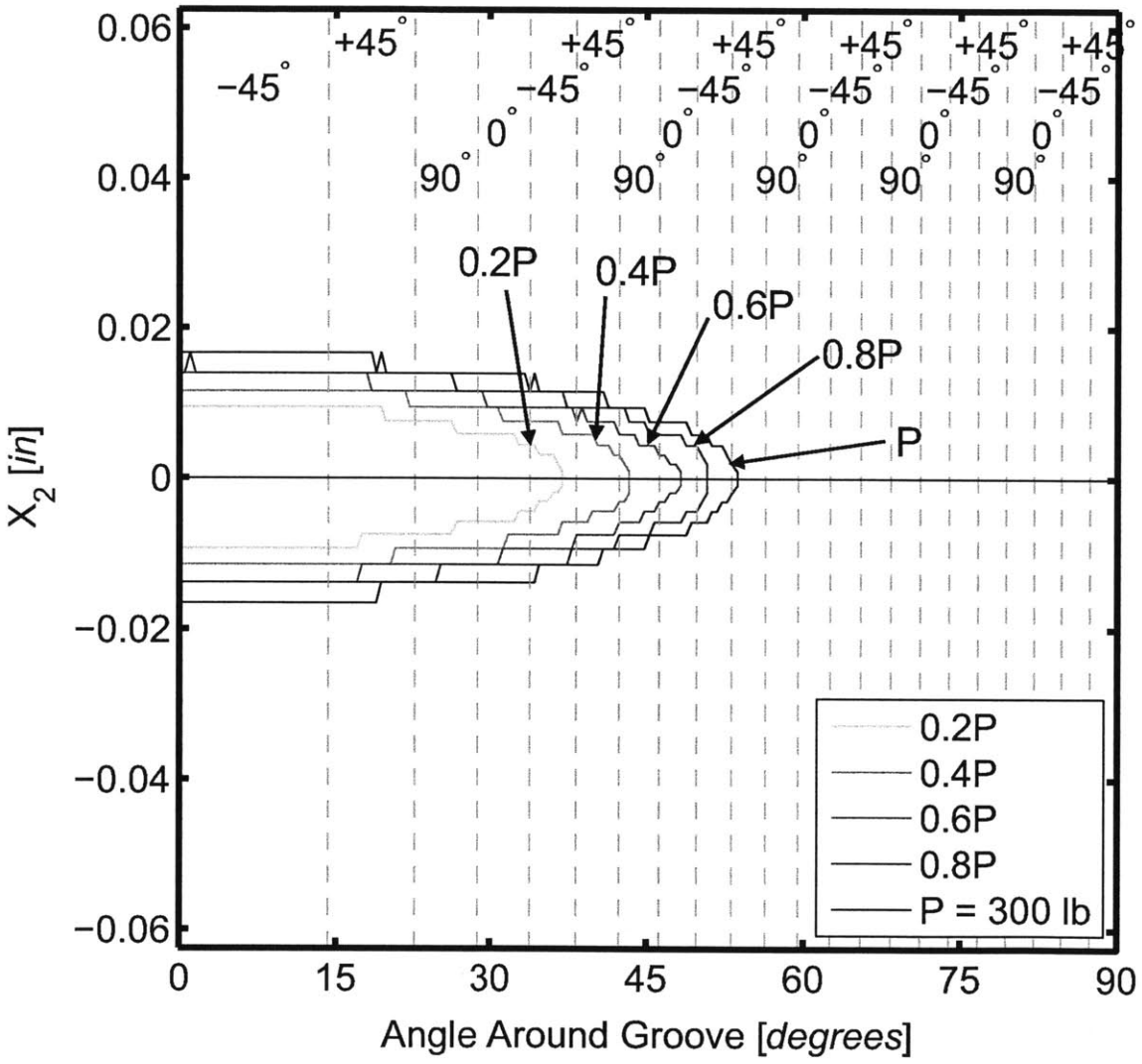

Figure 6.8 Contact area for three-dimensional model of T700/2510 $[\pm 45/0/90]_{10S}$ laminate loaded at 20%, 40%, 60%, 80%, and 100% of the maximum load of 300 lb.

The contact pressure comparisons at the various load levels illustrate the importance of the contact area, or contact angle, in determining the form of the contact pressure distribution. Lower contact areas focus the applied load in a smaller area. As these comparisons are normalized by the applied load, this increase in relative pressure near the bottom of the groove is apparent in the lower loads. As the loading increases, the contact area increases, allowing the load to spread out. This results in lower relative pressures near the bottom of the groove. Note that these changes do not represent decreases in pressure, only normalized pressure. Actual pressure does increase across the range of the groove angle, ϕ, as load increases. However, these comparisons show that the relative increase of pressure towards the center of the groove is significantly lower than the increase in pressure at higher values of ϕ.

It should also be noted that variation in the contact pressure distributions due to ply angle appears to become more defined as load increases. This behavior is likely due to the increase in contact area, which places a higher loading on plies higher up the groove wall, where the variation in the apparent stiffness of the plies is greater due to a greater portion of the load being applied in the 1-direction. Thus, this behavior would only become apparent at loadings that produce contact at higher groove angles. In addition, the changing loads emphasize that the pressure in any given ply also depends on the overall trend of the contact pressure. Thus if the global trend of the contact pressure is decreasing to near zero within a ply, the higher stiffness in that ply may not have as large of an apparent effect. For example, this behavior is seen in the three-dimensional case in the 0° ply near a value of ϕ of 30° at the $0.2P$ load, or in the 0° ply near a value of 45° at the $0.6P$ load.

The stress response also is nonlinearly dependent on the applied load. In the two-dimensional case, the stress responses for the stress fields of σ_{11}^*, σ_{33}^*, and σ_{13}^* are shown in Figures 5.14, 5.21, and 5.28, respectively, for the laminate loaded at 5000 lb/in, and in Figures 5.31, 5.32, and 5.33, respectively, for the laminate loaded at 1000 lb/in. A summary of the maximum normalized stresses for the case of the 1000 lb/in load and the case of the 5000 lb/in load is provided in Table 6.2. In the three-dimensional case, the stress responses for σ_{11}^* are shown in Figures 5.71, 5.72,

5.73, and 5.74 for the laminate loaded at 300 lb, and in Figures 5.107, 5.108, 5.109, and 5.110 for the laminate loaded at 60 lb. The stress responses for σ_{33}^* are shown in Figures 5.90, 5.91, and 5.92 for the laminate loaded at 300 lb, and in Figures 5.111, 5.112, and 5.113 for the laminate loaded at 60 lb. The stress responses for σ_{13}^* are shown in Figures 5.103 and 5.104 for the laminate loaded at 300 lb, and in Figures 5.114 and 5.115 for the laminate loaded at 60 lb. A summary of the maximum normalized stresses for the case of the 60 lb load and the case of the 300 lb load is provided in Table 6.3.

In the two-dimensional case, it is apparent that the extent of all three normalized stress fields is slightly larger at the lower load, by approximately 9% on average. In addition the maximum normalized stresses are much greater at the lower load, by between 12.6% and 83.8%, with much greater stress gradients near the high stress areas. Those stresses that had maximum values at off-axis locations generally have those locations shifted closer to the x_3-axis, and closer to the point of contact. These changes reflect the more concentrated loading seen in contact pressure distributions of the lower loads, where a higher percentage of the load is applied in a smaller area near the bottom of the groove. In the three-dimensional case, the normalized stress fields generally range across a greater distance in x_2, by approximately 12% on average, and across a reduced distance in x_1 at the lower load case as compared to the full load, by approximately 6% on average. The maximum normalized stresses are higher by between 25% and 214%, and the stress gradients are higher at the lower load across all stress fields as well, as in the two-dimensional case. These differences also reflect the way the footprint of the contact area from the indentor changes as load changes. As load increases, contact area increases by approximatley three times more in the 1-direction, or in the angle around the groove, ϕ, than it does comparatively in the 2-direction. In both the two-dimensional and three-dimensional models, the largest impact on stress is seen in the compression and shear values, with the maximum normalized stresses in compression being much higher in the lower loading, by 60-84% in the two-dimensional model and by 167-214% in the three-dimensional model. These results also fit well with the more concentrated loading area seen at the lower

Table 6.2 Maximum normalized stress values for two-dimensional models of T700/2510 $[\pm 45/0/90]_{10S}$ laminate loaded at 1000 lb/in and 5000 lb/in

Stress Type	**Load**		**% Difference**
	5000 lb/in *[psi/(lb/in)]*	1000 lb/in *[psi/(lb/in)]*	
Tensile σ_{11}	6.50	8.57	31.8%
Compressive σ_{11}	4.43	7.09	60.0%
Tensile σ_{33}	1.90	2.14	12.6%
Compressive σ_{33}	6.04	11.1	83.8%
Shear σ_{13}	2.49	4.52	81.5%

Table 6.3 Maximum normalized stress values for three-dimensional models of T700/2510 $[\pm 45/0/90]_{10S}$ laminate loaded at 60 lb and 300 lb

Stress Type	**Load**		**% Change**
	300 lb *[psi/lb]*	60 lb *[psi/lb]*	
Tensile σ_{11}	102	210	106%
Compressive σ_{11}	264	828	214%
Tension σ_{33}	36	45	25%
Compression σ_{33}	316	845	167%
Shear σ_{13}	90	169	88%

loading.

Overall, the results for the grooved composite are not a simple linear function of the applied load. The results show the normalized contact pressures and normalized stresses to be much higher at lower loads than at higher loads, indicating that the stresses are proportionally higher at smaller loads, although the absolute value of the stresses is still smaller at smaller loads. Moreover, the difference in scale of normalized stresses between two different loadings is not consistent across all stresses within a given laminate, indicating that no kind of scaling, linear or otherwise, is applicable to the results. Thus, any accurate analysis of a grooved composite requires numerical analysis at the load of interest to determine the appropriate response.

6.7 Comparison of Cylinder Loading and Sphere Loading

Two major loading configurations were studied in this work: the two-dimensional models representing loading from a cylindrical indentor, and the three-dimensional models representing loading from a spherical indentor. The two-dimensional models were originally envisioned as a simplified way to model the highest stresses from the three-dimensional case. The thinking was that the two-dimensional model could represent a slice of the three-dimensional model. Part of the focus of this work is to determine whether or not this is actually the case. While all of the T700/2510 laminates were modeled in both two and three dimensions, the comparison herein focuses on the quasi-isotropic T700/2510 $[\pm 45/0/90]_{10S}$ laminate as the representative case.

Before continuing with the discussion of results from the three-dimensional model, modeling effects particular to the three-dimensional model and this particular implementation must be examined. As described in Section 4.2, the three-dimensional finite element models utilize a 2-3 plane of symmetry at the groove centerline. This plane of symmetry was used because the computational cost of a model of the full

laminate is prohibitively high. However, this solution is not ideal due to the laminated nature of the structure. While the geometry of the structure is symmetric, the material properties are not. The direction of the orthotropic angled plies cause these to be particularly affected by the plane of symmetry due to the coefficients of mutual influence. A simple model was used to investigate the effects of using this plane of symmetry with a laminate. The investigation focused on a laminated $[0/\pm 45/90]_{4S}$ plate in pure in-plane tension in the 1-direction, perpendicular to the plane of symmetry, with one model using the plane of symmetry, one modeling the full laminate length. It was found that the longitudinal stresses, σ_{11}, at the plane of symmetry in the $\pm 45°$ plies decreased by an average of 31.9% from the case of the full laminate model. Stresses in the 0° and 90° plies consequently rose by 5.1% and 17.2%, respectively, to balance the load across the 2-3 cross-section of the laminate. Stresses within 5% of the value in the full laminate model are recovered within 3.5 ply thicknesses of the plane of symmetry, and stresses within 1% of the value in the full laminate model are recovered within 6 ply thicknesses. No such change in stress was observed at the symmetry boundary condition for a $[0/90]_{8S}$ laminate with identical loading. The lack of coefficients of mutual influence in the 0° and 90° ply orientations lead to no noticeable change in stress at the plane of symmetry. The loading of this simple in-plane tension case is clearly different than the unique loading presented in the grooved composite model, but similar principles still apply. This gives a sense of the possible extent of the higher error for the stresses local to the plane of symmetry.

A comparison of the contact pressure in the two-dimensional and three-dimensional cases is shown in Figure 6.9 loaded at 5000 lb/in and 300 lb, respectively. These pressures in this figure are not normalized for this initial comparison, and the contact pressure for the three-dimensional case is shown only along the centerline at x_2 equal to 0.0, as this is the slice location that the two-dimensional case was originally intended to simulate. It is apparent that there is a significant issue of scale between the two types of models. The contact pressure generated in the three-dimensional case is much greater than the contact pressure in the two-dimensional case. As discussed in Section 6.6, load magnitude has a significant effect on the contact pressure distribu-

tion, most importantly affecting the contact area. As can be seen, despite the vastly different loads, the contact lengths here are similar. However, the pressure values generated are much higher in the three-dimensional case. The difference between the two pressure distributions is essentially not of scale. This makes the two-dimensional case a poor predictor of a slice of the three-dimensional case. Previous results have indicated that increasing the load to scale up the magnitude of the pressure influences the contact length nonlinearly, with the pressure at the center of contact changing increasing at a significantly lower rate than at higher groove angles. This indicates that the two sets of results may be irreconcilable, as increasing the loading of the two-dimensional case to match the pressure magnitude of the three-dimensional case would cause an overestimation of the contact length.

The same two-dimensional contact pressure, normalized by the loading of 5000 lb/in, is shown in Figure 6.10, along with a contact pressure curve along the centerline at x_2 equal to 0.0 from the three-dimensional model at a lower loading of 240 lb. This value for the three-dimensional loading was chosen out of the various loadings that were modeled for this investigation in order to best match the contact length in the two-dimensional model loaded at 5000 lb/in. The three-dimensional contact pressure curve is normalized by the integrated vertical force along this curve. This value can be determined using an equation that determines the vertical component of the contact pressure and integrates that component along the arc length of the groove:

$$P = \int_0^{\pi} p_C(\phi) * \cos(\phi) * r_g \, \mathrm{d}\phi \tag{6.2}$$

where P is the integrated vertical load, p_C is the contact pressure as a function of groove angle, ϕ, and r_g is the radius of the groove. Using this equation, the integrated vertical force along the curve was found to be equal to 14,600 lb/in. This was done in an attempt to make a direct comparison to the two-dimensional case, which is also essentially normalized by the integrated vertical force. This normalization yields very similar curves for the two-dimensional and three-dimensional cases, and allows for the most direct comparison between the trends in each. The three-dimensional

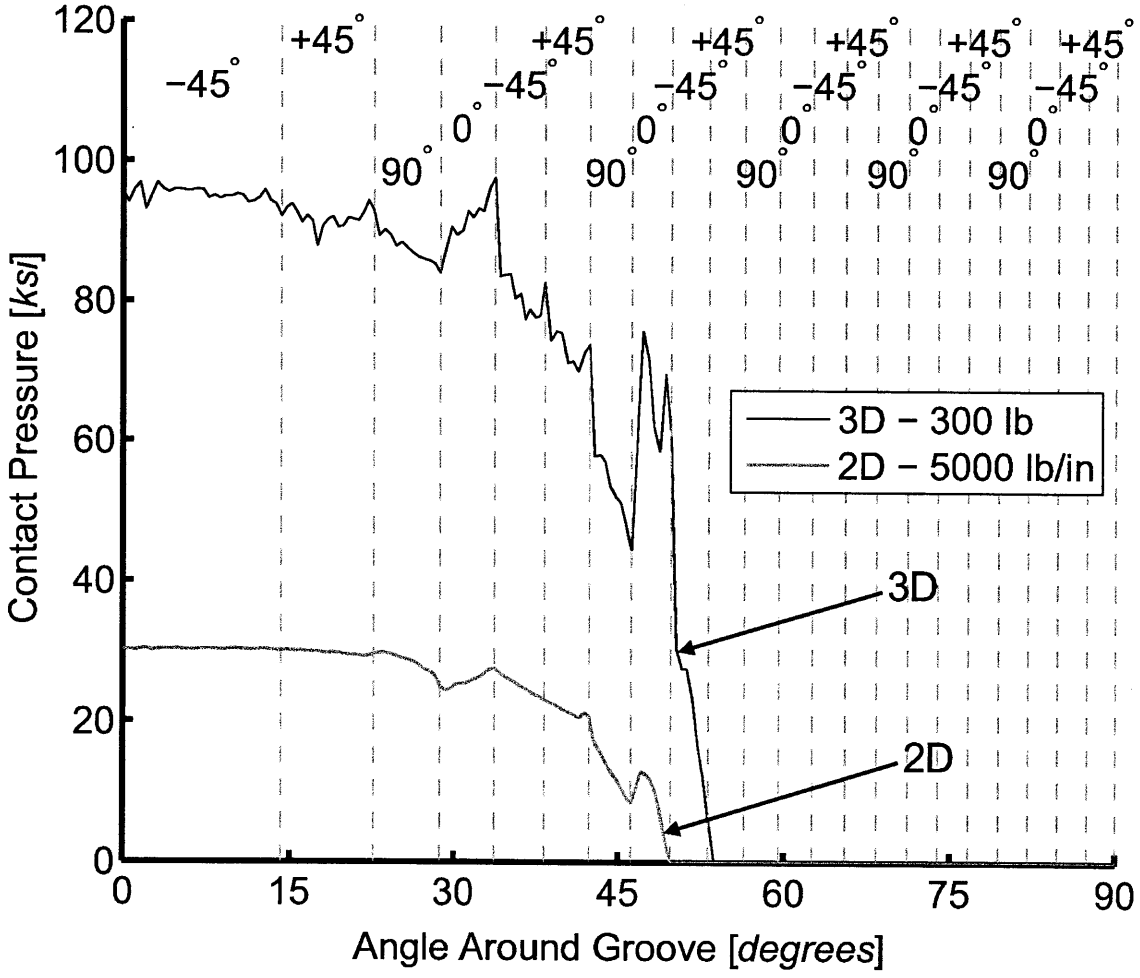

Figure 6.9 Raw contact pressure for the T700/2510 $[\pm 45/0/90]_{10S}$ laminate via two-dimensional model loaded at 5000 lb/in, and along x_2 equal to 0.0 via three-dimensional model loaded at 300 lb.

contact pressure curve is much more jagged and is clearly more affected by the contact discretization issues described in Section 6.3. At the base of the groove, the pressure tends to be slightly higher in the two-dimensional case in the $\pm 45°$ and $90°$ plies by approximately 5%, and slightly lower in the $0°$ ply by approximately 10%. In addition, pressure changes between neighboring plies tend to be a little sharper in the three-dimensional case, and more gradual in the two-dimensional case. However, despite the obvious similarities and minor differences between these two curves, the fact remains that the three-dimensional curve represents nearly a three-fold greater load compared to the two-dimensional model.

The other issue in this comparison deals with the stress response of the grooved laminate to the various applied loadings. Here again in the three-dimensional case it is appropriate to examine the stress distributions for the section cuts at x_2 equal to 0.0 in order to effectively compare with the two-dimensional case. The normalized stress distributions for σ_{11}^* are shown in Figures 5.14 and 5.73 for the two-dimensional and three-dimensional cases, respectively. The normalized stress distributions for σ_{33}^* are shown in Figures 5.21 and 5.92 for the two-dimensional and three-dimensional cases, respectively. The normalized stress distributions for σ_{13}^* are shown in Figures 5.28 and 5.104 for the two-dimensional and three-dimensional cases, respectively. In all these results, the stress fields look similar and carry many similar characteristics. However, it is apparent that the stresses in the three-dimensional case are generally greater in magnitude, with the stress gradients being much greater. This is consistent with the observation that the three-dimensional case places a much greater relative load in a comparable contact area. This results in increased stresses. A summary of the maximum stresses in the two-dimensional and three-dimensional cases is presented in Table 6.4. This shows that the influence of the model varies wildly depending on the stress field, and between tension and compression. The stresses most greatly influenced by the difference in three-dimensional modeling are the compressive aspects of σ_{11} and σ_{33}, with these stresses being 72% and 68% less, respectively, in the two-dimensional models. Comparing all the maximum stress magnitudes between the two-dimensional and three-dimensional cases, there is little consistency to indicate

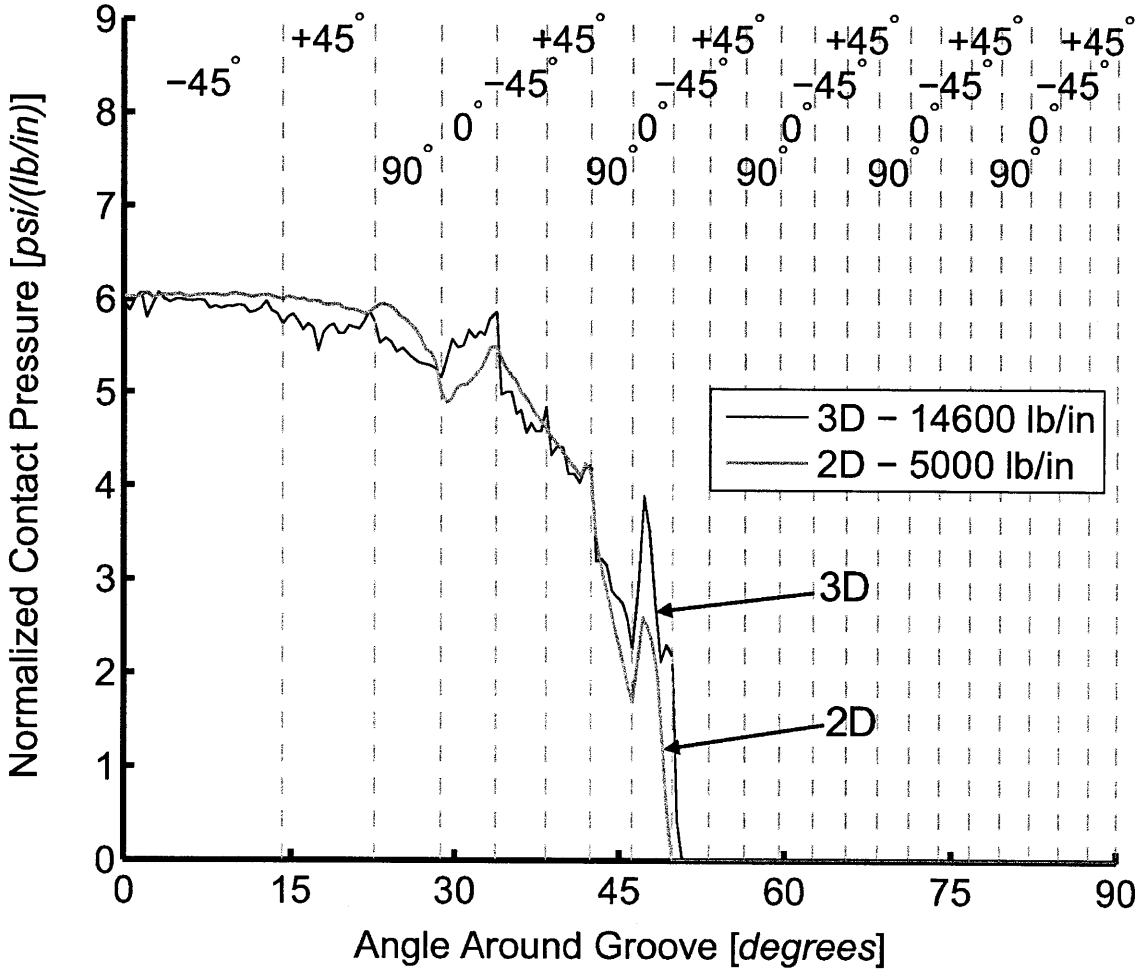

* Note: All pressures normalized by applied load, and given in units of [psi/(lb/in)].

Figure 6.10 Normalized contact pressure for the T700/2510 $[\pm 45/0/90]_{10S}$ laminate via two-dimensional model loaded at 5000 lb/in, and along x_2 equal to 0.0 via three-dimensional model loaded at 240 lb.

results from one case could be scaled or converted in some way to match the results for the other case.

The three-dimensional finite element models are suited to capture behavior in the 2-direction that the two-dimensional models miss. In the two-dimensional models, any variation in stresses, strains, and contact pressure in the 2-direction are assumed to be zero. However, there is actually substantial variation of contact pressure, p_C, in the 2-direction including in the integrated vertical force, as per equation (6.2). This leads to a high gradient $\partial p_C / \partial x_2$, as can be seen in the contact pressure contours from the three-dimensional models in Figures 5.38, 5.40, 5.42, 5.44, 5.46, and 5.48. This variation in contact pressure in the 2-direction must also effect a variation in each of the stress fields in the 2-direction as well. There is further added complexity to the stress response as effects from the gradient in contact pressure are combined with the effects of coupling behavior of the orthotropic plies due to material behavior, such as those of the coefficients of mutual influence, and the out-of-plane Poisson's ratios. Consequently, the results of the three-dimensional models show that there is substantial variation in the stress fields in the 2-direction. For example, isostress plots from section cuts taken along constant values of x_2 in the three-dimensional quasi-isotropic T700/2510 $[\pm 45/0/90]_{10S}$ laminate model are shown in Figures 5.71, 5.90, and 5.103 for the σ^*_{11}, σ^*_{33}, and σ^*_{13} stresses, respectively. The variation in the 2-direction is particularly apparent in the stress field for σ^*_{11}, as behavior is not symmetric about the 1-3 plane, and various features only appear away from the x_3-axis. The stress fields for σ^*_{33} and σ^*_{13} also show a large degree of variation in the 2-direction, but for the most part, these stresses decrease continuously in the 2-direction. No major features in these stress fields would be missed in a section cut at the x_1-x_3 plane, but the stress gradient in the 2-direction would not be captured. However, it should also be noted that, for laminates studied here, the maximum stress magnitudes in the three-dimensional cases largely occur in the x_1-x_3 plane, at values of x_2 of 0.0, or very close to it. This is illustrated in the summaries of maximum stress magnitudes in Tables 5.6, 5.7, 5.8, 5.9, and 5.10.

The comparison of the two- and three-dimensional cases is a complex one. It is

Table 6.4 Maximum stress values for the T700/2510 $[\pm 45/0/90]_{10S}$ laminate via the two-dimensional model loaded at 5000 lb/in and via the three-dimensional model loaded at 300 lb

Stress Type	**Model**		**% Difference**
	3-D $[ksi]$	2-D $[ksi]$	
Tensile σ_{11}	30.6	32.5	6.21%
Compressive σ_{11}	79.2	22.2	-72.0%
Tensile σ_{33}	10.8	9.50	-12.0%
Compressive σ_{33}	94.8	30.2	-68.1%
Shear σ_{13}	27.0	12.5	-53.7%

clear there is no consistency between the two models regarding the load applied and the contact length achieved. For any given contact length, the applied load seems to be much greater in the three-dimensional case. This generally increases the relative stresses and stress gradients in the laminate. In addition, behavior in the three-dimensional case is missed in the two-dimensional case just through a simplifying of the problem to a single plane, as is detailed in Section 5.3. Thus, it seems that any analysis of the groove and a spherical indentor system must be conducted in three-dimensions to accurately capture the behavior of the system. While the two-dimensional model is useful for examining trends through quick analysis, it can only reliably capture the actual stresses and strains of a system involving a cylindrical indentor.

Chapter 7

CONCLUSIONS AND RECOMMENDATIONS

In this work, the response of grooved laminates to out-of-plane conformal contact loading was examined using finite element analysis. This examination involves the effect of ply angle and load magnitude on the contact pressure and stress response of a grooved laminate. Modeling considerations were examined to determine the effectiveness of the Hertzian distribution in approximating the contact pressure, the effectiveness of a rigid body approximation for the indentor, and the use of a two-dimensional model in approximating the full three-dimensional model.

The conclusions that can be drawn from this work are that:

1. The Hertzian method cannot be used to determine contact pressure in the case of a grooved laminate due to an inability to accurately determine the appropriate contact length analytically. In the best case scenario, an approximation could be valid in cases where contact length is known. However, the Hertzian method fails to apply an accurate continuous deformation around the groove and thus fails to capture ply-to-ply variation in contact pressure.

2. The basic form of the distribution of contact pressure between the laminate and indentor is similar in form to the Hertzian case, but with significant local variations due to stiffness variation, primarily in the longitudinal direction, of

the plies.

3. The change in pressure between neighboring plies is dependent on the difference in the orientation angle of those plies and that effect on ply stiffness. This effect becomes more pronounced as the groove angle, ϕ, increases, due to an increase in the component of pressure applied along the longitudinal axis.

4. Contact pressure in stiff plies increases as stiffness of other plies in a laminate decrease, implying the contact pressure depends not only on the local stiffness of a ply, but also on the overall "groove stiffness," and the global stiffness of the laminate configuration.

5. For indentor modeling used with composite laminates, the rigid body approximation of the steel indentor is sufficiently accurate to capture laminate behavior, as compared to the case of a modeled linear elastic indentor, due to the large difference in stiffness between the high-stiffness steel and the low stiffness of the composite in the through-thickness direction. Differences in contact pressure between rigid and linear elastic indentors are minimal, but are higher at higher contact angles around the surface of the groove and in stiffer plies, where increased longitudinal stiffness works against the rigid body approximation.

6. Total vertical load magnitude is a primary factor in laminate response to contact loading, as it determines contact length, and thus the distribution of contact pressure.

7. Response of a grooved laminate, in the form of contact pressure and stress field, does not vary linearly with applied load due to the variation in the relation between load and contact length. Accurate analysis of the response of a grooved composite requires numerical analysis at the load of interest in order to accurately determine contact length and related area, and thus contact pressure and stress response.

8. At lower loads, stresses and contact pressure are relatively larger, and more

concentrated, due to the smaller contact length and related area, resulting in higher relative stresses and stress gradients.

9. There is significant variation between the two-dimensional models and three-dimensional models, particularly in determining the magnitude of the response. The two-dimensional model fails to capture variation in the direction along the groove, most importantly the variation of contact pressure, and the relationship of load to contact length. This variation in loading along the groove carries over to the stress response, where the effect is coupled with material effects due to the orthotropic and directional properties of the laminate plies, such as coefficient of mutual influence.

10. The two-dimensional model is sufficient to observe most trends in the stress field for the three-dimensional case, and therefore could be of of use in preliminary design work, such as selection of a laminate layup. However, a final analysis of the three-dimensional sphere loading of a grooved composite requires full three-dimensional modeling in order to accurately determine the response, specifically the magnitudes of values.

11. Stress behavior is dependent on the laminate and the particular stress, with stress fields between laminates showing some similar trends, but also high variability depending on the composition of the laminate. The through-thickness stress field response has little dependence on the laminate being modeled, the longitudinal stress is highly dependent on the laminate, and the shear stress is moderately dependent on the laminate.

12. Finite element meshes that are symmetric should be utilized for cases where the geometry is symmetric to minimize asymmetric variation due to discretization. This variation is small, but can be eliminated through proper modeling practices. In the case of a grooved composite, finite element meshes should be symmetric about the plane running through the thickness and along the groove.

Based on the results of this investigation, recommendations for further research

are that:

1. Full-length, three-dimensional models should be utilized to model the grooved laminate, without the use of a plane of symmetry, in order to assess the influence of the use of symmetry on the overall response of the groove laminate.

2. The use of nonlinear material behavior, accounting for plasticity and damage, should be investigated in the modeling of grooved laminates, particularly for the case of the three-dimensional, sphere-loaded model. High pressures and stresses local to the point of contact are likely to cause nonlinear material behavior, and the cumulative effects of damage at various loadings should be examined.

3. Effects of laminate properties, such as ply stacking sequence and ply thickness, on the "groove stiffness" and the overall response of the laminate should be assessed. Contact pressure appears to be highly dependent on ply angle and groove angle, such that a sufficiently optimized laminate could minimize stress gradients while maintaining a global laminate stiffness. To this end, the effect of neighboring and sub-surface plies on the contact pressure should also be assessed.

4. The influence of friction in the groove-indentor interaction, and the influence of accurate modeling of friction between the two bodies on the laminate response should be investigated.

REFERENCES

[1] The Boeing Company, "787 Dreamliner - Program Fact Sheet." http://www.boeing.com/commercial/787family/programfacts.html, 2011.

[2] D. Smock, "Boeing 787 Dreamliner Represents Composites Revolution." http://www.designnews.com/article/14313-Boeing_787_Dreamliner_Represents_Composites_Revolution.php, June 2007.

[3] Airbus, "A350 xwb / technology." http://www.airbus.com/aircraftfamilies/passengeraircraft/a350xwbfamily/technology-and-innovation/, 2011.

[4] M. Czajkowski, G. Clausen, and B. Sarh, "Telescopic Wing of an Advanced Flying Automobile," AIAA Paper 1997-5602, World Aviation Congress, Anaheim, CA, Oct. 13-16 1997.

[5] C. Bastien, "Response of a Grooved Plate Subjected to Out-of-Plane Contact Loading," Master's thesis, Massachusetts Institute of Technology, 2008.

[6] Y. Kobayashi, "Establishment of an Experimental Method for a Grooved Composite Subjected to Out-of-Plane Contact Loading," Master's thesis, Massachusetts Institute of Technology, 2009.

[7] H. Hertz, "Uber die beruhrung fester elastischer korper," *Journal Reine Angle Math*, vol. 92, p. 155, 1881.

[8] J. R. Willis, "Hertzian Contact of Anisotropic Bodies," *Journal of the Mechanics and Physics of Solids*, vol. 14, pp. 163–176, 1966.

[9] S. H. Yang and C. T. Sun, "Indentation Law for Composite Laminates," in *Composite Materials: Testing and Design*, pp. 425–449, American Society for Testing and Materials, 1982.

[10] T. M. Tan and C. T. Sun, "Use of Statistical Indentation Laws in the Impact Analysis of Laminated Composite Plates," *Journal of Applied Mechanics*, vol. 52, pp. 6–12, 1985.

[11] L. Keer and G. Miller, "Smooth Indentation of Finite Layer," *Journal of Engineering Mechanics*, vol. 109, pp. 706–717, 1983.

[12] B. V. Sankar and C. T. Sun, "Indentation of a Beam by a Rigid Cylinder," *International Journal of Solids Structures*, vol. 19, pp. 293–303, 1983.

[13] E. Wu and C. S. Yen, "The Contact Behavior Between Laminated Composite Plates and Rigid Spheres," *Journal of Applied Mechanics*, vol. 61, pp. 60–66, 1994.

[14] P. Lagace, J. Williamson, P. Tsang, E. Wolf, and S. Thomas, "A Preliminary Proposition for a Test Method to Measure (Impact) Damage Resistance," *Journal of Reinforced Plastics and Composites*, vol. 12, pp. 584–601, 1993.

[15] W. Jackson and C. Poe, "The Use of Impact Force as a Scale Parameter for the Impact Response of Composite Laminates," *Journal of Composite Technology and Research*, vol. 15, pp. 282–289, 1993.

[16] Y. Kwon and B. Sankar, "Indentation-Flexure and Low-Velocity Impact Damage in Graphite Epoxy Laminates," *Journal of Composites Technology and Research*, vol. 15, pp. 101–111, 1993.

[17] S. M. Lee and P. Zahuta, "Instrumented Impact and Static Indentation of Composites," *Journal of Composite Materials*, vol. 25, pp. 204–222, 1991.

[18] A. Nettles and M. Douglas, "A Comparison of Quasi-Static Indentation Testing to Low Velocity Impact Testing," *Composite Materials: Testing, Design, and Acceptance Criteria, ASTM STP 1416*, pp. 116–129, 2001.

[19] ASTM D6264/D6264M - 07, *Standard Test Method for Measuring the Damage Resistance of a Fiber-Reinforced Polymer-Matrix Composite to a Concentrated Quasi-Static Indentation Force.* American Society for Testing and Materials, December 2007.

[20] D. S. Cairns and P. A. Lagace, "Thick Composite Plates Subjected to Lateral Loading," *Journal of Applied Mechanics*, vol. 54, pp. 611–616, 1987.

[21] B. Sankar, "Interlaminar Shear Stresses in Composite Laminates Due to Static Indentation," *Journal of Reinforced Plastics & Composites*, vol. 8, pp. 458–471, 1989.

[22] A. Tangena and G. Hurkx, "Calculations of mechanical stresses in electrical contact situtations," *IEEE Transactions on Components, Hybrids, and Manufacturing Technology*, vol. 8, pp. 13–20, 1985.

[23] H. S. Jung, *Finite element modeling of static indentation damage in laminated composites.* PhD thesis, University of Florida, 1991.

[24] S. Liu, "Damage mechanics of cross-ply laminates resulting from transverse concentrated loads," in *ICCM/9 Composites Behaviour*, vol. V, International Committee on Composite Materials, 1993.

[25] A. Faulkner, K. C. Tang, S. Sen, and R. D. Arnell, "Finite element solutions comparing the normal contact of an elastic-plastic layered medium under loading by (a) a rigid and (b) a deformable indenter," *Journal of Strain Analysis*, vol. 33, no. 6, pp. 411–418, 1998.

[26] V. Tita, J. de Carvalho, and D. Vandepitte, "Failure analysis of low velocity impact on thin composite laminates: experimental and numerical approaches," *Composite Structures*, vol. 83, pp. 413–428, 2008.

[27] H. E. Johnson, L. A. Louca, S. Mouring, and A. S. Fallah, "Modelling impact damage in marine composite panels," *International Journal of Impact Engineering*, vol. 36, pp. 25–39, 2009.

[28] V. Rizov, "Failure behavior of composite sandwich structures under local loading," *Archives of Applied Mechanics*, vol. 79, pp. 205–212, 2009.

[29] C. Hoppel, T. Bogetti, and J. Gillespie, "Devices for Transmitting High Shear Loads in Composite Structures," *Proceedings of the American Society for Composites*, pp. 437–446, 1996.

[30] G. Montay, O. Sicot, X. Gong, A. Cherouat, and J. Lu, "Determination of the Residual Stresses in Composite Laminate Using the Compliance Method," in *Proceedings of the 7th International Conference on Residual Stresses (ICRS-7)*, vol. 490-491, pp. 533–538, Materials Science Forum, 2005.

[31] C. J. Bastien and P. A. Lagace, "Response of Grooved Laminated Plates to Out-of-Plane Contact Loading," in *Proceedings of the 50th AIAA/ASME/ASCE/AHS/ASC Structures, Structural Dyanmics and Materials Conference*, (Palm Springs, CA), 2009.

[32] H. K. Jeffrey, "Response of Grooved Composites to Transversely Distributed and Localized Spherical Contact Loading," Master's thesis, Massachusetts Institute of Technology, 2011.

[33] T. Harris and M. Kotzalas, *Essential Concepts of Bearing Technology*, ch. Rolling Bearing Analysis. CRC Press, 5 ed., 2007.

[34] Dassault Systemes, Simulia Corp., *Abaqus/CAE User's Manual v6.8*, 2008.

[35] Dassault Systemes, Simulia Corp., *Abaqus Analysis User's Manual v6.8*, 2008.

[36] Dassault Systemes, Simulia Corp., *Abaqus Theory Manual v6.8*, 2008.